



University of Pisa
Department of Mathematics

PhD Course in Mathematics
(XXX cycle, 2014-2017)

On Impact Monitoring of Near-Earth Asteroids

by

Dr. Alessio Del Vigna
delvigna@mail.dm.unipi.it

Thesis Submitted in Fulfilment of the Requirements
for the Degree of Doctor of Philosophy

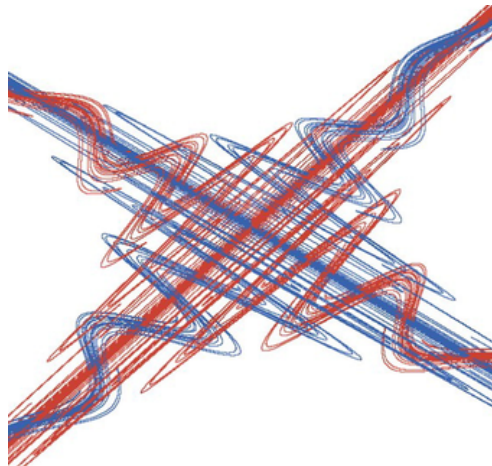
Supervisor
Prof Andrea Milani †
University of Pisa

PhD director
Prof Giovanni Alberti
University of Pisa

10 December 2018

“When one tries to depict the figure formed by these two curves and their infinity of intersections, each of which corresponds to a doubly asymptotic solution, these intersections form a kind of net, web or infinitely tight mesh; neither of these two curves can ever cross itself, but must fold back on itself in a very complex way in order to cross the links of the web infinitely many times. One is struck by the complexity of this figure that I am not even attempting to draw. Nothing can give us a better idea of the intricacy of the three-body problem, and of all the non-integrable problems of dynamics in general.”

(H. Poincaré, *New Methods of Celestial Mechanics*, 1899)



“What is it indeed that gives us the feeling of elegance in a solution, in a demonstration? It is the harmony of the diverse parts, their symmetry, their happy balance; in a word it is all that introduces order, all that gives unity, that permits us to see clearly and to comprehend at once both the ensemble and the details.”

(H. Poincaré, *Science and method*, 1908)

Acknowledgments

Finally these years of PhD is coming to an end and it is time to thank all the people that have supported me in writing this thesis, both directly and indirectly.



The first person I want to thank is my supervisor *Andrea Milani*. Unfortunately he passed away a couple of weeks before the defence of this thesis and the simple act of rewriting this part of the acknowledgments deepens my sense of loss. Andrea has been a source of continuous inspiration and a brilliant professor, full of knowledge and new ideas. For the research I decided to do, I could have never had a better supervisor.

I thank the referees of my thesis, *Giovanni B. Valsecchi* and *Steven R. Chesley*, for their suggestions that improved the quality of this manuscript.

I am grateful to the company *SpaceDyS* for having sponsored my PhD. SpaceDyS gave me the opportunity to work together with brilliant young researchers and, above all, wonderful persons. Without them, my days would have been much longer and less funny than they have been.



Thanks to *Sonia* for the growth that these years represented for us. Sharing this experience and my life with you is the best gift I could have ever asked for.

Thanks to *Alessio* and *Giuliaaaa* (oops! I meant *Giulia*), true friends, unlimited source of laughs, and because all four of us together are *GASA*¹.

Thanks to *Fabio* and *Lisa*, they are not just fabulous dance teachers but very much more. Having spent time with them and with all the ED-team has made my evenings nicer.

¹By quoting ourselves: “Giù, Allè, Sò, Allè”.

Thanks to *Francesca*, *Federica*, and *Laura*. It has been a stroke of luck that our paths crossed!



I have always had a passion for teaching and during my PhD I also had the pleasure to teach in several classes. Thus I would like to thank *Giuseppe Puglisi* for his trust and for the hilarious time spent together. He is the first professor I met when I was attending the high school: thanks to his lectures I immediately got into number theory and mathematics.

I also want to thank *Claudio Bonanno*. The passion in the research he does and his constant support allowed me to appreciate the beauty of dynamical systems and ergodic theory and to start working in this field.

Alessio Del Vigna
December 2018

Contents

Acknowledgments	i
Abstract	1
1 An overview of the Impact Monitoring	9
1.1 Motivations	9
1.2 Risk scales	10
1.3 Brief history	11
1.4 The case of Apophis	12
1.5 Impact monitoring: mathematical theory	13
1.5.1 Sampling of the confidence region	14
1.5.2 LOV propagation	15
1.5.3 Stretching and width	16
1.5.4 Return analysis	17
1.5.5 Geometry of the LOV trace on the TP	17
2 Imminent impactors	21
2.1 Very Short Arcs, sometimes too short	22
2.2 The Admissible Region	24
2.2.1 Excluding interstellar orbits	24
2.2.2 The inner boundary	27
2.2.3 Formal definition of the Admissible Region	30
2.3 Sampling of the Admissible Region	31
2.3.1 Case I: the rectangular grids	31
2.3.2 Case II: spider web	33
2.4 The Manifold Of Variations	33
2.5 Approach for probability computations	35
2.6 Probability density function computation	37

2.6.1	Spaces and maps	37
2.6.2	Conditional density on an affine subspace	39
2.6.3	From the residuals space to the MOV	41
2.6.4	From the MOV to the AR	43
2.6.5	From the AR to the sampling space	44
2.7	Extras on the probability density propagation	46
2.7.1	Conditional density on each attributable space	46
2.7.2	Full non-linear propagation	47
2.8	Use of the probability density function	49
2.8.1	Impact probability computation	49
2.8.2	Score computation	50
2.9	Results	50
2.9.1	Graphical representation of the results	52
2.9.2	Asteroid 2008 TC ₃	53
2.9.3	Asteroid 2014 AA	54
2.9.4	Asteroid 2014 QF ₄₃₃	54
2.9.5	Asteroid 2017 AE ₂₁	57
2.9.6	NEOCP object P10vxCt	59
2.10	Conclusions	62
3	Detecting the Yarkovsky effect among NEAs	65
3.1	Introduction	65
3.2	Method	67
3.2.1	Force model	67
3.2.2	Average semimajor axis drift	68
3.2.3	Statistical treatment of the astrometry	70
3.2.4	Starting sample of NEAs	72
3.2.5	Yarkovsky expected value	73
3.2.6	Filtering criterion	75
3.3	Accepted and significant results	76
3.4	Rejected results	79
3.5	Marginal significance	82
3.6	Direct radiation pressure detection	82
3.7	Comparison with JPL results	84
3.8	Impact monitoring with non-gravitational parameters	85
3.9	Conclusions and future work	86
4	Completeness of Impact Monitoring	95
4.1	Generic completeness definition	96
4.2	An optimal method for LOV sampling	98
4.3	Missing VI detection: possible causes	101

4.3.1	Duplicated points in the same return	101
4.3.2	Proof of completion for the decomposition scheme . . .	103
4.3.3	Extreme non-linear cases	105
4.4	Results	106
4.5	Analytical formulation for the time evolution	109
4.6	Comparison with JPL results	114
4.7	Conclusion and future work	116
5	The evolution of the LOV at close encounters	119
5.1	Extended Öpik's theory of close encounters	119
5.1.1	Coordinates on the b -plane	121
5.1.2	Pre-encounter state vector	122
5.1.3	The encounter	122
5.1.4	Propagation to the next encounter	123
5.2	Resonant returns	124
5.3	The wire approximation	125
5.3.1	Local minima and maxima of the post-encounter semi- major axis	125
5.4	Post-encounter local MOID along the wire	126
5.4.1	Numerical check	131
5.5	Rotation of the velocity along the wire	131
5.6	Conclusions	135
6	Semilinear method for impact corridor	137
6.1	The semilinear method	137
6.2	Determination of the impact corridor	139
6.3	Results	141
6.3.1	Evolution of the impact corridor for 2008 TC ₃	142
6.3.2	Apophis	144
A	Target Planes	147
A.1	Angular momentum	147
A.2	The first transformation	148
A.3	The second transformation	151
A.4	The third transformation	151
A.5	Modified Öpik elements	153
B	The Farey sequence	155
B.1	Arithmetical functions	155
B.1.1	Euler totient function	156
B.1.2	The Möbius function	156
B.2	Dirichlet series	158

B.3	The Farey sequence	160
C	Recap of manifolds and integration	163
D	Orbit determination: mathematical theory	167
D.1	The problem	167
D.2	The minimum principle	168
D.3	The least squares method	169
D.3.1	Non-linear least squares	169
	Bibliography	185

List of Figures

1.1	Graphical representation to compute the Torino Scale, and hence the associated color to classify the risk from white (no risk) to red (certain impact) passing through green, yellow and orange.	11
1.2	The quantities used to classify the behaviour of two consecutive TP points are obtained from the geocentric vectors P_i and their derivatives (with respect to the LOV parameter) S_i	18
2.1	<i>Top panel.</i> Grid sample of the $(\rho, \dot{\rho})$ space for the first 4 observations of 2008 TC ₃ . <i>Bottom panel.</i> Spider web for the first 7 observations of 2008 TC ₃	53
2.2	<i>Top panel.</i> Grid sample of the $(\rho, \dot{\rho})$ space for the first 3 observations of 2014 AA. <i>Bottom panel.</i> Spider web for the whole set of 7 observations of 2014 AA.	55
2.3	<i>Top panel.</i> Grid sample of the $(\rho, \dot{\rho})$ space for the first 4 observations of 2014 QF ₄₃₃ . <i>Bottom panel.</i> Enlargement of the second component. The black star in the second component represents the orbit of the object computed with all the available observations.	56
2.4	<i>Top panel.</i> Grid sample of the $(\rho, \dot{\rho})$ space for the first 3 observations of 2017 AE ₂₁ . <i>Bottom panel.</i> Grid sample for the whole set of 5 observations of 2017 AE ₂₁ . In both cases we do not have any reliable nominal orbit to use, and as a consequence we adopt the grid sampling.	58
2.5	<i>Top panel.</i> Grid sample of the $(\rho, \dot{\rho})$ space for the first 3 observations of P10vxCt. <i>Bottom panel.</i> Grid sample for their remeasurement of P10vxCt.	60

2.6	Plot of the two batches of observations reported in Table 2.2, for NEOCP object <i>P10vx Ct</i> . The red line represents the originally submitted tracklet, whereas the blue line the re-measured tracklet. The higher curvature of the first arc with respect to the second is clear.	61
3.1	Graphical representation of the partition of the detections set into classes on the plane $(\text{SNR}_{A_2}, \mathcal{S})$. We plot the accepted detections (green dots), the marginally significance detections (blue dots) plus the special cases (410777) 2009 FD and (99942) Apophis (blue asterisk), and the rejected detections (red crosses).	77
4.1	Graph of the step-size as a function of the LOV parameter σ , with the parameter choice as in (4.6). <i>Orange line</i> : step-size for the uniform-in-probability sampling. <i>Green line</i> : uniform step-size, as previously used by CLOMON-2.	100
4.2	Extended shower around the year 2069 for asteroid 2000 SG ₃₄₄ . For each virtual asteroid belonging to the shower, we plot the closest encounter date against the LOV index (black crosses). The virtual asteroids that appear more than one times in the same return are highlighted (orange triangles).	102
4.3	Application of the decomposition procedure to a return of the extended shower of 2000 SG ₃₄₄ . The return is decomposed into three sub-showers, represented with different marks and colors (orange, green, and gray, respectively). We mark with a black circle the first point (in terms of time) of each sub-shower: in particular, the first LOV indices of the three sub-showers are 1604, 1414 and 1766, respectively.	104
4.4	<i>Left panel</i> . Histogram of the number of virtual impactors (as of October 2016) as a function of the inverse of the impact probability, in the case of uniform sampling in σ . <i>Right panel</i> . Log-log plot of the histogram bar tips and corresponding regression line, providing $\alpha \simeq 0.678$	108
4.5	<i>Left panel</i> . Histogram of the number of virtual impactors (as of October 2016) as a function of the inverse of the impact probability, in the case of uniform-in-probability sampling. <i>Right panel</i> . Log-log plot of the histogram bar tips and corresponding regression line, providing $\alpha \simeq 0.664$	108

4.6	<i>Left panel.</i> Histogram of the inclination i (deg). <i>Right panel.</i> Histogram of the absolute magnitude H . Both the plots are referred to the set of 734 asteroids in the NEODyS Risk List (as of April 2018).	110
4.7	Log-log plot of the cumulative number of virtual impactors \mathcal{N} as a function of the relative time t_{rel} (y). The points selected for the linear fit are marked with green circles. The orange straight line is the best-fit line obtained from the linear fit. . .	112
4.8	Plot of the cumulative number of virtual impactors \mathcal{N} as a function of the relative time t_{rel} (y).	112
4.9	Histogram of the number of virtual impactors in the NEODyS Risk List as a function of the inverse of the impact probability (as of April 2018).	115
4.10	Histogram of the number of virtual impactors in the Sentry Risk List as a function of the inverse of the impact probability (as of April 2018).	115
5.1	The Earth encounter of 2012 TC ₄ on 12/10/2017. The plot shows the deformation of the LOV for $\xi_0 = -4$ and $\xi_0 = -2$ Earth radii. The black circle represents the Earth cross section. The black dots are the points belonging to the two LOVs points. The red dots show, for $\xi_0 = 4$, the corresponding points in the post-encounter b -plane and the blue dots do the same for $\xi_0 = -2$	128
5.2	Same as Figure 5.1, highlighting relevant b -plane loci (Valsecchi et al. 2018). The cyan hyperbola corresponds to $\partial \cos \vartheta' / \partial \zeta = 0$. The black straight line is the condition for $\vartheta' = \vartheta$ (Valsecchi et al. 2000), implying $a' = a$ and $\xi' = \xi$. The green circle is the condition $\cos \vartheta' = 0$ (in this particular case giving $a' = 1.05$ au), corresponding to $\xi' = \xi \sin \vartheta$	129
5.3	Same as Figure 5.1, but in this case the dots come from numerical integrations in the circular restricted three-body problem.	132
5.4	The possible rotation of \mathbf{U}' for the 2017 encounter of 2012 TC ₄ .	134
5.5	The possible rotation of \mathbf{U}' for the 2017 encounter of 2012 TC ₄ , for a value of ξ_0 resulting in $\gamma_{max} = 90$ deg.	134
5.6	The possible rotation of \mathbf{U}' for the 2017 encounter of 2012 TC ₄ , for a positive value of ξ_0 resulting in $\gamma_{max} = 39$ deg.	135
6.1	Graphical sketch of the application of the semilinear method described above in the steps (1)-(3).	141

6.2	Prediction of the impact region of 2008 TC ₃ using the first 12 observations (almost 18 hours before impact).	143
6.3	Prediction of the impact region of 2008 TC ₃ using the first 16 observations (about 12 hours before impact).	143
6.4	Prediction of the impact region of 2008 TC ₃ using the first 26 observations (about 11 hours and a half before impact). . . .	143
6.5	Prediction of the impact region of 2008 TC ₃ with 883 observations.	145
6.6	Enlargement of the previous plot between $h = 37$ km and $h = 0$ km.	145
6.7	<i>Top panel.</i> Semilinear prediction of the 2029 impact regions of Apophis, using the observations available on 2004 December 27. <i>Bottom panel.</i> Monte Carlo prediction of the 2029 impact locations of Apophis, using the same observational dataset of the above figure (JPL, private communication).	146

List of Tables

1.1	Classification of LOV segments on the TP between two consecutive VAs. The six fundamental types are listed first, followed by special cases that are unique to either CLOMON-2 or Sentry. ^(a) If both $ \sin \beta_1 \geq \sin \beta_{lim_1}$ and $ \sin \beta_2 \geq \sin \beta_{lim_2}$, CLOMON-2 only. For a discussion on the choice of the limit values for $\sin \beta_i$ refer to Milani et al. (2005b). ^(b) If both $\cos \beta_1 < 0$ and $\cos \beta_2 < 0$, Sentry only.	19
2.1	Results of systematic ranging applied to 2008 TC ₃ and 2014 AA. The columns contain the name of the object, number of observations used, time span covered by the observations, characteristic of the sampling used to compute the MOV (grid or spider web), score of the object (NEO, MBO or Distant), and impact probability.	55
2.2	Astrometric data for NEOCP object <i>P10vx Ct</i> . First tracklet with 3 observations (above), and remeasurement of the first tracklet from the discovery images (below).	59
3.1	Perturbing bodies included in the dynamical model in addition to the Sun, the planets and the Moon. They are 16 massive main belt bodies and Pluto. The last columns shows the references we used for each asteroid mass.	69
3.2	Values of the physical quantities for the asteroid (101955) Benu, used in equation (3.2).	73
3.3	Representative asteroids for some taxonomic classes: number/name, taxonomic type, densities as in Carry (2012) with their uncertainties, scaled densities applying the factor $1 - \mathcal{P}_B$	74

3.4	List of Yarkovsky detections with $\text{SNR}_{A_2} > 5$ and with $\mathcal{S} \leq 2$. The table is sorted by SNR_{A_2} , in decreasing order. The columns contain the asteroid name, the absolute magnitude H , the A_2 parameter with its uncertainty and signal-to-noise ratio SNR_{A_2} , the semimajor axis drift da/dt with its uncertainty, the indicator parameter \mathcal{S} , the geometric albedo p_v , the diameter D and the taxonomic class. Asteroids with no available information about the diameter are marked with an asterisk (*). Asteroids with albedo assigned according to Binzel et al. (2002) since no direct estimate is available are marked with a “d”. Asteroids with no albedo informations are marked with a dagger (†).	78
3.5	List of Yarkovsky detections with $3 \leq \text{SNR}_{A_2} < 5$ and with $\mathcal{S} \leq 2$. The table is sorted by SNR_{A_2} , in decreasing order. Columns and symbols are the same as in Table 3.4.	89
3.6	List of rejected Yarkovsky detections. Each group of asteroids in the table is sorted by SNR_{A_2} , in decreasing order. The columns are the same as in Table 3.4, but the one showing da/dt	90
3.7	List of marginal significance detections, which means $2.5 < \text{SNR}_{A_2} < 3$ and $\mathcal{S} \leq 2$. The table is sorted by SNR_{A_2} , in decreasing order (apart from the two special cases at the top). Columns and symbols are the same as in Table 3.4.	90
3.8	List of detections including both the Yarkovsky effect and solar radiation pressure, that is the set of asteroids for which the parameter A_1 was reliably determined with a signal-to-noise ratio $\text{SNR}_{A_1} > 3$	91
3.9	Comparison between the accepted results of this chapter ($\text{SNR}_{A_2} \geq 5$) and the JPL ones. The columns contain the asteroid name, the signal-to-noise ratio of our solution and of the JPL one, the ratio $\sigma_{A_2, \text{JPL}}/\sigma_{A_2}$ of the A_2 uncertainties as estimated by the two systems, the relative errors computed with our A_2 uncertainty and with the JPL A_2 uncertainty respectively, and the χ_{A_2} value.	91
3.10	Comparison between the accepted results of this chapter ($\text{SNR}_{A_2} < 5$) and the JPL ones. The columns are the same of Table 3.9.	92

3.11	Results of the comparison between the estimated values of A_2 and A_1 , as contained in this chapter and in the JPL database. In particular, the columns contain the asteroid name, the signal-to-noise ratio of our A_2 solution and of the JPL one, the signal-to-noise ratio of our A_1 solution and of the JPL one, the relative error in the A_2 parameter computed with our A_2 uncertainty and with the JPL A_2 uncertainty respectively, the relative error in the A_1 parameter computed with our A_1 uncertainty and with the JPL A_1 uncertainty respectively, the χ -value for A_2 and for A_1	92
3.12	Impact monitoring of asteroid 2001 BB ₁₆ with a non-gravitational model that includes the Yarkovsky effect. Table columns: calendar date (year, month, and day) for the potential impact for asteroid 2011 MD, approximate σ value of the virtual impactor location along the LOV, minimum distance (the lateral distance from the LOV to the centre of the Earth on the TP confidence region), stretching (how much the confidence region at the epoch has been stretched by the time of impact), probability of Earth impact (IP), and Palermo Scale (PS). The width of the TP confidence region is always few km, thus not reported.	93
3.13	Impact monitoring of asteroid 2011 MD with a non-gravitational model that includes both the Yarkovsky effect and solar radiation pressure. Columns as in Table 3.12.	93
3.14	Impact monitoring of asteroid 2011 MD with a non-gravitational model including solar radiation pressure only. Columns as in Table 3.12.	94

Abstract

This thesis is a collection of the work carried out during these three years of PhD at the Department of Mathematics with the Celestial Mechanics Group and at SpaceDyS, a spin-off of the group itself.

The central theme of this thesis is the impact monitoring of Near-Earth Asteroids (NEAs). The NEA population includes asteroids in a heliocentric orbit having perihelion distance $q \leq 1.3$ au. When an asteroid has just been discovered, its orbit is weakly constrained by the available astrometric observations and it might be the case that an impact with the Earth in the near future, *e.g.*, within the next 100 years, cannot be excluded. If additional observations are obtained, the uncertainty of the orbit shrinks and the impact may become incompatible with the available information. Thus a crucial issue is to be able to identify the cases that could have a threatening Earth close encounter within a century, as soon as new asteroids are discovered or as new observations are added to prior discoveries. The main goal of impact monitoring is to solicit astrometric follow up to either confirm or dismiss the announced risk cases, *i.e.* asteroids having some virtual impactor (VI) (Milani et al. 2000). This is achieved by communicating the impact date, the impact probability and the estimated impact energy.

This activity required an automated system that continually monitors the NEA catalogue. CLOMON-2 and Sentry are two independent impact monitoring systems that have been operational at the University of Pisa since 1999 and at JPL since 2002, providing the list of asteroids with a non-zero probability to impact the Earth within a century. The results of the two systems are carefully compared, and this guarantees that the potentially dangerous objects are identified very early (within a few hours from the dissemination of the astrometric data) and followed up until the observations succeed in contradicting the possibility of an impact. The mathematical theory developed to deal with the impact monitoring problem is mainly

contained in Milani et al. (1999), Milani et al. (2000), Milani et al. (2000), Chesley et al. (2002), Valsecchi et al. (2003), and Milani et al. (2005b). Since it is a recently studied problem, impact monitoring offers several interesting topics to investigate or improve. The aim of this thesis is to deal with some of them.

Chapter 1 is an introduction to the problem of impact monitoring and also contains a review of the general theory needed for the whole thesis. In particular, in Section 1.2 we introduce the risk scales used to quantify the risk posed by the possibility of an asteroid impact. The next two sections are devoted to the history of impact monitoring, from the first cases of hazard analysis at the end of the nineties, to the famous “Apophis crisis” on 2004 Christmas Day. In the last part (Section 1.5) we outline the mathematical theory needed to solve the problem, and on which CLOMON-2 and Sentry are currently based.

In Chapter 2 we present the problem of imminent impactors, which essentially is impact monitoring applied to Very Short Arcs (VSA). A very short arc is a set of few observations over a short time span, typically 3–5 observations spanning 1 hour (Milani et al. 2004). The difficulty when dealing with VSAs is that they are often too short for a full orbit determination. Nevertheless, since such a set of observations could belong to a real moving object, the problem of a short term impact monitoring actually exists and needs to be solved. Furthermore, there exists two small NEAs that have really impacted the Earth a few hours (less than 1 day) after their detection, namely 2008 TC₃ and 2014 AA, showing that a dedicated impact monitoring system for very short arcs is needed.

We have developed an initial orbit determination method, based on systematic ranging (Chesley 2005; Farnocchia et al. 2015c), an orbit determination technique that systematically explores a suitable grid in the topocentric range and range-rate space, and on the Admissible Region theory (Milani et al. 2004) to take into account the information contained in the short arc, although little. The combination of the two techniques provides a robust short term orbit determination method, which ends with the computation of a sampling of the Manifold Of Variations, a 2-dimensional compact manifold parametrized over the Admissible Region. The Manifold Of Variations represents the 2-dimensional analogue of the Line Of Variations (LOV), thus it is used to sample the set of possible orbits as a starting point for the short term impact monitoring.

One of the main problems in the impact risk assessment for imminent impactors is given by the computation of the impact probability. The second main results contained in Chapter 2 are a new mathematical method to

propagate the probability density function from the space of the astrometric residuals to the Manifold Of Variations and then to the range and range-rate space R . In previous works, this computation was conducted with the assumption of an *a priori* probability density function on the space R , and this step was needed to pass from the probability density function on the residuals space to a probability density function on the space R (see Section 2.5). Our computation is complete, rigorous, and uses no *a priori* probability distributions, since it only assumes that the residuals can be modeled with a Gaussian random variable.

This chapter corresponds to the paper Spoto et al. (2018), published on the international journal *Astronomy & Astrophysics*. One of the steps in the propagation of the probability density function is actually a further improvement to the method and it is mainly contained in Section 2.5.

In Chapter 3 we present our progress in the study of the effect of non-gravitational perturbations on an asteroid's orbit. Non-gravitational perturbations arise because outer space is not empty, but it is pervaded by electromagnetic radiation. Many non-gravitational perturbations are extremely small, and yet can significantly affect a NEA trajectory. The Yarkovsky effect is due to the recoil force undergone by a rotating body as a consequence of its anisotropic thermal emission (Vokrouhlický et al. 2000; Vokrouhlický et al. 2015a). The main manifestation of the Yarkovsky effect is a secular semimajor axis drift da/dt , which leads to a mean anomaly runoff that grows quadratically with time. Typical values of this perturbation for sub-kilometre NEAs are $da/dt \simeq 10^{-4}$ - 10^{-3} au/My. Because of its small size, the Yarkovsky effect can only be detected for asteroids with a well constrained orbit. Several efforts have been done in modelling and determining the Yarkovsky effect on the NEA population. Nugent et al. (2012) provided a list of 13 Yarkovsky detection, and later work increased this number to 21 (Farnocchia et al. 2013). The most recent census is from Chesley et al. (2016), which identified 42 NEAs with a valid Yarkovsky detection. Both Farnocchia et al. (2013) and Chesley et al. (2016) flag spurious cases based on whether the detected drift is compatible with the physical properties of the corresponding object and the Yarkovsky mechanism. Since the number of significant Yarkovsky detections in the NEA population is steadily increasing, we decided to update the list.

In this chapter, we present an updated set of near-Earth asteroids with a Yarkovsky-related semimajor axis drift detected from the orbital fit to the astrometry. We find 86 reliable detections after filtering for the signal-to-noise ratio of the Yarkovsky drift estimate and making sure the estimate is compatible with the physical properties of the analysed object. Further-

more, we find a list of 24 marginally significant detections, for which future astrometry could result in a Yarkovsky detection. A further outcome of the filtering procedure is a list of detections that we consider spurious because unrealistic or not explicable with the Yarkovsky effect. Among the smallest asteroids of our sample, we determined four detections of solar radiation pressure, in addition to the Yarkovsky effect. As the data volume increases in the near future, our goal is to develop methods to generate very long lists of asteroids with reliably detected Yarkovsky effect, with limited amounts of case-by-case specific adjustments. Furthermore, we discuss the improvements this work could bring to impact monitoring. In particular, we exhibit two asteroids for which the adoption of a non-gravitational model is needed to make reliable impact predictions.

The content of this chapter corresponds to the paper Del Vigna et al. (2018), published on the journal *Astronomy & Astrophysics*.

Chapter 4 concerns the completeness of the impact monitoring problem. The completeness limit indicates how efficient the search for virtual impactors of an impact monitoring system is. Each virtual impactor represents a possibility for the asteroid to impact the Earth at a certain date and with a certain probability. The generic completeness limit is a probability threshold, such that every virtual impactor with an impact probability above this value has to be detected (Milani et al. 2005b). An accurate measure and a decrease of the completeness limit value are very important issues in impact monitoring and we make improvements in both of them.

The completeness limit depends on the confidence region sampling: a goal of this chapter is to increase the completeness without increasing the computational load, for which we propose a new method to sample the LOV with respect to the previously one used in NEODyS. In particular, the step-size of the sampling is such that the probability of each LOV segment between consecutive points is kept constant and thus not uniform in the LOV parameter, since the probability density function on the LOV has a Gaussian distribution. Moreover, the sampling interval has been extended to the larger interval $[-5, 5]$ in the LOV parameter and a new decomposition scheme in sub-showers and sub-returns is provided to deal with the problem of duplicated LOV points appearing in the same return. The impact monitoring system CLOMON-2 has been upgraded with all these new features, resulting in a decrease of the impact probability IP^* corresponding to the generic completeness limit by a factor $\simeq 4$ and in an increase of the computational load by a factor $\simeq 2$.

Since the generic completeness limit is an analytic approximation, we statistically investigate the completeness actually reached by the system. For

this we used two different methods: a direct comparison with the results of the independent system Sentry at JPL and an empirical power-law to model the number of virtual impactors as a function of the impact probability. We found empirically that the number of detected virtual impactors with $IP > IP^*$ appears to grow according to a power-law, proportional to $IP^{-2/3}$. Several arguments provided in the chapter lead us to believe that we have experimentally found a fractal property of the set of the initial conditions leading to impacts in the chaotic dynamical system of planet crossing asteroids. An analytical model explaining this power-law is currently an open problem, but we think it is related to the way the number of virtual impactors within a time t_{rel} from the first observed close approach accumulates. We give an analytical model and we prove that this cumulative number grows with a power-law proportional to t_{rel}^3 . For this second power-law we found a number-theoretical argument based on Farey fractions (see Appendix B). However, for the connection between the two power-laws we have not yet found a model, which we suspect to hide in properties of the chaotic orbits of NEAs. The power-law allows us to detect a loss of efficiency in the virtual impactors search for impact probabilities near the generic completeness limit.

The content of this chapter corresponds to the paper Del Vigna et al. (2019), that has been accepted for publication on the international journal *Icarus*.

In Chapter 5 we use the analytical Öpik's theory to study the evolution of the Line Of Variations at a close encounter. The model on which Öpik's theory of close encounters is based is a simplified version of the restricted, circular, 3-dimensional 3-body problem (Öpik 1976). In fact, in the theory it is assumed that, far from the planet, the small body moves on an unperturbed heliocentric Keplerian orbit. The effect of the encounter is modelled as an instantaneous transition from the incoming asymptote of the planetocentric hyperbola to the outgoing one, taking place when the small body crosses the plane orthogonal to the small body unperturbed velocity vector and containing the centre of the planet. This plane is called the b -plane.

The first part of the chapter contains a review of Öpik's theory and of its extension to near misses, as presented in Valsecchi et al. (2003), in which the planetary encounter is studied in a suitable set of six coordinates. We provide the equations for the pre-encounter and the post-encounter state vector in this set of coordinates, and we also show the equations for the Keplerian propagation until the next encounter. The problem is seen as a mapping from the pre-encounter b -plane of a certain encounter to the pre-encounter b -plane of the next one. We also present the study of resonant returns on a given b -plane, providing the definition of resonant circles, which

are the locus of points such that if the small body asymptote passes through one of them it will have a fixed post-encounter semimajor axis. We end the review by presenting the wire approximation (Milani et al. 2005b), that mimics the behaviour of the LOV on the b -plane and, together with the resonant circles, is a useful tool in the analytic study of collision possibilities at subsequent returns.

The second part contains the new research in this field. As we already pointed out, a planetary encounter acts as an instantaneous rotation of the incoming velocity vector \mathbf{U} to the outgoing velocity vector \mathbf{U}' . In the framework of the analytical theory, it is possible to show that the modulus of this vector is conserved, that is $U' = U$. When we use the wire approximation for the LOV, we are not considering a single small body approaching the planet, but a whole line of fictitious small bodies. We are interested in studying the deflection caused by the encounter to the small bodies belonging to the wire. The conservation of \mathbf{U} implies that the post-encounter planetocentric velocity vector \mathbf{U}' spans a sphere of radius U . We prove that the post-encounter values of the angular variables accessible to a small body encountering the planet on the wire lay on the circle resulting from the intersection of a cone (whose aperture can be explicitly given), centred in the centre of the sphere, and the sphere itself.

The paper Valsecchi et al. (2019) corresponds to the content of this second part of Chapter 5, and has been submitted to the journal *Celestial Mechanics & Dynamical Astronomy*.

In Chapter 6 we propose an adaptation of the semilinear method (Milani 1999) for the prediction of the impact corridor on ground for an asteroid that have a non-zero chance of impacting the Earth in the future. The algorithm starts from an orbit for which an impact on Earth is possible at some epoch in the future (a virtual impactor representative orbit). Starting from it and using the covariance of the nominal solution, the semilinear method provides the boundary of the impact corridor on ground, corresponding to the portion of the initial uncertainty region that leads to the impact.

Given a virtual impactor, the impact region boundary at altitude h and confidence level σ is the result of the propagation of the intersection of the virtual impactor with the boundary of the confidence ellipsoid, until the surface at altitude h above the Earth is reached. The semilinear method starts considering the impact map, that is the result of the composition between the propagation until the impact time and the projection on the impact surface. First the initial covariance is linearly propagated using the differential of the impact map at the VI representative and then the linear approximation is exploited to select a representative curve on the boundary of the

ellipsoid in the initial conditions space. Then a uniform sample of points belonging to this curve is non-linearly propagated to obtain the boundary corresponding to the semilinear prediction.

Furthermore, the method has been validated using the real observational data of the well known past-impacted asteroid 2008 TC₃ and also a restricted dataset of Apophis. The comparison with the predictions performed with a Monte Carlo approach shows a very good agreement and, as an improvement, it consists of fewer propagations with respect to Monte Carlo approaches. The content of this chapter corresponds to on-going research and to a paper which is still in preparation.

Appendix A contains the equations for the transformation from the Modified Target Plane reference frame to the Target Plane reference frame, along with its Jacobian matrix. In particular, this leads to the definition of a suitable set of Öpik elements, which are very important, being the coordinate set used in the computations performed by CLOMON-2.

Appendix B contains the proof of the asymptotic growth of the number of terms in the Farey sequences. In particular, if \mathcal{F}_n is the n -th Farey sequence (*i.e.*, the sequence of irreducible fractions between 0 and 1 whose denominators do not exceed n , definition B.14), then $|\mathcal{F}_n| \sim \frac{3}{\pi^2}n^2$ and $\sum_{k=1}^n |\mathcal{F}_k| \sim \frac{1}{\pi^2}n^3$, as $n \rightarrow +\infty$. This appendix is self-contained, thus we report all the definitions and theorems which are needed to reach this result, with their proof.

Appendix C contains a summary of definitions on manifolds in \mathbb{R}^N and on integration on manifolds. In particular, we introduce the notion of volume form, which is a tool used in Chapter 2 for probability computations.

Appendix D contains the mathematical theory at the basis of the orbit determination problem, presented as a non-linear least squares problem.

Chapter 1

An overview of the Impact Monitoring

1.1 Motivations

The collision between the Earth and an asteroid can be described as an extreme event. On one hand, it is extremely rare: although tons of material enter the Earth's atmosphere on a daily basis, humankind has not yet witnessed the impact of a body belonging to the asteroid class. On the other hand, the effects of such an impact could be extremely catastrophic: the energy released in the process ranges from tens of Megatons (for 50 m bodies) to millions of Megatons (for bodies with several kilometers in diameter), reaching global consequences for asteroids with diameter greater than 1 km.

The extreme character of the impacts between the Earth and the asteroids makes it difficult for the general public to understand the true nature of the problem we are facing. The fact that this type of collisions is rare does not mean that they are impossible. In fact, there are evidences both indirect (craters on the surfaces of the rocky celestial bodies, including the Earth) and direct (collision of the comet Shomaker-Levy 9 with Jupiter in 1994) showing that this kind of episodes have occurred in the past and will take place again in the future. Among the population of asteroids, only those with orbits close to that of the Earth, which are known as Near Earth Asteroids, represent a real risk. There are a number of different measures that can be taken to mitigate this hazard. The most basic measures have a preventive nature and aim at cataloguing the whole NEA population. A complete catalogue of accurate orbits would allow us to know, well in advance, the asteroids that are on a collision course. The second type of measures, more

selective and targeted for a particular threatening asteroid, include different deflection techniques to avoid its collision with the Earth. Finally, if the previous actions fail, it is still possible to implement a third kind of measures, such as population evacuations before the impact or construction of refuges near the shock area, to mitigate the effects of a certain collision. It is worth noting that the success of the measures of the second and third kind heavily relies on the time interval ranging from the publication of a certain impact to the impact itself. Obviously, those predictions can only be made when there is enough information available on the asteroids, hence the importance of the cataloguing.

1.2 Risk scales

The risk scales try to quantify in a simple way the risk associated with the possible collision of an asteroid with the Earth and their purpose is to serve as a mean of communication for the astronomers and the general public when evaluating the seriousness of the potential collisions. In general terms, we can state that when evaluating the risk of an impact at least three factors have to be considered.

- (1) On one hand it is obvious that the risk has to be an increasing function of the probability of the impact, in such a way that less probable impacts lead to low risks and vice versa.
- (2) On the other hand, a risk scale must be sensitive to the energy released in the collision. This quantity is directly related to the size of the asteroid and its relative velocity with respect to our planet.
- (3) Finally, we cannot neglect the time left till the predicted possible impact since, for instance, a prediction well in advance would allow us to adopt measures aimed at the mitigation of the possible effects of the threat.

The first risk scale to be introduced was the *Torino Scale* (*TS*) (Binzel 2000). It uses numbers from 0 to 10 in combination with colors and words to classify the impact risks (see Figure 1.1). This scale is discrete and the fact that it takes into account the third factor only in a binary way makes it a bit inconvenient, so that a new scale was proposed, the *Palermo Scale* (*PS*) (Chesley et al. 2002). This scale is continuous, includes the three forementioned factors and is mainly used among professionals. Basically, the Palermo Scale compares the destructive effect of a certain impact with that of the whole population of asteroids, both known and unknown. Most of the asteroids posted in the Risk Page of NEODyS¹ and JPL are $TS = 0$

¹It is available at <http://newton.dm.unipi.it/neodys/index.php?pc=4.1>.

and $PS < -2$. The first notorious case was 2002 NT₇, since although it was $TS = 1$ - but very close to the $TS = 2$ region, on July 23, 2002 - it was the first asteroid to reach a positive PS value. 2002 NT₇ held this PS record until 2004 MN₄ (now named Apophis) came into scene beating any previous record, both in the Torino and the Palermo scales.

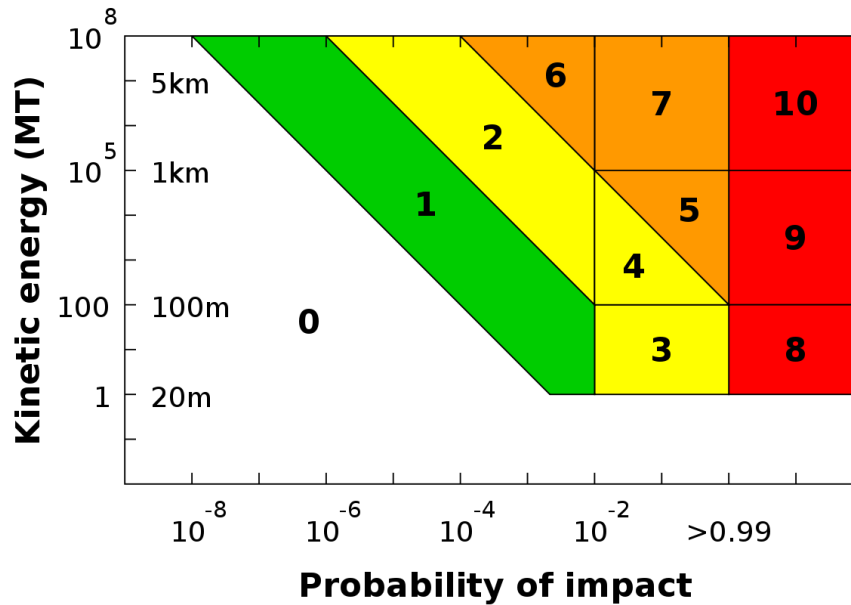


Figure 1.1. Graphical representation to compute the Torino Scale, and hence the associated color to classify the risk from white (no risk) to red (certain impact) passing through green, yellow and orange.

1.3 Brief history

One of the first serious analyses of the impact possibility of a real asteroid occurred in early 1998, for asteroid 1997 XF₁₁ (Marsden 1999). A possible impact in 2028 was proposed but then determined to never have been possible. During the subsequent discussions, however, potential impacts beyond 2028 were identified, despite the problems due to the non-linearity introduced from the 2028 close approach. Later, the possibility of those impacts was eliminated. Nonetheless, the 1997 XF₁₁ scare had the very beneficial effect of motivating significant research into impact hazard assessment and led to the identification of the concept of keyholes and the creation of automated non-linear impact monitoring systems.

The first verified potential impact of an NEO was reported shortly thereafter for asteroid 1999 AN₁₀ (Milani et al. 1999), although its impact probability was only of order 10^{-9} . Later the same year, 1998 OX₄ was found to have a small potential for a collision with Earth (Milani et al. 2000). The 1998 OX₄ case presented an interesting problem because the asteroid had become lost due to difficult observing circumstances and it was no longer possible to predict where to observe it again to solve the threat.

A solution to this problem would be to identify any threatening object shortly after its discovery, while its position should still be accurately predicted, thereby allowing appropriate follow-up tracking to be used to refine the orbit. This required an automated system that could continually monitor the near-Earth asteroids' catalogue as new discoveries are added and as new observations of previous discoveries flow in. The first version of such a system, called CLOMON, began operation at the University of Pisa by late 1999. CLOMON-2 (which is an evolution of CLOMON) was complemented in 2002 by the JPL Sentry system. These two computer-based impact monitoring systems were independently developed and continue to operate today, providing the operational redundancy and cross-verification that is needed for this problem.

1.4 The case of Apophis

Since the main topic of the thesis is the impact monitoring of NEAs, we have to mention asteroid (99942) Apophis. The whole story can be found in Sansaturio et al. (2008).

On December 20, 2004 the Minor Planet Center issued the Minor Planet Electronic Circular (MPEC) 2004-Y25 announcing the discovery of a new NEA with designation 2004 MN₄. Only two days later it was already apparent that this asteroid, currently known as Apophis, would be notorious: our close approach monitoring system was showing a virtual impactor in 2029 reaching the level 2 in the Torino Scale, the first such case since our monitoring system had been operational.

On December 23, Dave Tholen (University of Hawaii) obtained accurate remeasurements for all the bad June observations from Kitt Peak. The results of CLOMON-2 were a little less bad than the previous day, but still at the $TS = 2$ and $PS > 0$ level. The agreement between CLOMON-2 and Sentry was good to the point that there was no way to cast into doubt the existence of the 2029 VI, although the quality and time distribution of the data was not so good as desired. The results were published in the Risk Pages simultaneously and including a note stressing that the situation was bound to change as new data became available.

On Christmas Eve, the new available observations gave new outputs of CLOMON-2 with unprecedented $TS = 4$ and $PS > +1$. The NEODYs team posted the results near 20:00 CET and continued to make a call for observations. During the following two days (25-26) new observations started to flow in: the MPC issued four special MPECs (three on the 25th and one on the 26th) for 2004 MN₄. The NEODYs team was furiously changing all parts of the software which were not performing as expected because of the new dynamical features of the case. Certainly, 2004 MN₄ has proven to be a challenge for both monitoring systems. On December 27, we got the maximum IP ever: the infamous 1 in 38 chances of impact.

The MPC issued 4 new special MPECs. In particular, MPEC-Y70 contained pre-discovery observations for 2004 MN₄ from observatory code 691 (Spacewatch), which extended the arc back to March 2004. Moreover, Tholen sent time corrections to the June 19 observations. The NEODYs team processed this new data: the most outstanding result being that the 2029 VI had been ruled out, which brought an end to the "Aphophis crisis". The collaborative work to exclude the possibility of that impact provides a great example of the practices needed to handle a delicate situation in which the information that becomes public must be carefully presented and commented to avoid unnecessary concerns.

1.5 Impact monitoring: mathematical theory

The mathematical methods used in impact monitoring have been developed over the years, in a sequence of papers to which we refer the reader for a complete explanation: Milani et al. (1999), Milani et al. (2000), Chesley et al. (2002), Valsecchi et al. (2003), Milani et al. (2005a) and Milani et al. (2005b).

The classical impact monitoring procedure uses as initial condition at t_0 the solution $\mathbf{x}^* \in \mathbb{R}^N$ of a non-linear least squares fit, along with its covariance matrix $\Gamma := \Gamma(\mathbf{x}^*)$ Milani et al. (2010, Chapter 5). We denote with N the dimension of the parameter space. This space has dimension $N = 6$ when we solve for the six orbital elements, but it could have higher dimension if some other parameter is determined along with the orbital elements. A common situation is the determination of the Yarkovsky-related semimajor axis drift (Farnocchia et al. 2013; Chesley et al. 2016; Del Vigna et al. 2018). This has consequences also for the impact monitoring. Indeed, a dynamical model including non-gravitational forces is sometimes needed to make reliable impact predictions, especially if the hazard analysis time span is extended to time intervals longer than one century. In Chapter 3, this aspect is discussed in detail.

Given $m \geq N$ scalar observations we call $\boldsymbol{\xi} \in \mathbb{R}^m$ the vector of the observed-computed debiased astrometric *residuals*. The function

$$Q(\mathbf{x}) := \frac{1}{m} \boldsymbol{\xi}(\mathbf{x})^\top W \boldsymbol{\xi}(\mathbf{x})$$

is the *target function*, where $\mathbf{x} \in \mathbb{R}^N$ are the fit parameters and W is a symmetric positive definite weight matrix.

The nominal solution is surrounded by a set of orbits that are still compatible with the observational dataset, the so-called *confidence region*, that is defined to be

$$Z(\sigma) := \left\{ \mathbf{x} \in \mathbb{R}^N \mid Q(\mathbf{x}) \leq Q^* + \frac{\sigma^2}{m} \right\}, \quad (1.1)$$

where $\sigma > 0$ is a confidence level and $Q^* := Q(\mathbf{x}^*)$. The confidence region is the basic tool for the impact monitoring activity, since impact predictions have to take into account all the possible orbits compatible with the observational dataset and not the nominal solution only.

If we take the quadratic approximation for the target function around \mathbf{x}^* , the confidence region defined by (1.1) can be approximated by the *confidence ellipsoid*

$$Z_{lin}(\sigma) := \left\{ \mathbf{x} \in \mathbb{R}^N \mid (\mathbf{x} - \mathbf{x}^*)^\top C (\mathbf{x} - \mathbf{x}^*) \leq \sigma^2 \right\},$$

a region delimited by the $(N - 1)$ -dimensional ellipsoid given by the positive definite quadratic form associated to the normal matrix $C = C(\mathbf{x}^*)$. As explained in what follows, the confidence ellipsoid is just used for local computations, since the assumptions to use this approximation are not applicable to impact monitoring in general.

1.5.1 Sampling of the confidence region

The main goal of impact monitoring is to establish whether the confidence region contains virtual impactors. Thus the confidence region is sampled by a finite set of *Virtual Asteroids* (VAs). Since the dynamical system describing the asteroid orbits is not integrable, only a finite number of initial conditions can be computed and propagated over the selected time interval. This sampling has to be done in an efficient way, that is with a few but selected orbits, in such a way that they are as much as possible representative of the infinite set of possible orbits. The geometric sampling methods are one possible way to select the ensemble of virtual asteroids: for this class of methods the sampling takes place on the intersection between the confidence region and a differentiable manifold. In particular, Milani (1999) and Milani

et al. (2005a) introduced a 1-dimensional sampling method, in which the geometric object is a smooth line in the orbital elements space, the Line Of Variations. The main advantage of this approach is that the set of VAs has a geometric structure, that is they belong to a differentiable curve along which interpolation is possible.

Another sampling method, namely Monte Carlo, directly uses the probabilistic interpretation of the least squares principle, sampling the probability distribution in the orbital elements space to obtain a set of equally probable orbits (Chodas et al. 1996). More complex sampling methods, such as 2-dimensional ones, have been proposed in Tommei (2005) and recently have been recently used to deal with the problem of the imminent impactors (Farnocchia et al. 2015c; Spoto et al. 2018). This problem has been analysed and some improvements are discussed in Chapter 2.

1.5.2 LOV propagation

The LOV sampling computation provides a set of orbits $\{\mathbf{x}(\sigma_i)\}_{i=-M, \dots, M}$, corresponding to values $\{\sigma_i\}_{i=-M, \dots, M}$ of the LOV parameter. As introduced in Milani et al. (1999), the second step in impact monitoring consists in the propagation of each VA in the future. Through the LOV propagation, the Earth encounters of each VA are detected. To this aim, as a first step we associate to each close approach of a VA the plane passing through the Earth center and orthogonal to the unperturbed velocity of the VA², the so-called Target Plane (TP) (Valsecchi et al. 2003). To avoid geometric complications, we call “close” only those approaches with a distance from the Earth center of mass not exceeding some value, commonly fixed to $R_{TP} = 0.2$ au, and thus the TP is actually considered as a disk with radius R_{TP} . Lastly, to keep track of a close approach we define a function $\mathbf{g} : \mathbb{R}^N \rightarrow \mathbb{R}^2$ that maps an orbit \mathbf{x} that experiences a close encounter with the Earth to a point $\mathbf{y} = (\xi, \zeta) \in \mathbb{R}^2$ on the TP³. This function is the composition between the propagation from the initial epoch to the closest approach date and the conversion to the TP coordinates. Actually, inside a given close approach there can be several local minima of the geocentric distance: the definition of \mathbf{g} can be extended to each of these minima, and consequently there are several TP traces corresponding to a single orbit \mathbf{x} .

²That is, orthogonal to the incoming asymptote of the hyperbola defining the two-body approximation of the trajectory at the time of closest approach.

³The commonly used names for the TP coordinates are ξ and ζ , see Chapter 5. For a discussion on the choice of the coordinates (ξ, ζ) on the TP, see (Valsecchi et al. 2003; Milani et al. 2005b) and Appendix A of this thesis.

1.5.3 Stretching and width

First we introduce a notation that we are going to use here and throughout the whole thesis. Let $\mathbf{f} : U \rightarrow \mathbb{R}^m$ be a function defined on an open set $U \subseteq \mathbb{R}^n$. We indicate with $D\mathbf{f}_{\mathbf{x}^*}$ the differential of \mathbf{f} in \mathbf{x}^* . It is the linear map $D\mathbf{f}_{\mathbf{x}^*} : \mathbb{R}^n \rightarrow \mathbb{R}^m$ represented by the Jacobian matrix of \mathbf{f} computed in \mathbf{x}^* , that is the $m \times n$ matrix defined to be

$$(D\mathbf{f}_{\mathbf{x}^*})_{ij} := \frac{\partial f_i}{\partial x_j}(\mathbf{x}^*) \quad \text{for all } i = 1, \dots, m, j = 1, \dots, n.$$

Since the differential is a linear map, we shall use the same notation for the map and for the Jacobian matrix.

Two important quantities involved in impact monitoring are the stretching and the width at each VA. Since the TP analysis is performed locally, the linear approximation around each VA is allowed. Let $\bar{\mathbf{x}}$ be a LOV orbit and let $\bar{\mathbf{y}} := \mathbf{f}(\bar{\mathbf{x}})$ be the corresponding TP trace. The differential $D\mathbf{f}(\bar{\mathbf{x}})$ of \mathbf{f} in $\bar{\mathbf{x}}$ maps the confidence ellipsoid $Z_{lin}^X(\sigma)$ around $\bar{\mathbf{x}}$ onto the confidence ellipse $Z_{lin}^Y(\sigma)$ around $\bar{\mathbf{y}}$. By the covariance propagation law, the TP ellipse $Z_{lin}^Y(\sigma)$ is defined through the inequality

$$(\mathbf{y} - \bar{\mathbf{y}})^\top C(\bar{\mathbf{y}})(\mathbf{y} - \bar{\mathbf{y}}) \leq \sigma^2,$$

where $C(\bar{\mathbf{y}}) = \Gamma(\bar{\mathbf{y}})^{-1}$ and

$$\Gamma(\bar{\mathbf{y}}) = D\mathbf{f}(\bar{\mathbf{x}}) \Gamma(\bar{\mathbf{x}}) D\mathbf{f}(\bar{\mathbf{x}})^\top$$

is the 2×2 covariance matrix on the TP. The square root of the eigenvalues of $\Gamma(\bar{\mathbf{y}})$ are the lengths of the semimajor and semiminor axis of the ellipse $Z_{lin}^Y(1)$, that are respectively the *stretching* S and the *width* w at the LOV orbit $\bar{\mathbf{x}}$. If we have a LOV sampling, as in the case of impact monitoring, we have a further map $\mathbf{s} : \mathbb{R} \rightarrow \mathbb{R}^N$, which is the parameterization of the LOV as a differentiable curve, that is $\mathbf{s}(\sigma_i) = \mathbf{x}_i$. In this way we can consider the composite map $\mathbf{f} = \mathbf{g} \circ \mathbf{s}$ from the sampling space to the target plane, and thus the value of the *stretching along the LOV* in σ is

$$S(\sigma) := \left| \frac{d\mathbf{f}}{d\sigma}(\sigma) \right| = \left| \frac{\partial \mathbf{g}}{\partial \mathbf{x}}(\mathbf{s}(\sigma)) \cdot \frac{d\mathbf{s}}{d\sigma}(\sigma) \right|. \quad (1.2)$$

That is, the stretching along the LOV measures the displacement of two points on the target plane as a function of the separation between the corresponding points in the sampling space.

1.5.4 Return analysis

According to Milani et al. (2005b), the list of the close encounters of all the VAs is decomposed into *showers* and *returns*. In particular, first the close approaches are clustered by date to obtain the showers and then each shower is further divided in LOV segments with consecutive indices, the returns. Then each return is carefully analyzed to search for virtual impactors.

When there are many points on the TP in a given return it is easy to understand the LOV behaviour: the stretching is small and the linear theory is locally applicable. On the contrary, in strong non-linear cases the stretching is large and changes rapidly from point to point: in this case a local analysis is necessary in the neighborhood of each VA. We refer to Milani et al. (2005b) and Tommei (2006) for a discussion on the possible geometries of the LOV trace on a target plane and for a proper solution for each case. Here we only want to outline the basic idea of the return analysis with a simple example. The key point is that the virtual asteroids are not just a set of points but they sample a smooth curve, allowing us to interpolate between consecutive sample points. For instance, let us suppose two consecutive VAs \mathbf{x}_i and \mathbf{x}_{i+1} have TP trace points \mathbf{y}_i and \mathbf{y}_{i+1} straddling the Earth impact cross section. If the geometry of the TP trace is simple enough (principle of simplest geometry), an interpolation method provides a point on the LOV $\mathbf{x}_{i+\delta}$ with $0 < \delta < 1$ and such that $\mathbf{y}_{i+\delta}$ is inside the Earth impact cross section: then, around $\mathbf{x}_{i+\delta}$ there is a virtual impactor. If a virtual impactor has been found, by computing the probability density function with a suitable Gaussian approximation centred at $\mathbf{x}_{i+\delta}$ it is possible to estimate the probability integral on the impact cross section, that is the impact probability associated with the given VI.

1.5.5 Geometry of the LOV trace on the TP

This section is essentially based on Milani et al. (2005b). Let us denote with $P(\sigma)$ the trace on a given TP of the LOV point corresponding to the value σ of the LOV parameter. Let P_1 and P_2 be the geocentric position vectors on the TP of two consecutive VAs, corresponding to the values σ_1 and σ_2 of the LOV parameter, respectively. Let $\mathbf{S}_1 := \partial P_1 / \partial \sigma$ and $\mathbf{S}_2 := \partial P_2 / \partial \sigma$ be the corresponding derivative vectors. Let α_1 and α_2 be the angles between the derivative vectors and the ζ -axis (see Figure 1.2). We also set

$$\Delta\alpha := \alpha_1 - \alpha_2$$

and

$$\cos \beta_1 := \frac{(P_2 - P_1) \cdot \mathbf{S}_1}{|P_2 - P_1| |\mathbf{S}_1|} \quad \text{and} \quad \cos \beta_2 := \frac{(P_2 - P_1) \cdot \mathbf{S}_2}{|P_2 - P_1| |\mathbf{S}_2|}.$$

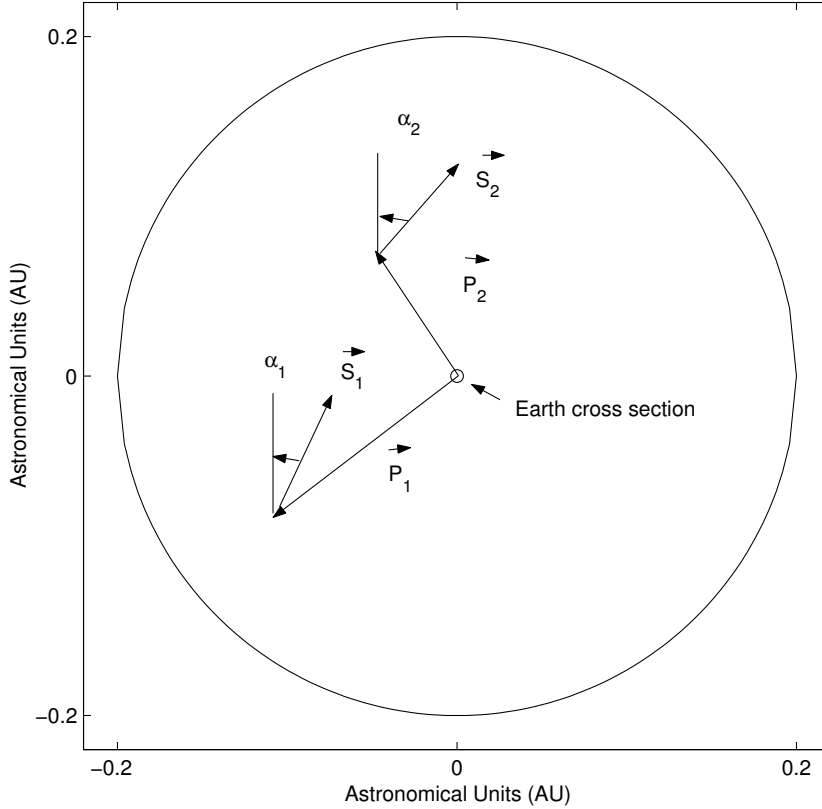


Figure 1.2. The quantities used to classify the behaviour of two consecutive TP points are obtained from the geocentric vectors P_i and their derivatives (with respect to the LOV parameter) S_i .

A key function is the derivative of the square distance from the Earth centre with respect to σ :

$$f(\sigma) := \frac{dr^2}{d\sigma}(\sigma), \quad (1.3)$$

where $r^2(\sigma) := \xi^2(\sigma) + \zeta^2(\sigma)$ is the squared distance of the point $P(\sigma)$ from the centre of the Earth. The sign of $f(\sigma)$ provides critical information because it indicates the local increase and decrease of the distance. For the classifications, we take into account the angle $\Delta\alpha$ between the two derivative vectors, the sign of the function $f(\sigma)$ in P_1 and P_2 , and the alignment of the two derivative vectors with respect to the vector between the two TP points, through the angles β_1 and β_2 .

In Milani et al. (2005b) six fundamental classifications of pairs of TP points are identified by using the first two quantities, plus some special cases when using also the third one. They are all listed in Table 1.1.

Table 1.1. Classification of LOV segments on the TP between two consecutive VAs. The six fundamental types are listed first, followed by special cases that are unique to either CLOMON-2 or Sentry. ^(a) If both $|\sin \beta_1| \geq \sin \beta_{lim_1}$ and $|\sin \beta_2| \geq \sin \beta_{lim_2}$, CLOMON-2 only. For a discussion on the choice of the limit values for $\sin \beta_i$ refer to Milani et al. (2005b). ^(b) If both $\cos \beta_1 < 0$ and $\cos \beta_2 < 0$, Sentry only.

	$\cos \Delta\alpha$	$f(\sigma_1) \cdot f(\sigma_2)$	$f(\sigma_2)$
SIMPLE MIN	> 0	< 0	> 0
SIMPLE MAX	> 0	< 0	< 0
NO EXTREMA	> 0	> 0	–
INT MIN	< 0	< 0	> 0
INT MAX	< 0	< 0	< 0
INT FAIL	< 0	> 0	–
ENTANGLED ^a	> 0	–	–
UNRELATED ^b	> 0	< 0	–

The first three classifications have the property that the curvature of the LOV trace on the TP between the two points is moderate, at most 90° .

- **SIMPLE MINimum.** In $[\sigma_1, \sigma_2]$ there is at least one point $\sigma = \sigma_{min}$ with $f(\sigma_{min}) = 0$ and which is a minimum for the distance from the Earth.
- **SIMPLE MAXimum.** In $[\sigma_1, \sigma_2]$ there is at least one maximum in the distance from Earth. This case is ignored under the hypothesis that in the interval is present only one maximum.
- **NO EXTREMA.** Both points are going away or both are approaching to the Earth, but the positions of \mathbf{S}_1 and \mathbf{S}_2 do not indicate the presence of extrema of the function $r^2(\sigma)$ in $[\sigma_1, \sigma_2]$. Also this case is ignored.

The next three classifications indicate a substantial curvature, generally a reversal, of the LOV between the two points P_1 and P_2 .

- **INTerrupted MINimum.** It is an *interrupted return*. The LOV seems to behave as in a SIMPLE MIN, but, for some value σ , it turns back and it goes away in the opposite direction. The tip of this interrupted can be before the Earth (the function $r^2(\sigma)$ has only one minimum), beyond the Earth (the function $r^2(\sigma)$ has two points of minimum and one point of maximum) or even inside the Earth.

- **INTerrupted MAXimum.** Opposite to the previous one, and in $[\sigma_1, \sigma_2]$ there is at least one maximum. Also this case is ignored.
- **INTerrupted FAILED.** It is a part of interrupted with maximum: in $[\sigma_1, \sigma_2]$ there at least one maximum and one minimum.

There are two special cases that are only considered by one of the two monitoring systems. Since they deserve a longer discussion, we refer to Milani et al. (2005b) for the entire analysis. Finally, there are three additional cases in which individual VAs, rather than pairs, are considered:

- **HEAD.** It is the first VA of a return with $f(\sigma) > 0$.
- **TAIL.** It is the last VA of a return with $f(\sigma) < 0$.
- **SINGLETON.** There is only one VA on the TP (in the return).

When the local geometry of the LOV has been studied as shown before and in case a minimum of $f(\sigma)$ could exist, the analysis is continued with iterative schemes to determine the actual minimum distance by interpolating between the consecutive points. For all the details we refer to Milani et al. (2005b).

Chapter 2

Imminent impactors

Short-arc orbit determination is a very important step when an asteroid is first discovered. In these cases the timing is essential, because we are interested in a rapid follow-up of a possible imminent impactor, which is an asteroid impacting the Earth shortly after its discovery, within the same apparition (interval of observability). The observations are so few that the standard differential correction procedure (Milani et al. 2010) of finding an orbit by a least-squares minimisation fails, and other methods need to be used to extract information on the orbit of the object.

Several initial orbit computation methods have been developed in the last 25 years. For instance, Muinonen et al. (1993) defined a Gaussian probability density on the orbital elements space using the Bayesian inversion theory. In particular, they determine asteroid orbital elements from optical astrometric observations using both *a priori* and *a posteriori* densities; the latter were computed with a Monte Carlo method.

The few observations in the short arc constrain the position and velocity of the object in the plane of sky, but they leave almost unknown the distance from the observer (topocentric range) and the radial velocity (topocentric range-rate). Thus, ranging methods have been developed over the years to replace or refine the Monte Carlo approach in the short arc orbit determination. There are two alternative approaches to the ranging methods: statistical and systematic methods.

The original statistical ranging method (Virtanen et al. (2001), Muinonen et al. (2001)) starts from the selection of a pair of astrometric observations. Then, the topocentric ranges at the epoch of the observations are randomly sampled. Candidate orbital elements are included in the sample of accepted elements if the χ^2 value between the observed and computed observations is within a pre-defined threshold. Oszkiewicz et al. (2009) improved the

statistical ranging using the Markov-Chain Monte Carlo (MCMC) to sample the phase space. The MCMC orbital ranging method is based on a bivariate Gaussian proposal probability density function for the topocentric ranges. Then, Muinonen et al. (2016) have developed a random-walk ranging method in which the orbital-element space is uniformly sampled, up to a χ^2 value, with the use of the MCMC method. The weights of each set of orbital elements are based on an *a posteriori* probability density value and the MCMC rejection rate. These authors have developed this method for the European Space Agency (ESA) Gaia mission, in the framework of Gaia alerts on potentially new discovered objects by Gaia (see Tanga et al. (2016)).

On the other hand, Chesley (2005) and Farnocchia et al. (2015c) introduced the so-called systematic ranging, which systematically explores a raster in the topocentric range and range-rate space $(\rho, \dot{\rho})$. This technique enables the description of asteroid orbital elements as a function of range and range-rate. Then, the systematic ranging also allows one to determine the subset of the sampling orbits that lead to an impact with the Earth.

In this chapter we describe a new approach to the systematic ranging, based on knowledge of the Admissible Region (AR) (Milani et al. 2004), and a new method to scan the region. The process has some main advantages to other methods described above as follows:

- (1) Our grid is more efficient, for two main reasons:
 - (a) We discard all the objects that are not in the AR, saving CPU time and making the systematic ranging more accurate in finding the region in the $(\rho, \dot{\rho})$ space of the possible orbital solutions.
 - (b) We use two different grids depending on the boundary of the AR. The first grid is larger and less dense, the second is based on a refinement using the value of the post-fit χ^2 of each point in the first grid (see Section 2.3).
- (2) The computation of the probability for the potential impactors (Section 2.6) as well as the computation of the scores (Section 2.8.2) are based on a rigorous probability propagation from the astrometric error model, without any assumption of *a priori* probability density functions on the range and range-rate space (see Section 2.5).

2.1 Very Short Arcs, sometimes too short

The rate of asteroid discoveries is continuously increasing, especially since automated CCD surveys have become operational. Their modes of oper-

ations, although they may differ in some details, are essentially the same. A number N of digital images of the same area on the celestial sphere is taken within a short time span, typically within a single night¹. Then the images are digitally blinked, that is a computer program is run on this set of frames to identify all changes among them. If an object is found to move along a straight line, with uniform velocity, in all N frames, then it should be the detection of a real moving object, provided the signal to noise ratio is large enough to make unlikely the presence of exactly aligned spurious signals. If the image is found in less than N frames it still can be a real object with marginal signal to noise, it could have been covered by a star image in some of the frames, but it could also be a spurious detection. Typically $3 \leq N \leq 5$, and 1 hour is the time span between the first and the last observation. Such a detection is reported to the Minor Planet Center (MPC) as a sequence of N observations. We shall call such a sequence a *Very Short Arc* (VSA).

This operation mode is optimal for detecting moving objects of asteroidal and cometary nature. Unfortunately, it is not at all optimal for determining the orbit of the detected object: these arcs are, in most cases, *too short* for a full orbit determination. When this is the case, we call the set of observations a *Too Short Arc* (TSA). As it is well known from the theory of preliminary orbit determination (Gauss 1809; Danby 1992), when three observations are used to compute an orbit, the curvature of the arc appears as a divisor in the orbit solution of Gauss' method. The smaller is the curvature, the less accurate is the orbit; taking into account the observational errors, in most cases it turns out to be impossible to apply the usual computational algorithm, consisting of a preliminary orbit determination by means of Gauss' method followed by a least squares fit (differential correction). When starting from a TSA, either Gauss' method fails or the differential correction procedure does not converge.

For this reason the TSAs are not considered discoveries, but just *detections*. This does not indicate that the observed object is fictitious, but just that its nature cannot be determined. Indeed without an orbit it is not possible to discriminate among different classes of objects, it is not possible to predict ephemerides allowing for follow-up and it is seldom possible to find an identification with a known object with a reliable orbit. In Milani et al. (2004), the authors dealt with the problem created by the existence of large databases of TSAs, and they proposed a solution. A TSA is recorded as a set of N observations, which means that a set of points on a straight line is what is actually detected, with deviations from alignment compatible with the random observational error. Thus from the TSA we can compute the

¹This is why these short sequences of observations are called *One Night Stand* (ONS).

straight line, either by linear regression or by other fitting procedure. Then a TSA is represented by an attributable, consisting of a reference time (just the mean of the observing times), two average angular coordinates and two corresponding angular rates at the reference time. An attributable provides no information on the range (the radial distance) and range-rate. Milani et al. (2004) proved that an attributable and therefore a TSA contains useful information.

2.2 The Admissible Region

We denote with \mathbf{r} and \mathbf{q} the heliocentric position vectors of the body and the observer on the Earth at time \bar{t} . Let $r = \|\mathbf{r}\|$, $q = \|\mathbf{q}\|$ be the Euclidean norms of these vectors. We also write

$$(\rho, \alpha, \delta) \in \mathbb{R}^+ \times \mathbb{S}^1 \times (-\pi/2, \pi/2)$$

for the spherical coordinates of the topocentric position $\boldsymbol{\rho} = \mathbf{r} - \mathbf{q}$ of the body, with $\rho = \|\boldsymbol{\rho}\|$.

Even though the observations are too scarce, we are able to compute the right ascension α , the declination δ , and their time derivatives $\dot{\alpha}$ and $\dot{\delta}$, by fitting both angular coordinates as a function of time with a polynomial model. These four quantities could be assembled together to form the *attributable* (Milani et al. 2005):

$$\mathcal{A} := (\alpha, \delta, \dot{\alpha}, \dot{\delta}) \in \mathbb{S}^1 \times (-\frac{\pi}{2}, \frac{\pi}{2}) \times \mathbb{R}^2$$

at a chosen time \bar{t} , which could be the time of the first observation or the mean of the observation times. The information contained in the attributable leaves the topocentric distance ρ and radial velocity $\dot{\rho}$ completely unknown. We would have a full description of the topocentric position and velocity of the asteroid in the attributable elements $(\alpha, \delta, \dot{\alpha}, \dot{\delta}, \rho, \dot{\rho})$, if ρ and $\dot{\rho}$ were known. The Admissible Region has been introduced to constrain the possible values of ρ and $\dot{\rho}$ with the hypothesis that the observed object is a Solar System body.

2.2.1 Excluding interstellar orbits

We introduce the following notation: let

$$\mathcal{E}_{\odot}(\rho, \dot{\rho}) := \frac{1}{2} \|\dot{\mathbf{r}}(\rho, \dot{\rho})\|^2 - k^2 \frac{1}{r(\rho)} \quad (2.1)$$

with $k = 0.01720209895$ the Gauss' constant, be the two-body energy of the heliocentric orbit of \mathcal{B} , in the approximation neglecting the mass of \mathcal{B} . The region \mathcal{D}_1 excluding interstellar orbits is the one that satisfies

$$\mathcal{E}_\odot(\rho, \dot{\rho}) \leq 0. \quad (2.2)$$

In particular, it can be proved that this region can have either one or two connected components. The heliocentric position of \mathcal{B} is given by

$$\mathbf{r} = \mathbf{q} + \rho \hat{\boldsymbol{\rho}}$$

where $\hat{\boldsymbol{\rho}}$ is the unit vector in the observation direction. Using the spherical coordinates (ρ, α, δ) , the heliocentric velocity $\dot{\mathbf{r}}$ of \mathcal{B} is

$$\dot{\mathbf{r}} = \dot{\mathbf{q}} + \dot{\rho} \hat{\boldsymbol{\rho}} + \rho \dot{\alpha} \hat{\boldsymbol{\rho}}_\alpha + \rho \dot{\delta} \hat{\boldsymbol{\rho}}_\delta,$$

where $\hat{\boldsymbol{\rho}}_\alpha = \partial \hat{\boldsymbol{\rho}} / \partial \alpha$, $\hat{\boldsymbol{\rho}}_\delta = \partial \hat{\boldsymbol{\rho}} / \partial \delta$ and $\dot{\mathbf{q}}$ is the heliocentric velocity of the observer. In coordinates

$$\begin{aligned} \hat{\boldsymbol{\rho}} &= (\cos \alpha \cos \delta, \sin \alpha \cos \delta, \sin \delta) \\ \hat{\boldsymbol{\rho}}_\alpha &= (-\sin \alpha \cos \delta, \cos \alpha \cos \delta, 0) \\ \hat{\boldsymbol{\rho}}_\delta &= (-\cos \alpha \sin \delta, -\sin \alpha \sin \delta, \cos \delta) \end{aligned}$$

$$\hat{\boldsymbol{\rho}} \cdot \hat{\boldsymbol{\rho}}_\alpha = \hat{\boldsymbol{\rho}} \cdot \hat{\boldsymbol{\rho}}_\delta = \hat{\boldsymbol{\rho}}_\alpha \cdot \hat{\boldsymbol{\rho}}_\delta = 0, \quad \|\hat{\boldsymbol{\rho}}\| = \|\hat{\boldsymbol{\rho}}_\delta\| = 1, \quad \|\hat{\boldsymbol{\rho}}_\alpha\| = \cos \delta.$$

Thus the squared norms of the heliocentric position and velocity are

$$r^2(\rho) = \rho^2 + 2\rho \mathbf{q} \cdot \hat{\boldsymbol{\rho}} + \|\mathbf{q}\|^2$$

and

$$\begin{aligned} \|\dot{\mathbf{r}}(\rho, \dot{\rho})\|^2 &= \dot{\rho}^2 + 2\dot{\rho} \dot{\mathbf{q}} \cdot \hat{\boldsymbol{\rho}} + \rho^2 (\dot{\alpha}^2 \cos^2 \delta + \dot{\delta}^2) + \\ &+ 2\rho (\dot{\alpha} \dot{\mathbf{q}} \cdot \hat{\boldsymbol{\rho}}_\alpha + \dot{\delta} \dot{\mathbf{q}} \cdot \hat{\boldsymbol{\rho}}_\delta) + \|\dot{\mathbf{q}}\|^2. \end{aligned}$$

We use the coefficients

$$\begin{aligned} c_0 &= \|\mathbf{q}\|^2 & c_3 &= 2\dot{\alpha} \dot{\mathbf{q}} \cdot \hat{\boldsymbol{\rho}}_\alpha + 2\dot{\delta} \dot{\mathbf{q}} \cdot \hat{\boldsymbol{\rho}}_\delta \\ c_1 &= 2\dot{\mathbf{q}} \cdot \hat{\boldsymbol{\rho}} & c_4 &= \|\dot{\mathbf{q}}\|^2 \\ c_2 &= \dot{\alpha}^2 \cos^2 \delta + \dot{\delta}^2 = \eta^2 & c_5 &= 2\mathbf{q} \cdot \hat{\boldsymbol{\rho}} \end{aligned}$$

and the polynomial expressions

$$\begin{aligned} \|\dot{\mathbf{r}}(\rho, \dot{\rho})\|^2 &= 2\mathcal{T}_\odot(\rho, \dot{\rho}) = \dot{\rho}^2 + c_1 \dot{\rho} + c_2 \rho^2 + c_3 \rho + c_4 \\ r^2 = S(\rho) &= \rho^2 + c_5 \rho + c_0, \quad W(\rho) = c_2 \rho^2 + c_3 \rho + c_4. \end{aligned}$$

By substituting the last expressions in (2.1), condition (2.2) reads

$$2\mathcal{E}_{\odot}(\rho, \dot{\rho}) = \dot{\rho}^2 + c_1\dot{\rho} + W(\rho) - \frac{2k^2}{\sqrt{S(\rho)}} \leq 0.$$

To have real solutions for $\dot{\rho}$, the discriminant of \mathcal{E}_{\odot} , as a polynomial of degree 2 in $\dot{\rho}$, must be non-negative, *i.e.*,

$$\frac{c_1^2}{4} - W(\rho) + \frac{2k^2}{\sqrt{S(\rho)}} \geq 0.$$

Let us set $\gamma = c_4 - c_1^2/4$ (note that $\gamma \geq 0$) and define

$$P(\rho) = c_2\rho^2 + c_3\rho + \gamma.$$

Then condition (2.2) implies

$$\frac{2k^2}{\sqrt{S(\rho)}} \geq P(\rho). \quad (2.3)$$

The polynomial $P(\rho)$ is non-negative for each ρ . In fact, it is the opposite of the discriminant of $\mathcal{T}_{\odot}(\rho, \dot{\rho})$, regarded as a polynomial in the variable $\dot{\rho}$, and \mathcal{T}_{\odot} , being a kinetic energy, is non-negative, thus its discriminant is non-positive. Also $S(\rho)$ is non-negative, thus we can square both sides of (2.3) and obtain an inequality involving a polynomial of degree 6. It can be written as

$$4k^4 \geq V(\rho) = P^2(\rho)S(\rho) = \sum_{i=0}^6 A_i\rho^i,$$

with coefficients

$$\begin{aligned} A_0 &= c_0\gamma^2, & A_1 &= c_5\gamma^2 + 2c_0c_3\gamma, \\ A_2 &= \gamma^2 + 2c_3c_5\gamma + c_0(c_3^2 + 2c_2\gamma), \\ A_3 &= 2c_3\gamma + c_5(c_3^2 + 2c_2\gamma) + 2c_0c_2c_3, \\ A_4 &= c_3^2 + 2c_2\gamma + 2c_2c_3c_5 + c_0c_2^2, \\ A_5 &= c_2(2c_3 + c_2c_5), & A_6 &= c_2^2. \end{aligned}$$

The most important property of the region defined by (2.2) is the following. For a proof, refer to Milani et al. (2004).

Theorem 2.1. *The region \mathcal{D}_1 defined by condition (2.2) has at most two connected components.*

To know the number of components of the region defined by (2.2) we have to compute the roots² of the degree six polynomial $V(\rho) - 4k^4$. In particular: if there is one positive root (with odd multiplicity) the region \mathcal{D}_1 has a single connected component with non-empty interior; if there are two positive roots (one simple and one with odd multiplicity) then there are two connected components, one with non-empty interior and one that is reduced to a point; if there are three positive simple roots then \mathcal{D}_1 has two connected components with non-empty interior.

2.2.2 The inner boundary

A difficulty in the practical usage of the region defined by condition (2.2) as a tool for the identification problem is that it is not a compact set, that is, the observed object could be at an arbitrarily small distance from the observer. This makes impossible to sample it with a finite number of points in such a way that the corresponding orbits are representative of all the possibilities. There are several ways to assign an inner boundary to the region where \mathcal{B} could be, based on different practical considerations:

- (1) an inner boundary can be assigned requiring that \mathcal{B} is not a satellite of the Earth, *i.e.*, by imposing a condition on the geocentric two-body energy $\mathcal{E}_\oplus(\rho, \dot{\rho})$;
- (2) a minimal distance can be dictated by physical limitations, such as the Earth atmosphere or the Earth radius R_\oplus in the geocentric approximation;
- (3) a minimal distance can be assigned by requiring that \mathcal{B} is not too small, if photometric measurements are supplied together with the astrometry used to compute the attributable.

Excluding satellites of the Earth

We look for a simple description of the region \mathcal{D}_2 satisfying the condition

$$\mathcal{E}_\oplus(\rho, \dot{\rho}) \geq 0.$$

A simplifying approximation is obtained by assuming that the observations are geocentric: with \mathbf{q}_\oplus the heliocentric position of the Earth centre, assum-

²There are fast and reliable algorithms in the Numerical Analysis literature providing the roots of a polynomial (as a complex vector), with rigorous upper bounds for the errors including rounding off. We use the algorithm by Bini (1996) and the corresponding public domain software.

ing $\mathbf{r} = \boldsymbol{\rho} + \mathbf{q}_\oplus$, the geocentric energy is

$$\mathcal{E}_\oplus(\boldsymbol{\rho}, \dot{\boldsymbol{\rho}}) := \frac{1}{2} \|\dot{\boldsymbol{\rho}}\|^2 - k^2 \mu_\oplus \frac{1}{\rho}, \quad (2.4)$$

where μ_\oplus is the ratio between the mass of the Earth and the mass of the Sun. By using $\|\dot{\boldsymbol{\rho}}(\boldsymbol{\rho}, \dot{\boldsymbol{\rho}})\|^2 = \dot{\rho}^2 + \rho^2 \eta^2$, where $\eta = \sqrt{\dot{\alpha}^2 \cos^2 \delta + \dot{\delta}^2}$ is the proper motion, (2.4) becomes

$$\dot{\rho}^2 + \rho^2 \eta^2 - 2k^2 \mu_\oplus \frac{1}{\rho} \geq 0,$$

that is

$$\dot{\rho}^2 \geq G(\rho), \quad \text{with } G(\rho) = \frac{2k^2 \mu_\oplus}{\rho} - \eta^2 \rho^2, \quad (2.5)$$

where $G(\rho) > 0$ for $0 < \rho < \rho_0 := \sqrt[3]{(2k^2 \mu_\oplus)/\eta^2}$. However, condition (2.4) is meaningful only inside the sphere of influence of the Earth, otherwise the dynamics of \mathcal{B} is dominated by the Sun, not by the Earth. Thus we need to introduce condition

$$\rho \geq R_{SI} := a_\oplus \sqrt[3]{\frac{\mu_\oplus}{3}} \simeq 0.010044 \text{ au}, \quad (2.6)$$

where R_{SI} is the radius of the sphere of influence, a_\oplus is the semimajor axis of the Earth. We call \mathcal{D}_3 the region defined by condition (2.6). To exclude the satellites of the Earth we have to assume that either (2.4) or (2.6) apply. If $\rho_0 \leq R_{SI}$ the region of the satellites to be excluded is defined simply by equation (2.5), and this occurs for

$$\rho_0^3 = \frac{2k^2 \mu_\oplus}{\eta^2} \leq R_{SI}^3 = a_\oplus^3 \frac{\mu_\oplus}{3}.$$

Thus, taking into account Kepler third law $a_\oplus^3 n_\oplus^2 \simeq k^2$ with n_\oplus the mean motion of the Earth, we have $\rho_0 \leq R_{SI}$ if and only if $\eta \geq \sqrt{6} n_\oplus$. Otherwise, if $\rho_0 > R_{SI}$, the boundary of the region containing satellites of the Earth is formed by a segment of the straight line $\rho = R_{SI}$ and the two arcs of the $\dot{\rho}^2 = G(\rho)$ curve with $0 < \rho < R_{SI}$.

The shape of the inner boundary

To understand the shape of the boundary of the Earth satellites region we need to find possible intersections between the curves $\mathcal{E}_\oplus = 0$ and $\mathcal{E}_\odot = 0$. However, if \mathcal{E}_\oplus is computed in a geocentric approximation, these intersections are physically meaningful only if they occur for $R_\oplus < \rho < R_{SI}$, that is, during a close approach to the Earth, but above its physical surface. In Milani et al. (2004) the following result is proved.

Theorem 2.2. *For $R_{\oplus} \leq \rho \leq R_{SI}$ the condition $\mathcal{E}_{\oplus}(\rho, \dot{\rho}) \leq 0$ implies $\mathcal{E}_{\odot}(\rho, \dot{\rho}) \leq 0$.*

This result shows that the intersections of the two zero-energy curves occur only where they do not matter. It also implies that the region of Solar System orbits excluding the satellites of the Earth does not have more connected components than the region satisfying condition (2.2) only. This applies only for particular values of the mass, radius and orbital elements of the planet on which the observer is located. It is a physical property of the Earth, not a general property of whatever planet.

The tiny object boundary

An alternative method to assign a lower limit to the distance is to impose that the object is not a “shooting star” (very small and very close to the Earth). We assume that the size is controlled by setting a maximum for the absolute magnitude H

$$H(\rho) \leq H_{max}. \quad (2.7)$$

If some value of the apparent magnitude is available, then the absolute magnitude H can be computed from h , the average of the measured apparent magnitudes, using the relation

$$H = h - 5 \log_{10} \rho - x(\rho),$$

where the correction $x(\rho)$ accounts for the distance from the Sun and the phase effect. For small ρ (e.g., $\rho < 0.01$ au) the correction $x(\rho)$ has a negligible dependence upon ρ because the distance from the Sun is $\simeq 1$ au and the phase is close to the angle between $\hat{\rho}$ and the opposition direction. Thus we can approximate $x(\rho)$ with a quantity x_0 independent of ρ . Also for larger values of ρ this is an acceptable approximation. Moreover, we are using ρ , the distance at the reference time \bar{t} , for all the epochs of the observations including photometry: this is a fair approximation unless the relative change of distance during the time span of the observed arc is relevant, which can happen only for very small distances. In this approximation, condition (2.7) becomes

$$\begin{aligned} H_{max} &\geq H = h - 5 \log_{10} \rho - x_0 \\ \Rightarrow \log_{10} \rho &\geq \frac{h - H_{max} - x_0}{5} = \log_{10} \rho_H, \end{aligned}$$

that is, given the apparent magnitude h , we have a minimum distance $\rho_H = \rho(H_{max})$ for the object to be of significant size. Thus the region satisfying condition (2.7) is just a half plane $\rho \geq \rho_H$. We call *shooting star limit* the straight line $\rho = \rho_H$.

Provided $\rho_H \geq R_\oplus$ it is possible to use the same arguments of the theorem on the intersection between the energy curves to show that condition (2.7) does not increase the number of connected components with respect to the region defined by excluding the satellites of the Earth. On the contrary, it is quite possible that the geometry of the region becomes simpler. If $H_{max} = 30$ and $h > 20$ the entire sphere of influence of the Earth is excluded by condition (2.7), thus conditions (2.6) is implied by (2.7), and condition (2.4) becomes irrelevant.

2.2.3 Formal definition of the Admissible Region

Let $R := \mathbb{R}^+ \times \mathbb{R}$ be the range/range-rate space. We recall the three regions we introduced so far.

- $\mathcal{D}_1 := \{(\rho, \dot{\rho}) \in R : \mathcal{E}_\odot(\rho, \dot{\rho}) \leq 0\}$, such that the body belongs to the Solar System;
- $\mathcal{D}_2 := \{(\rho, \dot{\rho}) \in R : \mathcal{E}_\oplus(\rho, \dot{\rho}) \geq 0\}$, such that the body is not a satellite of the Earth;
- $\mathcal{D}_3 := \{(\rho, \dot{\rho}) \in R : \rho \geq R_{SI}\}$, such that the orbit of the object is not controlled by the Earth.

We also add the region $\mathcal{D}_4 := \{(\rho, \dot{\rho}) : \rho \geq R_\oplus\}$, the one such that the body \mathcal{B} is outside the Earth.

Definition 2.3. Given an attributable \mathcal{A} at a time \bar{t} , the *Admissible Region* is the set

$$\text{AR}(\mathcal{A}) := \mathcal{D}_1 \cap (\mathcal{D}_2 \cup \mathcal{D}_3) \cap \mathcal{D}_4 \subseteq R.$$

In this way the AR turn out to be a compact subset of R . Moreover, we are now able to give a complete description of its boundary, that consists of the following portions of curves.

- (1) Part of the algebraic curve $\mathcal{E}_\odot(\rho, \dot{\rho}) = 0$ for $\rho > 0$. If the polynomial equation $V(\rho) - 4k^4 = 0$ has three positive roots there is another component, consisting of a simple closed curve, at larger values of ρ : this includes the case when this curve reduces to a single point, and it happens when the equation has a double positive root.
- (2) Two segments of the straight line $\rho = R_\oplus$.
- (3) Two portions of the curve $\dot{\rho}^2 = G(\rho)$ (corresponding to $\mathcal{E}_\oplus(\rho, \dot{\rho}) = 0$) and one segment of the straight line $\rho = R_{SI}$ in case $R_{SI} < \rho_0$. If $R_{SI} \geq \rho_0$ the two portions of the $\dot{\rho}^2 = G(\rho)$ are joined at $\rho = \rho_0$.

2.3 Sampling of the Admissible Region

Despite the formal definition given in the previous section (see Definition 2.3), for practical purposes, such as systematic ranging, it is better to define the AR as the set of all the couples $(\rho, \dot{\rho})$ satisfying the following conditions:

- (1) the object belongs to the Solar System, and it is not a too long period comet. We consider only the objects for which the value of the heliocentric energy is less than $-k^2/(2a_{max})$, where $a_{max} = 100$ au and $k = 0.01720209895$ is the Gauss' constant;
- (2) the corresponding object is not a satellite of the Earth, *i.e.*, the orbit of the object has a non-negative geocentric energy.
- (3) we discard the orbits corresponding to meteors too small to be source of meteorites, using the condition $H \leq H_{max}$, where $H_{max} = 34.5$ is the shooting star limit (see Section 2.2.2), and H is the absolute magnitude.

Even with this definition the AR turns out to be a compact subset of $R = \mathbb{R}^+ \times \mathbb{R}$ and to have at most two connected components, that means that it could be represented as the union of no more than two disjoint regions in the $(\rho, \dot{\rho})$ space. The AR has usually one component and the case with two components indicates the possibility for the object to be distant (perihelion $q > 28$ au).

Since the AR is compact, we can sample it with a finite number of points. We basically use two different sampling techniques, depending on the existence of a reliable nominal solution. A nominal solution is an orbit obtained by unconstrained differential corrections, starting from a preliminary orbit as first guess³. If the value of the geodesic curvature signal-to-noise ratio (SNR) (Milani et al. 2008) is greater than 3, we say that the nominal orbit is *reliable*. In case a reliable nominal solution does not exist we make use of a rectangular grid on $(\rho, \dot{\rho})$ to scan the Admissible Region; otherwise, if a reliable nominal solution exists we compute a spider web sampling in a neighbourhood of the nominal solution (Tommei 2006). Both techniques are described in more detail in Section 2.3.1 and 2.3.2, respectively.

2.3.1 Case I: the rectangular grids

When a reliable nominal solution does not exist, the systematic ranging is performed by a two-step procedure and in both steps it uses rectangular grids on R .

³For instance, the preliminary orbit can be obtained from the Gauss' method, (Milani et al. 2010).

First step. The selection of the grid depends on the number of connected components of the AR and on the values of the roots of $V(\rho) - 4k^4$. We call r_1 , r_2 and r_3 the positive roots of the polynomial, if they exist, The grid for the first step is selected according to this rules:

- (1) if the Admissible Region has one connected component and $r_1 < \sqrt{10}$ au we perform a uniform sampling in $\log_{10} \rho$ with a 50×50 grid over $(0, r_1] \times [\dot{\rho}_{min}, \dot{\rho}_{max}]$;
- (2) if the Admissible Region has one connected component and $r_1 \geq \sqrt{10}$ au we perform a uniform sampling in ρ with a 50×50 grid over $(0, r_1] \times [\dot{\rho}_{min}, \dot{\rho}_{max}]$;
- (3) if the Admissible Region has two connected components we perform a uniform sampling in ρ with a 100×100 grid over $(0, r_3] \times [\dot{\rho}_{min}, \dot{\rho}_{max}]$.

Nevertheless, since the AR has a shape dictated by a polynomial equation and it is not a rectangle, we check the value of the heliocentric energy for each grid point, and we discard those not satisfying condition 1. Orbits not satisfying condition 2 are discarded as well, except when we compute the probability for the asteroid to be a satellite of the Earth⁴.

Second step. Once we have a grid from the first step, we apply the doubly constrained differential corrections (see Section 2.4) to obtain a sample of full orbits based on the AR sampling. We also compute a χ value for each orbit obtained in this way, as in equation (2.10). The purpose of this preliminary step is to have a way to select the best orbits (in the sense of their χ value) among the ones obtained in the previous step. We select the minimum and the maximum value of ρ and $\dot{\rho}$ among all the points for which the doubly constrained differential corrections reached convergence and for which $\chi < 5$ (see Section 2.5). In this way we select a rectangle $[\rho_{min}, \rho_{max}] \times [\dot{\rho}_{min}, \dot{\rho}_{max}]$, smaller than the one employed in the first step. Moreover, using the first grid we also compute the probability for the object to be a NEO (see Section 2.8.2) and we use this value to select the grid for the second step. If the probability of being a NEO is $> 50\%$ the sampling is uniform grid in $\log_{10} \rho$, otherwise it is uniform in ρ . In both cases we use a 100×100 grid over $[\rho_{min}, \rho_{max}] \times [\dot{\rho}_{min}, \dot{\rho}_{max}]$.

⁴The object could be either an artificial satellite or an interplanetary orbit in a temporary Earth satellite capture (Granvik et al. 2012).

2.3.2 Case II: spider web

If a reliable nominal orbit exists, instead of using a grid (as in Section 2.3.1), we compute a spider web sampling in a suitable neighbourhood of the nominal solution. This is obtained by following the level curves of the quadratic approximation of the target function used to minimise the RMS of the observational residuals. The advantage of the use of the cobweb is that first it is faster than the systematic ranging, and second it is more accurate in the cases for which we have already a reliable nominal solution.

Let \mathbf{x}^* be the nominal solution with its uncertainty, represented by the 6×6 covariance matrix $\Gamma(\mathbf{x}^*)$. In a neighbourhood of \mathbf{x}^* , the target function can be well approximated by means of the quadratic form defined by the normal matrix $C(\mathbf{x}^*) = \Gamma^{-1}(\mathbf{x}^*)$. The matrix $C(\mathbf{x}^*)$ is positive definite, hence the level curves of the target function are concentric 5-dimensional ellipsoids in the 6-dimensional orbital elements space. The level curves on the $(\rho, \dot{\rho})$ space are represented by the marginal ellipsoids, defined by the normal matrix

$$C^{\rho\rho}(\mathbf{x}^*) = \Gamma_{\rho\rho}^{-1}(\mathbf{x}^*),$$

where $\Gamma_{\rho\rho}(\mathbf{x}^*)$ is the restriction of $\Gamma(\mathbf{x}^*)$ to the $(\rho, \dot{\rho})$ space (Milani et al. 2010, Section 5.4). To sample these curves we choose the maximum value $\sigma_{max} = 5$ for the confidence parameter. Then, for each level curve within the confidence level σ_{max} , we select the points corresponding to some fixed directions. We initially create a regular rectangular grid in the space of polar elliptic coordinates (r, ϑ) , that is we sample the rectangle $[0, \sigma_{max}] \times [0, 2\pi)$. Then we apply to the rectangle the following transformation, depending on the covariance matrix of the nominal orbit and on the orbit itself:

$$\begin{pmatrix} \rho \\ \dot{\rho} \end{pmatrix} = r \begin{pmatrix} \sqrt{\lambda_1} \cos \vartheta & -\sqrt{\lambda_2} \sin \vartheta \\ \sqrt{\lambda_2} \sin \vartheta & \sqrt{\lambda_1} \cos \vartheta \end{pmatrix} \mathbf{v}_1 + \begin{pmatrix} \rho^* \\ \dot{\rho}^* \end{pmatrix}, \quad (2.8)$$

where $\lambda_1 > \lambda_2$ are the eigenvalues of the 2×2 matrix $\Gamma_{\rho\rho}(\mathbf{x}^*)$, \mathbf{v}_1 is the unit eigenvector corresponding to the greatest eigenvalue λ_1 , and ρ^* and $\dot{\rho}^*$ are the range and range-rate values of the nominal solution.

2.4 The Manifold Of Variations

We describe how to obtain a sample of orbits compatible with the observational dataset starting from a sampling of the Admissible Region. This method is used twice in the rectangular sampling case, after the first step (as anticipated in Section 2.3.1) and after the second step, and it is used once in the spider web sampling case.

To obtain orbits from observations we use the least squares method (Milani et al. 2010, Chapter 5). Thus we recall that the target function is

$$Q(\mathbf{x}) = \frac{1}{m} \boldsymbol{\xi}(\mathbf{x})^\top W \boldsymbol{\xi}(\mathbf{x}),$$

where \mathbf{x} are the orbital elements, m is the number of observations used in the fit, and $\boldsymbol{\xi}$ is the vector of the observed-computed debiased astrometric residuals⁵, and W is the weight matrix (see Section 1.5). The choice of the weights for each observatory is fundamental, and it has to take into account the debiasing of the star catalogue systematic errors, unless the astrometric reduction has already been performed with an essentially bias-free star catalogue, for example the Gaia DR1 (Lindegren et al. 2016).

In general, as explained in Section 2.1, a full orbit determination is not possible for such short arcs. Anyway, just using the observational dataset it is possible to compute an attributable \mathcal{A}_0 at the mean epoch of the observations. The AR theory has been developed to obtain constraints on the values of $(\rho, \dot{\rho})$, so that we can merge the information contained in the attributable with the knowledge of an AR sampling. The basic idea of this method is to fix ρ and $\dot{\rho}$ at some specific values $\boldsymbol{\rho}_0 = (\rho_0, \dot{\rho}_0)$ obtained from the AR sampling, compose the full orbit $(\mathcal{A}_0, \rho_0, \dot{\rho}_0)$ and fit only the attributable part to the observations with a suitable differential corrections procedure.

Definition 2.4. Given a subset K of the AR, we define the *Manifold Of Variations* (MOV) as the set of points $(\mathcal{A}^*(\boldsymbol{\rho}_0), \boldsymbol{\rho}_0)$ such that $\boldsymbol{\rho}_0 \in K$ and $\mathcal{A}^*(\boldsymbol{\rho}_0)$ is the local minimum of the function

$$Q(\mathcal{A}, \boldsymbol{\rho})|_{\boldsymbol{\rho}=\boldsymbol{\rho}_0},$$

when it exists. We denote the Manifold Of Variations with \mathcal{M} .

Remark 2.5. In general \mathcal{M} is a two-dimensional manifold, since the differential of the map from the $(\rho, \dot{\rho})$ space to \mathcal{M} has rank 2 (see Section 2.6.4 for further details).

In the case of the systematic ranging, the set K coincide with the whole AR, sampled with a semi-logarithmic or uniform grid (see Section 2.3.1), whereas in the spider web case K coincide with an ellipse around $(\rho^*, \dot{\rho}^*)$ (see Section 2.3.2). For each sample point $\boldsymbol{\rho}_0 = (\rho_0, \dot{\rho}_0) \in K$ we fix $\rho = \rho_0$ and $\dot{\rho} = \dot{\rho}_0$ in the target function Q and then we look for $\mathcal{A}^*(\boldsymbol{\rho}_0)$ by means of an iterative procedure, the *doubly constrained differential corrections*, that are

⁵In case there is a bias in the observations (Farnocchia et al. 2015b), the residuals are computed following the classical definition of the residuals as observed-computed and also by subtracting the biases vector.

classical differential corrections performed on a 4-dimensional space rather than on a 6-dimensional one. The normal equation is $C_{\mathcal{A}}\Delta\mathcal{A} = D_{\mathcal{A}}$, where

$$C_{\mathcal{A}} := B_{\mathcal{A}}^{\top}WB_{\mathcal{A}}, \quad D_{\mathcal{A}} := -B_{\mathcal{A}}^{\top}W\xi, \quad B_{\mathcal{A}} := \frac{\partial\xi}{\partial\mathcal{A}}. \quad (2.9)$$

We indicate as K' the subset of K on which the doubly constrained differential corrections converge, giving a point on \mathcal{M} . In this way the sampling of \mathcal{M} is performed over $K' \subseteq K$.

Definition 2.6. For each orbit $\mathbf{x} \in \mathcal{M}$ we define the χ -value to be

$$\chi(\mathbf{x}) := \sqrt{m(Q(\mathbf{x}) - Q^*)}, \quad (2.10)$$

where Q^* is the minimum value of the target function defined as follows: it is $Q(\mathbf{x}^*)$ if a reliable nominal solution \mathbf{x}^* exists; it is the minimum value of $Q(\mathbf{x})$ on \mathcal{M} otherwise.

Remark 2.7. In other words $Q^* := \min_{\rho \in K'} Q(\mathcal{A}^*(\rho), \rho)$, and note that Q^* exists since Q is continuous and K' is compact.

By using this information, we can assign a probability to each subset of K' , because we are able to determine a probability density function on the sampling space (see Section 2.5). The first and most urgent application is the impact probability computation for a possible impactor. Moreover the probability density function is also necessary to compute the probability, hereinafter the *score*, of each object to belong to one of the following classes: Near-Earth Object (NEO), Main Belt Object (MBO), Distant Object (DO), likely a Kuiper Belt Object (KBO), or Scattered Object (SO) (see Section 2.8.2 for the conditions defining each class). The latter (SO) includes all the objects that do not belong to any other category.

2.5 Approach for probability computations

We obtain a probability distribution on the sampling space to be used for several applications, such as the computation of the impact probability and the score. We begin assuming that the residuals are a Gaussian random variable Ξ , with zero mean and covariance $\Gamma_{\xi} = W^{-1}$. Hence the probability density function on the residuals space is

$$\begin{aligned} p_{\Xi}(\xi) &= N(\mathbf{0}, \Gamma_{\xi})(\xi) = \frac{\sqrt{\det W}}{(2\pi)^{m/2}} \exp\left(-\frac{mQ(\xi)}{2}\right) = \\ &= \frac{\sqrt{\det W}}{(2\pi)^{m/2}} \exp\left(-\frac{1}{2}\xi^{\top}W\xi\right). \end{aligned} \quad (2.11)$$

Without loss of generality, we can assume that

$$p_{\Xi}(\boldsymbol{\xi}) = N(\mathbf{0}, I_m)(\boldsymbol{\xi}) = \frac{1}{(2\pi)^{m/2}} \exp\left(-\frac{1}{2}\boldsymbol{\xi}^\top \boldsymbol{\xi}\right), \quad (2.12)$$

where I_m is the $m \times m$ identity matrix. As explained in Milani et al. (2010, Section 5.7), this is obtained by using the normalised residuals in place of the true residuals; biases due to star catalogue can also be removed while forming the normalised residuals. With this technique, the probability density function becomes normalised to a standard normal distribution. Thus from now on, we will use $\boldsymbol{\xi}$ to indicate the normalised residuals, and the function F maps the orbital elements space to the normalised residuals space. With the use of normalised residuals, also the expression for the target function changes and becomes simpler:

$$Q(\mathbf{x}) = \frac{1}{m} \boldsymbol{\xi}(\mathbf{x})^\top \boldsymbol{\xi}(\mathbf{x}).$$

A possible approach to propagate the density (2.12) to the sampling space uses the Bayesian theory to combine the density coming from the residuals with a prior distribution. The *a posteriori* probability density function for $(\rho, \dot{\rho})$ is given in Muinonen et al. (1993) as

$$p_{post}(\rho, \dot{\rho}) \propto p(\boldsymbol{\xi}(\rho, \dot{\rho})) \cdot p_{prior}(\rho, \dot{\rho})$$

where p_{prior} is a prior distribution on the sampled space. We report some possible choices for the prior probability.

- *Jeffreys' prior.* It has been used for the first time in Granvik et al. (2009). It takes into account the partial derivatives of the vector of the residuals with respect to the coordinates $(\rho, \dot{\rho})$. Jeffreys' prior tends to favour orbits where the object is close to the observer, because of the sensitivity of the residuals for small topocentric distances. This approach coincides with a full non-linear propagation of the probability density function $p_{\Xi}(\boldsymbol{\xi})$ to the AR space. In Section 2.7.2 we investigate this approach, even if we decide to discard it since it results in spurious probabilities due to the over-weighting of close orbits as well as Jeffreys' prior.
- *Prior based on a population model.* This approach requires the choice of a metric on the absolute magnitude space, which is far from trivial.
- *Uniform distribution.* Uniform distribution in the $(\rho, \dot{\rho})$ space.

Farnocchia et al. (2015c) give a detailed description of all these possible choices, and they also analyse how the impact probability change according to different prior distributions. They conclude that the uniform distribution is a good choice for an *a priori* probability density function, because it represents a good compromise between a simple approach and the identification of potential impactors.

We propose a new method to propagate the probability density function $p_{\Xi}(\xi)$ back to the sampling space. This method is a rigorous propagation of the density function according to the probability theory, and it does not use any *a priori* assumption. Our approach is described in detail in Section 2.6 and it is based on the Admissible Region theory. Thus it is worth noticing that we limit our analysis to Solar System orbits (condition number 1 of Section 2.3), because interstellar objects are very rare. As a consequence, we use a Bayesian theory with a population limited to the Solar System, and all the probability computations we describe are actually conditional probabilities to the AR.

2.6 Probability density function computation

In this section we give the mathematical details to obtain a probability density function on the sampling space by starting just from the density $p_{\Xi}(\xi)$ on the residuals space and by propagating it back by some maps.

2.6.1 Spaces and maps

Let us introduce the following spaces:

- (1) S is the space of the sampling variables. We have that $S = \mathbb{R}^+ \times \mathbb{R}$ if the sampling is uniform in ρ , $S = \mathbb{R}^2$ if the sampling is uniform in $\log_{10} \rho$, and $S = \mathbb{R}^+ \times \mathbb{S}^1$ in the spider web case.
- (2) $K' \subseteq \mathbb{R} \times \mathbb{R}^+$ is the subset of the points of the Admissible Region such that the doubly constrained differential corrections give a point on the MOV;
- (3) $\mathcal{X} = A \times R$ is the 6-dimensional orbital elements space (in attributable coordinates), where $A := \mathbb{S}^1 \times (-\pi/2, \pi/2) \times \mathbb{R}^2$ is the attributable space and $R := \mathbb{R}^+ \times \mathbb{R}$;
- (4) \mathcal{M} is the Manifold Of Variations, a 2-dimensional submanifold of \mathcal{X} ;
- (5) \mathbb{R}^m is the residuals space, whose dimension is $m \geq 6$ since the least possible number of observations is 3.

Now we introduce the maps between these spaces. First, the residuals are a function of the fit parameters, that is $\boldsymbol{\xi} = F(\mathbf{x})$, with $F : \mathcal{X} \rightarrow \mathbb{R}^m$ a differentiable map. The second map that we define is between the AR space and the MOV.

Definition 2.8. The map $f_\mu : K' \rightarrow \mathcal{M}$ is defined to be

$$f_\mu(\boldsymbol{\rho}) := (\mathcal{A}^*(\boldsymbol{\rho}), \boldsymbol{\rho}),$$

where $\mathcal{A}^*(\boldsymbol{\rho}) \in A$ is the best-fit attributable obtained at convergence of the doubly constrained differential corrections.

Remark 2.9. For each $\boldsymbol{\rho} \in K'$ the vector $\mathcal{A}^*(\boldsymbol{\rho})$ minimises the restriction $Q(\mathcal{A}; \boldsymbol{\rho})$, that is a function of \mathcal{A} only. Note that this minimum exists since $\boldsymbol{\rho} \in K'$ and K' is by definition the subset of the Admissible Region on which convergence has been achieved.

Proposition 2.10. *The map f_μ is a global parameterization of \mathcal{M} as a 2-dimensional manifold.*

Proof. Here we refer to Appendix C, Theorem C.3. The set K' is a subset of \mathbb{R}^2 comprised between an open set and its closure, the map f_μ is of class at least C^1 and its Jacobian matrix is

$$(Df_\mu)_\rho = \frac{\partial f_\mu}{\partial \boldsymbol{\rho}}(\boldsymbol{\rho}) = \begin{pmatrix} \frac{\partial \mathcal{A}^*}{\partial \boldsymbol{\rho}}(\boldsymbol{\rho}) & \frac{\partial \mathcal{A}^*}{\partial \dot{\boldsymbol{\rho}}}(\boldsymbol{\rho}) \\ 1 & 0 \\ 0 & 1 \end{pmatrix} = \begin{pmatrix} \frac{\partial \mathcal{A}^*}{\partial \boldsymbol{\rho}}(\boldsymbol{\rho}) \\ I_2 \end{pmatrix}, \quad (2.13)$$

from which is clear that it is full rank on K' . This concludes the proof, proving \mathcal{M} to be a 2-dimensional manifold according to Theorem C.3. \square

The last map that we define goes from the sampling space to the AR space R .

Definition 2.11. The map $f_\sigma : S \rightarrow \mathbb{R}^+ \times \mathbb{R}$ is defined according to the following cases, depending on the sampling technique:

- (i) if the sampling is uniform in ρ , f_σ is the identity map;
- (ii) if the sampling is uniform in $\log_{10} \rho$, we have $S = \mathbb{R}^2$ and $f_\sigma(x, y) := (10^x, y)$ ⁶;
- (iii) if we are in the spider web case $S = \mathbb{R}^+ \times \mathbb{S}^1$ and the map f_σ is given by (2.8).

⁶This is equivalent to $f_\sigma(\log_{10} \rho, \dot{\rho}) := (\rho, \dot{\rho})$, for all $\rho \in \mathbb{R}^+$ and $\dot{\rho} \in \mathbb{R}$.

We then consider the following chain of maps

$$S \xrightarrow{f_\sigma} \mathbb{R}^+ \times \mathbb{R} \supseteq K' \xrightarrow{f_\mu} \mathcal{M} \subseteq \mathcal{X} \xrightarrow{F} \mathbb{R}^m$$

and we use it to compute the probability density function on S . We denote with a bold small letter the variables and with a bold capital letter the random variable, on each space. In this way we denote with \mathbf{s} the variables of the sampling space S and with \mathbf{S} be the corresponding random variable, as well as \mathbf{A} and \mathbf{R} for the random variables on the spaces A and R , respectively.

2.6.2 Conditional density on an affine subspace

Let m and N be two positive integers, with $m > N$. Let $B \in \mathcal{M}(m, N; \mathbb{R})$ a $m \times N$ matrix with full rank, that is $\text{rk}(B) = N$. Consider the affine N -dimensional subspace of \mathbb{R}^m given by

$$W := \{\boldsymbol{\xi} \in \mathbb{R}^m : \boldsymbol{\xi} = B\mathbf{x} + \boldsymbol{\xi}^*, \mathbf{x} \in \mathbb{R}^N\} = \text{Im}(B) + \boldsymbol{\xi}^*.$$

We can also assume that $\boldsymbol{\xi}^*$ is orthogonal to W , that is $\boldsymbol{\xi}^* \in \text{Im}(B)^\perp$: indeed, otherwise it is possible to subtract the component parallel to W . Given the random variable $\boldsymbol{\Xi}$ with the Gaussian distribution on \mathbb{R}^m as in (2.12), we want to find the conditional probability density $p_{\boldsymbol{\Xi}|W}$ of $\boldsymbol{\Xi}$ on W . Let $R \in \mathcal{M}(m; \mathbb{R})$ be an $m \times m$ rotation matrix and let $f_R : \mathbb{R}^m \rightarrow \mathbb{R}^m$ be the affine map

$$f_R(\boldsymbol{\xi}) := R(\boldsymbol{\xi} - \boldsymbol{\xi}^*).$$

Throughout this section, we use the notation $f_R(\boldsymbol{\xi}) =: \boldsymbol{\xi}_R = \begin{pmatrix} \boldsymbol{\xi}' \\ \boldsymbol{\xi}'' \end{pmatrix}$, with $\boldsymbol{\xi}' \in \mathbb{R}^{m-N}$ and $\boldsymbol{\xi}'' \in \mathbb{R}^N$. We choose R in such a way that for all $\boldsymbol{\xi}'' \in \mathbb{R}^N$

$$f_R^{-1} \begin{pmatrix} \mathbf{0} \\ \boldsymbol{\xi}'' \end{pmatrix} = R^\top \begin{pmatrix} \mathbf{0} \\ \boldsymbol{\xi}'' \end{pmatrix} + \boldsymbol{\xi}^* \in W. \quad (2.14)$$

Proposition 2.12. *Condition (2.14) holds for all $\boldsymbol{\xi}'' \in \mathbb{R}^N$ if and only if there exists an invertible matrix $A \in \mathcal{M}(N; \mathbb{R})$ such that $RB = \begin{pmatrix} \mathbf{0} \\ A \end{pmatrix}$.*

Proof. (\Leftarrow) Let $\begin{pmatrix} \mathbf{0} \\ \boldsymbol{\xi}'' \end{pmatrix} \in \mathbb{R}^m$. Since A is invertible there exists $\tilde{\mathbf{x}} \in \mathbb{R}^N$ such that $A\tilde{\mathbf{x}} = \boldsymbol{\xi}''$. Then

$$R^\top \begin{pmatrix} \mathbf{0} \\ \boldsymbol{\xi}'' \end{pmatrix} = R^\top \begin{pmatrix} \mathbf{0} \\ A \end{pmatrix} \tilde{\mathbf{x}} = R^\top RB\tilde{\mathbf{x}} = B\tilde{\mathbf{x}},$$

and hence $R^\top \begin{pmatrix} \mathbf{0} \\ \boldsymbol{\xi}'' \end{pmatrix} + \boldsymbol{\xi}^* = B\tilde{\mathbf{x}} + \boldsymbol{\xi}^* \in W$.

(\Rightarrow) Condition (2.14) implies that for all $\xi'' \in \mathbb{R}^N$ there exists $\tilde{\mathbf{x}} \in \mathbb{R}^N$ such that

$$\begin{pmatrix} \mathbf{0} \\ \xi'' \end{pmatrix} = RB\tilde{\mathbf{x}}.$$

Since the multiplication by RB is injective, such $\tilde{\mathbf{x}}$ is unique. Therefore there exists a well-defined map $P : \mathbb{R}^N \rightarrow \mathbb{R}^N$ such that $P(\xi'') = \tilde{\mathbf{x}}$. The map P is linear and injective since $\text{Ker } P = \{\mathbf{0}\}$, thus is a bijection. Let A be the $N \times N$ matrix associated to P^{-1} : it is now easy to prove that $RB = \begin{pmatrix} \mathbf{0} \\ A \end{pmatrix}$. \square

Proposition 2.13. *Let $U := \{\xi_R \in \mathbb{R}^m : \xi' = \mathbf{0}\}$. Then the following holds:*

- (i) $U = f_R(W) = R \text{Im } B$ and the map $f_R|_W : W \rightarrow U$ is a bijection;
- (ii) $R\xi^* = \begin{pmatrix} \xi'^* \\ \mathbf{0} \end{pmatrix}$ for some $\xi'^* \in \mathbb{R}^{m-N}$.

Proof. (i) (\supseteq) If $\xi \in W$ there exists $\tilde{\mathbf{x}} \in \mathbb{R}^N$ such that $\xi = B\tilde{\mathbf{x}} + \xi^*$. Then from Proposition 2.12 we have $f_R(\xi) = RB\tilde{\mathbf{x}} = \begin{pmatrix} \mathbf{0} \\ A \end{pmatrix} \tilde{\mathbf{x}} \in U$.

(\subseteq) Let $\mathbf{u} \in U$, so that $\mathbf{u} = \begin{pmatrix} \mathbf{0} \\ \xi'' \end{pmatrix}$ for some $\xi'' \in \mathbb{R}^N$. Define $\tilde{\mathbf{x}} = A^{-1}\xi''$. Thus a straightforward calculation shows that $f_R(B\tilde{\mathbf{x}} + \xi^*) = \mathbf{u}$, proving that $\mathbf{u} \in f_R(W)$.

(ii) Since $\xi^* \in (\text{Im } B)^\perp$ and R is an isometry, we have that $R\xi^* \in R(\text{Im } B)^\perp = (R \text{Im } B)^\perp = U^\perp$, by using (i). \square

Theorem 2.14. *The conditional probability density of Ξ'' is $N(\mathbf{0}, I_N)$, that is*

$$p_{\Xi''}(\xi'') = \frac{1}{(2\pi)^{N/2}} \exp\left(-\frac{1}{2}\xi''^\top \xi''\right)$$

Proof. By the standard propagation formula for probability density functions under the action of a continuous function, we have that

$$\begin{aligned} p_{f_R(\Xi)}(\xi_R) &= |\det R| p_{\Xi}(f_R^{-1}(\xi_R)) = \\ &= \frac{1}{(2\pi)^{m/2}} \exp\left(-\frac{1}{2}(R^\top \xi_R + \xi^*)^\top (R^\top \xi_R + \xi^*)\right) = \\ &= \frac{1}{(2\pi)^{m/2}} \exp\left(-\frac{1}{2}\left(\xi_R^\top \xi_R + 2\xi_R^\top R\xi^* + \xi^{*\top} \xi^*\right)\right). \end{aligned}$$

The conditional probability density of the variable $f_R(\Xi)$ on $f_R(W) = U$ (equality from Proposition 2.13 (i)) is obtained by using that $\xi' = \mathbf{0}$ on U

and the Proposition 2.13 (ii). We have

$$\begin{aligned} p_{f_R(\Xi)|f_R(W)}(\xi'') &= \frac{\frac{1}{(2\pi)^{m/2}} \exp\left(-\frac{1}{2}(\xi''^\top \xi'' + \xi^{*\top} \xi^*)\right)}{\int_{\mathbb{R}^N} \frac{1}{(2\pi)^{m/2}} \exp\left(-\frac{1}{2}(\xi''^\top \xi'' + \xi^{*\top} \xi^*)\right) d\xi''} = \\ &= \frac{1}{(2\pi)^{N/2}} \exp\left(-\frac{1}{2}\xi''^\top \xi''\right), \end{aligned}$$

where we have used that $\int_{\mathbb{R}^n} \exp\left(-\frac{1}{2}\mathbf{y}^\top \mathbf{y}\right) d\mathbf{y} = (2\pi)^{n/2}$ for all $n \geq 1$. Now the thesis follows by noting that the random variable $f_R(\Xi)|f_R(W)$ coincide with Ξ'' . \square

Corollary 2.15. *The conditional probability density of Ξ on W is*

$$p_{\Xi|W}(\xi) = \frac{1}{(2\pi)^{N/2}} \exp\left(-\frac{1}{2}(\xi - \xi^*)^\top (\xi - \xi^*)\right),$$

where $\xi \in W$.

Proof. From Proposition 2.13 (i) we know that $f_R|_W$ is a bijection. Thus for all $\xi'' \in \mathbb{R}^N$ there exists a unique $\xi \in W$ such that $\begin{pmatrix} \mathbf{0} \\ \xi'' \end{pmatrix} = f_R(\xi) = R(\xi - \xi^*)$. Now it suffices to use this in the equation for $p_{\Xi''}(\xi'')$ in Theorem 2.14. \square

2.6.3 From the residuals space to the MOV

The first step of the procedure is the propagation of the probability density function from the normalised residuals space to the Manifold Of Variations. We recall that we start from the following density (see equation (2.12)):

$$p_{\Xi}(\xi) = N(\mathbf{0}, I_m)(\xi) = \frac{1}{(2\pi)^{m/2}} \exp\left(-\frac{1}{2}\xi^\top \xi\right).$$

From section 2.4 We have defined Q^* to be the minimum value of the target function over \mathcal{M} , that is

$$Q^* := \min_{\rho \in K'} Q(\mathcal{A}^*(\rho), \rho).$$

Let us denote with $\rho^* \in K'$ the point in which the above minimum is attained and with $\mathbf{x}^* = f_\mu(\rho^*) = (\mathcal{A}^*(\rho^*), \rho^*)$ the corresponding point on the MOV \mathcal{M} . Lastly, let $\xi^* := F(\mathbf{x}^*) = \xi(\mathbf{x}^*)$.

Theorem 2.16. *By linearizing F around \mathbf{x}^* , the conditional probability density on $T_{\mathbf{x}^*}\mathcal{M}$ is given by*

$$p_{\mathbf{X}|T_{\mathbf{x}^*}\mathcal{M}}(\mathbf{x}) = \frac{\exp\left(-\frac{\chi^2(\mathbf{x})}{2}\right)}{\int_{T_{\mathbf{x}^*}\mathcal{M}} \exp\left(-\frac{\chi^2(\mathbf{y})}{2}\right) d\mathbf{y}}. \quad (2.15)$$

Proof. The map F is differentiable of class at least C^1 . The Jacobian matrix of F is the design matrix $B(\mathbf{x}) = \frac{\partial F}{\partial \mathbf{x}}(\mathbf{x}) \in \mathcal{M}(m, N; \mathbb{R})$. Since the doubly constrained differential corrections converge to \mathbf{x}^* , the matrix $B(\mathbf{x}^*)$ is full rank. It follows that the map F is a local parameterization of

$$V := F(\mathcal{M}) = \{\boldsymbol{\xi} \in \mathbb{R}^m : \boldsymbol{\xi} = F(\mathbf{x}), \mathbf{x} \in \mathcal{M}\},$$

that turns out to be a 2-dimensional submanifold of the residuals space \mathbb{R}^m , in a suitable neighbourhood of $\boldsymbol{\xi}^*$. Consider the differential

$$DF_{\mathbf{x}^*} : T_{\mathbf{x}^*}\mathcal{M} \rightarrow T_{\boldsymbol{\xi}^*}V,$$

where $T_{\boldsymbol{\xi}^*}V = \{\boldsymbol{\xi} \in \mathbb{R}^m : \boldsymbol{\xi} = \boldsymbol{\xi}^* + B(\mathbf{x}^*)(\mathbf{x} - \mathbf{x}^*), \mathbf{x} \in T_{\mathbf{x}^*}\mathcal{M}\}$ is a 2-dimensional affine subspace of \mathbb{R}^m . We claim that $\boldsymbol{\xi}^*$ is orthogonal to $T_{\boldsymbol{\xi}^*}V$: since \mathbf{x}^* is a local minimum of the target function Q

$$\mathbf{0} = \frac{\partial Q}{\partial \mathbf{x}}(\mathbf{x}^*) = \frac{2}{m} \boldsymbol{\xi}(\mathbf{x}^*)^\top B(\mathbf{x}^*),$$

that is $\boldsymbol{\xi}(\mathbf{x}^*) = \boldsymbol{\xi}^* \in B(\mathbf{x}^*)^\perp$. By applying Corollary 2.15 we have that

$$p_{\Xi|T_{\boldsymbol{\xi}^*}V}(\boldsymbol{\xi}) = \frac{1}{2\pi} \exp\left(-\frac{1}{2}(\boldsymbol{\xi} - \boldsymbol{\xi}^*)^\top (\boldsymbol{\xi} - \boldsymbol{\xi}^*)\right)$$

for $\boldsymbol{\xi} \in T_{\boldsymbol{\xi}^*}V$. The differential map is continuous and invertible (since it is represented by the matrix $A(\mathbf{x}^*)$, as in Proposition 2.12), thus we can use the standard formula for the transformations of random variables to obtain

$$p_{\mathbf{X}|T_{\mathbf{x}^*}\mathcal{M}}(\mathbf{x}) = \frac{\sqrt{\det C(\mathbf{x}^*)}}{2\pi} \exp\left(-\frac{1}{2}(\mathbf{x} - \mathbf{x}^*)^\top C(\mathbf{x}^*)(\mathbf{x} - \mathbf{x}^*)\right),$$

for $\mathbf{x} \in T_{\mathbf{x}^*}\mathcal{M}$, where $C(\mathbf{x}^*)$ is the 6×6 normal matrix of the differential corrections leading to \mathbf{x}^* . Furthermore, in the approximation used, we have

$$\chi^2(\mathbf{x}) = mQ(\mathbf{x}) - mQ^* = (\mathbf{x} - \mathbf{x}^*)^\top C(\mathbf{x}^*)(\mathbf{x} - \mathbf{x}^*),$$

so that for $\mathbf{x} \in T_{\mathbf{x}^*}\mathcal{M}$

$$p_{\mathbf{X}|T_{\mathbf{x}^*}\mathcal{M}}(\mathbf{x}) = \frac{\sqrt{\det C(\mathbf{x}^*)}}{2\pi} \exp\left(-\frac{\chi^2(\mathbf{x})}{2}\right).$$

Now the thesis follows by converting the constant to a normalising constant be means of an integral. \square

2.6.4 From the MOV to the AR

We use the results and definitions given in Appendix C. In particular, the definition of the integral of a continuous function on a manifold is the analogous of the theorem of change of variables for integrals, thus it can be used to propagate a probability density function on a manifold to a probability density function over the space that parametrizes the manifold itself.

Theorem 2.17. *Assuming (2.15), the probability density function of the variable \mathbf{R} is*

$$p_{\mathbf{R}}(\boldsymbol{\rho}) = \frac{\exp\left(-\frac{\chi^2(\boldsymbol{\rho})}{2}\right) \sqrt{G_{\mu}(\boldsymbol{\rho})}}{\int_{K'} \exp\left(-\frac{\chi^2(\boldsymbol{\rho})}{2}\right) \sqrt{G_{\mu}(\boldsymbol{\rho})} d\boldsymbol{\rho}},$$

where $\chi^2(\boldsymbol{\rho}) = \chi^2(\mathbf{x}(\boldsymbol{\rho}))$ and G_{μ} is the Gramian determinant

$$G_{\mu}(\boldsymbol{\rho}) = \det\left(I_2 + \left(\frac{\partial \mathcal{A}^*}{\partial \boldsymbol{\rho}}(\boldsymbol{\rho})\right)^{\top} \frac{\partial \mathcal{A}^*}{\partial \boldsymbol{\rho}}(\boldsymbol{\rho})\right). \quad (2.16)$$

Proof. We have already proved that the map $f_{\mu} : K' \rightarrow \mathcal{M}$ is a global parameterization of \mathcal{M} , thus from equation (C.1) we have that

$$p_{\mathbf{R}}(\boldsymbol{\rho}) = p_{\mathbf{X}|T_{\mathbf{x}^*}\mathcal{M}}(f_{\mu}(\boldsymbol{\rho})) \cdot \sqrt{\det\left[\left(\frac{\partial f_{\mu}}{\partial \boldsymbol{\rho}}(\boldsymbol{\rho})\right)^{\top} \frac{\partial f_{\mu}}{\partial \boldsymbol{\rho}}(\boldsymbol{\rho})\right]}$$

and the thesis follows since from equation (2.13)

$$\left[\frac{\partial f_{\mu}}{\partial \boldsymbol{\rho}}(\boldsymbol{\rho})\right]^{\top} \frac{\partial f_{\mu}}{\partial \boldsymbol{\rho}}(\boldsymbol{\rho}) = I_2 + \left(\frac{\partial \mathcal{A}^*}{\partial \boldsymbol{\rho}}(\boldsymbol{\rho})\right)^{\top} \frac{\partial \mathcal{A}^*}{\partial \boldsymbol{\rho}}(\boldsymbol{\rho}).$$

□

In order to evaluate (2.16) we have to explicitly determine the expression for the matrix

$$\frac{\partial \mathcal{A}^*}{\partial \boldsymbol{\rho}}(\boldsymbol{\rho}) \in \mathcal{M}(4, 2; \mathbb{R}),$$

that accounts for the variation of $\mathcal{A}^*(\boldsymbol{\rho})$ as a function of $\boldsymbol{\rho}$. This can be done using the definition of $\mathcal{A}^*(\boldsymbol{\rho})$ as best-fit attributable, that is the fact that $\mathcal{A}^*(\boldsymbol{\rho})$ is a local minimum of $Q(\mathcal{A}; \boldsymbol{\rho})$.

Proposition 2.18. *Neglecting terms containing the second derivatives of the residuals multiplied by the residuals themselves, for all $\boldsymbol{\rho} \in K'$ we have*

$$\frac{\partial \mathcal{A}^*}{\partial \boldsymbol{\rho}}(\boldsymbol{\rho}) = -C_{\mathcal{A}}(\mathcal{A}^*(\boldsymbol{\rho}), \boldsymbol{\rho})^{-1} B_{\mathcal{A}}(\mathcal{A}^*(\boldsymbol{\rho}), \boldsymbol{\rho})^{\top} B_{\boldsymbol{\rho}}(\mathcal{A}^*(\boldsymbol{\rho}), \boldsymbol{\rho}).$$

Proof. For every $\boldsymbol{\rho} \in K'$, by definition, the point $\mathbf{x}(\boldsymbol{\rho}) = (\mathcal{A}^*(\boldsymbol{\rho}), \boldsymbol{\rho}) \in \mathcal{M}$ is a zero of the function $g : \mathcal{X} \rightarrow \mathbb{R}$ given by

$$g(\mathbf{x}) := \frac{m}{2} \frac{\partial Q}{\partial \mathcal{A}}(\mathbf{x}) = B_{\mathcal{A}}(\mathbf{x})^{\top} \boldsymbol{\xi}(\mathbf{x}).$$

The function g is continuously differentiable and we have

$$\begin{aligned} \frac{\partial g}{\partial \mathcal{A}}(\mathbf{x}) &= \frac{\partial}{\partial \mathcal{A}} \left(\frac{\partial \boldsymbol{\xi}}{\partial \mathcal{A}}(\mathbf{x}) \right)^{\top} \boldsymbol{\xi}(\mathbf{x}) + \left(\frac{\partial \boldsymbol{\xi}}{\partial \mathcal{A}}(\mathbf{x}) \right)^{\top} \frac{\partial \boldsymbol{\xi}}{\partial \mathcal{A}}(\mathbf{x}) \simeq \\ &\simeq \left(\frac{\partial \boldsymbol{\xi}}{\partial \mathcal{A}}(\mathbf{x}) \right)^{\top} \frac{\partial \boldsymbol{\xi}}{\partial \mathcal{A}}(\mathbf{x}) = C_{\mathcal{A}}(\mathbf{x}), \end{aligned}$$

where we neglected terms containing the second derivatives of the residuals multiplied by the residuals themselves. The matrix $C_{\mathcal{A}}(\mathbf{x}(\boldsymbol{\rho}))$ is invertible, otherwise the doubly constrained differential corrections would have failed and this is not the case since $\boldsymbol{\rho} \in K'$. By applying the implicit function theorem, there exists a neighbourhood U of $\boldsymbol{\rho}$, a neighbourhood W of $\mathcal{A}^*(\boldsymbol{\rho})$, a continuously differentiable function $\mathbf{f} : U \rightarrow W$ such that, for all $\tilde{\boldsymbol{\rho}} \in U$ it holds

$$g(\mathcal{A}^*, \tilde{\boldsymbol{\rho}}) = \mathbf{0} \Leftrightarrow \mathcal{A}^* = \mathbf{f}(\tilde{\boldsymbol{\rho}}),$$

and

$$\frac{\partial \mathbf{f}}{\partial \boldsymbol{\rho}}(\tilde{\boldsymbol{\rho}}) = - \left(\frac{\partial g}{\partial \mathcal{A}}(\mathcal{A}^*(\tilde{\boldsymbol{\rho}}), \tilde{\boldsymbol{\rho}}) \right)^{-1} \frac{\partial g}{\partial \boldsymbol{\rho}}(\mathcal{A}^*(\tilde{\boldsymbol{\rho}}), \tilde{\boldsymbol{\rho}}). \quad (2.17)$$

We already computed $\frac{\partial g}{\partial \mathcal{A}}$, so we proceed with the other derivative, that is

$$\begin{aligned} \frac{\partial g}{\partial \boldsymbol{\rho}}(\mathbf{x}) &= \frac{\partial}{\partial \boldsymbol{\rho}} \left(\frac{\partial \boldsymbol{\xi}}{\partial \mathcal{A}}(\mathbf{x}) \right)^{\top} \boldsymbol{\xi}(\mathbf{x}) + \left(\frac{\partial \boldsymbol{\xi}}{\partial \mathcal{A}}(\mathbf{x}) \right)^{\top} \frac{\partial \boldsymbol{\xi}}{\partial \boldsymbol{\rho}}(\mathbf{x}) \simeq \\ &\simeq \left(\frac{\partial \boldsymbol{\xi}}{\partial \mathcal{A}}(\mathbf{x}) \right)^{\top} \frac{\partial \boldsymbol{\xi}}{\partial \boldsymbol{\rho}}(\mathbf{x}) = B_{\mathcal{A}}(\mathbf{x})^{\top} B_{\boldsymbol{\rho}}(\mathbf{x}). \end{aligned}$$

We finally use equation (2.17) with $\tilde{\boldsymbol{\rho}} = \boldsymbol{\rho}$ and the expressions for the derivatives of g to complete the proof. \square

2.6.5 From the AR to the sampling space

The last step in the propagation of the probability density function consists in applying the map $f_{\sigma} : S' \rightarrow K'$, where $S' := f_{\sigma}^{-1}(K')$ is the portion of the sampling space mapped onto K' . Since f_{σ} is a map between two 2-dimensional spaces, the propagation is simpler with respect to the previous map, since it is based through the computation of the Jacobian determinant of f_{σ} only.

Theorem 2.19. *Assuming (2.15), the probability density function of the variable \mathbf{S} is*

$$p_{\mathbf{S}}(\mathbf{s}) = \frac{\exp\left(-\frac{\chi^2(\mathbf{s})}{2}\right) \sqrt{G_{\mu}(\mathbf{s})} \sqrt{G_{\sigma}(\mathbf{s})}}{\int_{f_{\sigma}^{-1}(K')} \exp\left(-\frac{\chi^2(\mathbf{s})}{2}\right) \sqrt{G_{\mu}(\mathbf{s})} \sqrt{G_{\sigma}(\mathbf{s})} ds}, \quad (2.18)$$

where $\chi^2(\mathbf{s}) = \chi^2(\mathbf{x}(\boldsymbol{\rho}(\mathbf{s})))$, $G_{\mu}(\mathbf{s}) = G_{\mu}(\boldsymbol{\rho}(\mathbf{s}))$, and G_{σ} is the Gramian of the columns of $Df_{\sigma}(\mathbf{s})$, so that

$$\sqrt{G_{\sigma}(\mathbf{s})} = |\det Df_{\sigma}(\mathbf{s})|.$$

The determinant $\det Df_{\sigma}(\mathbf{s})$ depends on the sampling technique:

- (i) if the sampling is uniform in ρ then $\det Df_{\sigma}(\mathbf{s}) = 1$ for all $\mathbf{s} \in S = \mathbb{R}^+ \times \mathbb{R}$;
- (ii) if the sampling is uniform in the logarithm of ρ then $\det Df_{\sigma}(\mathbf{s}) = \log(10)\rho(\mathbf{s})$ for all $\mathbf{s} \in S = \mathbb{R}^2$;
- (iii) in the case of the spider web sampling $\det Df_{\sigma}(\mathbf{s}) = r\sqrt{\lambda_1\lambda_2}$ for all $\mathbf{s} \in \mathbb{R}^+ \times \mathbb{S}^1$.

Proof. Equation (2.18) directly follows from the transformation law for random variables between spaces of the same dimension: it suffices to change the variables from the old ones to the new ones and multiply for the modulus of the determinant of the Jacobian of the inverse transformation, that is f_{σ} . The computation of $\det Df_{\sigma}(\mathbf{s})$ is straightforward for the cases (i) and (ii). In the spider web case (iii) the map f_{σ} is given by (2.8) and its Jacobian matrix is

$$Df_{\sigma}(\mathbf{s}) = \begin{pmatrix} v_1^x \sqrt{\lambda_1} \cos \vartheta - v_1^y \sqrt{\lambda_2} \sin \vartheta & r(-v_1^x \sqrt{\lambda_1} \sin \vartheta - v_1^y \sqrt{\lambda_2} \cos \vartheta) \\ v_1^x \sqrt{\lambda_2} \sin \vartheta + v_1^y \sqrt{\lambda_1} \cos \vartheta & r(v_1^x \sqrt{\lambda_2} \cos \vartheta - v_1^y \sqrt{\lambda_1} \sin \vartheta) \end{pmatrix}$$

where $\lambda_1 > \lambda_2$ are the eigenvalues of $\Gamma_{\boldsymbol{\rho}\boldsymbol{\rho}}(\mathbf{x}(\mathbf{s}))$ and $\mathbf{v}_1 = (v_1^x, v_1^y)$ the unit eigenvector related to λ_1 . The determinant is thus

$$\det Df_{\sigma}(\mathbf{s}) = r\sqrt{\lambda_1\lambda_2}(\mathbf{v}_1 \cdot \mathbf{v}_1) = r\sqrt{\lambda_1\lambda_2}.$$

□

2.7 Extras on the probability density propagation

2.7.1 Conditional density on each attributable space

In this section we prove that the conditional density of the attributable \mathcal{A} given $\boldsymbol{\rho} = \boldsymbol{\rho}_0 \in K'$ is Gaussian. To this aim, we indicate with \mathbf{A} and \mathbf{R} the random variables defined on the space A and R , respectively.

Once $\boldsymbol{\rho}_0 \in K'$ has been fixed, consider the fibre of $\boldsymbol{\rho}_0$ with respect to the projection from \mathcal{X} to R , so that

$$H_{\boldsymbol{\rho}_0} := A \times \{\boldsymbol{\rho}_0\} = \{(\mathcal{A}, \boldsymbol{\rho}_0) : \mathcal{A} \in A\}.$$

The fibre $H_{\boldsymbol{\rho}_0}$ is diffeomorphic to A and thus $H_{\boldsymbol{\rho}_0}$ is a 4-dimensional submanifold of \mathcal{X} , actually a 4-dimensional affine subspace, and the collection $\{H_{\boldsymbol{\rho}_0}\}_{\boldsymbol{\rho}_0 \in K'}$ is a 4-dimensional foliation of $A \times K' \subseteq \mathcal{X}$. Theorem 2.20 gives a probability density function on each leave of this foliation. Moreover, let us denote by $\varphi_{\boldsymbol{\rho}_0} : A \rightarrow H_{\boldsymbol{\rho}_0}$ the canonical diffeomorphism between A and $H_{\boldsymbol{\rho}_0}$, that is $\varphi_{\boldsymbol{\rho}_0}(\mathcal{A}) := (\mathcal{A}, \boldsymbol{\rho}_0)$ for all $\mathcal{A} \in A$.

Theorem 2.20. *For each $\boldsymbol{\rho}_0 \in K'$, the conditional probability density function of \mathbf{A} given $\mathbf{R} = \boldsymbol{\rho}_0$ is*

$$\begin{aligned} p_{\mathbf{A}|\mathbf{R}=\boldsymbol{\rho}_0}(\mathcal{A}) &= N(\mathcal{A}^*(\boldsymbol{\rho}_0), C_{\mathcal{A}}(\boldsymbol{\rho}_0)^{-1})(\mathcal{A}) = \\ &= \frac{\sqrt{\det C_{\mathcal{A}}(\boldsymbol{\rho}_0)}}{(2\pi)^2} \exp\left(-\frac{1}{2}(\mathcal{A} - \mathcal{A}^*(\boldsymbol{\rho}_0))^{\top} C_{\mathcal{A}}(\boldsymbol{\rho}_0)(\mathcal{A} - \mathcal{A}^*(\boldsymbol{\rho}_0))\right), \end{aligned}$$

where we have used the compact notation $C_{\mathcal{A}}(\boldsymbol{\rho}_0) := C_{\mathcal{A}}(\mathcal{A}^*(\boldsymbol{\rho}_0), \boldsymbol{\rho}_0)$.

Proof. Define the map $G_{\boldsymbol{\rho}_0} := F \circ \varphi_{\boldsymbol{\rho}_0} : A \rightarrow \mathbb{R}^m$. The differential of $G_{\boldsymbol{\rho}_0}$ is represented by the design matrix $B_{\mathcal{A}} \in \mathcal{M}(m, 4; \mathbb{R})$ introduced in (2.9). Consider the point $\mathbf{x}_0 = (\mathcal{A}^*(\boldsymbol{\rho}_0), \boldsymbol{\rho}_0) \in H_{\boldsymbol{\rho}_0}$, where $\mathcal{A}^*(\boldsymbol{\rho}_0)$ is the best-fit attributable corresponding to $\boldsymbol{\rho} = \boldsymbol{\rho}_0$, that exists since $\boldsymbol{\rho}_0 \in K'$. Given that the doubly constrained differential corrections converge to \mathbf{x}_0 , the matrix $B_{\mathcal{A}}(\mathbf{x}_0)$ is full rank. It follows that the map $G_{\boldsymbol{\rho}_0}$ is a global parameterization of

$$V_{\boldsymbol{\rho}_0} := G_{\boldsymbol{\rho}_0}(A) = F(H_{\boldsymbol{\rho}_0}) = \{\boldsymbol{\xi} \in \mathbb{R}^m : \boldsymbol{\xi} = F(\mathcal{A}, \boldsymbol{\rho}_0), \mathcal{A} \in A\},$$

that turns out to be a 4-dimensional submanifold of the residuals space \mathbb{R}^m , at least in a suitable neighbourhood of $\boldsymbol{\xi}_0 := F(\mathbf{x}_0) = G_{\boldsymbol{\rho}_0}(\mathcal{A}_0(\boldsymbol{\rho}_0))$. The map $G_{\boldsymbol{\rho}_0}$ induces the tangent map between the corresponding tangent bundles

$$DG_{\boldsymbol{\rho}_0} : TA \rightarrow TV_{\boldsymbol{\rho}_0}.$$

In particular we consider the tangent application

$$(DG_{\rho_0})_{\mathcal{A}^*(\rho_0)} : T_{\mathcal{A}^*(\rho_0)}\mathcal{A} \rightarrow T_{\xi_0}V_{\rho_0}.$$

To use this map for the probability density propagation, we first need to have the probability density function on $T_{\xi_0}V_{\rho_0}$, that is an affine subspace of dimension 4 in \mathbb{R}^m . By Theorem 2.14 we have that the conditional probability density of Ξ on $T_{\xi_0}V_{\rho_0}$ is $N(\mathbf{0}, I_4)$. Let R represent the rotation of the residuals space \mathbb{R}^m such that condition (2.14) holds for all $\xi'' \in \mathbb{R}^4$, and let $A(\mathbf{x}_0) \in \mathcal{M}(4; \mathbb{R})$ as in Proposition 2.12, so that the matrix $A(\mathbf{x}_0)^{-1}$ represents the inverse map $((DG_{\rho_0})_{\mathcal{A}^*(\rho_0)})^{-1}$. By the transformation law of a Gaussian random variable under the linear map $A(\mathbf{x}_0)^{-1}$, we obtain a probability density function on the attributable space \mathcal{A} given by

$$p_{\mathbf{A}}(\mathcal{A}) = N(\mathcal{A}^*(\rho_0), \Gamma_{\mathcal{A}}(\mathcal{A}^*(\rho_0)))(\mathcal{A}),$$

where \mathbf{A} is the random variable on \mathcal{A} and

$$\Gamma_{\mathcal{A}}(\mathcal{A}^*(\rho_0)) = A(\mathbf{x}_0)^{-1}I_4(A(\mathbf{x}_0)^{-1})^\top = A(\mathbf{x}_0)^{-1}(A(\mathbf{x}_0)^{-1})^\top.$$

As a consequence, the normal matrix of the random variable \mathbf{A} is

$$A(\mathbf{x}_0)^\top A(\mathbf{x}_0) = B_{\mathcal{A}}(\mathbf{x}_0)^\top R^\top R B_{\mathcal{A}}(\mathbf{x}_0) = B_{\mathcal{A}}(\mathbf{x}_0)^\top B_{\mathcal{A}}(\mathbf{x}_0) = C_{\mathcal{A}}(\mathbf{x}_0),$$

which is in turn the normal matrix of the doubly constrained differential corrections leading to \mathbf{x}_0 , computed at convergence. This completes the proof since \mathcal{A} and $\mathcal{A} \times \{\rho_0\}$ are diffeomorphic and thus the density $p_{\mathbf{A}}(\mathcal{A})$ is also the conditional density of \mathbf{A} given $\mathbf{R} = \rho_0$. \square

2.7.2 Full non-linear propagation

In this section we derive the equation of the probability density function on the space R obtained by a full non-linear propagation of the probability density on the residuals space. In particular, the map F is not linearized around \mathbf{x}^* , as assumed in Theorem 2.19. This causes the inclusion in equation (2.15) of the contribution of the normal matrix C as it varies along the MOV, and not the fixed contribution $C(\mathbf{x}^*)$ coming from the orbit \mathbf{x}^* with minimum value of χ .

With the inclusion of all the non-linear terms, the resulting density of \mathbf{R} has the same form as the Jeffreys' prior and thus is affected by the same pathology discussed in Section 2.5 and in Farnocchia et al. (2015c). This is the motivation for which we adopted the approach presented in Section 2.6.

Theorem 2.21. *The probability density function of the variable \mathbf{R} resulting from a full non-linear propagation is*

$$p_{\mathbf{R}}(\boldsymbol{\rho}) = \frac{\exp\left(-\frac{\chi^2(\boldsymbol{\rho})}{2}\right) \sqrt{\det C^{\boldsymbol{\rho}\boldsymbol{\rho}}(\boldsymbol{\rho})}}{\int_{K'} \exp\left(-\frac{\chi^2(\boldsymbol{\rho})}{2}\right) \sqrt{\det C^{\boldsymbol{\rho}\boldsymbol{\rho}}(\boldsymbol{\rho})} d\boldsymbol{\rho}},$$

where $C^{\boldsymbol{\rho}\boldsymbol{\rho}} = \Gamma_{\boldsymbol{\rho}\boldsymbol{\rho}}^{-1}$ and $\Gamma_{\boldsymbol{\rho}\boldsymbol{\rho}} \in \mathcal{M}(2; \mathbb{R})$ is the restriction of the covariance matrix Γ to the R space.

Proof. We have already proved that the map $f_{\mu} : K' \rightarrow \mathcal{M}$ is a global parameterization of \mathcal{M} . From the properties of the map F it is easy to prove that the map $F \circ f_{\mu} : K' \rightarrow F(\mathcal{M})$ is a global parameterization of the 2-dimensional manifold $V = F(\mathcal{M})$. From equation (C.1) we have that

$$p_{\mathbf{R}}(\boldsymbol{\rho}) = p_{\Xi}(\boldsymbol{\xi}(\boldsymbol{\rho})) \cdot \sqrt{\det \left[\frac{\partial(F \circ f_{\mu})}{\partial \boldsymbol{\rho}}(\boldsymbol{\rho}) \right]^{\top} \frac{\partial(F \circ f_{\mu})}{\partial \boldsymbol{\rho}}(\boldsymbol{\rho})}.$$

By the chain rule

$$\frac{\partial(F \circ f_{\mu})}{\partial \boldsymbol{\rho}}(\boldsymbol{\rho}) = \frac{\partial F}{\partial \mathbf{x}}(\mathbf{x}(\boldsymbol{\rho})) \frac{\partial f_{\mu}}{\partial \boldsymbol{\rho}}(\boldsymbol{\rho}) = B(\mathbf{x}(\boldsymbol{\rho})) \begin{pmatrix} \frac{\partial \mathcal{A}^*}{\partial \boldsymbol{\rho}}(\boldsymbol{\rho}) \\ I_2 \end{pmatrix},$$

so that the Gramian matrix results to be

$$\begin{aligned} \left[\frac{\partial(F \circ f_{\mu})}{\partial \boldsymbol{\rho}} \right]^{\top} \frac{\partial(F \circ f_{\mu})}{\partial \boldsymbol{\rho}} &= \begin{pmatrix} \frac{\partial \mathcal{A}^*}{\partial \boldsymbol{\rho}} \\ I_2 \end{pmatrix}^{\top} B^{\top} B \begin{pmatrix} \frac{\partial \mathcal{A}^*}{\partial \boldsymbol{\rho}} \\ I_2 \end{pmatrix} = \\ &= \begin{pmatrix} \frac{\partial \mathcal{A}^*}{\partial \boldsymbol{\rho}} \end{pmatrix}^{\top} C_{\mathcal{A}\mathcal{A}} \frac{\partial \mathcal{A}^*}{\partial \boldsymbol{\rho}} + C_{\boldsymbol{\rho}\mathcal{A}} \frac{\partial \mathcal{A}^*}{\partial \boldsymbol{\rho}} + \begin{pmatrix} \frac{\partial \mathcal{A}^*}{\partial \boldsymbol{\rho}} \end{pmatrix}^{\top} C_{\mathcal{A}\boldsymbol{\rho}} + C_{\boldsymbol{\rho}\boldsymbol{\rho}}, \end{aligned}$$

where the matrices $C_{\mathcal{A}\mathcal{A}} = C_{\mathcal{A}}$, $C_{\mathcal{A}\boldsymbol{\rho}}$, $C_{\boldsymbol{\rho}\mathcal{A}} = C_{\mathcal{A}\boldsymbol{\rho}}^{\top}$, and $C_{\boldsymbol{\rho}\boldsymbol{\rho}}$ are the restrictions of the normal matrix $C(\mathbf{x}(\boldsymbol{\rho}))$ to the corresponding subspace. From Proposition 2.18 we have

$$\frac{\partial \mathcal{A}^*}{\partial \boldsymbol{\rho}} = -C_{\mathcal{A}}^{-1} B_{\mathcal{A}}^{\top} B_{\boldsymbol{\rho}} = -C_{\mathcal{A}}^{-1} C_{\mathcal{A}\boldsymbol{\rho}},$$

so that the previous expression becomes

$$\begin{aligned} \left[\frac{\partial(F \circ f_{\mu})}{\partial \boldsymbol{\rho}} \right]^{\top} \frac{\partial(F \circ f_{\mu})}{\partial \boldsymbol{\rho}} &= C_{\mathcal{A}\boldsymbol{\rho}}^{\top} C_{\mathcal{A}}^{-1} C_{\mathcal{A}\boldsymbol{\rho}} - 2C_{\mathcal{A}\boldsymbol{\rho}}^{\top} C_{\mathcal{A}}^{-1} C_{\mathcal{A}\boldsymbol{\rho}} + C_{\boldsymbol{\rho}\boldsymbol{\rho}} = \\ &= C_{\boldsymbol{\rho}\boldsymbol{\rho}} - C_{\mathcal{A}\boldsymbol{\rho}}^{\top} C_{\mathcal{A}}^{-1} C_{\mathcal{A}\boldsymbol{\rho}} = C^{\boldsymbol{\rho}\boldsymbol{\rho}} = \Gamma_{\boldsymbol{\rho}\boldsymbol{\rho}}^{-1}, \end{aligned}$$

where the last equality is proved in Milani et al. (2010), Section 5.4. \square

2.8 Use of the probability density function

2.8.1 Impact probability computation

Each point on the MOV can be thought as orbit compatible with the observations, and we call each point a Virtual Asteroid (VA). We propagate the VAs into the future, currently for 30 days from the date of the observations and we search for Virtual Impactors (VIs), which are connected sets of initial conditions leading to an impact (Milani et al. 2005b). If a VI has been found on the Modified Target Plane (MTP; Milani et al. (1999)), it is associated with a subset $\mathcal{V} \subseteq S$ of the sampling space, and hence its probability is

$$\begin{aligned} \mathbb{P}(\mathcal{V}) &= \int_{\mathcal{V}} p_{\mathbf{s}}(\mathbf{s}) d\mathbf{s} = \\ &= \frac{\int_{\mathcal{V}} \exp\left(-\frac{\chi^2(\mathbf{s})}{2}\right) \sqrt{G_{\mu}(\mathbf{s})} \sqrt{G_{\sigma}(\mathbf{s})} d\mathbf{s}}{\int_{f_{\sigma}^{-1}(K')} \exp\left(-\frac{\chi^2(\mathbf{s})}{2}\right) \sqrt{G_{\mu}(\mathbf{s})} \sqrt{G_{\sigma}(\mathbf{s})} d\mathbf{s}} \end{aligned} \quad (2.19)$$

If for a given object we find impacting solutions, we assign to the object an impact flag, which is an integer number related to the computation of the impact probability. In fact, the impact flag depends on the impact probability and on the arc curvature, as follows:

- (1) if $IP \leq 10^{-4}$ the impact flag is 0;
- (2) if $10^{-4} < IP \leq 10^{-3}$ the impact flag is 1;
- (3) if $10^{-3} < IP \leq 10^{-2}$ the impact flag is 2;
- (4) if $IP > 10^{-2}$ and the arc does not have significant curvature the impact flag is 3;
- (5) if $IP > 10^{-2}$ and the arc has significant curvature the impact flag is 4.

The significance of the curvature of an arc can be assessed through the computation of the covariance of the geodesic curvature and the acceleration, and in turn of the χ value. Following the approach of Milani et al. (2007), we say that an arc has significant curvature if $\chi^2 > 10$. The impact flag can take the integer values from 0 to 4: 0 indicates a negligible chance of collision with the Earth, whereas the maximum value 4 expresses an elevated impact risk ($\geq 1\%$). The impact flag is conceived as a simple and direct communication tool to assess the importance of collision predictions and give priority to the follow-up activities.

2.8.2 Score computation

When we perform the sampling of the Admissible Region, either by the two grids method or by the spider web technique, we also compute a score for the object (see Section 2.3) to belong to certain classes of Solar System objects. The score gives us a first insight into the nature of the object, even though the asteroid were not a potential impactor. Furthermore, the score is a rigorous probability of the object to belong to different classes (NEO, MBO, DO, and SO).

The four class that we included in the score computation are defined by the following conditions:

- **NEO**: Near Earth Object, an object with $q < 1.3$ au, where q is the perihelion distance (in au).
- **MBO**: Main Belt Object, belonging either to the Main Belt or to the Jupiter Trojans. In particular we choose the conditions

$$\left\{ \begin{array}{l} 1.7 \text{ au} < a < 4.5 \text{ au} \\ e < 0.4 \end{array} \right. \quad \text{or} \quad \left\{ \begin{array}{l} 4.5 \text{ au} < a < 5.5 \text{ au} \\ e < 0.3 \end{array} \right.$$

where a is the semi-major axis (in au), and e is the eccentricity.

- **DO**: Distant Object, characterised by $q > 28$ au.
- **SO**: Scattered Object, an asteroid not belonging to any of the previous classes.

In this way, each class corresponds to a subset of the sampling space S . As a consequence, the probability to belong to a certain class is the integral of the probability density $p_S(\mathbf{s})$ over the corresponding subset of S .

2.9 Results

We have set up a service dedicated to the scan of the Minor Planet Center NEO Confirmation Page⁷ (NEOCP). The service is called NEOScan. Its goal is to identify asteroids as NEOs, MBOs or distant objects to be confirmed or removed from the NEOCP, and to give early warning of imminent impactors, to trigger immediately follow-up observations. All the results are available at the web page <http://newton.dm.unipi.it/neodys2/NEOScan/index.html> and the software used is a new version of the OrbFit Software version 5.0⁸.

⁷http://www.minorplanetcenter.net/iau/NEO/toconfirm_tabular.html

⁸<http://adams.dm.unipi.it/orbfit/>

The service involves the following steps, based on the algorithm presented in Sections 2.3.2 and 2.5.

- Scanning of the NEOCP every 2 minutes. New cases or old cases just updated are immediately run.
- Computation and sampling of the Admissible Region using a 2-dimensional representation in the $(\rho, \dot{\rho})$ plane with a either grid or a spider web.
- Computation of the MOV, obtaining a set of VAs.
- Propagation of the VAs in the future (currently for 30 days).
- Projection on the Modified Target Plane, searching for VIs.
- If VIs exist, computation of the Impact Probability.

The time required to run one target strictly depends on the characteristics of the object, but usually it is between 15 and 20 minutes. When predicting possible imminent impacts, one of the most important requirements to fulfil is to minimise the number of unjustified alarms. We mark as non-significant the cases for which there are either less than 3 observations or the arc length is less than 30 minutes, unless there exists a nominal solution with a geodesic curvature SNR greater than 1. The classification of a certain case as non-significant does not mean we skip the computations: we anyway perform all the steps of the algorithm and assign the scores and the impact flag. Nevertheless, being non-significant automatically decreases the priority of the object in case of an alarm. Unfortunately, all of these techniques are not enough and some spurious cases remain. They could arise when the astrometry is either known to be erroneous or noisy, or anyway not reliable. We cannot solve this problem, because it is contained by the data on which the system performs the computations, and we acknowledge that the astrometric error models based on large number statistic are not enough to distinguish erroneous and accurate astrometry in a small sample (see comments in Section 2.10).

We have tested the algorithm on the two well known cases of NEAs that have impacted the Earth a few hours after the discovery, namely 2008 TC₃ and 2014 AA. We have already pointed out that the choice of the weights is very important in these cases: to be able to compare the results with Farnocchia et al. (2015c), we have chosen the same weights. Furthermore, we have also selected some cases among the objects that will not impact to show the importance of computing the score, and not only the impact probability, and to show the importance of having a system like the one we have developed.

There is another online system, namely Scout⁹ (Farnocchia et al. 2016), developed by the JPL team and that substantially accomplishes the same objective as NEOScan. Indeed, Scout continually monitors the objects on the NEOCP and for each provides orbital information, the impact risk analysis and the possibility to compute ephemerides. Thus, in the same vein as CLOMON-2 and Sentry, the two systems NEOScan and Scout are redundant system, in the sense that the comparison of their results provides verification and validation. More recently, Solin et al. (2018) present NEORANGER, a third system with analogous purposes as NEOScan and Scout. So far, the system is not online but, when available, it will constitute a third cross check for the hazard assessment of NEOCP objects.

2.9.1 Graphical representation of the results

We present our results with plots showing the AR and its sampling. Hereinafter we describe the colour code present in our figures. Concerning the AR, we make use of the following lines.

- The red solid line represents the level curve of the heliocentric energy equal to $-k^2/(2a_{max})$. Namely, it is the outer boundary of the AR, corresponding to the boundary of the region defined by condition 1 in Section 2.3.
- The green dashed line shows where the geocentric energy is equal to 0, also taking into account the condition about the radius of the Earth sphere of influence, as discussed in Section 2.3
- The magenta dashed line (which is parallel to the range-rate axis) represents the shooting star limit condition.
- The magenta solid lines (which are parallel to the range-rate axis) represent different values of the absolute magnitude.

We now provide a description of the colours used for the sampling points. No point is denoted if the four-dimensional differential corrections does not converge because the point does not belong to the MOV.

- The dots are indicated in blue if $\chi \leq 2$, and green if $2 < \chi \leq 5$.
- The dots are indicated in black if $\chi > 5$.
- In case a VI has been found, we show the points representing possible impacting orbits with red circles.
- The orange star represents the point with the minimum value of χ .

⁹<https://cneos.jpl.nasa.gov/scout/#/>

2.9.2 Asteroid 2008 TC₃

Asteroid 2008 TC₃ was discovered by Richard A. Kowalski at the Catalina Sky Survey on October 7, 2008. The object was spotted 19 hours before the impact, and it is the first body to be observed and tracked prior to falling on the Earth. After the discovery, hundreds of astrometric observations were submitted to the Minor Planet Center and these observations allowed the computation of the orbit and the prediction of the impact. We use the first tracklet composed by four observations, and then the first two tracklets (seven observations) to ascertain whether we could predict the impact.

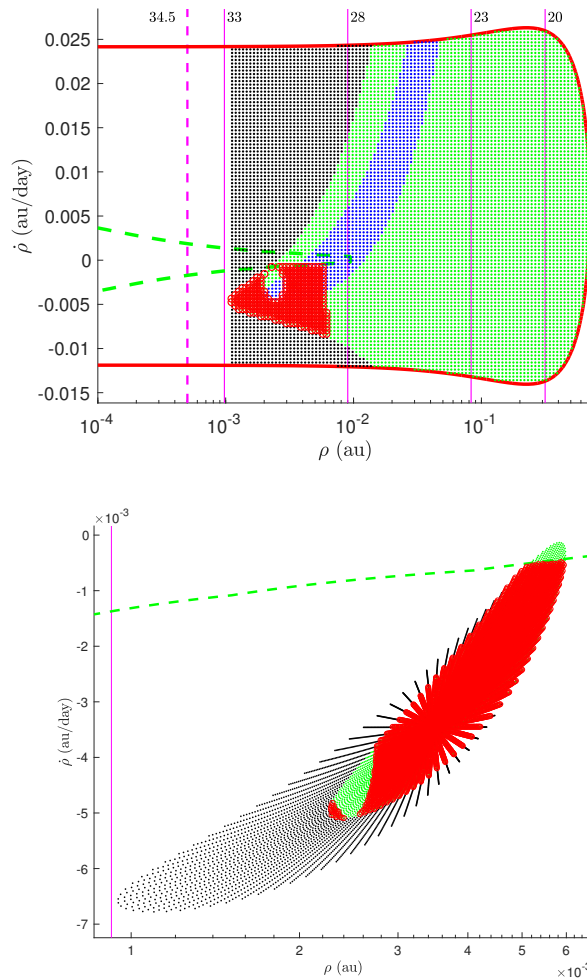


Figure 2.1. *Top panel.* Grid sample of the $(\rho, \dot{\rho})$ space for the first 4 observations of 2008 TC₃. *Bottom panel.* Spider web for the first 7 observations of 2008 TC₃.

We compute a uniform densified grid in $\log_{10} \rho$ (Figure 2.1, top panel) where we consider only the first four observations, since the unique positive root r_1 is $< \sqrt{10}$ au. Using seven observations we are able to compute a reliable nominal orbit and the consequent spider web using seven observations (Figure 2.1, bottom panel). Table 2.1 shows that with four observations and using the grid we are able to predict a possible impact of the object with the Earth with an impact probability of $\simeq 3.6\%$, and the score of the object to be classified as a NEA is 100%. This would have produced an alert for the observers that could have immediately followed up the object. With seven observations we can confirm the certainty that the asteroid is a NEA (score = 100%), and the impact probability increases to 99.7%. Both these results, in terms of impact probability, are in very good agreement with those reported in Farnocchia et al. (2015c, Table 2).

2.9.3 Asteroid 2014 AA

Asteroid 2014 AA was discovered by Richard A. Kowalski at the Catalina Sky Survey on the New Year's Eve of 2014. The object was discovered 21 hours before the impact, but it has not been intensively followed up as 2008 TC₃ because of the exceptional night in which it has been spotted. We initially used the first tracklet composed of three observations, and then the whole set of seven observations to test whether we could have predicted the impact with our method.

These two examples have several analogies. We compute a uniform densified grid in $\log_{10} \rho$ with the first tracklet, which contains only 3 observations (Figure 2.2, top panel), and we are able to compute a reliable orbit and the consequent spider web only with seven observations (Figure 2.2, bottom panel). Table 2.1 shows that using the first tracklet only, we are able to predict a possible impact with the Earth with an impact probability of $\simeq 3.0\%$, and the NEA score of the object is 100%. Again, this would have produced an alert for the observers that could have immediately followed up the object. As in the previous case, with the second tracklet we confirm both that the asteroid is a NEA (score = 100%) and the collision, since the impact probability increases to 100%. Also in this case the results are very compatible with those presented in Farnocchia et al. (2015c, Table 2).

2.9.4 Asteroid 2014 QF₄₃₃

The previous examples show how systematic ranging is capable of identifying imminent impactors. Although this is one of the most important applications of this technique, systematic ranging is also essential in the first short arc orbit determination process.

Table 2.1. Results of systematic ranging applied to 2008 TC₃ and 2014 AA. The columns contain the name of the object, number of observations used, time span covered by the observations, characteristic of the sampling used to compute the MOV (grid or spider web), score of the object (NEO, MBO or Distant), and impact probability.

Name	# Obs.	Time span (min)	Sampling Grid/Spider	Score			IP
				NEO	MBO	DO	
2008 TC ₃	4	43	$\log_{10} \rho$ - grid	100%	0	0	3.6%
2008 TC ₃	7	99	Spider	100%	0	0	99.7%
2014 AA	3	28	$\log_{10} \rho$ - grid	100%	0	0	3.0%
2014 AA	7	28	Spider	100%	0	0	100.0%

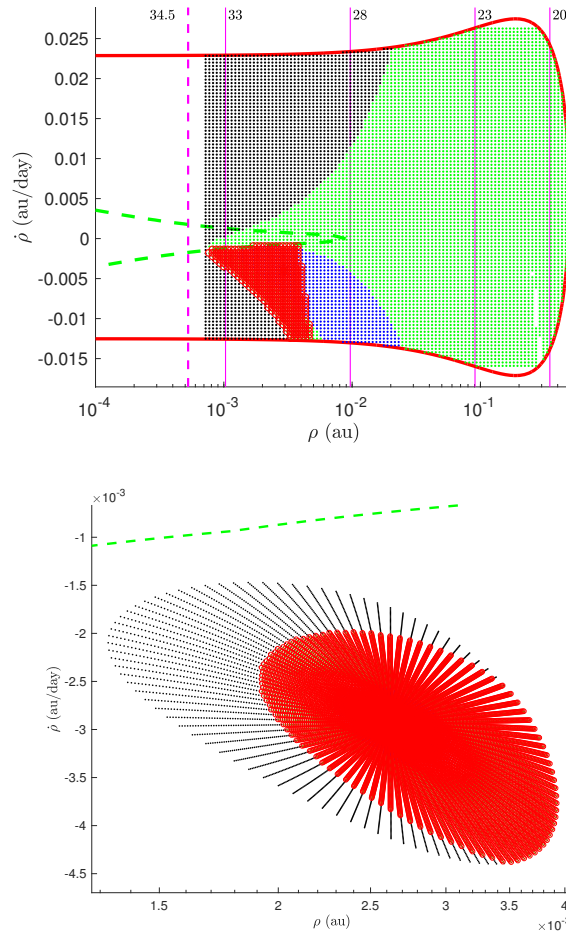


Figure 2.2. *Top panel.* Grid sample of the $(\rho, \dot{\rho})$ space for the first 3 observations of 2014 AA. *Bottom panel.* Spider web for the whole set of 7 observations of 2014 AA.

Asteroid 2014 QF_{433} was discovered by F51 - Pan-STARRS 1, Haleakala on August 26, 2014. The first four observations were posted on the NEO Confirmation Page, with the temporary designation TVPS7NV. This asteroid remained on the NEOCP until September 5, 2014. On that day (with 18 observations) it was confirmed to be a distant object by the Minor Planet Center.

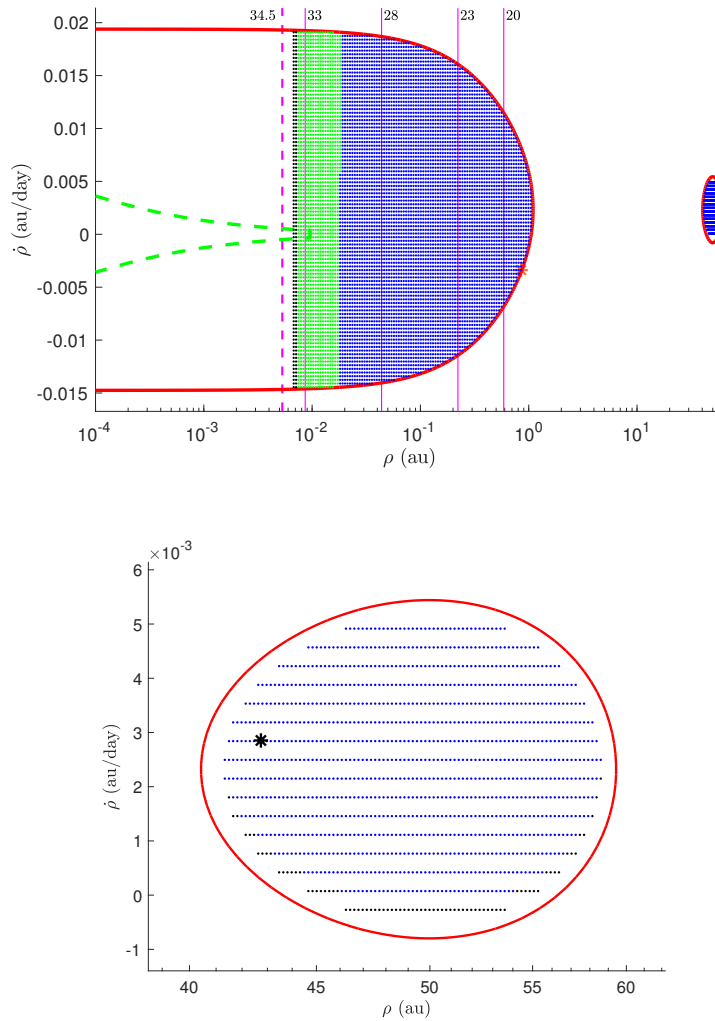


Figure 2.3. *Top panel.* Grid sample of the $(\rho, \dot{\rho})$ space for the first 4 observations of 2014 QF_{433} . *Bottom panel.* Enlargement of the second component. The black star in the second component represents the orbit of the object computed with all the available observations.

Figure 2.3 shows the results of systematic ranging on this asteroid with only four discovery observations and 51 minutes of arc length. In this case the AR has two connected components, indicating the possibility for the object to be distant. The values of the three positive roots of the equation of degree 6 are $r_1 = 1.103$ au, $r_2 = 40.072$ au, and $r_3 = 59.786$ au. The attributable is

$$\begin{aligned} \mathcal{A} &= (\alpha, \delta, \dot{\alpha}, \dot{\delta}) = \\ &= (5.7358902, -0.3008327, -3.35275 \cdot 10^{-4}, -9.94065 \cdot 10^{-5}), \end{aligned}$$

with α and δ in radians and $\dot{\alpha}$ and $\dot{\delta}$ in radians per day. The two plots in Figure 2.3 strongly suggests that the object is distant, since almost all the grid points corresponding to the MOV lie in the second connected component. As a consequence, the cumulative score for the Distant and Scattered classes is $\simeq 99\%$.

As a further validation, we take the orbital elements of this asteroid from the AstDyS database¹⁰, and we compute the range and the range-rate at the epoch of the attributable. The result is shown in the right panel of Figure 2.3: the black star represents the orbit of 2014 QF_{433} computed with all the available observations and is in perfect agreement with the systematic ranging sampling.

2.9.5 Asteroid 2017 AE_{21}

The case of 2017 AE_{21} shows the importance of score computation. This object is worthy of attention even though it is not an impactor; for instance, it could be a potential NEA.

Asteroid 2017 AE_{21} was discovered by F51 - Pan-STARRS 1, Haleakala on January 3, 2017. It appeared on the NEOCP as a tracklet of three observations spanning 30 minutes with the temporary designation P10yBuc. This object was confirmed to be a NEA on January 24, 2017, when it had five observations. With the first tracklet, our system produces an impact flag of 2, indicating a modest impact risk and an impact probability $IP = 2 \cdot 10^{-3}$. Moreover, the NEO score is 92%, which encouraged some follow-up observations of the object. The left panel of Figure 2.4 shows the result when using the first tracklet only. We do not have any reliable nominal orbit to use, and as a consequence we adopt the grid sampling. The portion of the grid corresponding to low χ values (blue points) is very wide, indicating a great uncertainty in the orbit determination, and the uncertainty region also contains impacting solutions.

¹⁰Asteroid Dynamics Site, available at <http://hamilton.dm.unipi.it/astdys/>

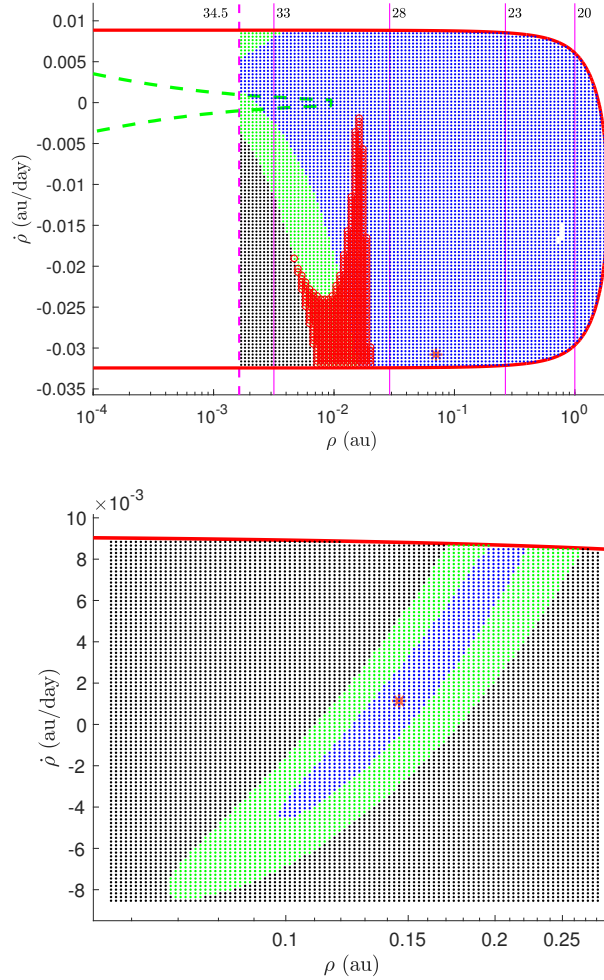


Figure 2.4. *Top panel.* Grid sample of the $(\rho, \dot{\rho})$ space for the first 3 observations of 2017 AE_{21} . *Bottom panel.* Grid sample for the whole set of 5 observations of 2017 AE_{21} . In both cases we do not have any reliable nominal orbit to use, and as a consequence we adopt the grid sampling.

With just two additional observations, the differential corrections still fail to compute a reliable nominal orbit, but now the good portion of the grid is located in a small subregion of the AR (see Figure 2.4, bottom panel). In this case the uncertainty region does not contain impacting orbits, thus we get an impact flag of 0, where $IP = 0$, whereas the NEO score increases to 100%. As a consequence, the new observations contradicts the low probability VI, but the follow-up suggestion coming from the high 98% NEO score of the first run is reliable.

2.9.6 NEOCP object *P10vx Ct*

As we stated in the introduction of this section, noisy astrometry can be the cause of unjustified alarms. In fact, if an object has a single tracklet of few observations and one of these is erroneous, the arc usually shows a significant curvature, implying that the object seems very close and fast moving. Most likely, it could be classified as an immediate impactor with very high impact probability.

Table 2.2. Astrometric data for NEOCP object *P10vx Ct*. First tracklet with 3 observations (above), and remeasurement of the first tracklet from the discovery images (below).

Date (UTC)	α	δ	R	Code
2016-06-08.29327	13 13 16.962	-20 25 56.90	21.0	F51
2016-06-08.30357	13 13 12.688	-20 28 31.36	20.9	F51
2016-06-08.32416	13 13 04.699	-20 33 46.35	21.0	F51

Date (UTC)	α	δ	R	Code
2016-06-08.293273	13 13 16.963	-20 25 56.53	20.3	F51
2016-06-08.303571	13 13 12.856	-20 28 33.24	20.5	F51
2016-06-08.324159	13 13 04.683	-20 33 46.33	20.4	F51

Object *P10vx Ct* was spotted by F51 - Pan-STARRS, Haleakala on June 8, 2016. The first time it appeared on the NEOCP it had a tracklet with three observations spanning about 44 minutes (see Table 2.2, upper table). It has never been confirmed, but it is in any case an important example to show the risk posed by noisy astrometric data. With the first three observations, our system computes a nominal solution compatible with a very close orbit, resulting in a spider web sampling over a small subset of the AR (see Figure 2.5, left panel). A very large percentage of the MOV orbits are solutions with possible impacts and it results in an impact probability of 99.2% and impact flag 4, considering the significance of the curvature. The second batch of observations consists of four positions, three of which are a remeasurement of the first tracklet obtained from the discovery images of the object, plus an additional observation. With this new astrometry, the impact was ruled out and the object was removed from the NEOCP.

To show the role of the remeasurements in the impact removal, we only consider the three remeasured observations (see Table 2.2, lower table). The second observation in the first tracklet was badly determined because it was off by about 3 arcsec from the corresponding observation in the second batch. The effect of this shift can be seen in the curvature parameters κ (geodesic

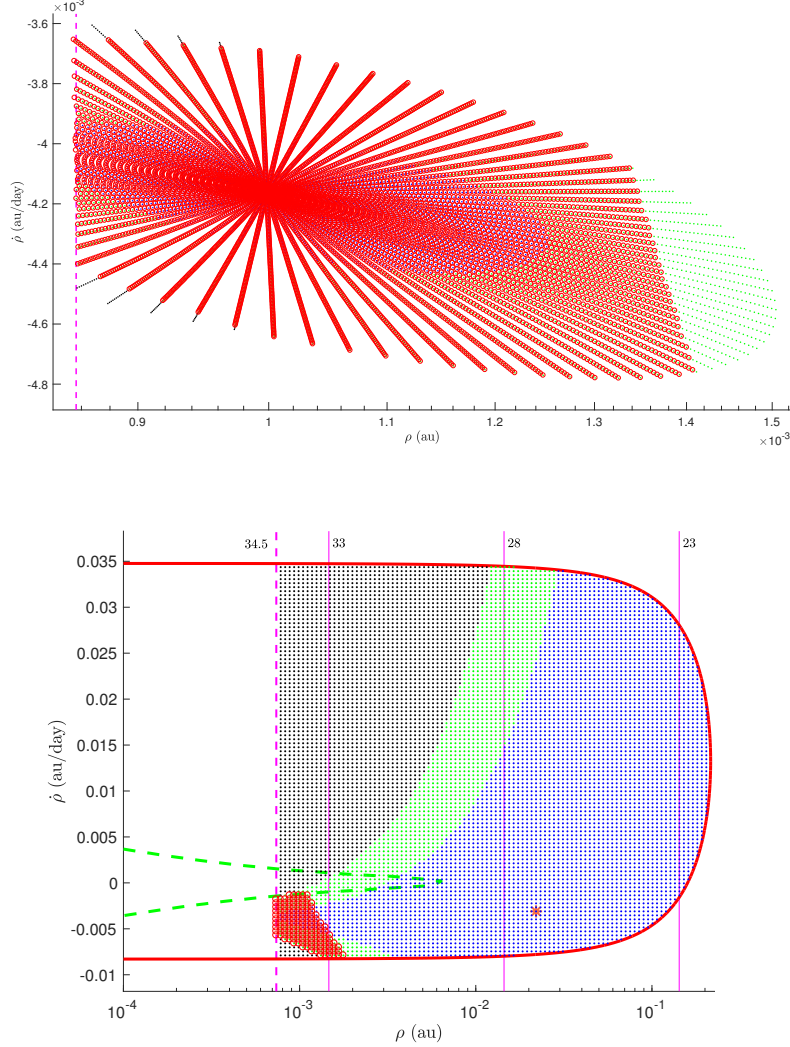


Figure 2.5. *Top panel.* Grid sample of the $(\rho, \dot{\rho})$ space for the first 3 observations of *P10vxCt*. *Bottom panel.* Grid sample for their remeasurement of *P10vxCt*.

curvature) and $\dot{\eta}$ (acceleration). For the first tracklet we have

$$\kappa_1 = (1.0073 \pm 0.1015) \cdot 10^{-3} \quad \text{and} \quad \dot{\eta}_1 = (3.218 \pm 1.013) \cdot 10^{-4},$$

while for the remeasured tracklet

$$\kappa_2 = (6.49 \pm 67.49) \cdot 10^{-5} \quad \text{and} \quad \dot{\eta}_2 = (-4.30 \pm 67.50) \cdot 10^{-5},$$

which are both significantly lower than the values obtained for the original tracklet (see Figure 2.6 for a graphic representation of the two arcs).

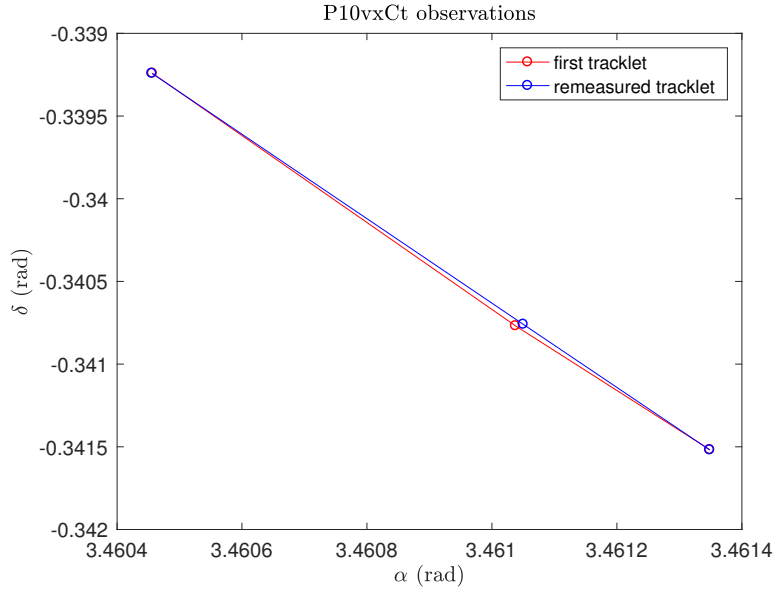


Figure 2.6. Plot of the two batches of observations reported in Table 2.2, for NEOCP object *P10vx Ct*. The red line represents the originally submitted tracklet, whereas the blue line the remeasured tracklet. The higher curvature of the first arc with respect to the second is clear.

Moreover, as we can see from the curvature uncertainties, both curvature components are not significantly different from zero. As a consequence, the impact solution is sharply downgraded in the remeasured observations alone; a nominal solution cannot be computed anymore, resulting in a grid sampling of the AR, and the impact orbits are a very small fraction of the MOV orbits (see Figure 2.5, right panel). Thus the impact probability lowers to about $IP = 7.5 \cdot 10^{-5}$, with an impact flag of 1.

Providing remeasured observations is not the only way to solve the problem caused by bad astrometry. The second observation is not as good as the other two, and let us suppose this information were provided along with the observation itself. In this case, we could have properly down-weighted the second observation to take into account the additional information, and the case would have been solved. To prove this claim, we assign a formal uncertainty of 3 arcsec to both the right ascension and the declination of the second observation. With this choice, the impact solution still remain, but with an impact probability $IP = 4.4 \cdot 10^{-4}$. Until this additional metadata will be provided together with the observations, cases like the one presented here can be solved only by a manual intervention after all the computations (remeasurement) or by a fast follow-up (see Section 2.10 for general comments on this issue).

2.10 Conclusions

One of the main issues in the impact hazard assessment for imminent impactors is given by the computation of the impact probability. The main results of this chapter are a new argument to propagate the probability density function from the space of the astrometric residuals to the Manifold Of Variation, a geometric device to sample the set of possible orbits available even after a very short observed arc, and then to the $(\rho, \dot{\rho})$ space R . In previous works, this computation was conducted with the assumption of an *a priori* probability density function on the space R , and this step was needed to pass from the probability density function on the residuals space to a probability density function on the space R (see Section 2.5). Our computation is complete, rigorous, and uses no *a priori* probability distributions, since it only assumes that the residuals can be modeled with a Gaussian random variable.

Does this new algorithm solve the problem of assessing the risk of imminent impacts from a freshly discovered asteroid, with observations limited to 1–2 tracklets? By using the Admissible Region and one of our grid samplings, we have shown how to approximate a probability integral on the portion of the MOV leading to an imminent impact, if it is found. However, to accept this integral as impact probability we need to check three conditions.

First, the probability density on the space of residuals needs to be based upon a probabilistic model of the astrometric errors, taking into account the past performances of the observatories. Second, the observations used in the computation must be “typical” of the observatory: even the best astronomical program produces a comparatively small subset of “faulty” observations, with errors much larger than the usual ones. Third, we should assume that the small sample of observations has statistical properties, such as mean and standard deviation (STD), close to the ones of the full distribution.

The first hypothesis is reasonable, in that a lot of work has been developed in the last 20 years to produce astrometric error models for asteroid observations (see Carpino et al. (2003), Chesley et al. (2010), Baer et al. (2011b), Farnocchia et al. (2015b)). These models are not perfect, but they represent an increasingly reliable source of statistical information. The second hypothesis is not trivial: the current format for asteroid observations does not contain sufficient metadata to discriminate the “weak observations” from the good ones. The full adoption of the new Astrometric Data Exchange Standard (ADES¹¹), approved by the IAU in 2015, will provide information such as SNR, timing uncertainty, and so on, allowing to adapt the weighting of the individual observations. The example of *P10vx Ct*

¹¹It is available at <https://github.com/IAU-ADES/ADES-Master>.

shows how just one lower quality observation can completely spoil the orbit results, generating a false impact alarm. This can be avoided either with re-measuring by the observer or with careful weighting by the orbit computer, provided such down-weighting is supported by the metadata.

The third hypothesis is the most troublesome. Assuming that the probability density of an astrometric error model is a perfect statistical description, then by the law of large numbers a large enough sample of N observations shall have approximately the same statistical properties of the model, with the differences going to zero for $N \rightarrow +\infty$ (law of large numbers). Unfortunately, $N = 3, 4, 5$ is not large enough for the law of large numbers to apply. For instance, a tracklet with $N = 3$ observations can have all the observations in one coordinate with errors > 2.5 STD: this statistical fluke would be very rare, occurring in a little more than 1 tracklet over 1 million. Still, if a large asteroid survey submits to the MPC more than one million tracklets per year, such a fluke may occur about once a year, whereas the discovery of imminent impactors is currently more rare (2 in 10 years). Detection of a rare astronomical event cannot be *a priori* discriminated from rare statistical events.

The tests on real cases discussed in this paper, and many more simulated, convinced us that our algorithm computes a reliable impact probability when the impact actually occurs. Nevertheless, we cannot show that our algorithm is immune from “false” alarms. They are not false in the sense of a wrong computation, or even worse a malicious disinformation, they are statistical flukes which cannot be avoided because of lack of information (hypothesis 2) and the need to use statistics on a small sample (hypothesis 3). The question is what should be done to mitigate the damage by these false alarms, given that we cannot avoid disseminating them: otherwise, how could we disseminate the alarm in the true case?

The only answer is to have a follow-up chain which does not waste resources: the discoverers could themselves either remeasure or follow-up on the short term, like 1 hour after discovery, the cases announced as possible impactors. Other telescopes should be available to perform follow-up, to avoid improper use of survey telescopes for a less demanding task. The ideal solution should be the availability of a *Wide Survey*, capable of covering the entire dark sky every night and of detecting, *e.g.*, an asteroid with absolute magnitude $H = 28$ at 0.03 au distance (near opposition). Then the same asteroid would be recovered by the survey the next day, before the impact, and without the need for auxiliary follow-up.

Chapter 3

Detecting the Yarkovsky effect among near-Earth asteroids from astrometric data

3.1 Introduction

Several complex phenomena cause asteroid orbital evolution to be a difficult problem. By definition, Near-Earth Asteroids (NEAs) experience close approaches with terrestrial planets, which are the main source of chaos in their orbital evolution. Small perturbations, such as non-gravitational perturbations, can significantly affect a NEA trajectory because of this chaoticity.

The *Yarkovsky effect* is due to the recoil force undergone by a rotating body as a consequence of its anisotropic thermal emission (Vokrouhlický et al. 2000; Vokrouhlický et al. 2015a). The main manifestation of the Yarkovsky effect is a secular semimajor axis drift da/dt , which leads to a mean anomaly runoff that grows quadratically with time. Typical values of this perturbation for sub-kilometre NEAs are $da/dt \simeq 10^{-4}$ - 10^{-3} au/My. Because of its small size, the Yarkovsky effect can only be detected for asteroids with a well constrained orbit.

The Yarkovsky effect is a non-gravitational perturbation that is generally split into a seasonal and a diurnal component. The seasonal component arises from the temperature variations that the heliocentric asteroid experiences as a consequence of its orbital motion. An explicit computation of the corresponding acceleration is not easy, even for a spherical body, and becomes very difficult for complex shaped bodies. On the other hand, the diurnal component is due to the lag between the absorption of the radia-

tion coming from the Sun, and the corresponding re-emission in the thermal wavelength. The surface of a rotating body illuminated by the Sun is warmed by solar radiation during the day and cools at night. It is worth noticing that the diurnal and the seasonal components have different consequences on the secular semimajor axis drift. In particular, the diurnal effect produces a positive drift for prograde rotators and a negative drift for retrograde rotators, whereas the seasonal secular drift is always negative. The magnitude of the diurnal effect is generally larger than that of the seasonal effect (Vokrouhlický et al. 2000).

The Yarkovsky effect is key to understanding several aspects of asteroid dynamics:

1. Non-gravitational forces can be relevant for a reliable impact risk assessment when in the presence of deep planetary encounters or when having a long time horizon for the potential impact search (Farnocchia et al. 2015a). As a matter of fact, both these factors call for a greater consideration of the sources of orbit propagation uncertainty, such as non-gravitational perturbations. Currently, there are four known cases that required the inclusion of the Yarkovsky effect in term of hazard assessment: (101955) Bennu (Milani et al. 2009; Chesley et al. 2014), (99942) Apophis (Chesley 2006; Giorgini et al. 2008; Vokrouhlický et al. 2015b; Farnocchia et al. 2013), (29075) 1950 DA (Giorgini et al. 2002; Farnocchia et al. 2014a), and (410777) 2009 FD (Spoto et al. 2014).
2. The semimajor axis drift produced by the Yarkovsky effect has sculpted the main belt for millions of years (Vokrouhlický et al. 2006). The Yarkovsky effect is crucial to understanding the ageing process of asteroid families and the transport mechanism from the main belt to the inner Solar System (Vokrouhlický et al. 2000). The Yarkovsky effect has still not been measured in the main belt, thus Spoto et al. (2015) used a calibration based on asteroid (101955) Bennu to compute the ages of more than 50 families in the main belt. The improvement in the detection of the Yarkovsky drift for NEAs represents a new step forward in creating a reliable chronology of the asteroid belt.
3. Yarkovsky detections provide constraints on asteroid physical properties. Two remarkable efforts in estimating the bulk density from the Yarkovsky drift have already been carried out for two potentially hazardous asteroids: (101955) Bennu (Chesley et al. 2014) and (29075) 1950 DA (Rozitis et al. 2014). Furthermore, the dependence of the Yarkovsky effect on the obliquity can be useful to model the spin axis obliquity distribution of NEAs (Tardioli et al. 2017).

There have been several efforts to model and determine the Yarkovsky effect on the NEA population. The first detection of the Yarkovsky effect was predicted for the asteroid (6489) Golevka in Vokrouhlický et al. (2000) and achieved in 2003 thanks to radar ranging of this object (Chesley et al. 2003). Later, the Yarkovsky effect played a fundamental role in the attribution of four 1953 precovery observations to the asteroid (152563) 1992 BF (Vokrouhlický et al. 2008). Moreover, Chesley et al. (2014) detected the Yarkovsky effect acting on (101955) Bennu from the astrometric observations and from high-quality radar measurements over three apparitions. Currently, asteroid Bennu has the best determined value for the Yarkovsky acceleration, which also led to an estimation of its bulk density (Chesley et al. 2014). More in general, Nugent et al. (2012) provided a list of 13 Yarkovsky detection, and later work increased this number to 21 (Farnocchia et al. 2013). The most recent census is from Chesley et al. (2016), which identified 42 NEAs with valid Yarkovsky detection. Both Farnocchia et al. (2013) and Chesley et al. (2016) flag spurious cases based on whether the detected drift is compatible with the physical properties of the corresponding object and the Yarkovsky mechanism. Since the number of significant Yarkovsky detections in the NEA population is steadily increasing, we decided to update the list.

3.2 Method

3.2.1 Force model

Usually, there is not enough information on the physical model of an asteroid to directly compute the Yarkovsky acceleration through a thermophysical model. Instead, evidence of the Yarkovsky-related drift may be detectable from the observational dataset via orbit determination. Indeed, a gravity-only model may not provide a satisfactory fit to the available data. A Yarkovsky detection is more likely when a very accurate astrometric dataset is available, especially in case of radar measurements at multiple apparitions or when the observational arc is long, thus allowing the orbital drift to become detectable. In such cases, a force model that also includes the Yarkovsky acceleration could result in a better fit to the observations.

We modelled the Yarkovsky perturbation with a formulation that depends on a single dynamical parameter, to be determined in the orbital fit together with the orbital elements. Since the secular perturbation caused by the Yarkovsky effect is a semimajor axis drift, we used a transverse acceleration

$$\mathbf{a}_t = A_2 g(r) \hat{\mathbf{t}} \quad (3.1)$$

as in Marsden et al. (1973) and Farnocchia et al. (2013). In equation (3.1)

A_2 is a free parameter and $g(r)$ is a suitable function of the heliocentric distance of the asteroid. In particular we assume a power law

$$g(r) = \left(\frac{r_0}{r}\right)^d,$$

where $r_0 = 1$ au is used as normalization factor. The exponent d depends on the asteroid and is related to the asteroid's thermophysical properties. Farnocchia et al. (2013) show that the value of d is always between 0.5 and 3.5. They used $d = 2$ for all asteroids because no thermophysical data are available. In our analysis we adopted the same values for d , apart from (101955) Bennu for which the value $d = 2.25$ is assumed (Chesley et al. 2014).

Typical values of the Yarkovsky acceleration for a sub-kilometre NEA are 10^{-15} – 10^{-13} au/d². As a consequence, to reliably estimate the Yarkovsky effect, the right-hand side of the equations of motion has to include all the accelerations down to the same order of magnitude. Our force model includes the gravitational accelerations of the Sun, the eight planets, and the Moon based on JPL's planetary ephemerides DE431 (Folkner et al. 2014). To ensure a more complete force model, we also include the contributions coming from 16 massive main belt bodies and Pluto. All the gravitational masses we used are listed in Table 3.1. Since we compare our results with the ones obtained by JPL, we point out that the JPL team uses the 16 most massive main belt asteroids as estimated by Folkner et al. (2014), which produces a slight difference, both in the list and in the masses.

The relativity model includes the relativistic contribution of the Sun, the planets and the Moon. In particular, we use the Einstein-Infeld-Hoffman equations, namely the equations of the approximate dynamics of a system of point-like masses due to their mutual gravitational interactions, in a first order post-Newtonian expansion, as described in Moyer (2003), Will (1993), and Einstein et al. (1938).

3.2.2 Average semimajor axis drift

For a given A_2 value and under the assumptions about the dynamical model, we want to estimate the average semimajor axis drift caused by the transverse acceleration \mathbf{a}_t . This estimate has been introduced in Farnocchia et al. (2013).

First we can estimate the semimajor axis drift by means of Gauss' perturbative equations:

$$\dot{a} = \frac{2a\sqrt{1-e^2}}{nr} A_2 g(r)$$

Table 3.1. Perturbing bodies included in the dynamical model in addition to the Sun, the planets and the Moon. They are 16 massive main belt bodies and Pluto. The last column shows the references we used for each asteroid mass.

Asteroid	Grav. mass (km ³ /s ²)	Reference
(1) Ceres	63.20	Standish et al. (1989)
(2) Pallas	14.30	Standish et al. (1989)
(3) Juno	1.98	Konopliv et al. (2011)
(4) Vesta	17.80	Standish et al. (1989)
(6) Hebe	0.93	Carry (2012)
(7) Iris	0.86	Carry (2012)
(10) Hygiea	5.78	Baer et al. (2011a)
(15) Eunomia	2.10	Carry (2012)
(16) Psyche	1.81	Carry (2012)
(29) Amphitrite	0.86	Carry (2012)
(52) Europa	1.59	Carry (2012)
(65) Cybele	0.91	Carry (2012)
(87) Sylvia	0.99	Carry (2012)
(88) Thisbe	1.02	Carry (2012)
(511) Davida	2.26	Carry (2012)
(704) Interamnia	2.19	Carry (2012)
(134340) Pluto	977.00	Folkner et al. (2014)

where a is the semimajor axis, e is the eccentricity and n is the proper motion. By averaging we obtain

$$\bar{a} = \frac{a\sqrt{1-e^2}A_2}{\pi} \int_0^T \frac{g(r)}{r} dt = \frac{A_2}{\pi n a} \int_0^{2\pi} r g(r) df$$

where T is the orbital period and f is the true anomaly. In case of our assumption $g(r) = \left(\frac{r_0}{r}\right)^d$ the semimajor axis drift is

$$\bar{a} = \frac{A_2(1-e^2)}{\pi n} \left(\frac{r_0}{p}\right)^d \int_0^{2\pi} (1+e\cos f)^{d-1} df.$$

By Taylor expansion, we have

$$\int_0^{2\pi} (1+e\cos f)^{d-1} df = \sum_{k=0}^{\infty} \binom{d-1}{k} e^k \mathcal{I}_k,$$

where

$$\mathcal{I}_k := \int_0^{2\pi} \cos^k f df.$$

The integral \mathcal{I}_k can be computed by a recursive relation. First, $\mathcal{I}_0 = 2\pi$ and $\mathcal{I}_1 = 0$. For $k \geq 2$ we can integrate by parts obtaining

$$\begin{aligned}\mathcal{I}_k &= (\sin f \cdot \cos^{k-1} f) \Big|_0^{2\pi} + (k-1) \int_0^{2\pi} \sin^2 f \cdot \cos^{k-2} f df = \\ &= (k-1)\mathcal{I}_{k-2} - (k-1)\mathcal{I}_k,\end{aligned}$$

from which it follows that

$$\mathcal{I}_k = \frac{k-1}{k} \mathcal{I}_{k-2}.$$

Thus $\mathcal{I}_{2h+1} = 0$ for every $h \geq 0$ (the odd powers of the cosine average out), and

$$\begin{aligned}\mathcal{I}_{2h} &= \frac{2h-1}{2h} \mathcal{I}_{2h-2} = \prod_{\ell=1}^h \frac{2\ell-1}{2\ell} \cdot \mathcal{I}_0 = \\ &= \frac{\prod_{\ell=1}^h (2\ell-1)}{2^h \cdot h!} \cdot \mathcal{I}_0 = \frac{(2k)!}{2^{2h} \cdot (h!)^2} \cdot \mathcal{I}_0 = \frac{1}{2^{2h}} \binom{2h}{h} \cdot \mathcal{I}_0\end{aligned}$$

Thus

$$\bar{a} = \frac{2A_2(1-e^2)}{n} \left(\frac{r_0}{p}\right)^d J(e, d),$$

where

$$J(e, d) := \sum_{h=0}^{\infty} \alpha_h e^{2h} = \sum_{h=0}^{\infty} \binom{d-1}{2h} \binom{2h}{h} \frac{1}{2^{2h}} e^{2h}.$$

The ratio

$$\frac{\alpha_{h+1} e^{2(h+1)}}{\alpha_h e^{2h}} = \frac{(d-2h-1)(d-2h-2)e^2}{4(h+1)^2} \rightarrow e^2$$

as $h \rightarrow +\infty$, and thus the series defining $J(e, d)$ is convergent for any eccentricity $0 < e < 1$. Furthermore, for integer d the sum of the series J can be analytically computed, for instance $J(e, 2) = 1$ and $J(e, 3) = 1 + \frac{1}{2}e^2$.

3.2.3 Statistical treatment of the astrometry

The statistical treatment of the astrometry is key to a reliable orbit determination. The differential corrections procedure provides the asteroid's nominal orbit and its uncertainty (Milani et al. 2010, Chap. 5), which strongly depend upon the observations accuracy and error modelling. For the computations done for this chapter, we used the debiasing and weighting scheme

provided in Farnocchia et al. (2015b). The JPL team uses the more recent Vereš et al. (2017) weighting scheme.

The astrometric data usually can contain outliers that can affect the solution of the orbit determination. To remove erroneous observations from the fit we apply the outlier rejection procedure described in Carpino et al. (2003).

Besides our default data treatment, we applied *ad hoc* modifications for the following cases:

(152563) 1992 BF. The four 1953 precovery observations of this NEA have been carefully re-measured in Vokrouhlický et al. (2008). We adopt the given positions and standard deviations, the latter being 0.5 arcsec in right ascension and 1 arcsec in declination.

2009 BD. This object is one of the smallest near-Earth asteroids currently known (Mommert et al. 2014a) and thus solar radiation pressure affects its orbit. A direct detection of the area-to-mass ratio is contained in Micheli et al. (2012), which provide high-quality astrometry from Mauna Kea and replace all the observations from the Tzec Maun Observatory (H10) with a single position. For these observations we set data weights based on the uncertainties provided by Micheli et al. (2012) and we include both the Yarkovsky effect and solar radiation pressure in the orbital fit (see Section 3.6).

2011 MD. As well as 2009 BD, this asteroid is very small and is among those for which we determined both the Yarkovsky effect and solar radiation pressure. 2011 MD has been observed during the 2011 very close approach with the Earth. Despite the short arc of three months, a very large number of optical observations of 2011 MD were collected, precisely 1555. Following the strategy presented in Mommert et al. (2014b), we relaxed the weights for the observations collected during the close approach¹ and we added the Spitzer detection (on 2014 February 11), which extends the observation arc by almost three years.

2015 TC₂₅. Asteroid 2015 TC₂₅ was discovered by the Catalina Sky Survey in October 2015, just two days before an Earth flyby at 0.3 lunar distances. It is one of the smallest asteroids ever discovered, about 2 m in diameter (Reddy et al. 2016), and the 2017 astrometry affords an estimate of solar

¹Indeed, timing errors are more relevant for observations performed at small geocentric distances.

radiation pressure. We are aware that for 2015 TC₂₅ the JPL team carried out a specific study (Farnocchia et al. 2017a), which adopted *ad hoc* weights based on observer-provided uncertainty estimates. To handle this case, we used the same data treatment as JPL.

Note that it is desirable to keep the number of “manual” interventions on the observational data as small as possible. Indeed we are trying to figure out how to automate the determination of the set of NEAs with significant and reliable Yarkovsky effect. Anyway, in some cases a manual intervention is needed to properly handle observational issues, *e.g.*, too many close observations taken during a very close approach and affected by timing errors or remeasurement of old observations.

3.2.4 Starting sample of NEAs

As first sample of asteroids, we started selecting those objects in NEODyS² having a formal uncertainty on the semimajor axis $\sigma(a) < 3 \cdot 10^{-9}$ au. The choice of the threshold for $\sigma(a)$ comes from an order of magnitude estimate: for an asteroid with diameter 1 km the Yarkovsky drift is about $3 \cdot 10^{-10}$ au/y, thus it causes a variation of $3 \cdot 10^{-9}$ au in ten years. The value of $\sigma(a)$ has to be the one computed at the mean epoch of the observations, since it is the best choice for the orbital fit quality. Moreover, this uncertainty threshold corresponds to a gravity-only fit: after the Yarkovsky coefficient is estimated the uncertainty of the semimajor axis sharply increases because of the strong correlation between A_2 and the semimajor axis.

The list of asteroids satisfying this criterion contained 519 objects (as of February 2018). As a second step, we extracted from the JPL database a set of 89 asteroids having A_2 determined³. Among them, only 16 were not contained in our first list, thus we added them. Furthermore, we considered all the reliable detections from Farnocchia et al. (2013) and it turned out that only 3 asteroids did not belong to any of the previous lists, thus we added them as well to our sample.

Summarizing, we started with a sample of $519 + 16 + 3 = 538$ objects. For each one of them we performed an orbital fit for the initial conditions together with the Yarkovsky parameter A_2 , without any *a priori* constraint. For a few of them we also estimated solar radiation pressure. As a result of the fit, we derived the signal-to-noise ratio SNR_{A_2} of the A_2 parameter, obtaining 101 detections with $\text{SNR}_{A_2} \geq 3$ and 437 with $\text{SNR}_{A_2} < 3$, most of which showing a negligible signal-to-noise ratio.

²The NEODyS database is available at <http://newton.dm.unipi.it>.

³The JPL Small-Body Database is available at <http://ssd.jpl.nasa.gov/sbdb.cgi>.

3.2.5 Yarkovsky expected value

By means of orbit determination, we determine a transverse acceleration directly from the astrometry. However, to claim that the measured acceleration is caused by the Yarkovsky effect we need to make sure that its magnitude is compatible with the physical properties of the object and the Yarkovsky mechanism. Therefore, we provide an expected value of the Yarkovsky-related orbital drift.

In Farnocchia et al. (2013), an expected value for A_2 is computed by exploiting the diameter of the asteroid and scaling from the corresponding value of (101955) Bennu, the best determined and most reliable Yarkovsky detection. In this chapter, we make use of the Yarkovsky calibration as in Spoto et al. (2015):

$$\left(\frac{da}{dt}\right)_{\text{exp}} = \left(\frac{da}{dt}\right)_{\mathcal{B}} \cdot \frac{\sqrt{a_{\mathcal{B}}}(1 - e_{\mathcal{B}}^2)}{\sqrt{a}(1 - e^2)} \frac{D_{\mathcal{B}} \rho_{\mathcal{B}} \cos \varphi}{D \rho \cos \varphi_{\mathcal{B}}} \frac{1 - A}{1 - A_{\mathcal{B}}}, \quad (3.2)$$

where D is the diameter of the asteroid, ρ is the density, φ is the obliquity (angle between the spin axis and the normal to the orbit plane), and A is the Bond albedo. The latter is computed from the geometric albedo p_v , using $A = \frac{1}{3}p_v$ (Muinonen et al. 2010). The symbols with a “ \mathcal{B} ” refer to asteroid (101955) Bennu, and the values we assume for them are listed in Table 3.2 with their references.

Table 3.2. Values of the physical quantities for the asteroid (101955) Bennu, used in equation (3.2).

Physical quantity	Symbol	Value	Reference
diameter	$D_{\mathcal{B}}$	(0.492 ± 0.020) m	Nolan et al. (2013)
density	$\rho_{\mathcal{B}}$	(1.26 ± 0.07) g/cm ³	Chesley et al. (2014)
geometric albedo	$(p_v)_{\mathcal{B}}$	0.046 ± 0.005	Emery et al. (2014)

For the diameter D we use the known physical value when available. When the asteroid’s shape is not so simple to be approximated by an ellipsoidal model, we use the dynamically equivalent equal volume ellipsoid dimensions to compute the equivalent diameter. In particular, this effort has been done for three asteroids, namely (4179) Toutatis (Hudson et al. 2003), (162421) 2000 ET₇₀ (Naidu et al. 2013), and (275677) 2000 RS₁₁ (Brauer et al. 2015). Otherwise, when no physical information are available, we estimate the diameter from the absolute magnitude H following the relation (Pravec et al. 2007)

$$D = 1329 \text{ km} \cdot 10^{-H/5} \cdot (p_v)^{-1/2},$$

where the geometric albedo p_v is assumed to be $p_v = 0.154$ if unknown.

As shown in equation (3.2), the density is required to estimate the strength of the Yarkovsky effect for asteroids with small diameters. Carry (2012) reports a large number of asteroid densities that we use as starting point. However, in general, density estimates are more reliable and accurate for massive bodies and there is a trend for a decreasing density with diameter, due to the increasing macroporosity⁴ resulting from the cascade of collisions suffered by the body (Carry 2012; Scheeres et al. 2015). We thus extrapolate the density of small asteroids from the density of large asteroids belonging to the same taxonomic class by increasing their macroporosity to that of Bennu ($\mathcal{P}_B = (40 \pm 10)\%$, from Chesley et al. (2014)). Such macroporosity is typical for (sub-)kilometre-sized asteroids, as illustrated by (25143) Itokawa, visited by the JAXA Hayabusa mission (Fujiwara et al. 2006). This is a modified version of the approach given in Spoto et al. (2015), still using Bennu for the scaling since it has the best estimated Yarkovsky acceleration and a comprehensive physical characterization⁵. Thus the scaled density is given by

$$\rho_s = (1 - \mathcal{P}_B)\rho, \quad (3.3)$$

where the density scaling factor is $1 - \mathcal{P}_B = 0.60$ and ρ is the known density of the large asteroid. Equation (3.3) follows from the above assumptions and from the definition of macroporosity. We selected the large asteroids (4) Vesta, (10) Hygiea, (15) Eunomia, and (216) Kleopatra as representative of the taxonomic classes V, C, S, Xe respectively. The density of the representative asteroids and their scaled values are listed in Table 3.3.

Table 3.3. Representative asteroids for some taxonomic classes: number/name, taxonomic type, densities as in Carry (2012) with their uncertainties, scaled densities applying the factor $1 - \mathcal{P}_B$.

Asteroid	Tax. type	ρ (g/cm ³)	ρ_s (g/cm ³)
(4) Vesta	V	3.58 ± 0.15	2.15
(10) Hygiea	C	2.19 ± 0.42	1.31
(15) Eunomia	S	3.54 ± 0.20	2.12
(216) Kleopatra	Xe	4.27 ± 0.15	2.56

⁴It is the fraction of volume occupied by voids.

⁵Previously Spoto et al. (2015) used the known density of (704) Interamnia, considered to be a large asteroid with similar composition to Bennu, to estimate porosity of the latter. Recently the composition of (101955) Bennu has been modelled by Clark et al. (2011), based on spectral observations, and it has been found to be closer to other large asteroids, such as (24) Themis and (2) Pallas.

We used three sources of asteroid physical information: the database of physical properties of near-Earth asteroids provided by E.A.R.N.⁶, the JPL Small-Body Database, and the data provided by the WISE mission, such as diameters and albedos (Mainzer et al. 2011). It is important to point out that we have no physical information for the large majority of the objects discussed in this chapter. For instance, for the 44% of our detections with $\text{SNR}_{A_2} > 2.5$ we have no physical data, for 62% we have no measured albedo values, and less than half of our detections can be assigned to a taxonomic class.

3.2.6 Filtering criterion

We use the Yarkovsky-related expected value as a filtering criterion to understand whether the estimated orbital drift da/dt is physically consistent with the Yarkovsky effect. If the estimated da/dt is significantly larger than the maximum absolute expected value (assuming $\cos \varphi = \pm 1$), the result is inconsistent with the Yarkovsky mechanism. We compute the indicator parameter

$$\mathcal{S} = \left| \frac{da/dt}{(da/dt)_{\text{exp}}} \right|.$$

Since most times there is very little to no physical information, we need some margin on the upper threshold for \mathcal{S} , which therefore should be larger than 1. We filter out the candidate detections with $\mathcal{S} > 2$. The current maximum value allowed for \mathcal{S} is empirical, but it could be refined. In particular, this upper threshold can be lowered when better data are available. Improving the computation of the expected value - thus decreasing the uncertainty of the indicator parameter \mathcal{S} - requires at least a reliable taxonomic type (for the scaling needed for the density) and better diameters. Values of \mathcal{S} greater than the maximum threshold indicate questionable results. These spurious detections should be investigated to find possible causes and solutions. In general, either the \mathcal{S} value is too high to be compatible with an acceptable detection or it is barely above the maximum threshold, in such a way that additional information would clarify the situation and allow us to decide whether the detection is accepted or refused. For further details see Section 3.4.

We point out that values $\mathcal{S} \ll 1$ are permitted. Indeed equation (3.2) employed asteroid size and bulk density, thus $\mathcal{S} \ll 1$ means that the orbital drift is significantly lower than the maximum expected value. Several phenomena can lower the Yarkovsky effect: obliquity $\varphi \simeq 90^\circ$, very large or very small thermal inertia, larger density than expected, or small rotation

⁶<http://earn.dlr.de/nea/>

angular velocity. For instance, asteroid (85774) 1998 UT₁₈ has a rotation period of about 34 h, and indeed the indicator \mathcal{S} is low ($\simeq 0.3$, cf. Table 3.4). The detections of this kind are significant detections of a weak Yarkovsky drift. A second class of weak Yarkovsky drifts can be defined: they are non-detections, that is $\text{SNR}_{A_2} < 3$, but the asteroid has physical properties that would permit a significant detection if the Yarkovsky effect were maximized. Chesley et al. (2016) refer to these detections as weak detections. Despite the low SNR, the result of the A_2 estimation can provide useful constraints on the asteroid's physical properties.

By combining the value of the SNR_{A_2} coming from the orbital fit with the value of the filtering parameter \mathcal{S} , we divided our detections in three categories.

- We consider *accepted* the detections satisfying both $\text{SNR}_{A_2} \geq 3$ and $\mathcal{S} \leq 2$.
- The category called *marginal significance* includes the asteroids for which $2.5 < \text{SNR}_{A_2} < 3$ and $\mathcal{S} \leq 2$, plus (410777) 2009 FD and (99942) Apophis, both remarkable for their impact monitoring.
- The detections with $\text{SNR}_{A_2} > 3$ and $\mathcal{S} > 2$ are *rejected* because they have a too high value for the indicator parameter \mathcal{S} , suggesting that the detected A_2 signal is unrealistic or not explicable with the Yarkovsky effect (see 2003 RM in Chesley et al. (2016), or (4015) Wilson-Harrington in Section 3.4).

The results only include detections, that is we do not list the asteroids for which we found no significant Yarkovsky signal from the observational dataset (85% of the initial sample). Figure 3.1 provides an overall view of our classification. In particular, we consider the plane $(\text{SNR}_{A_2}, \mathcal{S})$ and we mark the detections of each class (but the rejected) with a different color:

- the accepted detections are indicated with a green dot;
- the marginal significance detections are represented with a blue dot, except for (410777) 2009 FD and (99942) Apophis, which are indicated with a blue asterisk (special cases);
- the rejected detections are indicated with a red cross.

3.3 Accepted and significant results

As explained in Section 3.2.4, we started from the initial sample of NEAs and we performed an orbital fit including the Yarkovsky parameter A_2 . Then

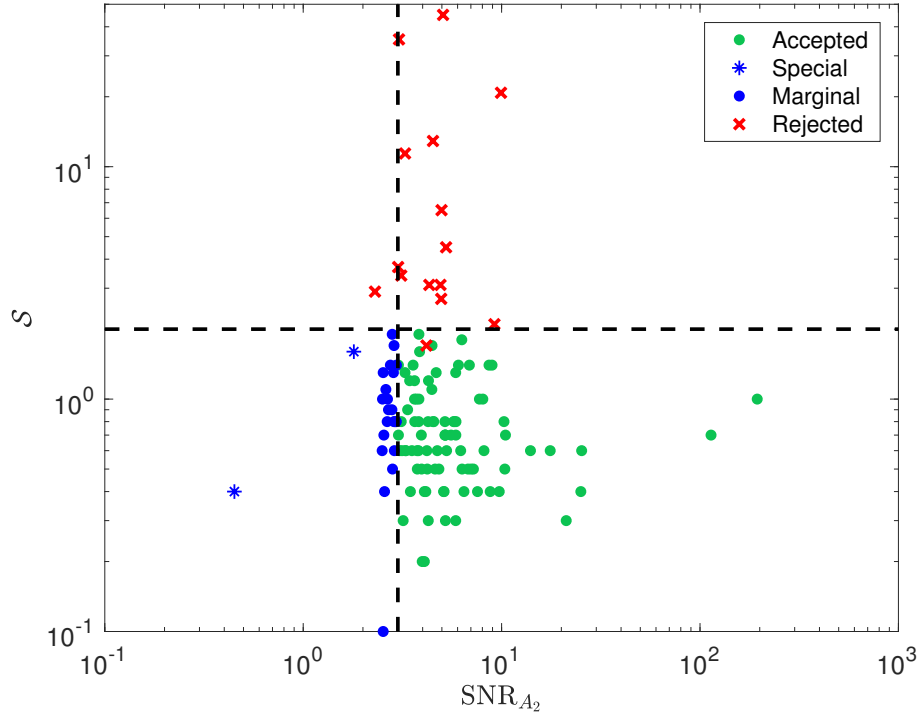


Figure 3.1. Graphical representation of the partition of the detections set into classes on the plane $(\text{SNR}_{A_2}, \mathcal{S})$. We plot the accepted detections (green dots), the marginally significance detections (blue dots) plus the special cases (410777) 2009 FD and (99942) Apophis (blue asterisk), and the rejected detections (red crosses).

we applied the filtering procedure, and obtained 86 detections, which are listed in Table 3.4 and Table 3.5. For each asteroid, we report the value of the absolute magnitude H , the A_2 parameter along with its uncertainty, the signal-to-noise ratio of A_2 , the value of the semimajor axis drift da/dt , the indicator parameter \mathcal{S} , and the available physical data such as the geometric albedo p_v , the diameter D , the density ρ , and the taxonomic class. As explained in Section 3.2.5, when no information on the diameter is available, we infer one from the absolute magnitude. We mark these cases with an asterisk (*) in the diameter column. When the albedo is not directly measured but the taxonomic class is known, we assigned the albedo according to Binzel et al. (2002) and marked the albedo value with a dagger (†). When the albedo is not known we assume $p_v = 0.154$, and mark it with a “d”. Note that 0.154 is a mean value, which has a low probability of being accurate because of the bimodality of the albedo distribution of near-Earth asteroids. Most asteroids are either significantly brighter or significantly darker. Thus, when a diameter D is derived from the absolute magnitude and this

default albedo, its relative uncertainty is larger, and in turn the value of S (containing the factor $1/D$) is uncertain.

Table 3.4. List of Yarkovsky detections with $\text{SNR}_{A_2} > 5$ and with $S \leq 2$. The table is sorted by SNR_{A_2} , in decreasing order. The columns contain the asteroid name, the absolute magnitude H , the A_2 parameter with its uncertainty and signal-to-noise ratio SNR_{A_2} , the semimajor axis drift da/dt with its uncertainty, the indicator parameter S , the geometric albedo p_v , the diameter D and the taxonomic class. Asteroids with no available information about the diameter are marked with an asterisk (*). Asteroids with albedo assigned according to Binzel et al. (2002) since no direct estimate is available are marked with a “d”. Asteroids with no albedo informations are marked with a dagger (†).

Asteroid	H	A_2 (10^{-15} au/d ²)	SNR_{A_2}	da/dt (10^{-4} au/My)	S	p_v	D (km)	Tax. class
(101955) Benu	20.6	-46.20 ± 0.24	194.27	-18.98 ± 0.10	1.0	0.046	0.492	B
(480883) 2001 YE ₄	20.9	-69.87 ± 0.61	113.66	-50.95 ± 0.45	0.7	0.154 ^d	0.229*	-
(2340) Hathor	20.2	-29.94 ± 1.18	25.32	-17.34 ± 0.69	0.6	0.6	0.21	S
(483656) 2005 ES ₇₀	23.7	-140.17 ± 5.59	25.08	-80.11 ± 3.19	0.4	0.154 ^d	0.061*	-
(152563) 1992 BF	19.7	-24.85 ± 1.17	21.17	-11.96 ± 0.56	0.3	0.287	0.272	Xc
2012 BB ₁₂₄	21.1	71.14 ± 4.05	17.58	29.42 ± 1.67	0.6	0.154 ^d	0.201*	-
(85990) 1999 JV ₆	20.2	-30.62 ± 2.19	13.98	-14.34 ± 1.03	0.6	0.095	0.451	Xk
(437844) 1999 MN	21.2	44.56 ± 4.26	10.46	41.35 ± 3.95	0.7	0.154 ^d	0.195*	S
(480808) 1994 XL ₁	20.8	-45.13 ± 4.35	10.38	-32.37 ± 3.12	0.5	0.154 ^d	0.237*	-
2007 TF ₆₈	22.7	-184.07 ± 17.91	10.28	-70.90 ± 6.90	0.8	0.154 ^d	0.099*	-
(1566) Icarus	16.3	-3.75 ± 0.39	9.73	-4.85 ± 0.50	0.4	0.14	1.44	S
(468468) 2004 KH ₁₇	21.9	-65.83 ± 8.08	8.15	-44.11 ± 5.41	0.6	0.072	0.197	C
(138175) 2000 EE ₁₀₄	20.3	-106.50 ± 11.89	8.95	-49.37 ± 5.51	1.4	0.154 ^d	0.297*	-
(1862) Apollo	16.1	-3.70 ± 0.42	8.76	-1.89 ± 0.22	0.4	0.26	1.4	Q
(2062) Aten	17.1	-13.18 ± 1.53	8.64	-5.89 ± 0.68	1.4	0.2	1.3	S
(162004) 1991 VE	18.1	26.97 ± 3.35	8.04	21.73 ± 2.70	1.0	0.154 ^d	0.824*	-
2006 TU ₇	21.9	166.67 ± 21.55	7.73	98.51 ± 12.74	1.0	0.154 ^d	0.141*	-
2011 PU ₁	25.5	-375.52 ± 49.66	7.56	-148.60 ± 19.65	0.4	0.154 ^d	0.027*	-
(6489) Golevka	19.0	-12.04 ± 1.67	7.21	-5.10 ± 0.71	0.5	0.151	0.53	Q
2011 EP ₅₁	25.3	-359.14 ± 51.20	7.01	-185.09 ± 26.39	0.5	0.154 ^d	0.029*	-
(33342) 1998 WT ₂₄	17.8	-27.87 ± 4.05	6.88	-16.91 ± 2.46	1.4	0.75	0.415	Xe
(3361) Orpheus	19.2	18.27 ± 2.70	6.77	7.88 ± 1.16	0.5	0.357	0.348	Q
(364136) 2006 CJ	20.1	-29.16 ± 4.52	6.46	-34.99 ± 5.42	0.4	0.154 ^d	0.317*	-
(499998) 2011 PT	24.0	-234.96 ± 37.16	6.32	-91.30 ± 14.44	0.5	0.154 ^d	0.053*	-
(138404) 2000 HA ₂₄	19.1	45.05 ± 7.15	6.30	19.95 ± 3.17	1.8	0.154 ^d	0.517*	S
2006 CT	22.3	-112.43 ± 18.09	6.22	-48.14 ± 7.74	0.6	0.154 ^d	0.119*	-
(3908) Nyx	17.3	25.45 ± 4.20	6.06	9.86 ± 1.63	1.4	0.23	1	V
(363599) 2004 FG ₁₁	21.0	-59.90 ± 10.17	5.89	-42.39 ± 7.20	0.8	0.306	0.152	V
1999 UQ	21.7	-110.45 ± 18.77	5.88	-44.85 ± 7.62	0.7	0.154 ^d	0.152*	-
2003 YL ₁₁₈	21.6	-172.62 ± 29.42	5.87	-90.31 ± 15.39	1.3	0.154 ^d	0.165*	-
(154590) 2003 MA ₃	21.6	-77.01 ± 13.11	5.87	-37.11 ± 6.32	0.3	0.530	0.086	-
2005 EY ₁₆₉	22.1	-137.02 ± 23.70	5.78	-53.80 ± 9.30	0.8	0.154 ^d	0.128*	-
(10302) 1989 ML	19.4	74.98 ± 13.09	5.73	28.76 ± 5.02	0.8	0.51	0.248	-
2000 PN ₈	22.1	123.75 ± 22.26	5.56	49.28 ± 8.87	0.7	0.154 ^d	0.131*	-
(506590) 2005 XB ₁	21.9	92.68 ± 17.54	5.28	44.88 ± 8.49	0.6	0.154 ^d	0.143*	-
(350462) 1998 KG ₃	22.1	-61.35 ± 11.79	5.21	-24.52 ± 4.71	0.3	0.154 ^d	0.129*	-
(216523) 2001 HY ₇	20.5	58.55 ± 11.23	5.21	31.33 ± 6.01	0.7	0.154 ^d	0.267*	-
(363505) 2003 UC ₂₀	18.3	-7.48 ± 1.44	5.20	-4.05 ± 0.78	0.7	0.028	1.9	C
(99907) 1989 VA	17.9	16.51 ± 3.19	5.18	12.71 ± 2.46	0.7	0.24	0.55	S
(66400) 1999 LT ₇	19.3	-43.09 ± 8.33	5.18	-29.44 ± 5.69	0.8	0.182	0.411	-
(377097) 2002 WQ ₄	19.5	-23.66 ± 4.61	5.13	-10.37 ± 2.02	0.4	0.154 ^d	0.423*	-
2000 CK ₅₉	24.2	-192.46 ± 37.77	5.10	-74.48 ± 14.62	0.4	0.154 ^d	0.05 *	-

Some of the asteroids included in Table 3.4 and Table 3.5 deserves dedicated comments.

(1566) *Icarus*. It is known that the 1968 observations of (1566) *Icarus* are affected by large timing errors. A possible solution to this problem is to

include timing errors in the observations uncertainty possibly even removing the systematic timing errors. A possible alternative is to properly treat the correlation between the right ascension and the declination. This operation will be made easier after the adoption of the new Astrometric Data Exchange Standard (ADES⁷). For now, it is possible to adapt the weighting scheme to underweight the observations during the 1968 close approach: this was done by the JPL team, not by the Pisa one. By comparing the result of the two groups, and also with the one in Greenberg et al. (2017a), we can claim that the detection of the Yarkovsky effect is confirmed, even if there is a significant difference between the standard deviations (see Section 3.7), which is explained by the different weighting scheme.

(3908) Nyx. Asteroid (3908) Nyx is classified as V-type, but it has many properties inconsistent with (4) Vesta. Thus the density scaling is not performed using the density of Vesta as for the other V-type asteroids. Asteroid (5381) Sekhmet is a V-type with a diameter which is comparable to the one of Nyx. The density of Sekhmet is (1.30 ± 0.65) g/cm³ (Carry 2012), compatible with the estimate in Farnocchia et al. (2014b), and we assume this value also for Nyx.

3.4 Rejected results

In this section we consider the significant detections that we rated as spurious, *i.e.*, for which we obtained a Yarkovsky detection greater than one would reasonably expect from the Yarkovsky effect. Despite the signal-to-noise ratio is less than 3, we also add (4015) Wilson-Harrington to this category as a “special” case, as explained below.

Reasons for refusing a detection can be the following:

- Dynamical model problems can occur in few cases, such as (4179) Toutatis and (4015) Wilson-Harrington.
- Sometimes the results are strongly dependent on few observations, typically old isolated observations, which are separated by a long time interval from the bulk of the dataset. In these cases we usually reject the detection, unless the precovery has been carefully remeasured, as for (152563) 1992 BF.
- Solutions with Yarkovsky affected by observational data of questionable reliability.

⁷<http://github.com/IAU-ADES/ADES-Master>.

The list of all the rejected detections contains 15 cases, see Table 3.6. Below we provide dedicated comments for each rejected detection.

(4179) Toutatis Even though this asteroid shows a very significant Yarkovsky effect detection, we have to point out that Toutatis is especially large (see Table 3.4, diameter from Hudson et al. (2003)), thus non-gravitational perturbations are comparatively small with respect to gravitational ones. A test we performed with a larger number (343) of perturbing asteroid shows that the estimated A_2 value depends upon the list of perturbers included and their uncertain masses. Moreover, light curve investigations showed a non-principal axis rotation, as presented in Mueller et al. (2002) and Spencer et al. (1995). For all these reasons we cannot rely on the current estimate of the Yarkovsky drift of Toutatis.

(4015) Wilson-Harrington. This asteroid was initially discovered in 1949 as a comet at the Palomar Sky Survey. It was named 107P/Wilson-Harrington, but then it was lost. Thirty years later the asteroid 1979 VA was discovered and, after the 1988 apparition, it was numbered as (4015) 1979 VA. On August 13, 1992, the IAU circular 5585 (Bowell et al. 1992) reported that the asteroid (4015) 1979 VA and the comet 107P/Wilson-Harrington were indeed the same object. Furthermore, no cometary activity was noted during the well-observed 1979-80 apparition, confirming that it is actually an extinct comet. The detection of the Yarkovsky parameter is indeed significant, but the \mathcal{S} value indicates a value of the non-gravitational acceleration that is too large than the one expected from the Yarkovsky effect. Since the observed arc contains the time span of cometary activity, the most likely interpretation is that the large detected transverse acceleration is caused by the out-gassing rather than the Yarkovsky effect. Furthermore, a dynamical model assuming a constant value for A_2 , as it is the one we employed, is not enough representative of the real orbital dynamics, given that the cometary activity has ceased. Thus in this case we consider that a non-gravitational effect has been detected, but not Yarkovsky.

In some cases, a spurious detections is due to poor optical astrometry, often affecting isolated old observations. In this case we rejected the detection, and a remeasurement of these old observations would be desirable to clarify the situation: the Yarkovsky signal could significantly increase as well as disappear. This is the case for the asteroids listed below.

(260141) 2004 QT₂₄. The detected signal is strongly dependent on four observations in 1993 and 1998 from Siding Spring Observatory DSS.

(350751) 2002 AW. This asteroid has two isolated observations in 1991 from Palomar Mountain-DSS.

(39565) 1992 SL. This asteroid has one isolated observation in 1950 from Palomar Mountain.

(4486) Mithra. This asteroid has a signal which is strongly dependent on a single isolated observation in 1974 from Crimea-Nauchnij (MPC code 095).

(474158) 1999 FA. This object has one isolated observation in 1978, from Siding Spring Observatory. In agreement with Farnocchia et al. (2013), we consider that the 1978 observation would need to be remeasured before accepting the Yarkovsky detection for (474158) 1999 FA.

(162421) 2000 ET₇₀. This asteroid has two isolated observations in 1977 from European Southern Observatory, La Silla DSS.

There are detections which have to be rated as spurious, because \mathcal{S} indicates a Yarkovsky drift which is way larger than expected, despite the fact that the signal-to-noise ratio of the A_2 parameter is ≥ 3 . This holds for 2010 KP₁₀, (308635) 2005 YU₅₅, (139359) 2001 ME₁, (142561) 2002 TX₆₈, and (192563) 1998 WZ₆. To confirm the reliability of our filtering criterion, we checked each spurious detections. They show problematic astrometry, which resulted in an incorrect determination of the Yarkovsky effect.

A separate comment holds for (175706) 1996 FG₃, since it is a binary asteroid (Scheirich et al. 2015). The signal found for the Yarkovsky detection is likely due to the astrometric data treatment, as confirmed by the fact that it disappears when the weighting scheme proposed in Vereš et al. (2017) is applied. Once we have a Yarkovsky detection for this object it will be possible to compare with the Yarkovsky theory for binary asteroids as described by Vokrouhlický et al. (2005).

A remarkable case is (433) Eros. This asteroid shows a significant value for the Yarkovsky effect, but a very high value for the indicator parameter. Moreover, the obliquity of Eros is known to be $\simeq 89^\circ$ (Yeomans et al. 2000), therefore we would expect a value for \mathcal{S} much less than 1. Thus this detection is spurious, likely caused by historical data dating back to 1893 for which it is challenging to come up with a reliable statistical treatment.

3.5 Marginal significance

We now consider the marginal significance class, containing the detections for which $2.5 < \text{SNR}_{A_2} < 3$ and $\mathcal{S} \leq 2$. These detections are physically meaningful since they satisfy the filtering on \mathcal{S} , but the signal to noise for the A_2 parameter as determined from the observations is not enough for a reliable detection. In addition, as mentioned before, we include two special cases in this category, namely (410777) 2009 FD and (99942) Apophis. These two objects show acceptable values of the indicator \mathcal{S} but the signal-to-noise ratio of the A_2 parameter is very low (cf. Table 3.7). Nevertheless, we decided to keep them because the Yarkovsky drift plays a fundamental role for its impact predictions (see the introduction). In this way we grouped 24 detections in this class, which are listed in Table 3.7.

(99942) Apophis. Similarly to Toutatis, also Apophis has a complex rotation, as shown in Vokrouhlický et al. (2015b). However, the Yarkovsky effect is not significantly weakened by the tumbling state. Vokrouhlický et al. (2015b) used the available rotation state, shape, size and thermophysical model of Apophis to predict the Yarkovsky semimajor axis drift. The drift obtained by fitting the astrometric data is compatible with the model prediction. We obtained $da/dt = (-24.50 \pm 13.58) \cdot 10^{-4}$ au/Myr for the fitted value, which is completely consistent with Vokrouhlický et al. (2015b). There is no question that the Yarkovsky effect has to be taken into account for Apophis to predict future motion, especially for impact hazard assessment (Chesley 2006; Giorgini et al. 2008; Farnocchia et al. 2013).

(410777) 2009 FD. The Yarkovsky effect found is below the significance level, and nevertheless it has to be taken into account for long-term impact monitoring purposes (Spoto et al. 2014).

Maintaining a list of marginal significance detections is useful because they are candidates for future detections as observational data improves and increases.

3.6 Direct radiation pressure detection

Solar radiation pressure is a more complicated perturbation to detect. So far, solar radiation pressure has only been detected for very small objects ($H > 27$) that experienced Earth encounters. Thus we started selecting the smallest asteroids of the initial sample (more precisely, those with $H > 24$)

since the effect becomes larger for smaller size objects, and we tried to detect solar radiation pressure (SRP) along with the Yarkovsky parameter.

The acceleration caused by solar radiation pressure is radial and can be modelled with a single parameter A_1 ,

$$\mathbf{a}_r = A_1 g(r) \hat{\mathbf{r}}.$$

In this equation A_1 is a free parameter, and $g(r) = 1/r^2$, where r is the heliocentric distance. Physically, the value of A_1 depends mostly on the the area-to-mass ratio \mathcal{A}/M . The relation between them is the following

$$A_1 = \frac{\Phi_{\odot}}{c} \cdot C_R \cdot \mathcal{A}/M,$$

where c is the speed of light, Φ_{\odot} is the solar radiation energy flux at 1 au, whose value is $\Phi_{\odot} \simeq 1.361 \text{ kW/m}^2$, and C_R is a coefficient (of the order of 1) depending upon shape and optical properties of the surface.

The starting sample of asteroids for which we attempted an 8-dimensional fit contained 10 objects. We found four accepted detections, *i.e.*, $\text{SNR}_{A_1} \geq 3$, which are listed in Table 3.8. Notice that for three asteroids of this category, namely 2011 MD, 2012 LA, and 2015 TC₂₅, the Yarkovsky detection is not significant and thus the \mathcal{S} value, though above the threshold in one case, does not provide any information. Concerning the area-to-mass ratio we would compare the value of \mathcal{A}/M with an expected value, as we do with the secular semimajor axis drift da/dt , but this is not possible for now since the diameter is very uncertain and the other physical properties are currently unknown. Other fitted values of the area-to-mass ratio has already been determined for 2009 BD (Micheli et al. 2012), 2012 LA (Micheli et al. 2013) and 2011 MD (Micheli et al. 2014), though without including the Yarkovsky effect in the dynamical model. Asteroid 2006 RH₁₂₀ is listed separately from the others, since we consider it spurious, as we explain in what follows.

2006 RH₁₂₀. This strange detection has already been discussed in Chesley et al. (2016). Our results are very compatible with those of that chapter, and we agree with the motivations provided to reject this detection. The most likely explanation for the high transverse acceleration can be the presence of some non-conservative force, *e.g.*, mass-shedding, outgassing or micrometeorite flux, that can become as relevant as the Yarkovsky effect for objects of this size. The area-to-mass ratio, which results in a significant detection, is not compatible with the hypothesis that 2006 RH₁₂₀ is an artificial object.

3.7 Comparison with JPL results

As we already mentioned, the JPL database is regularly updated with the asteroids for which the orbital fit shows evidence of the Yarkovsky effect. The same is done for solar radiation pressure when appropriate. The results produced by two independent software sets are expected to be different, but compatible. In order to compare them we compute the relative errors

$$\varepsilon_r(A_2) := \frac{|A_2 - A_2^{\text{JPL}}|}{\sigma_{A_2}} \quad \text{and} \quad \varepsilon_r^{\text{JPL}}(A_2) := \frac{|A_2 - A_2^{\text{JPL}}|}{\sigma_{A_2, \text{JPL}}},$$

where the superscript “JPL” refers to the JPL solution. To quantify the difference between the results presented in this chapter and the JPL ones, we use the quantity

$$\chi_{A_2} := \frac{|A_2 - A_2^{\text{JPL}}|}{\sqrt{\sigma_{A_2}^2 + \sigma_{A_2, \text{JPL}}^2}}$$

from Milani et al. (2010, Sec. 7.2). We consider compatible two solutions for which $\chi_{A_2} \leq 1$.

Starting from the list of our accepted detections, we compared the results every time an asteroid is included in the JPL database of Yarkovsky effect detections. The results of the comparison are contained in Table 3.9 and 3.10. Just for five asteroids in this list both the relative errors are greater than 1, even though never above 2.5. Using the metric given by χ_{A_2} , we identify just 3 asteroids (marked with a star in Table 3.9 and 3.10) whose detections are not fully compatible with respect to our criteria. Anyway, a χ_{A_2} moderately above 1 for 3 cases out of 92 being compared shows a strong agreement between our results and the JPL’s ones.

Note that this result is not a null test, that is the expected value of the difference in the estimated values of A_2 is not zero. This because the two computations have used two different astrometric error models, Farnocchia et al. (2015b) at NEODyS and Vereš et al. (2017) at JPL. The comparative results described in the last three columns indicate an exceptionally good agreement. This agreement may be interpreted as a validation of the procedures used both at NEODyS and at JPL, both to compute the Yarkovsky effect constants and to select the cases in which the results are reliable.

The comparison was also performed for the shorter list of objects for which we have both A_2 and A_1 , that is both Yarkovsky effect and direct radiation pressure were included in the dynamical model. Table 3.11 contains the signal-to-noise ratios for both parameters in both solutions, and all the metrics for the discrepancies. Apart from the results for 2006 RH₁₂₀, which are rated as spurious, the accepted results are fully consistent.

3.8 Impact monitoring with non-gravitational parameters

A force model including non-gravitational forces is sometimes needed to make reliable impact predictions, especially if we want to extend the hazard analysis time span to longer intervals with respect to one century (the default time span adopted by the current impact monitoring systems). More precisely, the non-gravitational model plays a fundamental role also in the LOV computation and propagation (Milani et al. 2005a; Milani et al. 2005b; Milani et al. 2000). If an asteroid with a very well constrained orbit experiences a very deep close approach, the post-encounter situation is equal to the one of a poorly determined orbit, with the difference that the large uncertainty of the asteroid state is due to the divergence of nearby orbits caused by the encounter, and not to the poor constraints of the initial conditions. In this case, the initial confidence region is very small, thus the use of the linear approximation of the LOV is allowed. In case such an encounter occurs the linear LOV direction is derived by analysing that encounter and mapping back the corresponding LOV trace on the target plane (TP) (Valsecchi et al. 2003) to the space of initial conditions. This method has been used in Spoto et al. (2014) to properly assess the impact risk of (410777) 2009 FD, exploiting its 2185 scattering encounter with the Earth. The same formalism can be used even when we are not in the presence of a scattering encounter, but the close encounter is so deep that the LOV will turn out to be quite stretched at the next encounter, as in the cases analysed below.

So far, just four asteroids required such special treatment for a proper impact risk assessment, namely (101955) Bennu, (99942) Apophis, (29075) 1950 DA, and (410777) 2009 FD, but this list is expected to grow as a consequence of the work presented in this chapter. Below we show two examples of asteroids for which we found virtual impactors using a non-gravitational model and that have no possible impacts with a purely gravitational model. We are aware that such a work could be done on many asteroids with accepted Yarkovsky detections, but this is beyond the scope of this chapter.

2001 BB₁₆. Currently, this asteroid has a low MOID value, $\simeq 0.0043$ au, but no chance of impacting the Earth in the next century. 2001 BB₁₆ has a deep close approach with the Earth in 2082, which causes an increase of the stretching of two orders of magnitude with respect to the next 2086 encounter, whereas the stretching value remains essentially constant until the 2082 close approach. We used this close approach to derive the LOV direction and we performed the impact monitoring through 2200 employing

a non-gravitational model including the Yarkovsky effect. The results are shown in Table 3.12. In particular we found two VIs at the very end of the 22nd century, which we would not find with a gravity-only model.

2011 MD. This is a very small asteroid, about 6 m in diameter, as determined in Mommert et al. (2014b). In this case as well, the MOID value is very low, $\simeq 0.00036$ au and it has no virtual impactor in the next century. In 2049, this asteroid will experience two very close approaches with the Earth, causing an increase of two orders of magnitude in the stretching between these encounters and the following one in 2067. We used the first 2049 close approach (the deepest of the two) to compute the LOV direction in the space of initial conditions. We thus performed the impact monitoring using a dynamical model including both the Yarkovsky effect and solar radiation pressure. The results are shown in Table 3.13. When we only include solar radiation pressure, the orbit uncertainty shrinks and thus the number of VIs is much lower than before (see Table 3.14). Both Table 3.13 and Table 3.14 list the virtual impactors with $IP \geq 10^{-7}$, since this threshold is the completeness limit used for the LOV sampling (Del Vigna et al. 2019). It is worth noting that this asteroid is so small that it would not reach the ground in case of a real impact, because it would be burnt in the atmosphere. Therefore this case is not studied for practical purposes of planetary defense, but rather to show that, in some cases, a non-gravitational model is needed to make reliable impact predictions and also that different models of non-gravitational perturbations can give very different results.

3.9 Conclusions and future work

In this chapter we significantly increased the knowledge of non-gravitational perturbations on near-Earth asteroids, based on actual measurements, rather than on modelling. The number of significant and reliable Yarkovsky detections in the NEA catalogue is expected to grow continuously. In fact, the data volume of future surveys, the increased astrometric accuracy for optical observations, more accurate star catalogue debiasing techniques, and expanded efforts in radar astrometry provide ever better constraints to measure this small effect. We identified 86 near-Earth asteroids with significant and reliable Yarkovsky detection, thus doubling the list provided in Chesley et al. (2016). For few exceedingly small asteroids, we attempted to directly detect solar radiation pressure together with the Yarkovsky-related acceleration. For such cases, solar radiation pressure is needed to obtain a more satisfactory orbital fit.

There are several research centres handling the computation of asteroid orbits as an industrial production, like recomputing either all the orbits of more than 500,000 numbered asteroids every time a change in the error model occurs, or a large portion of them just to take into account new observations and new asteroid discoveries. There are important scientific goals such as asteroid families and impact monitoring that can only be achieved by maintaining and constantly updating such large lists of orbits.

We dedicated a significant effort in clarifying a number of marginal and/or spurious cases, not only to recover a few dubious cases but also to refine the methodology and therefore be ready for the future increase of significant detections. Indeed, the problem to be faced in the near future is not another increase by a factor two, rather an increase by orders of magnitude. The second Gaia data release (April 2018) will contain about 1.7 billion of sources brighter than magnitude 21 and $\simeq 14000$ asteroids with astrometry reaching the sub-milliarcsec accuracy in an optimal range of magnitude $G \simeq 12-17$ (Gaia Collaboration: Brown et al. 2018; Gaia Collaboration: Spoto et al. 2018). The stellar catalogue produced by Gaia will represent the starting point for a new debiasing and weighting scheme. Moreover, the combination of Gaia asteroid observations with the already available ones will produce a sharp increase in the number of objects for which the Yarkovsky effect will be detectable. Thus the challenge in works like this is not to establish a new record list of Yarkovsky and/or radiation pressure detections, but rather to develop an automated calculation of orbits with estimated non-gravitational parameters.

The computations of orbits with non-gravitational effects is still very far from being an automated process. To avoid spurious detections, we used the most recent error models for the observations and a filtering criterion, based on an estimate of the Yarkovsky effect based upon a physical model of the asteroid. Unfortunately, both of these tools are still incomplete. The error models suffer from the continued unavailability of metadata, such as the signal-to-noise of individual observations, with the result that observations with different quality are bundled together and the statistical analysis of the residuals does not yet allow a correct derivation of uncertainty of the measurement error. The physical models of asteroids, needed to estimate the expected Yarkovsky effect, are very rough approximations when the main physical data are not available, as it is the case for the majority of the asteroids in our tables. Moreover, such small perturbations can be sensitive to old isolated, and possibly bad astrometric positions.

In conclusion, we made a step in the right direction by developing and testing the use of different error models, and by using the difference in the results as an estimate of the sensitivity of the results on the error model. We

developed and tested the use of a filter for spurious cases, which is based on an estimate of the expected Yarkovsky effect, which is roughly the same as the Yarkovsky calibration used to compute the age of asteroid families Milani et al. (2014) and Spoto et al. (2015). Both tools improved our capability of obtaining a list of reliable Yarkovsky detections, as well as a much shorter list of radiation pressure detections for natural bodies.

Table 3.5. List of Yarkovsky detections with $3 \leq \text{SNR}_{A_2} < 5$ and with $S \leq 2$. The table is sorted by SNR_{A_2} , in decreasing order. Columns and symbols are the same as in Table 3.4.

Asteroid	H	A_2		SNR_{A_2}	da/dt		S	p_v	D	Tax. class
		$(10^{-15} \text{ au/d}^2)$			(10^{-4} au/My)					
(29075) 1950 DA	17.1	-6.03	\pm 1.25	4.83	-2.65	\pm 0.55	0.5	0.07	2	-
(162117) 1998 SD ₁₅	19.1	-15.55	\pm 3.28	4.74	-7.76	\pm 1.64	0.6	0.154 ^d	0.51 *	S
2001 BB ₁₆	23.0	345.54	\pm 73.84	4.68	163.59	\pm 34.96	1.3	0.154 ^d	0.086*	-
(138852) 2000 WN ₁₀	20.1	36.04	\pm 7.80	4.62	16.80	\pm 3.64	0.5	0.154 ^d	0.316*	-
(455176) 1999 VF ₂₂	20.7	-69.25	\pm 15.23	4.55	-56.46	\pm 12.41	0.8	0.154 ^d	0.248*	-
(399308) 1993 GD	20.6	102.49	\pm 22.73	4.51	43.94	\pm 9.75	0.8	0.3	0.18	-
(7336) Saunders	18.8	39.34	\pm 8.82	4.46	14.29	\pm 3.20	1.7	0.18 †	0.553*	S
(1685) Toro	14.3	-3.76	\pm 0.84	4.45	-1.68	\pm 0.38	1.1	0.26	3.75	S
(4034) Vishnu	18.3	-66.24	\pm 15.48	4.28	-34.03	\pm 7.95	1.2	0.52	0.42	-
(85774) 1998 UT ₁₈	19.1	-6.64	\pm 1.55	4.27	-2.67	\pm 0.62	0.3	0.042	0.939	C
(310442) 2000 CH ₅₉	19.8	52.16	\pm 12.25	4.26	29.04	\pm 6.82	0.8	0.154 ^d	0.366*	-
(2100) Ra-Shalom	16.2	-4.65	\pm 1.10	4.22	-2.67	\pm 0.63	0.5	0.14	2.24	C
(326354) 2000 SJ ₃₄₄	22.8	-158.81	\pm 37.77	4.20	-65.15	\pm 15.49	0.6	0.154 ^d	0.093*	-
(481442) 2006 WO ₃	21.6	-62.26	\pm 15.00	4.15	-36.97	\pm 8.90	0.4	0.154 ^d	0.164*	-
(306383) 1993 VD	21.4	-29.85	\pm 7.32	4.08	-19.46	\pm 4.77	0.2	0.154 ^d	0.174*	-
(441987) 2010 NY ₆₅	21.5	-37.87	\pm 9.28	4.08	-18.65	\pm 4.57	0.4	0.071	0.228	C
2008 CE ₁₁₉	25.6	-143.47	\pm 36.04	3.98	-57.16	\pm 14.36	0.2	0.154 ^d	0.026*	-
(85953) 1999 FK ₂₁	18.1	-9.85	\pm 2.49	3.95	-9.63	\pm 2.44	0.5	0.32	0.59	S
(348306) 2005 AY ₂₈	21.6	-91.12	\pm 23.12	3.94	-61.39	\pm 15.58	0.7	0.154 ^d	0.166*	-
(65679) 1989 UQ	19.4	-37.59	\pm 9.74	3.86	-17.95	\pm 4.65	1.6	0.033	0.918	C
1995 CR	21.7	-85.94	\pm 22.44	3.83	-155.89	\pm 40.71	1.0	0.18 †	0.143*	S
(232691) 2004 AR ₁	19.8	-116.25	\pm 30.33	3.83	-50.45	\pm 13.16	1.9	0.154 ^d	0.369*	-
(265482) 2005 EE	21.2	93.97	\pm 24.62	3.82	42.07	\pm 11.02	0.8	0.154 ^d	0.197*	-
(136818) Selqet	19.0	24.44	\pm 6.42	3.81	12.18	\pm 3.20	0.6	0.15 †	0.548*	X
(425755) 2011 CP ₄	21.1	52.62	\pm 13.99	3.76	96.46	\pm 25.65	0.5	0.154 ^d	0.201*	-
(192559) 1998 VO	20.4	-33.01	\pm 8.81	3.75	-14.25	\pm 3.80	0.6	0.28	0.216	S
(163023) 2001 XU ₁	19.2	47.27	\pm 12.70	3.72	32.04	\pm 8.61	1.0	0.154 ^d	0.479*	-
(5604) 1992 FE	17.2	-24.03	\pm 6.61	3.64	-12.68	\pm 3.49	1.2	0.48	0.55	V
(397326) 2006 TC ₁	19.0	33.65	\pm 9.23	3.65	12.68	\pm 3.48	0.8	0.154 ^d	0.54 *	-
(208023) 1999 AQ ₁₀	20.4	-44.41	\pm 12.21	3.64	-20.66	\pm 5.68	1.0	0.154 ^d	0.281*	S
(437841) 1998 HD ₁₄	20.9	-87.22	\pm 24.35	3.58	-41.83	\pm 11.68	1.4	0.18 †	0.205*	Q
(413260) 2003 TL ₄	19.5	-36.09	\pm 10.21	3.53	-20.36	\pm 5.76	0.6	0.22	0.38	-
(4581) Asclepius	20.7	-40.76	\pm 11.76	3.47	-19.62	\pm 5.66	0.4	0.154 ^d	0.241*	-
(136582) 1992 BA	19.9	-54.38	\pm 16.17	3.36	-20.03	\pm 5.96	0.9	0.154 ^d	0.363*	-
(467351) 2003 KO ₂	20.4	97.34	\pm 28.27	3.44	65.59	\pm 19.05	1.2	0.154 ^d	0.277*	-
(7341) 1991 VK	16.8	-6.04	\pm 1.84	3.29	-2.54	\pm 0.77	0.6	0.18 †	1.344*	S
(256004) 2006 UP	23.0	-174.21	\pm 53.10	3.28	-64.61	\pm 19.69	0.6	0.154 ^d	0.084*	-
(450300) 2004 QD ₁₄	20.6	-116.65	\pm 35.73	3.26	-57.61	\pm 17.65	1.3	0.154 ^d	0.263*	-
(477719) 2010 SG ₁₅	25.2	-237.31	\pm 74.49	3.19	-90.57	\pm 28.43	0.3	0.154 ^d	0.031*	-
(37655) Illapa	17.8	-13.41	\pm 4.26	3.15	-10.81	\pm 3.43	0.6	0.154 ^d	0.938*	-
(267759) 2003 MC ₇	18.7	-29.24	\pm 9.36	3.12	-10.97	\pm 3.51	0.8	0.154 ^d	0.611*	-
(310842) 2003 AK ₁₈	19.7	-33.50	\pm 10.94	3.06	-17.83	\pm 5.82	0.6	0.154 ^d	0.385*	-
(162783) 2000 YJ ₁₁	20.6	-127.26	\pm 42.13	3.02	-49.85	\pm 16.50	1.4	0.154 ^d	0.257*	-
(152671) 1998 HL ₃	20.1	-55.64	\pm 18.40	3.02	-25.68	\pm 8.49	0.7	0.2	0.298	-

Table 3.6. List of rejected Yarkovsky detections. Each group of asteroids in the table is sorted by SNR_{A_2} , in decreasing order. The columns are the same as in Table 3.4, but the one showing da/dt .

Asteroid	H	A_2 (10^{-15} au/d ²)		SNR_{A_2}	S	p_v	D (km)	Tax. class
(4179) Toutatis	15.2	-5.95	\pm 0.65	9.20	2.1	0.13	4.45	S
(4015) Wilson-Harrington	16.0	-16.48	\pm 7.16	2.30	2.9	0.046	3.821	C
(260141) 2004 QT ₂₄	18.3	530.90	\pm 53.46	9.93	20.8	0.42	0.454*	S
(350751) 2002 AW	20.7	-579.13	\pm 116.36	4.98	6.5	0.154 ^d	0.243*	B
(39565) 1992 SL	18.4	-100.52	\pm 20.41	4.92	3.1	0.154 ^d	0.698*	-
(4486) Mithra	15.4	-83.37	\pm 18.47	4.51	12.9	0.297	1.849	V
(474158) 1999 FA	20.6	-93.01	\pm 22.25	4.18	1.7	0.18 [†]	0.233*	S
(162421) 2000 ET ₇₀	18.0	-33.73	\pm 10.80	3.12	3.4	0.15 [†]	2.26	-
(308635) 2005 YU ₅₅	21.6	-317.23	\pm 60.43	5.25	4.5	0.065	0.306	C
(139359) 2001 ME ₁	16.6	-307.68	\pm 60.74	5.07	45.0	0.04	3.15 *	C
(433) Eros	10.8	-1.96	\pm 0.40	4.96	2.7	0.25	16.84	S
(175706) 1996 FG ₃	18.3	-55.77	\pm 12.90	4.32	3.1	0.072	1.196	C
2010 KP ₁₀	23.4	2981.28	\pm 915.15	3.26	11.4	0.101	0.087	-
(142561) 2002 TX ₆₈	18.1	-466.98	\pm 153.85	3.04	35.3	0.154 ^d	0.801*	Xe
(192563) 1998 WZ ₆	17.3	-54.76	\pm 18.17	3.01	3.7	0.30	0.8	V

Table 3.7. List of marginal significance detections, which means $2.5 < \text{SNR}_{A_2} < 3$ and $S \leq 2$. The table is sorted by SNR_{A_2} , in decreasing order (apart from the two special cases at the top). Columns and symbols are the same as in Table 3.4.

Asteroid	H	A_2 (10^{-15} au/d ²)		SNR_{A_2}	da/dt (10^{-4} au/My)	S	p_v	D (km)	Tax. class
(99942) Apophis	18.9	-53.39	\pm 29.60	1.80	-24.50 \pm 13.58	1.6	0.30	0.375	S
(410777) 2009 FD	22.1	21.49	\pm 47.40	0.45	11.18 \pm 24.66	0.4	0.01	0.472	-
(162080) 1998 DG ₁₆	19.8	-37.93	\pm 12.84	2.95	-19.51 \pm 6.61	1.4	0.035	0.777	C
(85770) 1998 UP ₁	20.4	-34.77	\pm 11.84	2.94	-16.77 \pm 5.71	0.8	0.154 ^d	0.282*	S
(162142) 1998 VR	18.7	17.59	\pm 5.98	2.94	8.88 \pm 3.02	0.8	0.18 [†]	0.6	S
2002 LY ₁	22.4	-166.14	\pm 57.73	2.88	-84.31 \pm 29.30	0.8	0.154 ^d	0.114*	-
(474163) 1999 SO ₅	20.9	-79.89	\pm 27.78	2.88	-32.69 \pm 11.37	0.8	0.154 ^d	0.22 *	-
(242191) 2003 NZ ₆	19.0	38.23	\pm 13.29	2.88	24.07 \pm 8.37	0.6	0.334	0.370	-
(215588) 2003 HF ₂	19.4	-79.07	\pm 27.60	2.87	-58.53 \pm 20.43	1.7	0.118	0.488	-
(162181) 1999 LF ₆	18.2	-22.41	\pm 7.86	2.85	-8.70 \pm 3.05	1.3	0.175	0.729	S
(164207) 2004 GU ₉	21.1	-69.93	\pm 24.83	2.82	-30.24 \pm 10.74	0.5	0.219	0.163	-
2001 QC ₃₄	20.1	-73.87	\pm 26.33	2.81	-30.61 \pm 10.91	1.9	0.154 ^d	0.329*	Q
(283457) 2001 MQ ₃	18.9	-38.45	\pm 13.73	2.80	-13.80 \pm 4.93	0.9	0.154 ^d	0.56 *	-
2007 PB ₈	21.2	-160.83	\pm 58.50	2.75	-90.77 \pm 33.01	1.4	0.154 ^d	0.198*	-
(230111) 2001 BE ₁₀	19.2	-28.81	\pm 10.72	2.69	-15.61 \pm 5.81	0.9	0.253	0.4	S
1999 SK ₁₀	19.7	-45.84	\pm 17.24	2.66	-18.21 \pm 6.85	1.0	0.346	0.259	S
(338292) 2002 UA ₃₁	19.0	-35.78	\pm 13.48	2.65	-22.29 \pm 8.40	0.8	0.154 ^d	0.538*	-
(334412) 2002 EZ ₂	20.1	-119.39	\pm 45.75	2.61	-45.46 \pm 17.42	1.1	0.40	0.21	-
(376879) 2001 WW ₁	22.0	-63.88	\pm 24.83	2.57	-25.03 \pm 9.73	0.4	0.154 ^d	0.135*	-
(416151) 2002 RQ ₂₅	20.6	55.10	\pm 21.64	2.55	24.49 \pm 9.62	0.7	0.154 ^d	0.262*	C
(503941) 2003 UV ₁₁	19.5	6.66	\pm 2.63	2.53	5.62 \pm 2.22	0.1	0.376	0.26	Q
(471240) 2011 BT ₁₅	21.7	-196.07	\pm 77.53	2.53	-80.55 \pm 31.85	1.3	0.154 ^d	0.154*	-
1994 CJ ₁	21.5	-138.42	\pm 55.12	2.51	-53.87 \pm 21.45	1.0	0.154 ^d	0.167*	-
(54509) YORP	22.6	-74.61	\pm 29.88	2.50	-33.45 \pm 13.40	0.6	0.154 ^d	0.1	S

Table 3.8. List of detections including both the Yarkovsky effect and solar radiation pressure, that is the set of asteroids for which the parameter A_1 was reliably determined with a signal-to-noise ratio $\text{SNR}_{A_1} > 3$.

Asteroid	A_2 (10^{-15} au/d ²)		SNR_{A_2}	S	A_1 (10^{-15} au/d ²)		SNR_{A_1}	A/M (m ² /ton)	D (m)
2009 BD	-1152	± 82	14.0	0.2	57 663	± 8674	6.7	0.3	4
2012 LA	-4907	± 12 832	0.4	2.2	81 216	± 16 312	5.0	0.4	10*
2011 MD	-2006	± 3049	0.7	0.5	75 074	± 24 396	3.1	0.3	6
2015 TC ₂₅	-4433	± 2754	1.6	1.4	160 079	± 20 065	8.0	0.7	3*
2006 RH ₁₂₀	-50 469	± 3787	13.3	9.0	124 099	± 4747	26.1	0.6	4*

Table 3.9. Comparison between the accepted results of this chapter ($\text{SNR}_{A_2} \geq 5$) and the JPL ones. The columns contain the asteroid name, the signal-to-noise ratio of our solution and of the JPL one, the ratio $\sigma_{A_2, \text{JPL}}/\sigma_{A_2}$ of the A_2 uncertainties as estimated by the two systems, the relative errors computed with our A_2 uncertainty and with the JPL A_2 uncertainty respectively, and the χ_{A_2} value.

Asteroid	SNR_{A_2}	$\text{SNR}_{A_2}^{\text{JPL}}$	$\sigma_{A_2, \text{JPL}}/\sigma_{A_2}$	$\varepsilon_r(A_2)$	$\varepsilon_r^{\text{JPL}}(A_2)$	χ_{A_2}	
(101955) Benu	192.50	182.10	1.06	0.23	0.22	0.173	
(480883) 2001 YE ₄	114.54	72.38	1.58	0.29	0.18	0.149	
(2340) Hathor	25.37	24.29	1.06	0.29	0.28	0.204	
(483656) 2005 ES ₇₀	25.08	18.39	1.39	0.40	0.29	0.236	
(152563) 1992 BF	21.24	27.49	0.81	1.05	1.30	0.816	
2012 BB ₁₂₄	17.57	9.00	1.86	0.83	0.45	0.392	
(85990) 1999 JV ₆	13.98	12.58	1.22	1.37	1.12	0.869	
(437844) 1999 MN	10.46	8.42	1.17	0.59	0.50	0.381	
(480808) 1994 XL ₁	10.37	11.81	0.93	0.61	0.66	0.446	
2007 TF ₆₈	10.28	6.02	1.55	0.95	0.62	0.517	
(1566) Icarus	9.62	3.79	2.10	1.64	0.78	0.705	
(138175) 2000 EE ₁₀₄	8.96	6.86	1.20	0.72	0.60	0.460	
(1862) Apollo	8.81	7.23	1.12	0.71	0.63	0.476	
(2062) Aten	8.61	7.34	1.07	0.79	0.74	0.541	
(468468) 2004 KH ₁₇	8.15	6.55	1.28	0.27	0.21	0.167	
(162004) 1991 VE	8.05	6.10	1.14	1.07	0.93	0.704	
2006 TU ₇	7.73	5.58	1.40	0.08	0.06	0.045	
2011 PU ₁	7.56	6.00	1.01	1.52	1.51	1.074	*
(6489) Golevka	7.21	7.91	0.87	0.32	0.36	0.239	
2011 EP ₅₁	7.01	6.46	0.98	0.71	0.72	0.505	
(33342) 1998 WT ₂₄	6.88	5.27	1.22	0.43	0.35	0.273	
(3361) Orpheus	6.77	7.10	1.09	0.99	0.91	0.668	
(364136) 2006 CJ	6.45	8.26	0.74	0.32	0.44	0.261	
(499998) 2011 PT	6.32	7.40	0.81	0.30	0.37	0.236	
(138404) 2000 HA ₂₄	6.30	2.05	2.82	0.53	0.19	0.177	
2006 CT	6.22	5.82	0.99	0.45	0.45	0.319	
(3908) Nyx	6.06	4.62	1.29	0.08	0.06	0.047	
(363599) 2004 FG ₁₁	5.89	3.81	1.56	0.05	0.03	0.027	
1999 UQ	5.88	3.39	1.87	0.43	0.23	0.205	
2003 YL ₁₁₈	5.87	4.71	1.18	0.32	0.28	0.210	
(154590) 2003 MA ₃	5.87	4.75	1.19	0.25	0.21	0.159	
2005 EY ₁₆₉	5.78	4.29	1.22	0.57	0.47	0.360	
(10302) 1989 ML	5.73	4.58	1.02	1.06	1.03	0.738	
2000 PNs	5.56	5.43	1.07	0.25	0.23	0.172	
(506590) 2005 XB ₁	5.28	5.59	1.09	0.78	0.72	0.531	
(216523) 2001 HY ₇	5.21	4.52	1.09	0.29	0.27	0.198	
(350462) 1998 KG ₃	5.20	5.75	0.89	0.11	0.12	0.079	
(363505) 2003 UC ₂₀	5.19	2.57	1.22	2.06	1.68	1.302	*
(99907) 1989 VA	5.18	3.63	1.30	0.45	0.34	0.273	
(66400) 1999 LT ₇	5.17	4.37	1.20	0.06	0.05	0.037	
(377097) 2002 WQ ₄	5.13	3.93	1.32	0.05	0.04	0.029	
2000 CK ₅₉	5.10	5.76	0.87	0.10	0.11	0.074	

Table 3.10. Comparison between the accepted results of this chapter ($\text{SNR}_{A_2} < 5$) and the JPL ones. The columns are the same of Table 3.9.

Asteroid	SNR_{A_2}	$\text{SNR}_{A_2}^{\text{JPL}}$	$\sigma_{A_2, \text{JPL}} / \sigma_{A_2}$	$\varepsilon_r(A_2)$	$\varepsilon_r^{\text{JPL}}(A_2)$	χ_{A_2}
(29075) 1950 DA	4.82	4.17	1.03	0.51	0.49	0.351
(162117) 1998 SD ₁₅	4.74	4.35	1.23	0.62	0.51	0.394
2001 BB ₁₆	4.68	4.86	1.14	0.86	0.75	0.567
(138852) 2000 WN ₁₀	4.62	4.29	1.04	0.17	0.16	0.116
(455176) 1999 VF ₂₂	4.55	3.99	1.27	0.51	0.40	0.313
(399308) 1993 GD	4.51	4.45	0.98	0.17	0.17	0.120
(1685) Toro	4.48	4.33	0.85	0.81	0.95	0.618
(7336) Saunders	4.46	2.76	1.22	1.08	0.89	0.686
(4034) Vishnu	4.28	4.31	1.15	0.66	0.57	0.433
(85774) 1998 UT ₁₈	4.28	3.44	1.11	0.48	0.44	0.325
(310442) 2000 CH ₅₉	4.26	2.60	1.38	0.68	0.50	0.402
(2100) Ra-Shalom	4.23	3.10	1.14	0.69	0.61	0.456
(326354) 2000 SJ ₃₄₄	4.20	6.92	0.65	0.28	0.44	0.237
(481442) 2006 WO ₃	4.15	3.97	0.94	0.41	0.44	0.300
(441987) 2010 NY ₆₅	4.08	3.88	1.03	0.07	0.07	0.047
(306383) 1993 VD	4.08	1.61	1.35	1.91	1.42	1.137
2008 CE ₁₁₉	3.98	3.43	1.57	1.41	0.90	0.756
(85953) 1999 FK ₂₁	3.96	4.94	0.89	0.44	0.49	0.327
(348306) 2005 AY ₂₈	3.94	4.23	0.75	0.76	1.01	0.606
(65679) 1989 UQ	3.86	3.74	1.07	0.14	0.13	0.097
(232691) 2004 AR ₁	3.83	2.28	1.08	1.38	1.29	0.942
1995 CR	3.83	2.23	1.42	0.65	0.46	0.374
(265482) 2005 EE	3.82	1.58	1.48	1.46	0.99	0.818
(136818) Selqet	3.81	2.08	1.37	0.96	0.70	0.566
(425755) 2011 CP ₄	3.76	3.37	1.24	0.40	0.33	0.254
(192559) 1998 VO	3.75	3.77	0.92	0.26	0.29	0.194
(163023) 2001 XU ₁	3.72	2.94	1.05	0.63	0.60	0.432
(397326) 2006 TC ₁	3.65	3.45	0.98	0.26	0.27	0.188
(208023) 1999 AQ ₁₀	3.64	2.27	1.14	1.05	0.93	0.696
(5604) 1992 FE	3.64	3.46	1.24	0.64	0.52	0.402
(437841) 1998 HD ₁₄	3.58	3.26	0.87	0.73	0.84	0.551
(413260) 2003 TL ₄	3.53	2.85	1.02	0.61	0.60	0.429
(4581) Asclepius	3.47	2.57	1.20	0.39	0.32	0.247
(467351) 2003 KO ₂	3.44	2.93	1.34	0.49	0.37	0.294
(136582) 1992 BA	3.36	3.43	1.18	0.70	0.59	0.449
(256004) 2006 UP	3.28	3.65	0.95	0.18	0.19	0.133
(7341) 1991 VK	3.28	3.72	1.07	0.68	0.64	0.465
(450300) 2004 QD ₁₄	3.26	1.99	2.03	0.78	0.38	0.342
(477719) 2010 SG ₁₅	3.19	2.78	1.01	0.39	0.38	0.272
(37655) Illapa	3.15	2.67	1.14	0.10	0.09	0.065
(267759) 2003 MC ₇	3.12	3.57	0.87	0.01	0.02	0.010
(310842) 2003 AK ₁₈	3.06	2.60	1.31	0.35	0.27	0.214
(162783) 2000 YJ ₁₁	3.02	3.38	0.94	0.16	0.17	0.114
(152671) 1998 HL ₃	3.02	3.16	0.98	0.06	0.06	0.042
(85770) 1998 UP ₁	2.94	3.01	1.42	1.34	0.94	0.771
(474163) 1999 SO ₅	2.88	3.51	1.02	0.72	0.70	0.501
(283457) 2001 MQ ₃	2.80	3.91	0.87	0.61	0.70	0.462
(376879) 2001 WW ₁	2.57	3.07	0.76	0.24	0.31	0.188
(99942) Apophis	1.80	2.54	0.74	0.09	0.12	0.069
(410777) 2009 FD	0.45	0.04	1.22	0.51	0.42	0.321

Table 3.11. Results of the comparison between the estimated values of A_2 and A_1 , as contained in this chapter and in the JPL database. In particular, the columns contain the asteroid name, the signal-to-noise ratio of our A_2 solution and of the JPL one, the signal-to-noise ratio of our A_1 solution and of the JPL one, the relative error in the A_2 parameter computed with our A_2 uncertainty and with the JPL A_2 uncertainty respectively, the relative error in the A_1 parameter computed with our A_1 uncertainty and with the JPL A_1 uncertainty respectively, the χ -value for A_2 and for A_1 .

Asteroid	SNR_{A_2}	$\text{SNR}_{A_2}^{\text{JPL}}$	SNR_{A_1}	$\text{SNR}_{A_1}^{\text{JPL}}$	$\varepsilon_r(A_2)$	$\varepsilon_r^{\text{JPL}}(A_2)$	$\varepsilon_r(A_1)$	$\varepsilon_r^{\text{JPL}}(A_1)$	χ_{A_2}	χ_{A_1}
2009 BD	14.0	13.9	6.7	6.3	0.12	0.12	0.44	0.45	0.084	0.315
2012 LA	0.4	0.3	5.0	6.9	0.22	0.37	0.04	0.05	0.189	0.029
2011 MD	0.7	0.3	3.1	3.1	0.32	0.25	0.11	0.10	0.198	0.074
2015 TC ₂₅	1.6	1.6	8.0	7.6	0.06	0.05	0.11	0.11	0.039	0.076
2006 RH ₁₂₀	13.3	11.1	26.1	23.4	0.16	0.13	1.62	1.36	0.100	1.043

Table 3.12. Impact monitoring of asteroid 2001 BB₁₆ with a non-gravitational model that includes the Yarkovsky effect. Table columns: calendar date (year, month, and day) for the potential impact for asteroid 2011 MD, approximate σ value of the virtual impactor location along the LOV, minimum distance (the lateral distance from the LOV to the centre of the Earth on the TP confidence region), stretching (how much the confidence region at the epoch has been stretched by the time of impact), probability of Earth impact (IP), and Palermo Scale (PS). The width of the TP confidence region is always few km, thus not reported.

Date	σ	Distance (R_{\oplus})	Stretching (R_{\oplus})	IP	PS
2195/01/15.525	-3.404	3.17	$5.20 \cdot 10^3$	$2.91 \cdot 10^{-7}$	-6.35
2199/01/15.844	-3.164	2.10	$8.36 \cdot 10^4$	$5.02 \cdot 10^{-8}$	-7.12

Table 3.13. Impact monitoring of asteroid 2011 MD with a non-gravitational model that includes both the Yarkovsky effect and solar radiation pressure. Columns as in Table 3.12.

Date	σ	Distance (R_{\oplus})	Stretching (R_{\oplus})	IP	PS
2083/06/13.856	2.720	6.44	$2.86 \cdot 10^4$	$3.54 \cdot 10^{-7}$	-8.29
2098/06/07.618	0.428	6.38	$9.00 \cdot 10^5$	$4.33 \cdot 10^{-7}$	-8.29
2099/06/08.786	0.370	5.68	$3.70 \cdot 10^5$	$1.32 \cdot 10^{-6}$	-7.81
2102/06/13.699	-0.250	6.40	$5.23 \cdot 10^4$	$7.61 \cdot 10^{-6}$	-7.06
2110/05/28.604	-0.993	5.52	$1.48 \cdot 10^6$	$2.09 \cdot 10^{-7}$	-8.66
2113/06/09.765	0.330	4.09	$9.48 \cdot 10^5$	$6.90 \cdot 10^{-7}$	-8.15
2116/06/08.850	0.258	6.37	$2.61 \cdot 10^6$	$1.57 \cdot 10^{-7}$	-8.81
2116/06/08.870	0.258	6.24	$3.78 \cdot 10^6$	$1.14 \cdot 10^{-7}$	-8.95
2118/06/07.317	0.472	6.12	$1.52 \cdot 10^6$	$2.65 \cdot 10^{-7}$	-8.59
2118/06/10.605	1.496	4.80	$3.54 \cdot 10^5$	$5.66 \cdot 10^{-7}$	-8.26
2119/06/14.086	-0.670	6.55	$3.30 \cdot 10^4$	$9.22 \cdot 10^{-6}$	-7.05
2119/06/14.181	-0.670	1.70	$9.79 \cdot 10^5$	$6.57 \cdot 10^{-7}$	-8.20
2120/06/04.434	0.520	5.51	$3.44 \cdot 10^6$	$1.69 \cdot 10^{-7}$	-8.79
2122/06/11.859	1.223	5.48	$1.25 \cdot 10^6$	$2.07 \cdot 10^{-7}$	-8.72
2123/06/08.803	0.416	4.78	$1.28 \cdot 10^6$	$4.34 \cdot 10^{-7}$	-8.40
2132/06/09.046	0.184	6.30	$3.78 \cdot 10^6$	$1.13 \cdot 10^{-7}$	-9.02
2137/06/11.124	1.218	6.18	$2.09 \cdot 10^6$	$1.01 \cdot 10^{-7}$	-9.08
2139/06/12.675	1.240	5.83	$8.80 \cdot 10^5$	$2.58 \cdot 10^{-7}$	-8.68
2140/06/12.052	1.301	4.52	$7.04 \cdot 10^5$	$3.98 \cdot 10^{-7}$	-8.50
2151/06/12.350	-0.796	6.93	$1.66 \cdot 10^6$	$1.20 \cdot 10^{-7}$	-9.05
2151/06/12.604	-0.732	6.44	$2.90 \cdot 10^6$	$1.05 \cdot 10^{-7}$	-9.11
2151/06/12.780	-0.762	2.96	$3.16 \cdot 10^6$	$1.76 \cdot 10^{-7}$	-8.89
2155/06/11.940	-0.439	6.54	$5.27 \cdot 10^4$	$5.87 \cdot 10^{-6}$	-7.37
2155/06/11.984	-0.436	2.86	$2.98 \cdot 10^5$	$2.29 \cdot 10^{-6}$	-7.78
2155/06/12.054	-0.439	2.92	$8.38 \cdot 10^4$	$8.04 \cdot 10^{-6}$	-7.24
2155/06/12.168	-0.437	7.06	$1.96 \cdot 10^4$	$1.44 \cdot 10^{-5}$	-6.98
2158/06/11.842	-2.091	7.19	$2.80 \cdot 10^5$	$1.19 \cdot 10^{-7}$	-9.08
2182/06/09.849	0.041	4.51	$5.95 \cdot 10^6$	$1.09 \cdot 10^{-7}$	-9.18

Table 3.14. Impact monitoring of asteroid 2011 MD with a non-gravitational model including solar radiation pressure only. Columns as in Table 3.12.

Date	σ	Distance (R_{\oplus})	Stretching (R_{\oplus})	IP	PS
2133/12/05.197	-0.476	0.27	$1.98 \cdot 10^6$	$3.58 \cdot 10^{-7}$	-8.52
2140/11/25.578	-0.352	4.66	$5.53 \cdot 10^6$	$1.12 \cdot 10^{-7}$	-9.05
2147/11/27.042	0.212	4.79	$1.17 \cdot 10^5$	$5.13 \cdot 10^{-6}$	-7.41
2168/05/22.293	0.081	4.70	$2.13 \cdot 10^6$	$2.87 \cdot 10^{-7}$	-8.72
2169/11/26.849	-0.053	5.48	$1.92 \cdot 10^6$	$2.76 \cdot 10^{-7}$	-8.74
2186/11/21.935	-0.633	6.87	$1.56 \cdot 10^6$	$1.46 \cdot 10^{-7}$	-9.06

Chapter 4

Completeness of Impact Monitoring

Some asteroids with an Earth-crossing orbit may impact our planet. A crucial issue is to be able to identify the cases that could have a threatening Earth close encounter within a century, as soon as new asteroids are discovered or as new observations are added to prior discoveries. The main goal of impact monitoring is to solicit astrometric follow-up to either confirm or more likely dismiss the announced risk cases, *i.e.*, asteroids having some virtual impactors (Milani et al. 2000). This is achieved by communicating the impact date, the impact probability and the estimated impact energy.

This activity requires an automated system that continually monitors the Near-Earth Asteroids (NEAs) catalogue. CLOMON-2 and Sentry¹ are two independent impact monitoring systems that have been operational at the University of Pisa since 1999 and at JPL since 2002, providing the list of asteroids with a non-zero probability to impact the Earth within a century (Milani et al. 2005b). There is a constant comparison between the results of the two systems and, as required by the International Astronomical Union, the results are carefully cross-checked before any public announcement of an impact risk above an agreed level, as measured by the Palermo Scale (Chesley et al. 2002). There is a probability threshold called *generic completeness limit* that the two systems set as a goal. Above this threshold the search for impact possibility has to be complete, that is every virtual impactor (*i.e.*, each connected set of initial conditions leading to a collision with a planet) with an impact probability greater than the completeness limit has to be detected. Desirably, the generic completeness levels of the two concurrent impact monitoring systems need to be as close as possible, in order to have a common threshold down to which the two systems can be compared.

¹<http://cneos.jpl.nasa.gov/sentry/>

Since the generic completeness limit is a theoretical quantity, defined under some simplified assumptions, the level of completeness actually reached by the system has to be measured *a posteriori*. If the generic completeness limit in impact probability is somewhat lower than the actual level achieved, it means that there is a loss of efficiency in the VI search, that is some VI which could in theory be detected is missed in the scan. Finding possible causes and trying to decrease the number of missed VIs leads to an improvement of the whole system, filling as much as possible the gap between the two completeness limits. There are two methods to measure this quantity: the first is based on an empirical law to model the number of virtual impactors as a function of the impact probability; the second is a direct comparison with the results of an other independent system, namely Sentry, since we do not have a “ground truth”, that is a practical way to generate an absolutely complete list of all possible VIs above a given impact probability IP . We analysed the results of the application of our method by exploiting both the techniques.

4.1 Generic completeness definition

This chapter is focused on the completeness of impact monitoring, that is on the completeness of the VI search. The *completeness limit* can be formally defined as the highest impact probability VI that can escape the detection. Given the complexity of the problem of impact monitoring, this completeness cannot be computed and thus we use an approximate definition, which assumes idealized circumstances. The *generic completeness limit* is the highest impact probability VI that could possibly escape detection, if the associated return on the target plane is fully linear (Milani et al. 2005b), that is under the hypothesis of full linearity of the map \mathbf{f} introduced in Section 1.5.3. Under this generic assumption the trace of the VAs on the target plane is simply a straight line on the TP: if there is a VI, this line intersects the impact cross section D on the TP in a chord of the circle bounding D .

For a VI to be detectable by the system, at least one LOV orbit has to cross the target plane. For now, we make the assumption that one point on the TP is sufficient for the VI detection (see Section 4.3 for a discussion on this choice). The stretching is a key quantity to estimate the number of LOV orbits that intersects the target plane of a given encounter: the higher is the stretching, the greater is the separation between two consecutive points on the TP. In particular, if the stretching becomes too high, the separation on the TP could exceed the diameter $2R_{TP}$ of the TP itself, thus no point crosses the TP and the virtual impactor is not detected with certainty. As a consequence, to have at least one point on the TP, the stretching cannot

exceed a maximum value S_{max} . Assuming a uniform step-size $\Delta\sigma$ for the LOV sampling, the condition $S \cdot \Delta\sigma \leq 2R_{TP}$ must hold, which implies

$$S \leq \frac{2R_{TP}}{\Delta\sigma} =: S_{max}. \quad (4.1)$$

We now convert the previous inequality into a condition concerning the impact probability. We can define a probability density function on the LOV as the restriction of the Gaussian probability density function defined on the orbital elements space². This density is

$$p(\sigma) := \frac{1}{\sqrt{2\pi}} e^{-\frac{\sigma^2}{2}}, \quad (4.2)$$

where σ is the LOV parameter. Under our assumptions, the impact probability of the VI is given by integrating $p(\sigma)$ over the inverse image of the diametrical chord contained in the LOV projection on the TP. The integration domain is an interval in the σ -space: assuming that stretching is S , its length is given by $2b_{\oplus}/S$. As a consequence, the following estimation holds:

$$IP \simeq \frac{2b_{\oplus}}{S} \cdot p(0) \geq \frac{1}{\sqrt{2\pi}} \frac{2b_{\oplus}}{S_{max}} = \frac{\Delta\sigma}{\sqrt{2\pi}} \cdot \frac{b_{\oplus}}{R_{TP}}.$$

where b_{\oplus} is the radius of the Earth impact cross section on the TP, which takes into account the gravitational focusing (Valsecchi et al. 2003). Since the generic completeness limit IP^* is the minimum impact probability of a VI for which condition (4.1) is satisfied, we have

$$IP^* := \frac{\Delta\sigma}{\sqrt{2\pi}} \cdot \frac{b_{\oplus}}{R_{TP}}.$$

This quantity depends on the amount of gravitational focusing, and can be higher for asteroids with a low velocity at infinity. To obtain a uniform threshold, we can use a typical value for b_{\oplus} , *e.g.*, $b_{\oplus} = 2R_{\oplus}$. This is an approximation, but we need to chose a fixed value applicable to all asteroids with VIs, thus we are using a value appropriate for low relative velocity NEA, taking into account that these have larger probability of having VIs. In this way we have an approximated value for the generic completeness limit:

$$IP^* = \frac{\Delta\sigma}{\sqrt{2\pi}} \cdot \frac{2R_{\oplus}}{R_{TP}}. \quad (4.3)$$

²The probability density defined on the orbital elements space is the propagation of the Gaussian density assumed for the residuals, and it is Gaussian with mean \mathbf{x}^* (the nominal solution) and covariance matrix $\Gamma = \Gamma(\mathbf{x}^*)$, the covariance matrix of the orbit determination least squares fit (Milani et al. 2010).

With the previous simple equation we can provide an estimate of the completeness reached by CLOMON-2 while it was operating with a uniform LOV sampling. As shown in Milani et al. (2005b), we obtain³

$$IP^* \simeq 4.24 \cdot 10^{-7},$$

corresponding to a maximum stretching value of $S_{max} = 3.8 \cdot 10^6 R_{\oplus}$. In the case at least two points on the TP are required for the detection of a VI, the generic completeness limit IP^* would be simply twice as much.

4.2 An optimal method for LOV sampling

Before the switch to the new method presented in this chapter, CLOMON-2 performed the LOV sampling by means of uniformly spaced points in the parameter σ , and over the interval $|\sigma| \leq 3$. Since the probability density on the LOV is the Gaussian defined by (4.2), a uniform step in σ is not optimal because the probability of each sampling interval is too high around $\sigma = 0$, whereas it becomes too low near the LOV endpoints. This is the reason to use a step-size that is inversely proportional to the probability density. The new sampling is such that the probability of the interval among two consecutive points of the sampling is constant. It means that if $\{\sigma_i\}_{i=1, \dots, N}$ are the sampling nodes, then

$$\mathbb{P}([\sigma_i, \sigma_{i+1}]) := \int_{\sigma_i}^{\sigma_{i+1}} p(\sigma) d\sigma$$

is constant, *i.e.*, it does not depend on i . As a consequence, the sample points will be more dense around the value $\sigma = 0$ (nominal solution) whereas they become more sparse moving towards the tips. Furthermore, to avoid too long intervals at LOV tails, when the interval length exceeds a certain threshold $\Delta\sigma_{max}$ the sampling becomes uniform to the threshold value. This technical detail is needed to bound the step-size, since too large values of $\Delta\sigma$ could result in divergence of the algorithms to find VIs, effectively cutting the LOV tails out from the analysis. To avoid this loss and also to keep a better control of the cases in which a geometrically large VI occurs for large values of σ , the sampling interval has been extended to $|\sigma| \leq \sigma_{max} = 5$ (and also to cover the same interval as JPL's Sentry system).

We now derive a condition for the step-size to guarantee a constant probability to each sampling interval. This is achieved by repeating the

³The TP radius adopted for the close approaches detection was $R_{TP} = 0.2 \text{ au} \simeq 4700 R_{\oplus}$, the LOV sampling was performed with 2401 virtual asteroids over the interval $|\sigma| \leq 3$, thus $\Delta\sigma = 0.0025$.

same argument of Section 4.1, not around the nominal solution, but around the VA corresponding to a generic σ value. In particular, to have at least one point on the TP corresponding to the LOV parameter σ , the stretching must satisfy the condition

$$S(\sigma) \leq \frac{2R_{TP}}{\Delta\sigma(\sigma)} =: S_{max}(\sigma).$$

Under linearity assumptions, the impact probability of the VI around the value σ of the LOV parameter is given by

$$IP(\sigma) \simeq \frac{2b_{\oplus}}{S(\sigma)} \cdot p(\sigma) \geq \frac{2b_{\oplus}}{S_{max}(\sigma)} \cdot p(\sigma).$$

We can define

$$IP^*(\sigma) := \frac{b_{\oplus}}{R_{TP}} \Delta\sigma(\sigma) \cdot p(\sigma), \quad (4.4)$$

which is the minimum probability of a detectable VI around the value σ of the LOV parameter. To ensure the detection of a VI with probability $IP^*(\sigma)$ for all $|\sigma| \leq \sigma_{max}$, we have to define the generic completeness as

$$IP^* := \sup_{|\sigma| \leq \sigma_{max}} IP^*(\sigma).$$

Notice that we can take the supremum since $IP^*(\sigma)$ is bounded from above. Using (4.4), this implies the following condition on the step-size:

$$\Delta\sigma(\sigma) \leq \frac{R_{TP}}{b_{\oplus}} IP^* \frac{1}{p(\sigma)}.$$

We have thus proved the following result.

Theorem 4.1. *Let us assume that the LOV projection on the TP is a straight line passing through the Earth center, that $\mathbf{f}(\sigma) = \mathbf{0}$ for some σ is the Earth centre and that it is the only point on the TP. Suppose that the generic completeness level is IP^* . Then the step-size of the LOV sampling at σ satisfies the following inequality:*

$$\Delta\sigma(\sigma) \leq \frac{R_{TP}}{b_{\oplus}} IP^* \frac{1}{p(\sigma)}.$$

By assuming $b_{\oplus} = 2R_{\oplus}$ as above, we can select the step-size to be the maximum allowed value given the previous inequality.

The computation of $\Delta\sigma_i := \Delta\sigma(\sigma_i)$ starts from the value $\sigma_0 = 0$ (corresponding to the nominal solution), and by recursion we compute

$$\begin{cases} \Delta\sigma_i = \min \left\{ \frac{R_{TP}}{2R_{\oplus}} IP^* \frac{1}{p(\sigma_i)}, \Delta\sigma_{max} \right\}, & i \geq 0 \\ \sigma_{i+1} = \sigma_i + \Delta\sigma_i, & i \geq 1 \end{cases} \quad (4.5)$$

for the sampling of the interval $0 \leq \sigma \leq \sigma_{max}$. For the negative side, that is the interval $-\sigma_{max} \leq \sigma \leq 0$, the nodes are $\{\sigma_{-i}\}_{i \geq 0}$ with $\sigma_{-i} = -\sigma_i$ for all $i = -M, \dots, M$. By definition of IP^* , the step-size is chosen in such a way that the inverse image of the diametrical chord has the same probability for all σ . And this in turn implies that each sampling interval has the same probability. Of course this holds only for the intervals with length not exceeding $\Delta\sigma_{max}$.

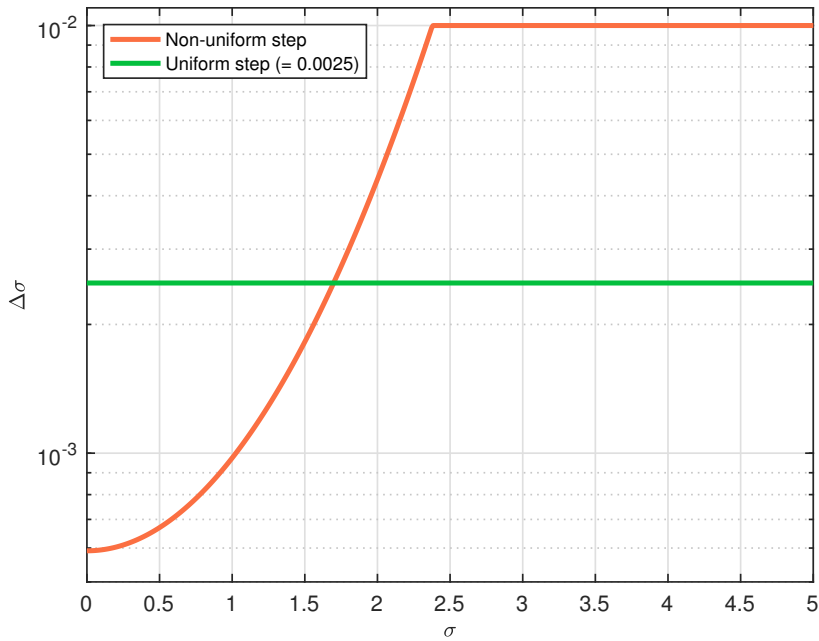


Figure 4.1. Graph of the step-size as a function of the LOV parameter σ , with the parameter choice as in (4.6). *Orange line*: step-size for the uniform-in-probability sampling. *Green line*: uniform step-size, as previously used by CLOMON-2.

The method allows one to choose the completeness limit before the sampling procedure starts. Thus the number of VAs per LOV side is known only at the end, since the procedure (4.5) stops when σ_{max} is exceeded. This is somewhat different with respect to the previous method, for which we first established the number of VAs per LOV side and as a consequence the completeness level was determined (as in equation (4.3)). To observe the behaviour of the step-size as a function of the LOV parameter σ refer to Figure 4.1. It was generated using the following values, which are the same used for the current impact monitoring computations:

$$IP^* = 1 \cdot 10^{-7}, \quad \sigma_{max} = 5, \quad \Delta\sigma_{max} = 0.01. \quad (4.6)$$

This choice of parameters leads to the computation of at most 4719 multiple solutions⁴, whereas at most 2401 VAs were computed with the previous sampling method (Milani et al. 2005a). This gives about twice the computational load than before, that however permits a decrease by a factor $\simeq 4$ in the generic completeness limit, since the value corresponding to the previous uniform sampling was $IP^* \simeq 4.24 \cdot 10^{-7}$, as computed in Section 4.1.

4.3 Missing VI detection: possible causes

The goal we posed by the generic completeness limit is to find all the virtual impactors with probability greater than IP^* . This goal might not be achieved in actual computations, that is some VI is not detected by the scan. The identification of the causes and the development of possible solutions are important issues in impact monitoring. In what follows, we discuss two examples we encountered in this study.

4.3.1 Duplicated points in the same return

In Section 1.5.4 we have defined showers and returns as particular dynamically related subsets of the set of close encounters of all the virtual asteroids. The associated iterative procedure properly works as long as the showers are well-defined. Indeed, there are cases in which there is not a clear clustering in time among the encounters, causing the presence of very long showers (also called extended showers) in the decomposition. As a consequence, some virtual asteroids appear multiple times in the same return, and this must be avoided for the subsequent TP analysis to be successful. In general, several phenomena may cause this problem, for instance temporary capture of the asteroid by the Earth, Earth-like orbit (as for 2000 SG₃₄₄) and encounters with low relative velocity. There are also cases in which a close approach, defined in time as the interval in which the distance from the encountered body is less than some D_{min} (for the Earth $D_{min} = 0.2$ au), contains multiple occurrences of a local minimum distance, and this also generates returns with duplicated points. Such bad cases are not so rare as one may think, especially if we use a denser LOV sampling. The problem affects $\simeq 25\%$ of the asteroids in the NEODyS risk list (as of April 2018).

An example of such situation is given by asteroid 2000 SG₃₄₄, already used to present the problem of duplicated virtual asteroids in Milani et al. (2005b), Figure 6. We show a figure which cannot be identical to the one

⁴The number of VAs may actually be lower, because we terminate the sampling when the residuals become too large, currently when $\chi > 5$.

in Milani et al. (2005b) since, even if the observational data set is exactly the same, it is currently treated with a different astrometric error model. Figure 4.2 shows a single extended shower for 2000 SG₃₄₄ lasting for about one year. In this situation the previous algorithm identifies a single shower around the year 2069. Figure 4.2 shows the closest encounter date of the points belonging to the extended shower, against the LOV index. The clustering into returns is clear from the picture, but there are returns with multiple occurrence of the same virtual asteroid, as highlighted in orange.

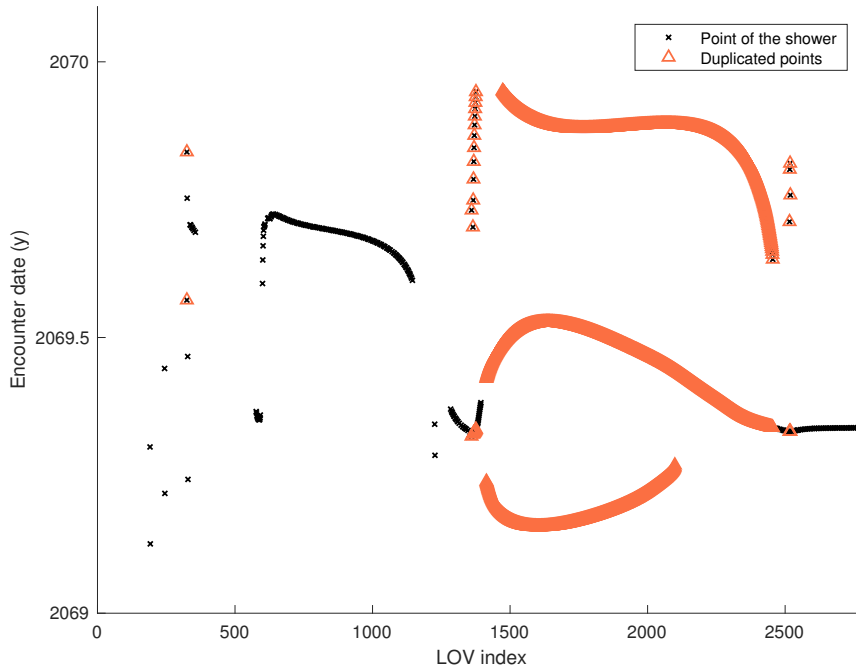


Figure 4.2. Extended shower around the year 2069 for asteroid 2000 SG₃₄₄. For each virtual asteroid belonging to the shower, we plot the closest encounter date against the LOV index (black crosses). The virtual asteroids that appear more than one times in the same return are highlighted (orange triangles).

To handle such cases, we decided to introduce a further splitting procedure every time a return contains duplicated virtual asteroids. This leads to the definition of sub-showers and sub-returns. First, we sort the return by ascending closest approach time, then we scan and divide it as follows: we cut the return every time a virtual asteroid is already present among the previous ones, starting from the previous cut. Each subset obtained in this way is called a *sub-shower*. Second, each sub-shower is divided into contiguous LOV segments, called *sub-returns*, in the same way we obtain the returns from the showers. Section 4.3.2 contains a mathematical description of the procedure just described, with a formal proof of completion. Thus

the decomposition algorithm ensures that each sub-return is free from duplicated virtual asteroids. Then we use, as returns of the original shower, all the sub-returns of all the sub-showers. Figure 4.3 shows the outcome of the application of the splitting procedure to the return going from LOV index 1414 to 2779. As a graphical representation of the algorithm, we pass a horizontal line from the bottom to the top of the plot to scan the return by ascending closest approach time and we make a cut when we encounter a duplication. The return is decomposed into three sub-showers (represented with different marks and colors), each of which is further decomposed in contiguous LOV segments.

It is apparent from Figure 4.3 that our algorithm splits more than the minimum possible, *e.g.*, in this figure it can be seen that there are two cuts splitting dynamically related encounters (the second and third horizontal lines starting from the bottom). However, this has no negative consequences on the performance of the VI detection, because even the LOV interval between the last index of a sub-return and the first of the next is actually scanned, by using the algorithms for the tail and head of the return (Milani et al. 2005b). The split is different from the one performed by Sentry, but the result in terms of impact monitoring is the same.

In the work carried out for the switch to the new sampling of the Line Of Variations, we implemented the splitting procedure into sub-showers and sub-returns, thus the results presented in Section 4.4 take already into account also this improvement.

4.3.2 Proof of completion for the decomposition scheme

In this section we provide a detailed description of the procedure to decompose a return with duplications into sub-returns, giving a mathematical proof of completion.

A return \mathcal{R} is given by a contiguous LOV segment, that is the indexes of the corresponding virtual asteroids are consecutive. Let $\mathcal{I}_{\mathcal{R}}$ be this set of indexes. Let $n_{\mathcal{R}}$ the number of distinct close approaches of the return \mathcal{R} . We rigorously define the return to be

$$\mathcal{R} := \{(i_k, t_k) : i_k \in \mathcal{I}_{\mathcal{R}}\}_{k=1, \dots, n_{\mathcal{R}}},$$

considering \mathcal{R} as the set of couples given by the LOV index and the corresponding closest approach time. We also assume that the sequence of times $(t_k)_{k=1, \dots, n_{\mathcal{R}}}$ is non-decreasing, that is $t_{k+1} \geq t_k$ for all k . We now suppose that the return contains a duplication, that is there exist $k_1, k_2 \in \{1, \dots, n_{\mathcal{R}}\}$ such that $k_1 \neq k_2$ and $i_{k_1} = i_{k_2}$, in such a way that the return has to be further decomposed.

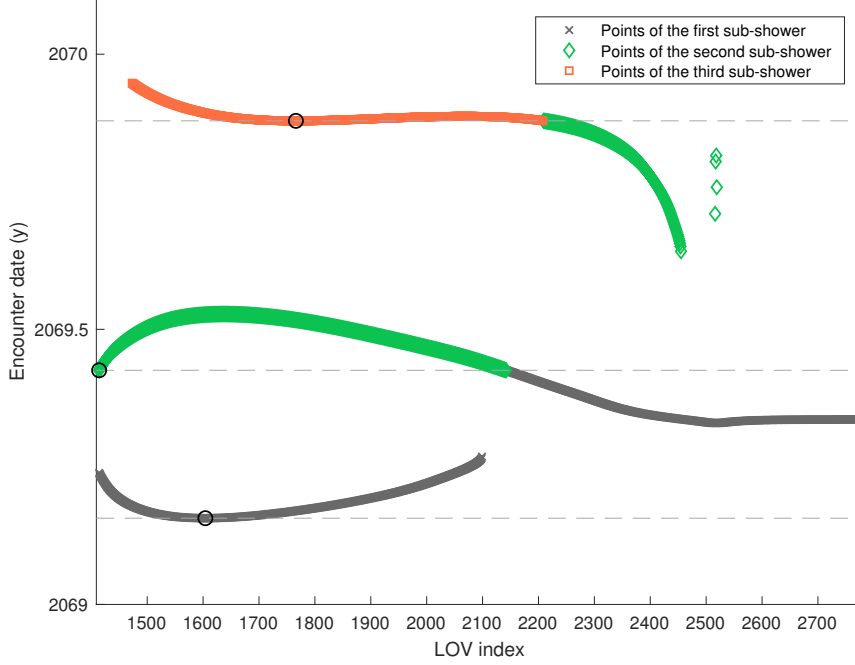


Figure 4.3. Application of the decomposition procedure to a return of the extended shower of 2000 SG₃₄₄. The return is decomposed into three sub-showers, represented with different marks and colors (orange, green, and gray, respectively). We mark with a black circle the first point (in terms of time) of each sub-shower: in particular, the first LOV indices of the three sub-showers are 1604, 1414 and 1766, respectively.

For $1 \leq s \leq n_{\mathcal{R}}$ define $I_s := \{i_k : 1 \leq k < s\}$. We now want to recursively define the sequence $(s_n)_{n \geq 1}$ of the beginning points of the sub-showers. Let $s_1 = 1$ and, for $n \geq 0$ define

$$s_{n+1} = \min_{s_n < s \leq n_{\mathcal{R}}} \{s : i_s \in I_s \setminus I_{s_n}\}$$

or $s_{n+1} = n_{\mathcal{R}}$ in case the minimum does not exist because the set is empty. By definition $(s_n)_{n \geq 1}$ is a non-decreasing sequence. Since $s_n \leq N$ for all $n \geq 1$, there exists n_s such that

$$s_1 < s_2 < \dots < s_{n_s} \quad \text{and} \quad s_n = n_{\mathcal{R}} \text{ for } n > n_s.$$

The integer n_s is the number of sub-showers in \mathcal{R} . For $1 \leq n \leq n_s$ let $\mathcal{I}_n := I_{s_{n+1}} \setminus I_{s_n}$ be the set of the indexes of each sub-shower. Note that the indexes in \mathcal{I}_n are pairwise distinct by construction. Moreover, the collection $\{\mathcal{I}_n\}_{1 \leq n \leq n_s}$ is a partition of $\{1, \dots, n_{\mathcal{R}}\}$. The sub-showers of \mathcal{R} are thus defined to be

$$\mathcal{S}_n := \{(i_k, t_k) : k \in \mathcal{I}_n\}$$

for $1 \leq n \leq n_s$ and

$$\mathcal{R} = \bigsqcup_{n=1}^{n_s} \mathcal{S}_n.$$

There is no guarantee that the indexes in a sub-showers are consecutive, thus each sub-shower is further decomposed in sub-returns by taking contiguous LOV segments. Rigorously, for each $1 \leq n \leq n_s$ there exist an integer $r_n \geq 0$ and a collection of r_n subsets $\{\mathcal{R}_{n,m}\}_{m=1,\dots,r_n} \subset \mathcal{S}_n$ such that the indexes of $\mathcal{R}_{n,m}$ are a maximal set of consecutive numbers among the indexes of \mathcal{S}_n and such that

$$\mathcal{S}_n = \bigsqcup_{m=1}^{r_n} \mathcal{R}_{n,m}.$$

In this way we obtain

$$\mathcal{R} = \bigsqcup_{n=1}^{n_s} \bigsqcup_{m=1}^{r_n} \mathcal{R}_{n,m},$$

the decomposition of \mathcal{R} in sub-returns. Given this formal procedure, since the initial number of close approaches contained in starting return is finite, it is proven that the procedure has a finite number of steps, at the end of which there are no duplicate points.

4.3.3 Extreme non-linear cases

When there is a strong non-linearity due to previous close approaches, the stretching is large and rapidly varying, causing the LOV behaviour to be complex. Thus strong non-linearity of the map \mathbf{g} introduced in Section 1.5.3 can lead to unsuccessful detections of virtual impactors.

Inside a return, only some intervals between consecutive VAs can contain a minimum of the closest approach distance and they are identified by a geometric classification (Milani et al. 2005b). The analysis continues by checking if the minimum distance could be small and, if so, by applying iterative schemes and interpolation along the LOV to determine the minimum distance and the corresponding LOV orbit, respectively. In most cases, both CLOMON-2 and Sentry use the *modified regula falsi* applied to the continuous function $f(\sigma) = \frac{dr^2}{d\sigma}(\sigma)$, introduced in (1.3), over the interval $[\sigma_1, \sigma_2]$ under consideration, where $r^2(\sigma)$ is the square of the distance from the Earth centre. This algorithm is convergent, but failure may occur if for some value of σ in the interval the function is undefined. It happens in case the TP of the encounter around that date is missed, which generally indicates that the two TP points under consideration do not actually belong to the same return (Milani et al. 2005b).

Another typical situation that may determine an unsuccessful detection is caused by singletons. They are returns consisting of one single point on the target plane, due to a very high value of the stretching at the corresponding LOV point and indicating an extremely non-linear situation. By definition the modified *regula falsi* cannot be applied in this case. The solution adopted by CLOMON-2 is the Newton method with bounded steps (Milani et al. 2005b): this method cannot diverge, but can fail to converge either by finding a value of σ for which the TP is missed, as in the previous case, or by exceeding a preset maximum number of iterations without achieving convergence with the required accuracy. In both cases there is the possibility that a VI actually exists in the analysed LOV segment, but the method fails in detecting it. A possible solution is to resort to a densification technique. If we suitably densify the LOV sampling around the orbit corresponding to the singleton, and obtain a return with 4-5 points on the target plane instead of a lone point, this makes the TP analysis easier and more effective. Indeed, Figure 4.5 shows that the power-law fits well only for values of IP corresponding to at least 4 points on the TP. We did not implement the densification of the sampling, though we intend to include it in our future work as discussed in Section 4.7.

4.4 Results

After the switch to the new sampling method, the actual level of completeness reached by the system has to be measured in some way and compared with the one corresponding to the previous method. To perform this analysis we make use of the histograms of the number of virtual impactors \mathcal{N} as a function of the inverse of the impact probability IP (for the sake of clarity we used $\log_{10}(1/IP)$ on the horizontal axis). We made a histogram for the ensemble of VIs obtained using a uniform step-size in σ (previous sampling method employed by CLOMON-2) and a second one for the results of the new sampling method, uniform in probability, on the same set of asteroids, with the observations available at the same date. We used the data contained in the NEODYs database immediately before and after CLOMON-2 switched to the new method, namely on 29 October 2016. As a sample, we used the 571 asteroids in the NEODYs Risk List at that time, thus computed with the uniform sampling in the LOV parameter σ . As a result of the application of the new method we obtain a set of 558 asteroids with virtual impactors out of 571. The two histograms are shown in Figure 4.4 and 4.5 (left panel). The first thing that stands out is the very different total number of virtual impactors: the application of the new method almost doubled this number, causing an increase from 13604 to 25942 virtual impactors.

In both the histograms there are two vertical lines corresponding to two different values of impact probability:

- the orange line represents the impact probability corresponding to the assumption that a VI is detectable with at least one target plane point (which is the minimum requirement), in full linear conditions⁵;
- the red line represents the impact probability corresponding to the assumption that at least two target plane points are needed for the detection of a virtual impactor.

The part of the histogram on the left of the orange line corresponds to $IP > IP^*$, namely to the impact probabilities of the virtual impactors that the system should detect with certainty. The number of virtual impactors \mathcal{N} is expected to grow as the impact probability goes down to IP^* . Even looking just to the histogram bars we notice that the growth of \mathcal{N} seems to slightly slow down close to the vertical lines with respect to what one would expect. To highlight this behaviour we fitted the histogram contour for $IP > IP^*$ with a suitable law: the best-fit line is represented in light blue in both plots of Figure 4.4 and 4.5 and it was obtained with a linear correlation coefficient > 0.99 in both cases. In particular, we performed a linear fit of the histogram contour in a log-log scale: Figure 4.4 and 4.5 (right panel) show the points corresponding to the histogram bar tips, those selected for the fit, and the best-fit line. A linear fit in the log-log plot corresponds to a power-law for the number of virtual impactors, that is

$$\mathcal{N} = n(IP) = c_1 \cdot \left(\frac{IP^*}{IP} \right)^\alpha \quad \text{if } IP \geq IP^*. \quad (4.7)$$

As a result we obtained the estimation $\alpha \simeq 0.678$ for the histogram related to the uniform sampling, and $\alpha \simeq 0.664$ for the histogram related to the uniform-in-probability sampling. These results are remarkably close, even if obtained with different sampling of the LOV. Furthermore, other results of this paper (see Section 4.5 and Section 4.6) seem to confirm this numerical evidence. At this point we are still not able to provide a full interpretation of the value of $\alpha \simeq 2/3$ as a mathematical property of the ensemble of all the VIs. Nevertheless, as a first step in this direction, in Section 4.5 we outline a possible model to explain the growth of the number of virtual impactors \mathcal{N} as a function of the time.

For $IP < IP^*$, the probability to find a virtual impactor with impact probability IP is roughly the ratio IP/IP^* . Thus the expected number of

⁵This is the assumption used for the computation of the generic completeness limit, as stated at the beginning of Section 4.1.

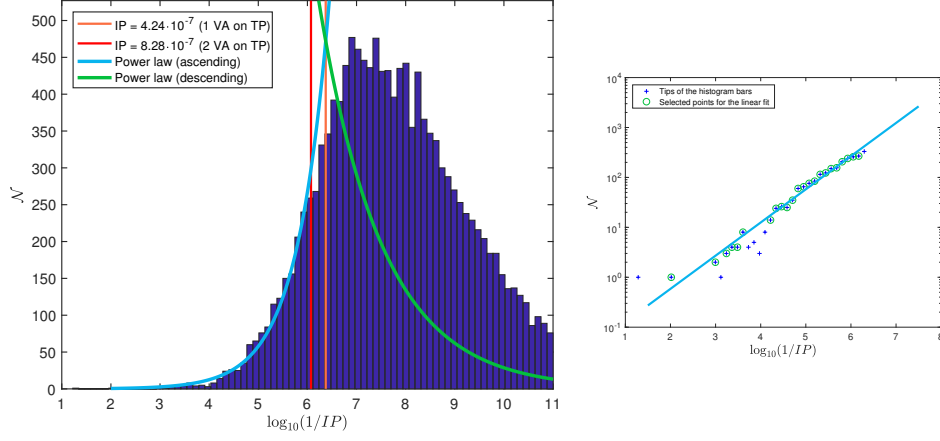


Figure 4.4. *Left panel.* Histogram of the number of virtual impactors (as of October 2016) as a function of the inverse of the impact probability, in the case of uniform sampling in σ . *Right panel.* Log-log plot of the histogram bar tips and corresponding regression line, providing $\alpha \simeq 0.678$.

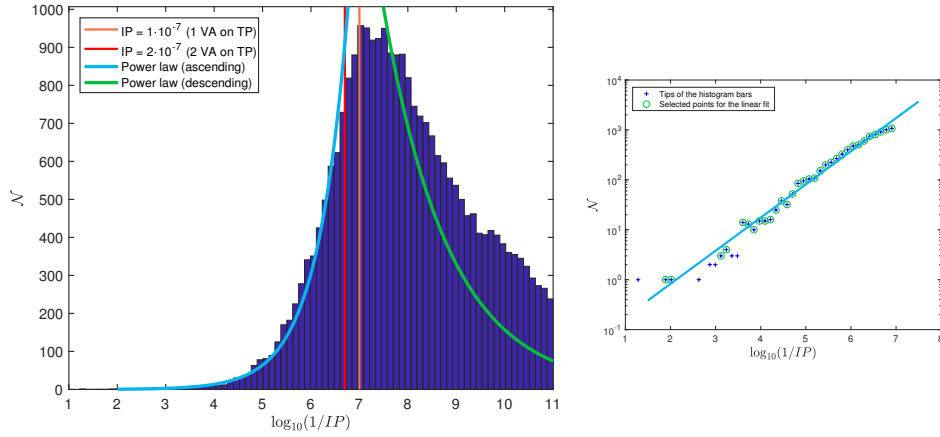


Figure 4.5. *Left panel.* Histogram of the number of virtual impactors (as of October 2016) as a function of the inverse of the impact probability, in the case of uniform-in-probability sampling. *Right panel.* Log-log plot of the histogram bar tips and corresponding regression line, providing $\alpha \simeq 0.664$.

virtual impactor is

$$\mathcal{N} = n(IP) \cdot \frac{IP}{IP^*} = c_1 \cdot \left(\frac{IP^*}{IP} \right)^{\alpha-1} \quad \text{if } IP < IP^*.$$

This equation corresponds to the descending green line in both plots. We notice that this line does not fit the right side histogram contour: there are

more virtual impactors than expected from this law. For the results obtained with the new sampling, this can be explained by considering that the LOV sampling returns to be uniform in σ close to the LOV tails, and thus in that region the LOV is over-sampled with respect to what would be needed to reach the completeness level IP^* . With the old sampling, the production of VIs with low impact probability is still larger, because the sampling was not optimized specifically for $IP > IP^*$.

The differences between the fitted ascending curve corresponding to equation (4.7) and the histogram clearly show that there is a loss of efficiency in finding virtual impactors with impact probability slightly above the completeness level. Indeed, for these impact probability values the expected number of VIs, based on the empirically fitted power-law, is larger than the number of actually detected ones. To define the generic completeness limit we make the assumption that even a single point on the target plane allows the system to detect the virtual impactor, but from a practical point of view this completeness level cannot be reached due to non-convergence of the iterative schemes in some difficult cases, as explained in Section 4.3. Actually, this does not happen only with a single point on the target plane (singleton), but even with very few points. As discussed in Section 4.7, a densification of the LOV sampling is the way to fill the gap between the actual completeness level and the theoretical generic completeness. A possible densification technique could convert returns with very few points into return with at least 4-5 points. As a result, the used iterative methods (such as *regula falsi* and Newton's method with bounded steps) should converge in a larger number of cases and the VI search could be more efficient and complete.

4.5 Analytical formulation for the time evolution

We analyse the behaviour of the cumulative number of virtual impactors \mathcal{N} as a function of the time elapsed from the initial conditions. As starting sample we used all the asteroids in the NEODyS Risk List (as of April 2018), which contained 734 objects and 32906 virtual impactors, without considering the special cases⁶. The histograms of Figure 4.6 show the distribution of the inclination i and of the absolute magnitude H among the considered objects. As clear from simple arguments, the majority of the sample contains small low-inclination asteroids: for instance, 95.5% of the sample has absolute magnitude $H > 22$ and 71% has inclination $i < 5$ deg.

⁶The four special cases are (101955) Bennu, (99942) Apophis, (29075) 1950 DA, and (410777) 2009 FD. These are currently the only asteroids that required the inclusion of

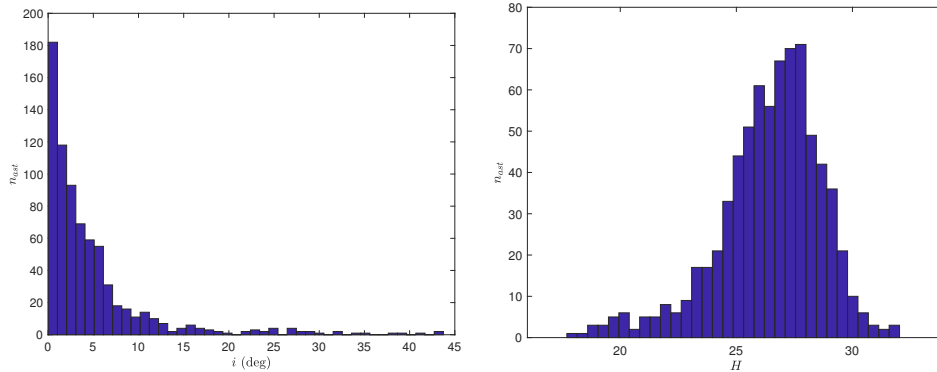


Figure 4.6. *Left panel.* Histogram of the inclination i (deg). *Right panel.* Histogram of the absolute magnitude H . Both the plots are referred to the set of 734 asteroids in the NEODyS Risk List (as of April 2018).

The sample of virtual impactors for the time evolution has to be complete, that is it has to contain all the possible virtual impactors with IP down to a certain threshold. Thus the results of the new sampling of the LOV are a good starting point, since the new method ensures a complete virtual impactors search down to $IP^* = 1 \cdot 10^{-7}$. To take into account the loss of completeness due to singletons, as discussed in Section 4.3 and 4.4, we selected the virtual impactors with $IP > 2 \cdot 10^{-7}$: the filtered set contains 6084 virtual impactors, corresponding to 473 asteroids. We then applied a second filter, considering the virtual impactors corresponding to low-inclination asteroids, *i.e.*, $i < 5$ deg, since the discussion below holds in an exact way in the planar case. In the end we analysed a sample of 5313 virtual impactors with $IP > 2 \cdot 10^{-7}$ and $i < 5$ deg.

For a single asteroid, the accumulation of virtual impactors with time depends on the time elapsed since the first observed close approach. We call this relative time t_{rel} , assuming as origin ($t_{rel} = 0$) the time of the first observed close approach. The exact computation of t_{rel} for each asteroid in the risk list would be complicated, but, by taking into account Figure 4.6 (right panel), we see that the vast majority of the asteroids in the risk list is composed by very small objects. As a consequence, they can only be discovered during a close approach. For almost all of the asteroids in the risk list the centre of the observed arc is thus a good approximation of the origin $t_{rel} = 0$. Thus, for each asteroid in the risk list, we sorted the set of its virtual impactors by time and we computed the relative time of each one of them with respect to the centre of the observed arc. Figure 4.7 is the log-log plot of the cumulative number of virtual impactors up to each value

the Yarkovsky effect for the impact monitoring.

of the relative time (blue and green marks). The log-log plot clearly shows a linear growth, which we try to determine with a linear fit. However, for a more accurate fit we have to cut out the tails of the ostensible line. The tail for low relative times because its contribution is weakened by small number statistics. In the tail for high relative times the growth seems to slow down, but this is due to the fact that the maximum relative time for which the scan for VIs has been performed changes from asteroid to asteroid. Thus we performed the linear fit over a suitable interval $t_1 \leq t_{rel} \leq t_2$. This fit corresponds to a power-law, that is

$$\mathcal{N} = c_2 \cdot t_{rel}^\beta \quad \text{if } t_1 \leq t_{rel} \leq t_2.$$

Choosing $t_1 = 40$ y and $t_2 = 99$ y we obtained $\beta = (3.001 \pm 0.001)$, with a linear correlation coefficient 0.9994. The points marked with green circles in Figure 4.7 are those selected for the linear fit, and the orange straight line is the resulting best-fit line. The histogram in Figure 4.8 is the cumulative histogram of the number of virtual impactors as a function of the relative time. The plot represents the same quantity of Figure 4.7 with an histogram, but not in a log-log scale. The colours have the same meaning as for Figure 4.7: the green part corresponds to the tail of the log-log plot used for the linear fit and the orange line is the best fit power-law. Given the approximations introduced in the model, this fit is remarkably good and identifies the power-law proportional to t_{rel}^3 with very low uncertainty.

We now give a qualitative argument to explain why the tail of the cumulative histogram follows a power-law with exponent $\simeq 3$. We do this in the framework of the analytical theory of close encounters as developed in Valsecchi et al. (2003), whose results agree with those of the circular restricted three-body problem (Valsecchi et al. 2018). We consider the target plane coordinates ξ and ζ : the former corresponds to the signed local MOID, whereas the latter is related to the timing of the encounter. We use the wire approximation (Valsecchi et al. 2003; Milani et al. 2005b), that is we assume that the LOV projection on the target plane of a given encounter is a continuous sequence of points, all with the same value of ξ and differing only for the value of ζ .

The condition for a collision at a resonant return to take place is that the ratio of the period of the small body and that of the Earth is k/h , with k and h relatively prime integers. Then, following the first encounter, after h heliocentric revolutions of the small body and k revolutions of the Earth, both the Earth and the small body will be back to the same position (Milani et al. 1999; Valsecchi et al. 2003). This situation means that the post-encounter semimajor axis a' has to have precisely a certain value, say a'_* , with the corresponding mean motion n'_* . For the Kepler's third law, the

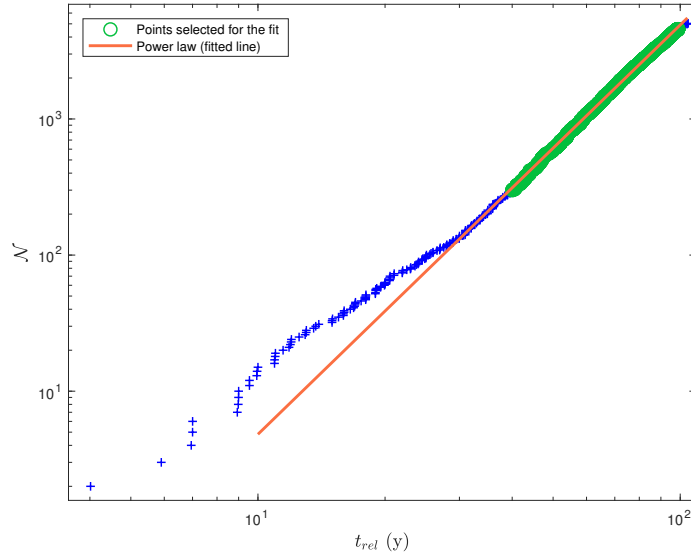


Figure 4.7. Log-log plot of the cumulative number of virtual impactors \mathcal{N} as a function of the relative time t_{rel} (y). The points selected for the linear fit are marked with green circles. The orange straight line is the best-fit line obtained from the linear fit.

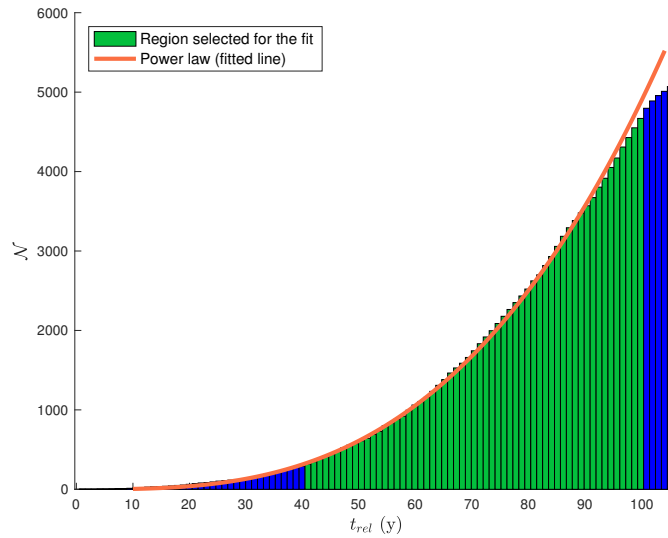


Figure 4.8. Plot of the cumulative number of virtual impactors \mathcal{N} as a function of the relative time t_{rel} (y).

latter has to be

$$n'_* = \left(\frac{h}{k}\right)^{2/3}. \quad (4.8)$$

As shown in Valsecchi et al. (2003) and in the appendix of Spoto et al. (2014), the values of a' are constrained between a maximum and a minimum, say a'_{max} and a'_{min} , to which correspond n'_{min} and n'_{max} respectively. Consider now the time interval in which we are interested: since $t_2 \simeq 99$ y, it is clear that we have to consider all the values of $n'_{min} \leq n' \leq n'_{max}$ that, expressed as in (4.8), have $k < 99$. Thus the number of collision possibilities, *i.e.*, of virtual impactors, is proportional to the number of encounter opportunities. This number accumulates in the same way as the number of elements of $\mathcal{F}_n^{r,s}$, which is the set of irreducible fractions between two integers r and $s > r$, and whose denominators do not exceed n (see Appendix B). Theorem B.20 states that the number of elements of $\mathcal{F}_n^{r,s}$ grows like n^2 and that it accumulates as n^3 , which is the result highlighted from the fit of Figure 4.8.

The above reasoning holds in an exact way, even for a single small body, in the planar circular restricted three-body problem with Jacobi constant \mathcal{J} sufficiently high to ensure the small body will not be expelled on a hyperbolic orbit, *i.e.*, $\mathcal{J} > 2\sqrt{2}$ (Carusi et al. 1982). The hypotheses on which our analytical estimate is based are an approximation of the more complex problem of asteroid close approaches, nevertheless the general trend turns out to be confirmed by our statistical analysis. If we add back to the list of asteroids with VIs (with $IP > 2 \cdot 10^{-7}$) the ones with not low inclination, $i > 5$ deg, the fit for the slope in the log-log plot gives $\beta = 2.829$, indicating that the model we have proposed can represent accurately the statistics of the VIs time distribution only in the low inclination case, as expected.

Note that the slope predicted by the Farey number-theoretical arguments refers to the number of close approaches to the Earth, not to the number of collisions. The fact that the histogram of VIs as a function of t_{rel} follows the same power-law expected for the number of close approaches indicates that, on average, the number of collisions is proportional to the number of close approaches. This is by no means an obvious result. The possibility of an impact during such a close approach is controlled by the MOID (Minimum Orbital Intersection Distance) at the time of the encounter: if the MOID is larger than the radius b_{\oplus} of the Earth impact cross section, collisions cannot occur. The MOID changes both as a consequence of short-periodic perturbations and because of secular perturbations slowly changing the MOID through the Lidov-Kozai cycle (Gronchi et al. 2001). The empirical finding that the impact probability and the probability of a close approach are proportional, at least as a mean over thousands of cases, would indicate that the MOID can be modeled as a random variable.

4.6 Comparison with JPL results

We performed a global comparison between the results of CLOMON-2 and Sentry. An asteroid-by-asteroid comparison is beyond the scope of this chapter, thus we present a statistical comparison using histograms like those shown in Section 4.4. In particular, we take the ensemble of all the virtual impactors computed by CLOMON-2 and Sentry at the same epoch (April 2018). Figure 4.9 refers to the results of CLOMON-2 and Figure 4.10 to the ones of Sentry: both plots represent the number of virtual impactors \mathcal{N} as a function of the inverse of the impact probability IP .

Both plots show a very good agreement in the ascending part up to $IP \simeq 2IP^* = 2 \cdot 10^{-7}$ (vertical red line). To strengthen this argument we also performed a linear fit of the histogram contour for $IP > IP^*$, as in equation (4.7). The exponent of the power-law resulted to be $\alpha \simeq 0.664$ for the CLOMON-2 results and $\alpha \simeq 0.679$ for the Sentry results. The number of VIs obtained by Sentry at $IP \simeq 2IP^*$ is somewhat lower than our number and it is the cause for the difference in the values of the multiplicative constant c_1 of equation (4.7) obtained from both fits.

For much lower impact probabilities, the two plots show some differences. The loss of efficiency in the region between the two vertical lines is a common feature, but our histogram is increasing whereas the one related to Sentry begins to slightly decrease. Overall the behaviour of the two systems in the detection of VIs with $IP > IP^*$ is very well consistent, which was one of the goals of the improvements in our system, that is the reason why we wanted to decrease our generic completeness. The biggest difference is in the right parts of the histograms: our plot is strictly decreasing, corresponding to the fact that the number of expected virtual impactors grows but the probability to detect them simultaneously decreases, whereas the histogram related to Sentry shows a peak around $IP \simeq 10^{-9}$. This behaviour might be explained by differences in the computation techniques, in particular in the treatment of the off-LOV virtual impactors (Milani et al. 2005b), which usually have very low impact probabilities. To explain the details in the differences between the two histograms, they would need to be investigated in collaboration with the JPL team.

In conclusion, the global comparison confirms a very good agreement between the two systems. The differences we found are mostly explained by technicalities of the methods used in the impact monitoring computations and anyway mostly regard very low probability VIs. Of course this does not exclude differences, in particular in the computed IP for each virtual impactor, which necessarily arise because we are currently using two different error models for the astrometric observations, also taking into account that

these error models are incomplete for lack of metadata. The fact that the results for $IP > IP^*$ are very similar in terms of the number of VIs found is a very significant result, since two different error models have been used.

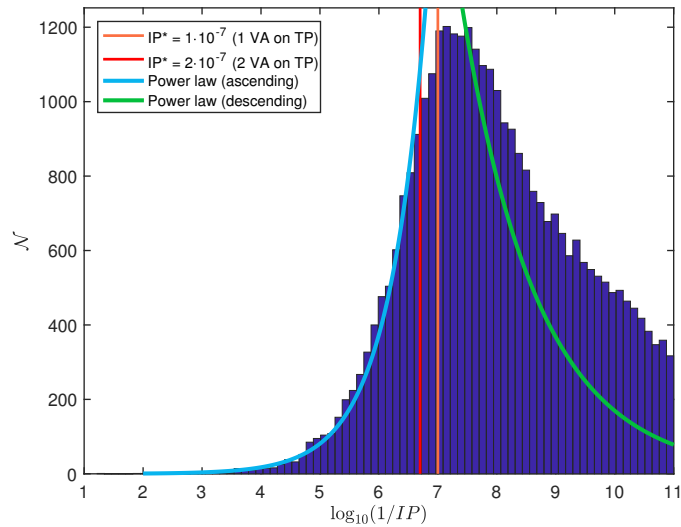


Figure 4.9. Histogram of the number of virtual impactors in the NEODYs Risk List as a function of the inverse of the impact probability (as of April 2018).

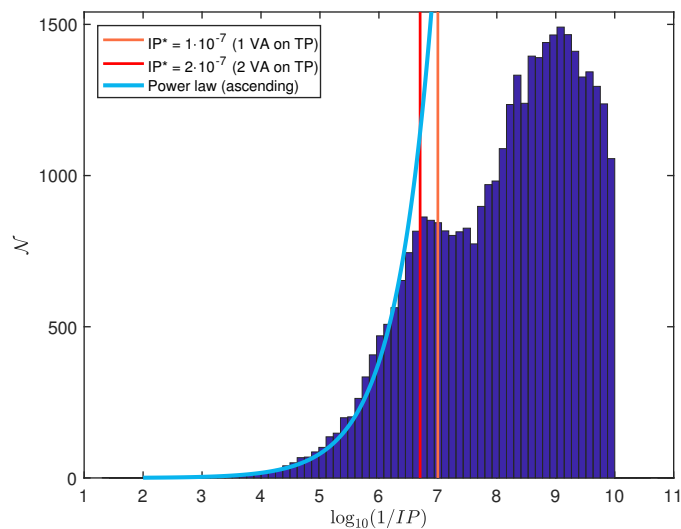


Figure 4.10. Histogram of the number of virtual impactors in the Sentry Risk List as a function of the inverse of the impact probability (as of April 2018).

4.7 Conclusion and future work

We reported on two improvements of our impact monitoring system CLOMON-2 with respect to what was described in (Milani et al. 2005b). The first one was a correct handling of the cases in which a return on the target plane of the Earth includes two instances of the same virtual asteroid. This was done by using a recursive splitting of the showers, thus radically eliminating these duplications. The second was to decrease the impact probability corresponding to the generic completeness, which was previously $\simeq 4 \cdot 10^{-7}$, to $1 \cdot 10^{-7}$. We did not achieve this result by brute force, that is by using four times more virtual asteroids, but by using a sampling of the Line Of Variations optimized by a uniform probability for each segment, at least for the portion closer to the nominal solution.

Both improvements have been implemented in the operational software and fully tested, by recomputing the entire risk list, that is the asteroids known to have VIs. Note that both the improvements we have implemented were removing differences between the algorithm used in the Sentry system of JPL and our CLOMON-2. Thus, having implemented these two improvements, we were for the first time able to perform a full statistical comparison between the global results of CLOMON-2 and those of Sentry, since the two systems should now be giving more similar results.

When we first produced this kind of histograms of the number of VIs found in all the risk list asteroids, as a function of variables such as $1/IP$ and the stretching S , we found empirically that the number of detected virtual impactors with $IP > IP^*$ appeared to grow according to a power-law, proportional to $IP^{-2/3}$. As shown in the figures of this chapter, we have tested that this result, numerically quite accurate, was obtained with the risk list as computed with different sampling of the LOV and with different values of IP^* (compare Figure 4.7 and Figure 4.8), as computed at different dates (compare Figure 4.8 and Figure 4.9), and for risk lists at the same date but computed with different software and different astrometric error models (compare Figure 4.9 and Figure 4.10). Thus we are lead to believe that we have experimentally found a fractal property of the set of the initial conditions leading to impacts in the chaotic dynamical system of planet crossing asteroids. We must admit we do not yet have a model explaining this power-law. We suspect it is related to the power-law by which the cumulative number of VIs within a time t_{rel} from the first observed close approach grows proportional to the power-law t_{rel}^3 , for which we have found a number-theoretical argument. However, for the connection between the two power-laws we have not yet found a model, which we suspect to hide in properties of the chaotic orbits of near-Earth asteroids.

Still, the use of the empirical law $IP^{-2/3}$ allows us to explore, for the first time, the effective completeness of the impact monitoring systems: of course this completeness cannot extend beyond the generic completeness limit IP^* . The results are encouraging, in that both CLOMON-2 and Sentry are not just statistically consistent, but also consistent with the empirical power-law, down to an $IP \simeq 2 \cdot 10^{-7}$. This is a significant achievement, because we never had a “ground truth” against which to assess our performance. Since the two impact monitoring systems are currently using two different error models for astrometric observations, by using the standard argument that the difference between the last two models can be considered an estimate of the inaccuracies remaining in the last one, this indicates also robustness of our results with respect to the astrometric error model.

The discussion above clearly indicates the directions we should move in our future work. First, we would like to close the gap between the generic completeness at $IP^* = 10^{-7}$ and the effective completeness (resulting from the comparison with the power-law) at $IP \simeq 2 \cdot 10^{-7}$. In principle we know how to do this by densification of the cases in which a return contains too few points on the target plane, but we would like to find a solution which is not brute force and this requires some effort, but appears feasible. Second, we need to investigate in depth the issue of the VI histogram power-law, to understand if indeed it is a fractal property and provide at least an approximate model explaining it, possibly starting from the success in explaining the power-law with respect to time. This requires some new idea, thus we are not able to claim that we shall solve this problem, but we shall try. Also other researchers are welcome to try.

Chapter 5

The evolution of the LOV at close encounters

The outcome of a planetary fly-by of a planet crossing small body strongly depends on its coordinates on the target plane of the encounter. The associated uncertainty is a function of the uncertainty in the orbital elements at the time of the encounter, and in most cases of interest is dominated by the uncertainty in the time of closest approach. A suitable choice of the target plane coordinates is such that one coordinate represents the local minimum distance between the orbit of the small body and that of the planet, and the other is proportional to the timing of the encounter. In this way, the uncertainty is mostly along a line parallel to one of the coordinate axes, and can be modelled by the so-called Line Of Variations. The LOV approach is a crucial ingredient of the impact monitoring software developed at the University of Pisa and at the JPL. In this study the post-encounter evolution of fictitious small bodies belonging to the LOV is studied in the framework of the analytic theory of close encounters. We show the consequences of the encounter on the local minimum of the distance between the orbit of the planet and that of the small body, and get a global picture of the way in which the planetocentric velocity vector is affected by the encounter. The analytical results are compared with those of numerical integrations of the circular restricted three-body problem.

5.1 Extended Öpik's theory of close encounters

The analytic theory of close encounters has been developed over the years, starting from Öpik (1976), in a sequence of papers (Carusi et al. 1990; Valsec-

chi et al. 2003; Valsecchi 2006; Valsecchi et al. 2016; Valsecchi et al. 2015), to which we refer the reader. The basic assumptions are that the small body is massless and the planet moves on a circular orbit about the Sun, similarly to what is assumed in the circular restricted 3-dimensional three-body problem. However, far from the planet, the small body is assumed to move on an unperturbed heliocentric Keplerian orbit, not being subject to the perturbation by the planet. The effect of the encounter is modelled as an instantaneous transition from the incoming asymptote of the planetocentric hyperbola to the outgoing one, taking place when the small body crosses the plane orthogonal to the small body unperturbed velocity vector and containing the centre of the planet. This plane is called the *b-plane*. In particular, the model ignores the perturbation due to the Sun and the time it actually takes for the small body to travel along the curved path that “joins” the two asymptotes.

To simplify the formulas, we use a system of units such that the distance of the planet from the Sun is 1 (recall that the planet is on a circular orbit around the Sun), and the period of the planet is 2π . We also assume that both the mass of the Sun and the gravitational constant are equal to 1. We disregard the mass of the planet in the heliocentric orbit of both the planet and the small body, thus the heliocentric velocity of the planet is also 1.

We use a planetocentric reference frame (X, Y, Z) such that the Y -axis coincides with the direction of motion of the planet, and the Sun is on the negative X -axis. In this system, the components of the unperturbed planetocentric velocity vector \mathbf{U} of the small body are (Carusi et al. 1990)

$$\begin{pmatrix} U_x \\ U_y \\ U_z \end{pmatrix} = \begin{pmatrix} \pm\sqrt{2 - 1/a - a(1 - e^2)} \\ \sqrt{a(1 - e^2)} \cos i - 1 \\ \pm\sqrt{a(1 - e^2)} \sin i \end{pmatrix} \quad (5.1)$$

and the planetocentric velocity is

$$U = \sqrt{3 - \frac{1}{a} - 2\sqrt{a(1 - e^2)} \cos i}.$$

This can be rewritten as $U = \sqrt{3 - T}$, where T is the Tisserand parameter with respect to the planet. The direction of the incoming asymptote is defined by two angles, ϑ and φ , such that

$$\begin{pmatrix} U_x \\ U_y \\ U_z \end{pmatrix} = \begin{pmatrix} U \sin \vartheta \sin \varphi \\ U \cos \vartheta \\ U \sin \vartheta \cos \varphi \end{pmatrix}.$$

The angles ϑ and φ can be computed from the orbital elements (Valsecchi et al. 2003):

$$\vartheta = \arccos \frac{\sqrt{a(1-e^2)} \cos i - 1}{\sqrt{3 - 1/a - 2\sqrt{a(1-e^2)} \cos i}}, \quad (5.2)$$

$$\varphi = \arctan \frac{\pm \sqrt{2 - 1/a - a(1-e^2)}}{\pm \sqrt{a(1-e^2)} \sin i}. \quad (5.3)$$

The numerator in the expression of φ is positive if the encounter takes place in the post-perihelion branch of the orbit of the small body, and negative otherwise, whereas the denominator is positive if the encounter takes place at the ascending node of the orbit, and negative otherwise.

In the (X, Y, Z) frame, the motion of the small body along the incoming asymptote is

$$\begin{pmatrix} X(t) \\ Y(t) \\ Z(t) \end{pmatrix} = \begin{pmatrix} U_x(t-t_0) + X_0 \\ U_y(t-t_0) + Y_0 \\ U_z(t-t_0) \end{pmatrix},$$

where t_0 is the time of node crossing by the small body, and the planetocentric coordinates of the node at time t_0 are $X_0 = X(t_0)$, the nodal distance, and $Y_0 = Y(t_0)$, which measures how early or late the planet is for the encounter.

5.1.1 Coordinates on the b -plane

Let us consider the vector \mathbf{b} extending from the planet to the intersection of the incoming asymptote with the b -plane. Its modulus is $b := |\mathbf{b}|$, and it is called the *impact parameter*. We use a coordinate system (ξ, η, ζ) such that (ξ, ζ) are coordinates on the b -plane and the η -axis is directed along \mathbf{U} . The ξ -axis is perpendicular to the heliocentric velocity of the planet, and the ζ -axis is in the direction opposite to the projection on the b -plane of the heliocentric velocity of the planet. The transformation from the planetocentric reference frame (X, Y, Z) to the b -plane frame (ξ, η, ζ) is accomplished by first rotating by an angle $-\varphi$ about Y then rotating by $-\vartheta$ about ξ (which is perpendicular to the old Y -axis and to \mathbf{U}), that is

$$\begin{pmatrix} \xi \\ \eta \\ \zeta \end{pmatrix} = \mathbf{R}_{-\vartheta}^{\xi} \mathbf{R}_{-\varphi}^Y \begin{pmatrix} X \\ Y \\ Z \end{pmatrix}.$$

It can be shown that the local Minimum Orbital Intersection Distance (MOID, *i.e.*, the minimum distance between the orbit of the small body and

that of the Earth) is given by ξ , and that it is tied to the distance from the node X_0 by the simple expression (Valsecchi et al. 2003)

$$\xi = X_0 \cos \varphi.$$

5.1.2 Pre-encounter state vector

In its original formulation, Öpik's theory of close encounters does not use a complete set of state variables. In a complete formulation, the six orbital elements of the small body have to be transformed to a set also containing six coordinates. They have been introduced in Valsecchi et al. (2003), to form the state vector

$$\mathbf{V} := (U, \vartheta, \varphi, \xi, \zeta, t_0),$$

where t_0 is the time of the ecliptic crossing by the small body. Equation (5.1), (5.2) and (5.3) provide formulas to compute the first three coordinates of the pre-encounter state vector \mathbf{V} starting from the pre-encounter orbital elements of the small body.

To compute ξ and ζ , we neglect terms of the second order in the miss distance at the node, that is $\mathcal{O}(X_0^2 + Y_0^2)$. As a consequence, the components of the vector \mathbf{b} extending from the planet to the intersection of the incoming asymptote with the b -plane, are

$$\xi = \cos \varphi \left[\frac{a(1 - e^2)}{1 \pm e \cos \omega} - 1 \right]$$

$$\zeta = \xi \cos \vartheta \tan \varphi - \sin \vartheta \left(1 + \frac{\xi}{\cos \varphi} \right) \tan \left(\Omega - \lambda_p - \frac{\pi}{2} \pm \frac{\pi}{2} \right),$$

where the upper sign applies at encounters at the ascending node, and λ_p is the longitude of the planet at time t_0 .

5.1.3 The encounter

As a consequence of the encounter with the planet, \mathbf{U} is rotated into \mathbf{U}' , aligned with the outgoing asymptote, without changing the length: $U' = U$. The rotation is instantaneous, and occurs when the small body crosses the b -plane. The deflection angle γ between the two vectors is a function of U , the mass of the planet m , and the impact parameter b according to

$$\tan \frac{\gamma}{2} = \frac{m}{bU^2} = \frac{c}{b},$$

where $c := m/U^2$ needs to be small to allow us to apply this theory¹.

The close encounter can be seen as an operator \mathbf{E} that maps the pre-encounter state vector \mathbf{V} , with components $(U, \vartheta, \varphi, \xi, \zeta, t_0)$, into the post-encounter one \mathbf{V}' , with components $(U', \vartheta', \varphi', \xi', \zeta', t'_0)$

$$\mathbf{V}' := \mathbf{E}\mathbf{V}.$$

The components of the post-encounter state vector, as functions of the pre-encounter state vector components (with $b = \sqrt{\xi^2 + \zeta^2}$), are

$$\begin{aligned} U' &= U \\ \cos \vartheta' &= \frac{(\xi^2 + \zeta^2 - c^2) \cos \vartheta + 2c\zeta \sin \vartheta}{\xi^2 + \zeta^2 + c^2} \end{aligned} \quad (5.4)$$

$$\sin \vartheta' = \frac{\sqrt{[(\xi^2 + \zeta^2 - c^2) \sin \vartheta - 2c\zeta \cos \vartheta]^2 + 4c^2\xi^2}}{\xi^2 + \zeta^2 + c^2} \quad (5.5)$$

$$\sin \varphi' = \frac{[(\xi^2 + \zeta^2 - c^2) \sin \vartheta - 2c\zeta \cos \vartheta] \sin \varphi - 2c\xi \cos \varphi}{(\xi^2 + \zeta^2 + c^2) \sin \vartheta'} \quad (5.6)$$

$$\cos \varphi' = \frac{[(\xi^2 + \zeta^2 - c^2) \sin \vartheta - 2c\zeta \cos \vartheta] \cos \varphi + 2c\xi \sin \varphi}{(\xi^2 + \zeta^2 + c^2) \sin \vartheta'} \quad (5.7)$$

$$\xi' = \frac{\xi \sin \vartheta}{\sin \vartheta'}$$

$$\zeta' = \frac{(\xi^2 + \zeta^2 - c^2)\zeta \sin \vartheta - 2(\xi^2 + \zeta^2)c \cos \vartheta}{(\xi^2 + \zeta^2 + c^2) \sin \vartheta'}$$

$$t'_0 = t_0 + \frac{2c[\xi \sin \varphi(2\zeta \cos \vartheta - \xi \tan \varphi) - \cos \varphi(\xi^2 \sin^2 \vartheta + \zeta^2)]}{U \sin \vartheta \{[(b^2 - c^2) \sin \vartheta - 2c\zeta \cos \vartheta] \cos \varphi + 2c\xi \sin \varphi\}}.$$

Particularly noteworthy is the expression for ξ' , which gives the post-encounter local MOID. We discuss its implications in Section 5.4.

5.1.4 Propagation to the next encounter

After the first close approach, the motion until the next encounter is treated as a Keplerian propagation. It can be seen as an operator \mathbf{P} that maps the post-encounter state vector \mathbf{V}' in the pre-next-encounter one \mathbf{V}'' , with components $(U'', \vartheta'', \varphi'', \xi'', \zeta'', t''_0)$

$$\mathbf{V}'' = \mathbf{P}\mathbf{V}'.$$

¹Analytic theory of close encounters works as long as the region of space in which the encounter takes place is “small,” so that the interaction can be thought as instantaneous. This assumption breaks down as the Tisserand parameter approaches 3, *i.e.*, when the encounters take place at low planetocentric velocity.

The transformation is given by:

$$\begin{aligned}
 U'' &= U' \\
 \vartheta'' &= \vartheta' \\
 \varphi'' &= \varphi' \\
 \xi'' &= \xi' \\
 \zeta'' &= \zeta' - (\text{mod}[h \cdot 2\pi a'^{3/2} + \pi, 2\pi] - \pi) \sin \vartheta' \\
 t_0'' &= t_0' + h \cdot 2\pi a'^{3/2},
 \end{aligned}$$

where h is the number of revolutions of the small body in its orbit, and a' is the post-first-encounter semimajor axis

$$a' = \frac{b^2 + c^2}{(b^2 + c^2)(1 - U^2) - 2U[(b^2 - c^2) \cos \vartheta + 2c\zeta \sin \vartheta]}.$$

5.2 Resonant returns

The orbital period of the planet is 2π , and that of the small body after the encounter is $2\pi a'^{3/2}$ (by the third Kepler's law). If the two periods are commensurable, that is

$$(a')^{3/2} = k/h,$$

with h and k integers, then after h periods of the asteroid k periods of the planet have elapsed, and both the planet and the small body will be back again in the same position of the previous encounter. Such a subsequent encounter is called a *resonant return*. Also if the ratio of the period is not exactly k/h , but is close, a subsequent encounter can take place, but the planet will be earlier or later for the encounter than it was at the previous one.

Valsecchi et al. (2003) proved that the locus of the points on a b -plane leading to a resonant return is a circumference, called *resonant circle* and sometimes referred to as Valsecchi circles. A given resonance corresponds to a certain value of a' , *i.e.*, of ϑ' , say a'_* and ϑ'_* . They are related by

$$\cos \vartheta'_* = \frac{1 - U^2 - 1/a'_*}{2U}.$$

as follows from equations (5.2) and (5.1). The value of ϑ'_* can be also computed from the geometry of the deflection (see (5.4)) as

$$\cos \vartheta'_* = \frac{(b^2 - c^2) \cos \vartheta + 2c\zeta \sin \vartheta}{b^2 + c^2}.$$

Replacing b^2 with $\xi^2 + \zeta^2$ and rearranging terms we obtain

$$\xi^2 + \zeta^2 - \frac{2c \sin \vartheta}{\cos \vartheta'_* - \cos \vartheta} \zeta + \frac{c^2 (\cos \vartheta'_* + \cos \vartheta)}{\cos \vartheta'_* - \cos \vartheta} = 0.$$

This is the equation of a circle centred on the ζ -axis. If $|R|$ is the radius of such a circle, and D the value of the ζ -coordinate of its centre, its equation is

$$\xi^2 + \zeta^2 - 2D\zeta + D^2 - R^2 = 0,$$

with

$$D = \frac{c \sin \vartheta}{\cos \vartheta'_* - \cos \vartheta} \quad \text{and} \quad R = \frac{c \sin \vartheta'_*}{\cos \vartheta'_* - \cos \vartheta}. \quad (5.8)$$

5.3 The wire approximation

In the *wire approximation* we consider the encounter of a stream of small bodies spaced in mean anomaly (that is, in true anomaly and therefore in ζ), all on the same orbit, with given local MOID ξ_0 (Valsecchi et al. 2003). Thus the small bodies have the same U , ϑ , φ and $\xi = \xi_0$.

As a consequence of the encounter, U does not change and t_0 does not concern us here. What changes are the angles ϑ and φ , that are transformed into ϑ' and φ' . Section 5.1.3 gives the relevant equations to compute the post-encounter quantities (remember that here $\xi = \xi_0$).

5.3.1 Local minima and maxima of the post-encounter semi-major axis

We want to compute the position of the local minima and maxima of the semimajor axis after a planetary encounter. Since the post-first-encounter semimajor axis a' is monotonically related to the post-first-encounter value of the angle ϑ'

$$a' = \frac{1}{1 - U^2 - 2U \cos \vartheta'}$$

$$\frac{\partial a'}{\partial \zeta} = \frac{2U}{(1 - U^2 - 2U \cos \vartheta')^2} \frac{\partial \cos \vartheta'}{\partial \zeta},$$

the problem of finding the local maxima and minima of a' as functions of ζ reduces to that of finding the zeroes of $\partial \cos \vartheta' / \partial \zeta$. In the wire approximation, with $\xi = \xi_0$, $\cos \vartheta'$ is given by

$$\cos \vartheta' = \frac{(\xi_0^2 + \zeta^2 - c^2) \cos \vartheta + 2c\zeta \sin \vartheta}{\xi_0^2 + \zeta^2 + c^2}.$$

The derivative of $\cos \vartheta'$ with respect to ζ is

$$\frac{\partial \cos \vartheta'}{\partial \zeta} = \frac{2c[2c\zeta \cos \vartheta + (\xi_0^2 - \zeta^2 + c^2) \sin \vartheta]}{(\xi_0^2 + \zeta^2 + c^2)^2}$$

and since the denominator is always positive, the problem is to find the zeroes of the numerator. The latter is of degree 2 in ζ , thus there are only a point ζ_+ of maximum and a point ζ_- of minimum of $\cos \vartheta'$, and thus of a' . From

$$\sin \vartheta \zeta^2 - 2c \cos \vartheta \zeta - \sin \vartheta (\xi_0^2 + c^2) = 0$$

we obtain

$$\zeta_{\pm} = \frac{c \cos \vartheta \pm \sqrt{c^2 + \xi_0^2 \sin^2 \vartheta}}{\sin \vartheta}. \quad (5.9)$$

The difference

$$\zeta_+ - \zeta_- = 2\sqrt{\frac{c^2}{\sin^2 \vartheta} + \xi_0^2}$$

gives us the size of the most interesting region, where the largest variations of final semimajor axis take place.

5.4 Post-encounter local MOID along the wire

On the post-encounter b -plane the size of the post-encounter impact parameter b' must be the same as that of the pre-encounter one b , due to the conservation of the planetocentric orbital angular momentum. Thus the post-encounter local MOID ξ' is bounded:

$$0 \leq \xi' \leq b = \sqrt{\xi^2 + \zeta^2}.$$

Moreover, since ϑ and ϑ' take values between 0 deg and 180 deg (Carusi et al. 1990), ξ and ξ' have the same sign (remember that they are defined on two different planes).

Let us now discuss the variation in size of the local MOID due to the encounter for the wire $\xi = \xi_0$. Equations (5.4) and (5.5) show that the larger the value of $|\zeta|$ the closer ϑ' will be to ϑ and thus the closer ξ' will be to ξ_0 . For smaller values of $|\zeta|$, there must be a minimum and a maximum value of $\sin \vartheta'$, that correspond respectively to the maximum and minimum values of ξ' . To find them, let us consider the derivative of $\sin \vartheta'$ with respect to ζ :

$$\frac{\partial \sin \vartheta'}{\partial \zeta} = \frac{\partial \sin \vartheta'}{\partial \cos \vartheta'} \frac{\partial \cos \vartheta'}{\partial \zeta} = -\frac{\cos \vartheta'}{\sin \vartheta'} \frac{\partial \cos \vartheta'}{\partial \zeta}.$$

The zeroes of $\partial \sin \vartheta' / \partial \zeta$ include those of $\partial \cos \vartheta' / \partial \zeta$, as well as the values of ζ such that $\cos \vartheta' = 0$. As regards the zeroes of $\partial \cos \vartheta' / \partial \zeta$, these can be found by zeroing the numerator of this derivative, since its denominator cannot be negative. The corresponding two values of ζ are given by equation (5.9). Concerning the values of ζ such that $\cos \vartheta' = 0$, they are given by the intersections of the straight line $\xi = \xi_0$ with the circle with centre $(0, D)$ and radius $|R|$ given by equation (5.8) by imposing the condition $\cos \vartheta' = 0$, that is

$$D = -\frac{c \sin \vartheta}{\cos \vartheta} \quad \text{and} \quad R = -\frac{c}{\cos \vartheta}.$$

The equation of such circle is

$$\xi^2 + \zeta^2 - 2D\zeta + D^2 = R^2$$

and its intersections with the straight line $\xi = \xi_0$ are the roots of the equation

$$\zeta^2 + \frac{2c\zeta \sin \vartheta}{\cos \vartheta} + \xi_0^2 - c^2 = 0.$$

They are

$$\zeta_{1,2} = \frac{-c \sin \vartheta \pm \sqrt{c^2 - \xi_0^2 \cos^2 \vartheta}}{\cos \vartheta}.$$

Summarizing, the zeroes of $\partial \sin \vartheta' / \partial \zeta$ are the following:

$$\begin{aligned} \zeta_{\pm} &= \frac{c \cos \vartheta \pm \sqrt{c^2 + \xi_0^2 \sin^2 \vartheta}}{\sin \vartheta} \\ \zeta_{1,2} &= \frac{-c \sin \vartheta \pm \sqrt{c^2 - \xi_0^2 \cos^2 \vartheta}}{\cos \vartheta}. \end{aligned}$$

Note that for

$$|\xi_0| > |R| = \frac{c}{|\cos \vartheta|}$$

there is no intersection of the circle corresponding to $\cos \vartheta' = 0$ with the straight line $\xi = \xi_0$, so that there are no real values for the roots $\zeta_{1,2}$.

The values of ξ' corresponding to ζ_{\pm} are

$$\xi'_{\pm} = \frac{\sqrt{c^2 + \xi_0^2 \sin^2 \vartheta} \pm c \cos \vartheta}{\sin \vartheta},$$

whereas those of ξ' corresponding to $\zeta_{1,2}$, when present, are

$$\xi'_{1,2} = \xi_0 \sin \vartheta.$$

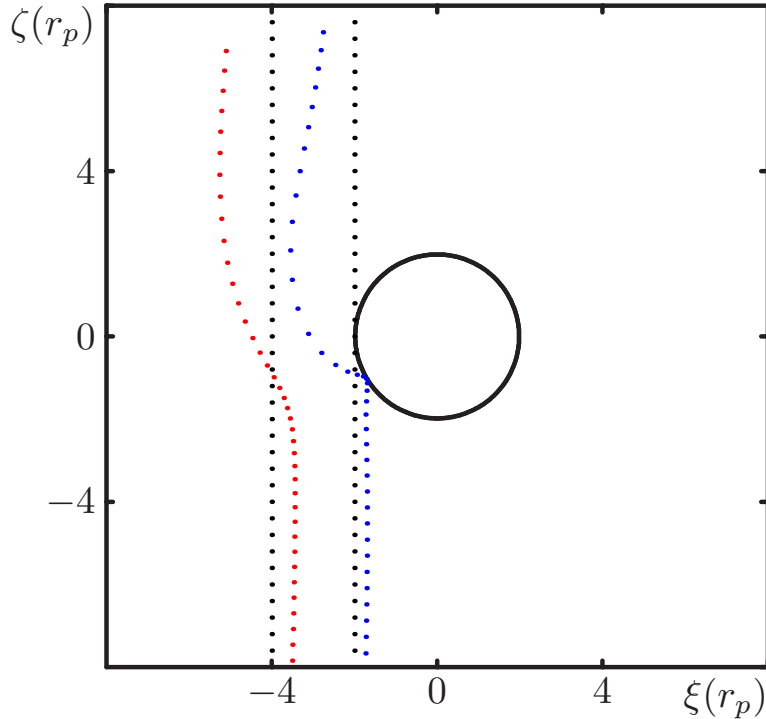


Figure 5.1. The Earth encounter of 2012 TC₄ on 12/10/2017. The plot shows the deformation of the LOV for $\xi_0 = -4$ and $\xi_0 = -2$ Earth radii. The black circle represents the Earth cross section. The black dots are the points belonging to the two LOVs points. The red dots show, for $\xi_0 = 4$, the corresponding points in the post-encounter b -plane and the blue dots do the same for $\xi_0 = -2$.

To see how the above expressions work in practice, we apply the analytical theory to the encounter of 2012 TC₄ with the Earth that has taken place on 12 October 2017. Figure 5.1 shows the b -plane relative to this encounter. The black circle centred in the origin is the gravitational cross-section of the Earth, and the unit adopted for the axes is the physical radius of our planet. The black dots represent the points of the wire for two different values of ξ , namely $\xi_0 = -4$ and $\xi_0 = -2$ Earth radii. The blue dots show the post-encounter values ξ' and ζ' corresponding to each pair (ξ_0, ζ) , for $\xi_0 = -4$ Earth radii, whereas the blue dots are the same for $\xi_0 = -2$ Earth radii. Note that to each pair (ξ_0, ζ) corresponds a post-encounter pair (ξ', ζ') defined on a different post-encounter b -plane. In Figure 5.1 we plot both on the same b -plane in order to show how the wire is deformed as a consequence of the close encounter. It is noteworthy how the variation of the local MOID can be, at least in this case, comparable to the radius of the Earth (see the blue dots).

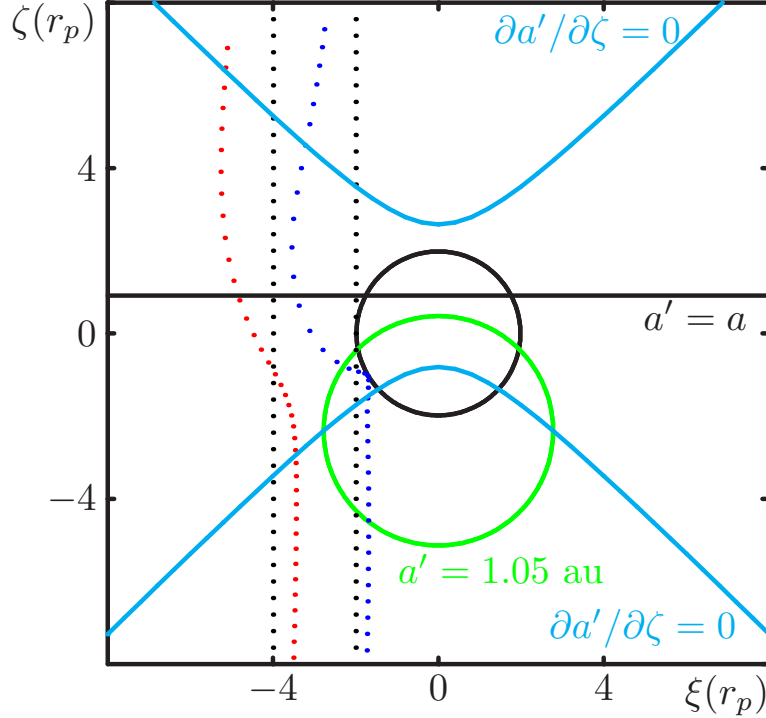


Figure 5.2. Same as Figure 5.1, highlighting relevant b -plane loci (Valsecchi et al. 2018). The cyan hyperbola corresponds to $\partial \cos \vartheta' / \partial \zeta = 0$. The black straight line is the condition for $\vartheta' = \vartheta$ (Valsecchi et al. 2000), implying $a' = a$ and $\xi' = \xi$. The green circle is the condition $\cos \vartheta' = 0$ (in this particular case giving $a' = 1.05$ au), corresponding to $\xi' = \xi \sin \vartheta$.

Figure 5.2 is similar to Figure 5.1, but also shows the relevant b -plane loci (Valsecchi et al. 2018) whose intersections with the LOV give origin to specific values of ξ' . These loci are the following:

- (1) the condition $\partial \cos \vartheta' / \partial \zeta = 0$, shown by the cyan hyperbola;
- (2) the condition $\vartheta' = \vartheta$, shown by the black horizontal straight line;
- (3) the condition $\cos \vartheta' = 0$, shown by the green circle.

Let us examine the LOV with $\xi_0 = -4$ Earth radii, going from positive ζ values towards negative ones. For large positive values of ζ , as already mentioned, ϑ' tends to ϑ , so the variation of ξ is small. Going towards $\zeta = 0$, the LOV crosses the hyperbola for $\zeta = \zeta_+$. This corresponds to the maximum of $\cos \vartheta'$, *i.e.*, to the minimum of $\sin \vartheta'$ and thus to the maximum

of ξ' . The values of ϑ' , φ' and ξ' are given by

$$\cos \vartheta'_+ = \frac{\sqrt{c^2 + \xi_0^2 \sin^2 \vartheta} \cos \vartheta + c}{\sqrt{c^2 + \xi_0^2 \sin^2 \vartheta + c \cos \vartheta}} \quad (5.10)$$

$$\sin \vartheta'_+ = \frac{\xi_0 \sin^2 \vartheta}{\sqrt{c^2 + \xi_0^2 \sin^2 \vartheta + c \cos \vartheta}}$$

$$\sin \varphi'_+ = \frac{\xi_0 \sin \vartheta \sin \varphi - c \cos \varphi}{\sqrt{c^2 + \xi_0^2 \sin^2 \vartheta}} \quad (5.11)$$

$$\cos \varphi'_+ = \frac{\xi_0 \sin \vartheta \cos \varphi + c \sin \varphi}{\sqrt{c^2 + \xi_0^2 \sin^2 \vartheta}} \quad (5.12)$$

$$\xi'_+ = \frac{\sqrt{c^2 + \xi_0^2 \sin^2 \vartheta} \cos \vartheta + c}{\sin \vartheta}.$$

The next locus encountered by the $\xi_0 = -4$ Earth radii LOV is $\cos \vartheta' = \cos \vartheta$: in this case, the local MOID is unchanged, $\xi' = \xi_0$. Finally, the LOV encounters the other branch of the hyperbola, in ζ_- . Here, the values of ϑ' , φ' and ξ' are given by:

$$\cos \vartheta'_- = \frac{\sqrt{c^2 + \xi_0^2 \sin^2 \vartheta} \cos \vartheta - c}{\sqrt{c^2 + \xi_0^2 \sin^2 \vartheta - c \cos \vartheta}} \quad (5.13)$$

$$\sin \vartheta'_- = \frac{\xi_0 \sin^2 \vartheta}{\sqrt{c^2 + \xi_0^2 \sin^2 \vartheta - c \cos \vartheta}}$$

$$\sin \varphi'_- = \frac{\xi_0 \sin \vartheta \sin \varphi - c \cos \varphi}{\sqrt{c^2 + \xi_0^2 \sin^2 \vartheta}} \quad (5.14)$$

$$\cos \varphi'_- = \frac{\xi_0 \sin \vartheta \cos \varphi + c \sin \varphi}{\sqrt{c^2 + \xi_0^2 \sin^2 \vartheta}} \quad (5.15)$$

$$\xi'_- = \frac{\sqrt{c^2 + \xi_0^2 \sin^2 \vartheta} \cos \vartheta - c}{\sin \vartheta}.$$

A noteworthy feature is that $\varphi'_+ = \varphi'_-$ and we return on this in Section 5.5.

Coming now to the $\xi_0 = -2$ Earth radii LOV, the crossings of the hyperbola and of the straight line are as before. However, this LOV crosses also the green circle corresponding to $\cos \vartheta' = 0$: actually, one of these crossings happens to take place at the border of the cross-section of the Earth.

Anyway, at these two crossings we have

$$\begin{aligned}\cos \vartheta'_{1,2} &= 0, & \sin \vartheta'_{1,2} &= 1 \\ \xi'_{1,2} &= \xi_0 \sin \vartheta.\end{aligned}$$

5.4.1 Numerical check

To test the validity of the theoretical predictions about the variation of the local MOID along the LOV, we proceeded as in Section 4 of Valsecchi et al. (2018). That is, we integrated the equations of the circular restricted three-body problem using the RA15 integrator (Everhart 1985) with initial conditions corresponding to the 12 October 2017 encounter of 2012 TC₄.

We found the pre-encounter values of ω corresponding to ξ_0 equal to -2 and -4 Earth radii and then we integrated sets of initial conditions equally spaced in ζ , thus reproducing the two LOVs of interest. Then we determined the post-encounter values ξ' and ζ' , and plotted them in Figure 5.3, that has to be compared with Figure 5.1. The theoretical behaviour of the LOV is very well confirmed by the numerical integrations.

5.5 Rotation of \mathbf{U} along the wire

The conservation of U implies that the pre-encounter and post-encounter velocity vectors \mathbf{U} and \mathbf{U}' span a sphere of radius U in the XYZ -space, centred in the origin and on which the angles ϑ and φ define a system of parallels and meridians. In fact, ϑ is a colatitude measured from the Y -axis (the direction of motion of the planet) and φ is a longitude, counted from the ZY -plane.

We now show that the post-encounter values of ϑ' and φ' accessible to a small body encountering the planet “on the wire” lay on the circle resulting from the intersection of the cone of aperture $\gamma_{max}(\xi_0, c)$, centred in the centre of the sphere, and the sphere itself. The angle γ_{max} is the maximum deflection for given ξ_0 , obtained for $\zeta = 0$ from (Carusi et al. 1990):

$$\cos \gamma_{max} := \frac{\xi_0^2 - c^2}{\xi_0^2 + c^2}.$$

On the U -sphere let us consider the meridian $\varphi_C = \varphi_+ = \varphi_-$ and on it let us consider point C , whose colatitude ϑ_C is halfway between ϑ'_+ and ϑ'_- , so that

$$\vartheta_C = \frac{\vartheta'_+ + \vartheta'_-}{2}.$$

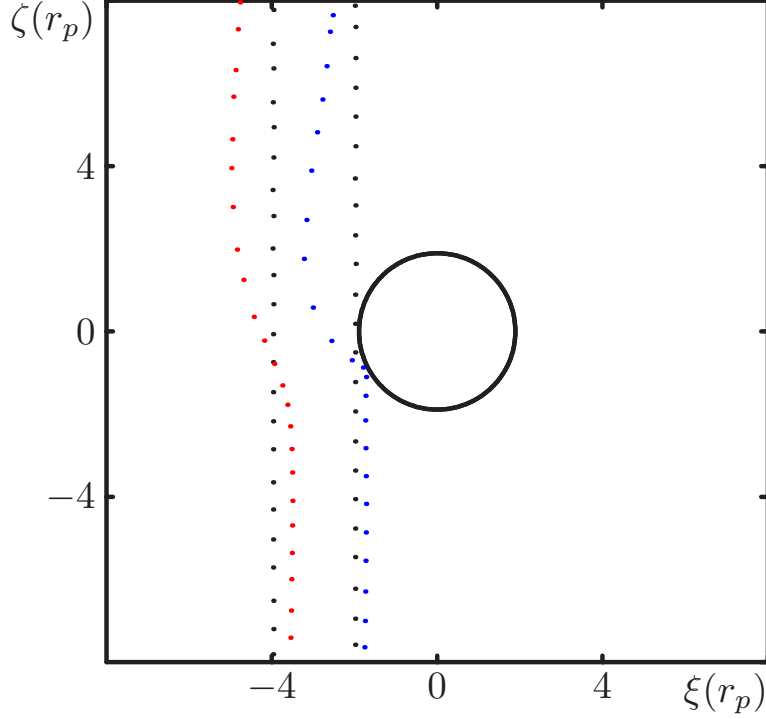


Figure 5.3. Same as Figure 5.1, but in this case the dots come from numerical integrations in the circular restricted three-body problem.

From equations (5.10), (5.13), (5.11), (5.12) we can compute ϑ_C and φ_C as a function of c , ϑ , φ , ξ_0 :

$$\begin{aligned} \cos \vartheta_C &= \frac{\xi_0 \cos \vartheta}{\sqrt{\xi_0^2 + c^2}}, & \sin \vartheta_C &= \frac{\sqrt{\xi_0^2 \sin^2 \vartheta + c^2}}{\sqrt{\xi_0^2 + c^2}} \\ \sin \varphi_C &= \frac{\xi_0 \sin \vartheta \sin \varphi - c \cos \varphi}{\sqrt{c^2 + \xi_0^2 \sin^2 \vartheta}}, & \cos \varphi_C &= \frac{\xi_0 \sin \vartheta \cos \varphi + c \sin \varphi}{\sqrt{c^2 + \xi_0^2 \sin^2 \vartheta}}, \end{aligned}$$

Thus, in the XYZ -frame the coordinates of C are

$$\begin{aligned} C_X &= U \sin \vartheta_C \sin \varphi'_\pm = \frac{U(\xi_0 \sin \vartheta \sin \varphi - c \cos \varphi)}{\sqrt{\xi_0^2 + c^2}} \\ C_Y &= U \cos \vartheta_C = \frac{U \xi_0 \cos \vartheta}{\sqrt{\xi_0^2 + c^2}} \\ C_Z &= U \sin \vartheta_C \cos \varphi'_\pm = \frac{U(\xi_0 \sin \vartheta \cos \varphi + c \sin \varphi)}{\sqrt{\xi_0^2 + c^2}}. \end{aligned}$$

On the other hand, the post-encounter values ϑ' , φ' for a generic initial condition “on the wire”, of coordinates (ξ_0, ζ) , can be computed using equations (5.4), (5.5), (5.6), (5.7). The corresponding point on the U -sphere has coordinates

$$\begin{aligned} X &= U \sin \vartheta' \sin \varphi' \\ Y &= U \cos \vartheta' \\ Z &= U \sin \vartheta' \cos \varphi' \end{aligned}$$

It is then a straightforward computation to show that the square of its distance from C is

$$D_C^2 = (X - C_X)^2 + (Y - C_Y)^2 + (Z - C_Z)^2 = \frac{2U^2 \left(\sqrt{\xi_0^2 + c^2} - \xi_0 \right)}{\sqrt{\xi_0^2 + c^2}}.$$

i.e., it belongs to the circle on the U -sphere centred in C and of radius D_C .

Thus the post-encounter values of ϑ' and φ' accessible to a small body encountering the planet “on the wire” define the circle resulting from the intersection of the cone of aperture γ_{max} , centred in the centre of the sphere, and the sphere itself. The pole of the spherical cap delimited by the circle is the point C . It is clear that, the smaller becomes ξ_0 relative to c , the larger becomes the radius of the circle until, for $\xi_0 = 0$, it becomes the great circle corresponding to the φ -meridian. Moreover, for $\xi_0 \neq 0$ the circle is tangent to the φ -meridian in the point of spherical coordinates (ϑ, φ) .

Figure 5.4 helps to visualize the situation in the case of the already mentioned recent encounter of 2012 TC₄ with the Earth. It shows \mathbf{U} in the XYZ -frame and the sphere that is spanned by \mathbf{U}' for all possible values of ξ and ζ . The red circle is the intersection of the sphere with the XY -plane and the angles ϑ and φ are indicated. For the the real asteroid, ξ_0 had a negative value and γ_{max} amounted to about 57 deg. Thus, we report in green the circle spanned by \mathbf{U}' for that ξ_0 .

Figure 5.5 shows the situation for a value of ξ_0 still negative but closer to 0, for which γ_{max} would amount to 90 deg. We are here plotting the behaviour of \mathbf{U}' also for deflections that would imply a perigee of the real asteroid smaller than the radius of the Earth, in order to give the overall view of the geometry involved. Obviously, in a realistic computation, parts of the green circle would be forbidden, due to the impact.

Finally, Figure 5.6 shows what happens when ξ_0 changes sign. As already mentioned, for $\xi_0 = 0$ the green circle becomes a great circle. Afterwards, the green circle starts to shrink on the other side, as ξ_0 starts to increase after having passed through 0. In the figure we plotted the green circle corresponding to a value of $\gamma_{max} = 39$ deg.

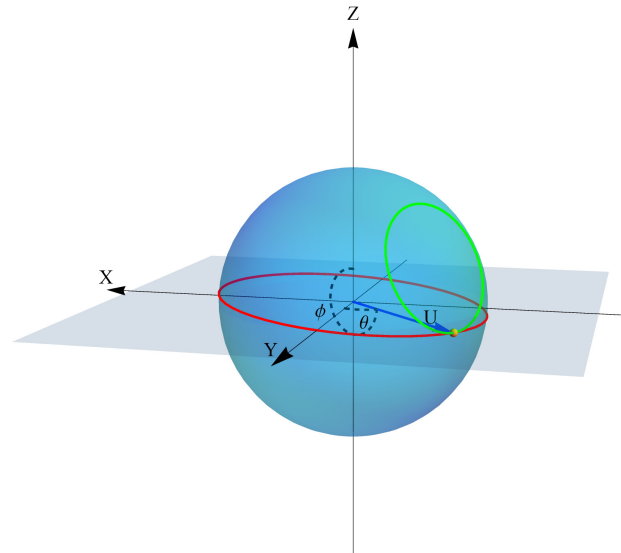


Figure 5.4. The possible rotation of \mathbf{U}' for the 2017 encounter of 2012 TC₄.

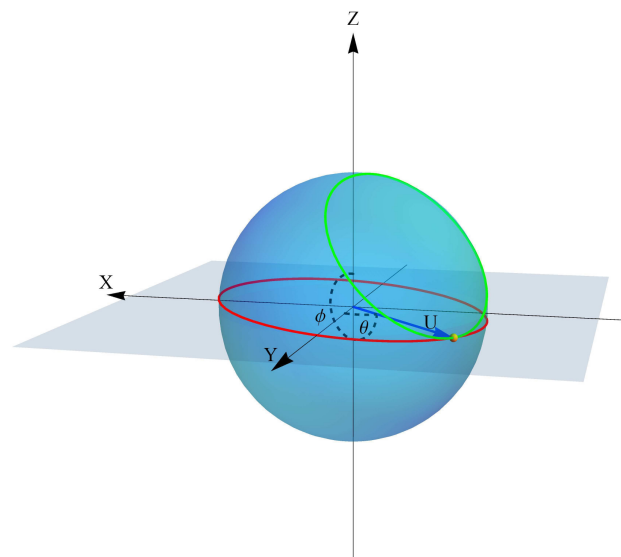


Figure 5.5. The possible rotation of \mathbf{U}' for the 2017 encounter of 2012 TC₄, for a value of ξ_0 resulting in $\gamma_{max} = 90$ deg.

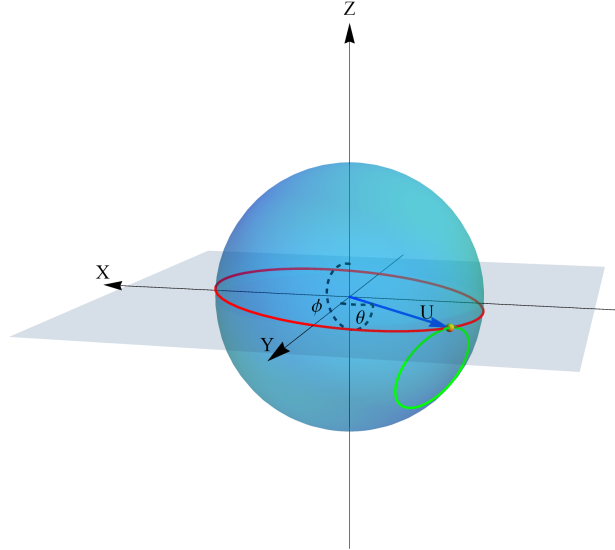


Figure 5.6. The possible rotation of \mathbf{U}' for the 2017 encounter of 2012 TC₄, for a positive value of ξ_0 resulting in $\gamma_{max} = 39$ deg.

5.6 Conclusions

We have discussed how a close encounter, in which the local MOID is well determined, and the timing is somewhat uncertain, can be modelled with the wire approximation, in which the LOV on the b -plane is described by $\xi = \xi_0$ and ζ taking any value within the uncertainty range. Explicit expressions can be given to describe the behaviour of the LOV after the encounter. In particular, we are able to describe the variation of the local MOID as a consequence of the encounter, that in some cases can be of the order of the Earth radius, and thus have consequences for the possibility of impacts at subsequent returns. Numerical integrations in the circular restricted three-body problem confirm that the theoretical results on the variation of the local MOID are satisfactorily accurate. Moreover, the theory allows us to give the overall geometrical description of how the planetocentric velocity vector is deflected at the encounter, as a function of the MOID of the points along the LOV. In fact, for a LOV of given ξ_0 , the post-encounter values of ϑ' and φ' give the circle resulting from the intersection of the cone of aperture $\gamma_{max} = \gamma_{max}(\xi_0, c)$, centred in the centre of the sphere spanned by \mathbf{U}' , and the sphere itself.

Comparison of these results with those obtained in realistic situations for asteroids possibly impacting the Earth, will be the subject of future work.

Chapter 6

Use of a semilinear method to determine the impact corridor

6.1 The semilinear method

Let us consider the space \mathbb{R}^N of the orbital elements, a “target space” $\mathcal{Y} \subseteq \mathbb{R}^2$, and a function $\mathbf{F} : \mathbb{R}^N \rightarrow \mathcal{Y}^1$. Let us call \mathbf{x} and \mathbf{y} the variables in the spaces \mathbb{R}^N and \mathcal{Y} , respectively. Let us assume to have a nominal solution $\mathbf{x}^* \in \mathbb{R}^N$ and let $\mathbf{y}^* := \mathbf{F}(\mathbf{x}^*)$.

In the linear approximation, the confidence ellipsoid $Z_{lin}^X(\sigma)$ in the space of orbital elements (see Section 1.5) is mapped onto an elliptic disk in the target space, which we denote by $Z_{lin}^Y(\sigma)$. It is defined by the inequality

$$(\mathbf{y} - \mathbf{y}^*)^\top C_Y (\mathbf{y} - \mathbf{y}^*) \leq \sigma^2$$

and is the image of $Z_{lin}^X(\sigma)$ by the linear map $D\mathbf{F}_{\mathbf{x}^*}$. As it is known from the theory of Gaussian probability distributions, the covariance matrices of the variables X and Y are related by

$$C_Y^{-1} := \Gamma_Y = D\mathbf{F}_{\mathbf{x}^*} \Gamma_X D\mathbf{F}_{\mathbf{x}^*}^\top.$$

The easily computable elliptic disks $Z_{lin}^Y(\sigma)$ are good approximations whenever the non-linearity of the function \mathbf{F} is small. Unfortunately, this is not the case when the orbits have to be propagated for a long time, and especially when close approaches take place. A good compromise between

¹As usual, either $N = 6$, if we consider a set of six orbital elements (in whatever coordinates), or $N > 6$ if some dynamical parameter is included (Milani et al. 2010, Chapter 1).

computational efficiency and accurate representation of non-linear effects is obtained by the *semilinear confidence boundaries* in the target space, as presented in Milani (1999) and Milani et al. (1999). The boundary ellipse $\mathcal{E}_Y := \partial Z_{lin}^Y(\sigma)$ is the image by the linear map $D\mathbf{F}_{\mathbf{x}^*}$ of an ellipse $\mathcal{E}_X(\sigma)$ in the orbital elements space, which lies on the surface of the ellipsoid $Z_{lin}^X(\sigma)$. We define the semilinear confidence boundary $K(\sigma)$ as the non-linear image in the target space of the ellipse $\mathcal{E}_X(\sigma)$, that is

$$K(\sigma) := \mathbf{F}(\mathcal{E}_X(\sigma)).$$

By the Jordan curve theorem, the closed curve $K(\sigma)$ is the boundary of some subset $Z(\sigma)$ in \mathcal{Y} . We use $Z(\sigma)$ as an approximation to $\mathbf{F}(Z_{lin}^X(\sigma))$, which is the set of all possible predictions on the target space compatible with the observations.

To compute the semilinear confidence boundary $K(\sigma)$ we can proceed as follows. The rows of the Jacobian matrix $D\mathbf{F}_{\mathbf{x}^*}$ span a 2-dimensional subspace \mathcal{H} in the orbital elements space \mathbb{R}^N , which can be decomposed as

$$\mathbb{R}^N = \mathcal{H} \oplus \mathcal{G},$$

where $\mathcal{G} := \mathcal{H}^\perp$ is a $(N-2)$ -dimensional subspace². Let us make the following decomposition:

$$\mathbf{x} - \mathbf{x}^* = \begin{pmatrix} \mathbf{g} - \mathbf{g}^* \\ \mathbf{h} - \mathbf{h}^* \end{pmatrix},$$

where \mathbf{h} represents two coordinates in the space \mathcal{H} and \mathbf{g} represents $N-2$ coordinates in the orthogonal space. In this coordinate system the normal matrix C_X can be decomposed as

$$C_X = \begin{pmatrix} C_{\mathbf{g}\mathbf{g}} & C_{\mathbf{g}\mathbf{h}} \\ C_{\mathbf{h}\mathbf{g}} & C_{\mathbf{h}\mathbf{h}} \end{pmatrix}.$$

The equation

$$\mathbf{g} - \mathbf{g}^* = -C_{\mathbf{g}\mathbf{g}}^{-1}C_{\mathbf{g}\mathbf{h}}(\mathbf{h} - \mathbf{h}^*)$$

defines a 2-dimensional subspace in \mathbb{R}^N , containing the points of the confidence ellipsoid $Z_{lin}^X(\sigma)$ with tangent space orthogonal to \mathcal{H} . This is called regression subspace of \mathbf{g} given \mathbf{h} (Milani et al. 2010, Section 5.4). The space \mathcal{H} can be mapped to the regression subspace by means of the map

$$\mathbf{h} - \mathbf{h}^* \mapsto \begin{pmatrix} \mathbf{h} - \mathbf{h}^* \\ -C_{\mathbf{g}\mathbf{g}}^{-1}C_{\mathbf{g}\mathbf{h}}(\mathbf{h} - \mathbf{h}^*) \end{pmatrix}. \quad (6.1)$$

²Without any further indication, we mean that the orthogonal subspace is taken with respect to the Euclidean scalar product in \mathbb{R}^N .

The linear map $D\mathbf{F}_{\mathbf{x}^*}$ can be described as the composition of the orthogonal projection on \mathcal{H} and of an invertible linear map

$$A : \mathcal{H} \rightarrow \mathcal{Y}.$$

Then $A^{-1}(K_{lin}^Y(\sigma))$ is an ellipse in \mathcal{H} , and the ellipse $\mathcal{E}_X(\sigma)$ on the surface of the ellipsoid is its image under the map defined by (6.1). Whatever the method of representation of the region $\mathbf{F}(Z_{lin}^X(\sigma))$, in the end we can only explore it by computing a finite number of orbits. To increase the level of resolution of this representation, however, the dimensionality of the space being sampled matters. The region $Z_{lin}^X(\sigma)$ is N -dimensional, and to increase the resolution by a factor 10 the number of orbits grows by a factor 10^N . The semilinear confidence boundary $K(\sigma)$ is a 1-dimensional curve, and the resolving power increases linearly with the number of orbits computed. In practice, even very complicated and strongly nonlinear examples can be dealt with only a few tens to a few hundred orbit propagations.

6.2 Determination of the impact corridor

We propose an adaptation of the semilinear method for the prediction of the impact corridor on ground for an asteroid that have a non-zero chance of impacting the Earth in the future. The algorithm needs an impacting orbit: in general the nominal solution does not impact the Earth, but still $IP > 0$ and thus there exists a set of orbits leading to an impact and still compatible with the observations. It suffices to suitably select one of these orbits, the VI representative (Milani et al. 2000), and use it as a starting point for the algorithm. Then the semilinear method provides the boundary of the impact corridor, roughly corresponding to the portion of the initial uncertainty region that leads to the impact. It is worth pointing out that the semilinear method is an approximation, thus it works if the impact probability values are high enough: in particular, we considered only impact probability $IP > 1 \cdot 10^{-3}$.

Let \mathbf{x}_0 be the nominal orbit and Γ_0 its covariance matrix, both provided at some epoch t_0 . Since the nominal orbit may not impact, what matters is the VI representative orbit. Let \mathbf{x}_{imp} be the orbit of the VI representative, provided at the same initial epoch t_0 as the nominal orbit. For a fixed altitude h , with $0 \leq h \leq h_{max} := 100$ km, the *impact surface* \mathcal{S}_h is the surface at height h above the Earth surface³ and its points are expressed using geodetic longitude and latitude coordinates.

³Note that even if we assume an ellipsoidal model for the Earth surface, \mathcal{S}_h is not an ellipsoid for $h > 0$.

Definition 6.1. Fix $\sigma > 0$ and h such that $0 \leq h \leq h_{max}$. The *impact region boundary* $\mathcal{B}_{\sigma,h}$ at altitude h and confidence level σ is the result of the propagation of the intersection of the virtual impactor with the boundary of the confidence ellipsoid $Z_{in}^X(\sigma)$, until the surface at altitude h above the Earth is reached.

Definition 6.2. The *impact corridor* \mathcal{C}_σ corresponding to the confidence level σ is the union of the boundaries of the impact regions from altitude h_{max} to the ground ($h = 0$). That is

$$\mathcal{C}_\sigma := \bigcup_{0 \leq h \leq h_{max}} \mathcal{B}_{\sigma,h}.$$

Definition 6.3. Let $W \subseteq \mathbb{R}^6$ be a neighbourhood of \mathbf{x}_{imp} such that each initial condition in W leads to an impact. The *impact map*

$$\mathbf{F}_h : W \rightarrow \mathcal{S}_h$$

is given by the composition between the propagation from the initial conditions to the impact time with the surface \mathcal{S}_h and the projection on \mathcal{S}_h .

The application of the semilinear method consists in following the steps described in Section 6.1, which we briefly recall (see also Figure 6.1 for a graphical representation).

- (1) The confidence region $Z_{in}^X(\sigma)$ is linearly propagated using the differential of \mathbf{F}_h at \mathbf{x}_{imp} . This allows one to obtain the linear confidence region $Z_{in}^Y(\sigma)$ on the tangent space to \mathcal{S}_h in $\mathbf{F}_h(\mathbf{x}_{imp})$.
- (2) The linear approximation given by $(D\mathbf{F}_h)_{\mathbf{x}_{imp}}$ is exploited to select a curve $\mathcal{E}_X(\sigma)$ on the boundary of the initial confidence ellipsoid $Z_{in}^X(\sigma)$, in fact an ellipse.
- (3) A finite sampling of the ellipse $\mathcal{E}_X(\sigma)$ is then non-linearly propagated with \mathbf{F}_h to obtain the semilinear confidence boundary at altitude h .

The points of this sample do not necessarily impact. For virtual impactors with $IP = 1$ all the points of the curve $\mathcal{E}_X(\sigma)$ lead to an impact. Thus to obtain a satisfactory sample of the semilinear boundary it suffices to sample the curve with few hundred points. On the contrary, for a virtual impactor with $0 < IP < 1$ so few points are usually not enough to obtain a clear representation of the semilinear boundary, even with the possibility to obtain no impacting points at all. Indeed the fraction of impacting points among the sampling is roughly proportional to IP , thus impact probabilities of the

order of 0.001 require about 100,000 points to obtain a proper visualization of the impact corridor. Such high number of orbits to propagate leads in turn to very long computational times, in such a way that an optimization procedure is needed to propagate the least possible number of non-impacting orbits, which do not contribute to the semilinear boundary sample. Different procedures can be implemented by exploiting the symmetry of the ellipse $\mathcal{E}_X(\sigma)$ with respect to the weak direction, *i.e.*, the direction of the semimajor axis. Indeed, if the stretching is high, we can also assume an approximated symmetry of the two impacting segments with respect to the semimajor axis. This assumption is not reliable for very low values of the stretching, and some other expedient could be found in these cases.

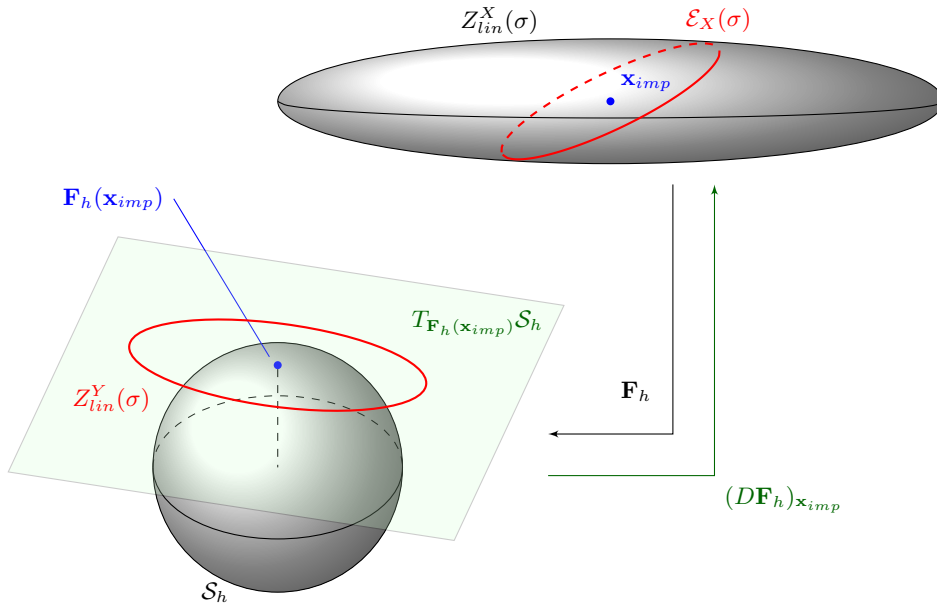


Figure 6.1. Graphical sketch of the application of the semilinear method described above in the steps (1)-(3).

6.3 Results

We tested our method on two asteroids, namely 2008 TC₃ and (99942) Apophis. Asteroid 2008 TC₃ impacted the Earth a few hours after its discovery: it was the first ever predicted impact of a near-Earth object. The locations of the meteorites recovered from the desert floor mark the asteroid's actual ground track and provide a unique opportunity to validate

impact location models such as the one presented in this chapter. We have already presented the “Apophis crisis” of December 2004 (Section 1.4): it is currently known that Apophis will not impact the Earth on 2029, but we can consider the observational dataset which gave the 2029 virtual impactor and compare the related impact corridor with the one computed by an independent system and with a different method, namely the JPL impact corridor computed with a Monte Carlo simulation. In both cases we obtain a remarkable agreement between the two results.

The semilinear method succeeds in providing the boundary of the impact region on ground, with a comparatively smaller number of propagations with respect to Monte Carlo approaches. Indeed it samples a 1-dimensional curve instead of a region in the 6-dimensional orbital elements space.

Concerning the graphical representation of the impact corridor, whatever the method that computes the impact locations, the output is likely to be a data file with geocentric coordinates representing points on the Earth surface. It is then needed to plot them on the terrestrial globe, and we exploited the already existing software Google Earth/Maps for the figures of this chapter.

6.3.1 Evolution of the impact corridor for 2008 TC₃

As already presented in Section 2.9.2, 2008 TC₃ is a small asteroid that impacted the Earth on 2008 October 7. When it was first detected (about 20 h before impact), 2008 TC₃ was still farther away than the Moon. Once it was recognized and announced as an impactor, it received considerable attention from the observers in such a way that now we have available an observational dataset composed by nearly 900 observations. Furthermore, the locations of the many meteorites recovered from the desert floor mark the asteroid’s actual ground track and provide a unique opportunity to validate impact location models such as the one presented in this chapter.

First we predicted the impact regions of 2008 TC₃ using reduced observational datasets, simulating the computations that would have been done immediately after the impact risk announcement. For each altitude h we show with different colours three different impact regions, namely those corresponding to the confidence levels $\sigma = 1$, $\sigma = 3$ and $\sigma = 5$. Figure 6.2, 6.3 and 6.4 show the impact regions for altitudes 0 and 100 km, computed using 12, 16, and 26 observations, respectively. The blue line is the nominal ground track. In all 2008 TC₃ images the locations of the recovered meteorites reported in Shaddad et al. (2010) are shown, with larger and darker circles for larger masses.

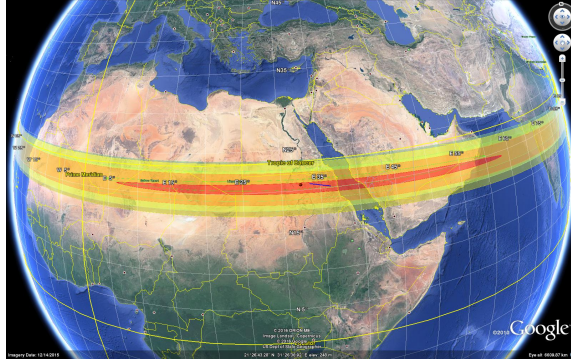


Figure 6.2. Prediction of the impact region of 2008 TC₃ using the first 12 observations (almost 18 hours before impact).



Figure 6.3. Prediction of the impact region of 2008 TC₃ using the first 16 observations (about 12 hours before impact).

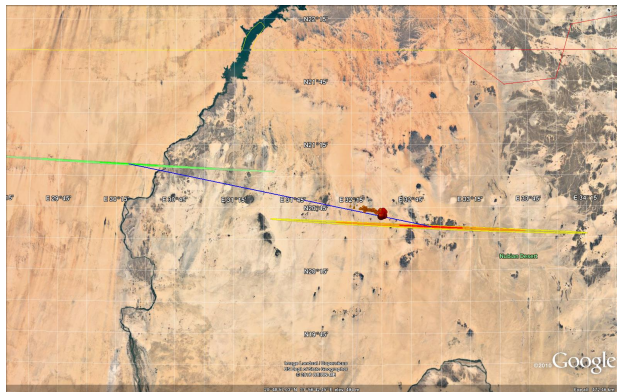


Figure 6.4. Prediction of the impact region of 2008 TC₃ using the first 26 observations (about 11 hours and a half before impact).

Finally, we analysed the results when using the full dataset of 883 observations available before impact. This case is linear and the orbit is over-determined, so that the $1\text{-}\sigma$ uncertainty region is very small, $\simeq 0.05 \times 0.5$ km at impact on ground. In Figure 6.5 we show the 2008 TC_3 impact regions on ground and for altitudes corresponding to 37 km, 65.4 km and 100 km. Figure 6.6 is just an enlargement of Figure 6.5 between $h = 37$ km and $h = 0$ km. Detections of the actual atmospheric impact event suggested an atmospheric entry at 65.4 km, followed by an airburst explosion at an altitude of 37 km, with an energy equivalent to about one kiloton of TNT explosives. This explain why both Figure 6.6 and Figure 6.5 also show the regions at altitudes 37 km and 65.4 km, in addition to those on the ground and at $h = 100$ km.

The JPL team provides a precise estimate of the trajectory of 2008 TC_3 and its impact ground track in Farnocchia et al. (2017b). They perform the orbit determination after a careful analysis of the astrometric dataset and in the selection of the weights to assign to each observation. From one side they accounted for the expected quality of some observers, and for the other side they deweighted the observations toward the end of the arc since they show a gradually poorer quality. Moreover, they employed a high-precision force model, containing the Newtonian terms for the Sun, the planets, Pluto, the Moon, and the most 16 massive main-belt bodies, as well as the relativistic terms for eight planets and the quadrupole term of the Earth gravity field. The outcome of the impact location prediction on ground has been compared to that obtained by our method, starting from the same nominal orbit and using the same force model. The differences between the two predictions are as large as 3 m, suggesting that the propagation error is at the few meter level and showing a very good agreement between the two methods.

6.3.2 Apophis

We already presented the story of Apophis in Section 1.4. A few months after its discovery, Apophis was recognized as a potentially hazardous asteroid, with a peak impact probability of $\simeq 2.7\%$ in April 2029, as computed by both Sentry and NEODyS (see Section 1.4 for a more detailed report). On 2004 December 27 the Spacewatch survey reported precovery observations that ruled out any impact possibility for 2029. However, there will be a historically close approach with the Earth, estimated to be a 1 in 800 year event on average, for an object of that size.

We recovered the situation for Apophis corresponding to 2004 December 27⁴: this set corresponds to the situation just before the availability of

⁴The set of observations taken is the one of MPEC 2004-Y69.



Figure 6.5. Prediction of the impact region of 2008 TC₃ with 883 observations.



Figure 6.6. Enlargement of the previous plot between $h = 37$ km and $h = 0$ km.

the precovery observations which ruled out the 2029 impact chance. We computed a full least squares solution by using the debiasing and weighting scheme provided in Farnocchia et al. (2015b) and, to ensure a more complete force model, we also include the contributions coming from 16 massive main belt bodies and Pluto. Furthermore we included the effect of Earth oblateness in the vicinity of Earth, *i.e.*, when the distance is less than 0.1 au. Starting from this nominal solution, we computed the impact monitoring in Equinoctial elements and by using the uniform-in-probability sampling of the LOV, as presented in Chapter 4. This computation results in a virtual impactor with impact on 2029 April 13 and with probability 2.42%. We use the corresponding VI representative to apply our method, and the result

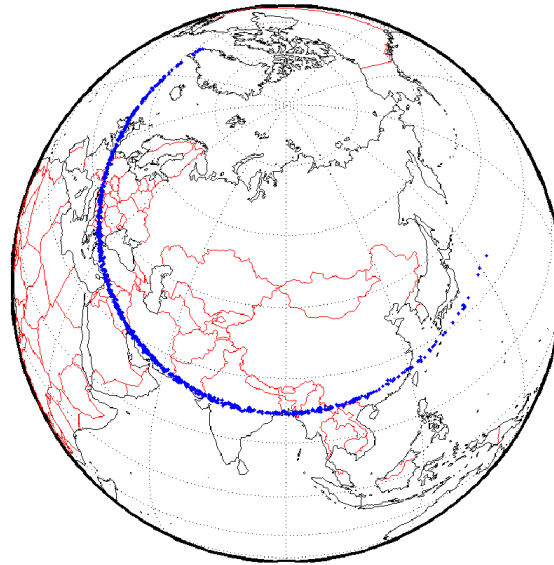
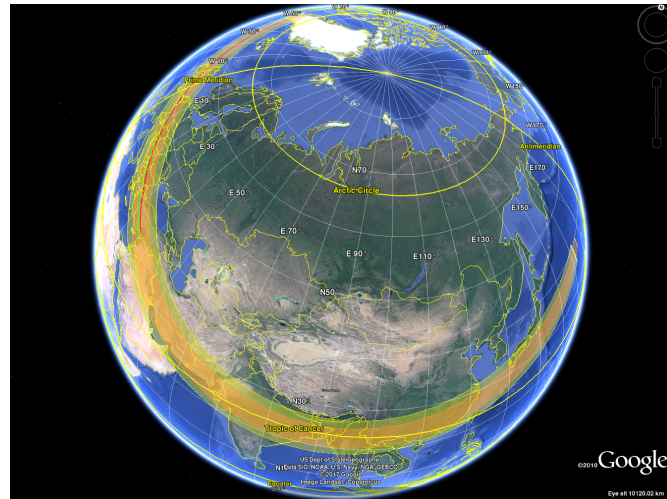


Figure 6.7. *Top panel.* Semilinear prediction of the 2029 impact regions of Apophis, using the observations available on 2004 December 27. *Bottom panel.* Monte Carlo prediction of the 2029 impact locations of Apophis, using the same observational dataset of the above figure (JPL, private communication).

is shown in Figure 6.7 (top panel), whereas the bottom panel shows the impact corridor computed with the same observational dataset by the JPL team using a Monte Carlo method⁵.

⁵Private communication by Steven R. Chesley.

Appendix A

Target Planes

Hereinafter we describe the transformation from the Modified Target Plane (MTP) reference system to the Target Plane (TP) reference system (Tommei 2006). This transformation uses three maps:

$$(\mathbf{x}, \mathbf{y}) \mapsto (\mathbf{x}', \mathbf{y}') \mapsto (\mathbf{x}^{TP}, \mathbf{y}^{TP}) \mapsto (\bar{\mathbf{x}}, \bar{\mathbf{y}}).$$

The first map is the rotation bringing the MTP to coincide with the TP. The second is the scaling mapping the Earth cross section on the MTP to that on the TP (they have different radii due to the gravitational focusing to take into account for the TP). The third is a basis change, and leads to the definition of a suitable set of Öpik elements. We also provide the derivatives of all this maps.

The set of the so-called modified Öpik elements is defined through a further map:

$$(\bar{\mathbf{x}}, \mathbf{y}^{TP}) \mapsto (U, \alpha, \delta, \xi, \zeta, \eta),$$

and it is very important, being the coordinate set used in the computations performed by CLOMON-2.

A.1 Angular momentum

Let $\mathbf{x} = (x_1, x_2, x_3)$, $\mathbf{y} = (y_1, y_2, y_3)$ be respectively the position and velocity of the asteroid at the MTP crossing. Since $\mathbf{J} = \mathbf{x} \times \mathbf{y}$, the components of the angular momentum $\mathbf{J} = (J_1, J_2, J_3)$ are

$$J_h = \sum_{i=1}^3 \varepsilon_{ijh} x_i y_j.$$

In the previous equation we have used the Levi-Civita symbol

$$\varepsilon_{ijk} = \begin{cases} 1 & \text{if } (i j k) \text{ is an even permutation} \\ -1 & \text{if } (i j k) \text{ is an odd permutation} \\ 0 & \text{if two indexes have the same value} \end{cases}$$

We shall assume that $\mathbf{x} \cdot \mathbf{y} = 0$, so that, if $\|\mathbf{x}\| = d$ and $\|\mathbf{y}\| = V$, we have $\|\mathbf{J}\| = dV$.

A.2 The first transformation

The first map

$$(\mathbf{x}, \mathbf{y}) \mapsto (\mathbf{x}', \mathbf{y}')$$

is a rotation by $\frac{\gamma}{2}$ around the normalized angular momentum vector $\mathbf{j} = (j_1, j_2, j_3)$. We shall write $\mathbf{x}' = (x'_1, x'_2, x'_3)$ and $\mathbf{y}' = (y'_1, y'_2, y'_3)$ for the components of the image of this map.

Let us define

$$H_{Roy} := \sqrt{j_1^2 + j_2^2}.$$

If I and Ω are the inclination and the longitude of pericentre of the asteroid, we have

$$\begin{aligned} \cos I &= j_3 & \cos \Omega &= -\frac{j_2}{H_{Roy}} & \cos \frac{\gamma}{2} &= \sqrt{1 - \sin^2 \frac{\gamma}{2}} \\ \sin I &= H_{Roy} & \sin \Omega &= \frac{j_1}{H_{Roy}} \end{aligned}$$

We define the rotation matrices

$$\mathbf{R}_{\Omega}^{(3)} = \begin{pmatrix} \cos \Omega & -\sin \Omega & 0 \\ \sin \Omega & \cos \Omega & 0 \\ 0 & 0 & 1 \end{pmatrix} \quad \mathbf{R}_I^{(1)} = \begin{pmatrix} 1 & 0 & 0 \\ 0 & \cos I & -\sin I \\ 0 & \sin I & \cos I \end{pmatrix}$$

$$\mathbf{R}_{\gamma/2}^{(3)} = \begin{pmatrix} \cos \frac{\gamma}{2} & -\sin \frac{\gamma}{2} & 0 \\ \sin \frac{\gamma}{2} & \cos \frac{\gamma}{2} & 0 \\ 0 & 0 & 1 \end{pmatrix},$$

and

$$\mathcal{R} := \mathbf{R}_{\Omega}^{(3)} \cdot \mathbf{R}_I^{(1)} \cdot \mathbf{R}_{-\gamma/2}^{(3)} \cdot \mathbf{R}_{-I}^{(1)} \cdot \mathbf{R}_{-\Omega}^{(3)}.$$

The rotation $\mathbf{R}_{-I}^{(1)} \cdot \mathbf{R}_{-\Omega}^{(3)}$ brings the x_3 axis to coincide with the direction of $\hat{\mathbf{j}}$. The first map can be written as

$$(\mathbf{x}', \mathbf{y}') = (\mathcal{R}\mathbf{x}, \mathcal{R}\mathbf{y}).$$

We shall now compute the Jacobian matrix of the transformation: the rotation matrix \mathcal{R} depends on γ and on the direction of the angular momentum \mathbf{j} . Setting $s := \sin \frac{\gamma}{2}$ we have

$$\begin{aligned}\frac{\partial x'_i}{\partial x_j} &= \mathcal{R}_{i,j} + \sum_{k=1}^3 \frac{\partial \mathcal{R}_{i,k}}{\partial s} \frac{\partial s}{\partial x_j} x_k + \sum_{h=1}^3 \sum_{k=1}^3 \frac{\partial \mathcal{R}_{i,k}}{\partial j_h} \frac{\partial j_h}{\partial x_j} x_k \\ \frac{\partial x'_i}{\partial y_j} &= \mathcal{R}_{i,j} + \sum_{k=1}^3 \frac{\partial \mathcal{R}_{i,k}}{\partial s} \frac{\partial s}{\partial y_j} x_k + \sum_{h=1}^3 \sum_{k=1}^3 \frac{\partial \mathcal{R}_{i,k}}{\partial j_h} \frac{\partial j_h}{\partial y_j} x_k \\ \frac{\partial y'_i}{\partial x_j} &= \mathcal{R}_{i,j} + \sum_{k=1}^3 \frac{\partial \mathcal{R}_{i,k}}{\partial s} \frac{\partial s}{\partial x_j} y_k + \sum_{h=1}^3 \sum_{k=1}^3 \frac{\partial \mathcal{R}_{i,k}}{\partial j_h} \frac{\partial j_h}{\partial x_j} y_k \\ \frac{\partial y'_i}{\partial y_j} &= \mathcal{R}_{i,j} + \sum_{k=1}^3 \frac{\partial \mathcal{R}_{i,k}}{\partial s} \frac{\partial s}{\partial y_j} y_k + \sum_{h=1}^3 \sum_{k=1}^3 \frac{\partial \mathcal{R}_{i,k}}{\partial j_h} \frac{\partial j_h}{\partial y_j} y_k\end{aligned}$$

Derivatives with respect to s

By using the conservation of angular momentum, we obtain

$$s = \frac{Gm}{V^2 d - Gm}.$$

Setting $\hat{\mathbf{x}} := \frac{\mathbf{x}}{d}$ and $\hat{\mathbf{y}} := \frac{\mathbf{y}}{V}$ we have

$$\frac{\partial s}{\partial d} = -\frac{V^2}{Gm} s^2, \quad \frac{\partial s}{\partial \mathbf{x}} = \frac{\partial s}{\partial d} \hat{\mathbf{x}}, \quad \frac{\partial s}{\partial V} = -\frac{2Vd}{Gm} s^2, \quad \frac{\partial s}{\partial \mathbf{y}} = \frac{\partial s}{\partial V} \hat{\mathbf{y}}.$$

Moreover

$$\frac{\partial \mathcal{R}}{\partial s} = \mathbf{R}_{\Omega}^{(3)} \cdot \mathbf{R}_I^{(1)} \cdot \frac{\partial}{\partial s} \mathbf{R}_{-\gamma/2}^{(3)} \cdot \mathbf{R}_{-I}^{(1)} \cdot \mathbf{R}_{-\Omega}^{(3)}$$

where

$$\frac{\partial}{\partial s} \mathbf{R}_{-\gamma/2}^{(3)} = \begin{pmatrix} -\tan(\gamma/2) & 1 & 0 \\ -1 & -\tan(\gamma/2) & 0 \\ 0 & 0 & 0 \end{pmatrix}.$$

Derivatives with respect to \mathbf{j}

Now we give the expression for the derivatives of the rotation \mathcal{R} with respect to the normalized angular momentum \mathbf{j} .

$$\begin{aligned} \frac{\partial \mathcal{R}}{\partial j_k} &= \frac{\partial}{\partial j_k} \left[\mathbf{R}_\Omega^{(3)} \right] \cdot \mathbf{R}_I^{(1)} \cdot \mathbf{R}_{-\gamma/2}^{(3)} \cdot \mathbf{R}_{-I}^{(1)} \cdot \mathbf{R}_{-\Omega}^{(3)} + \\ &+ \mathbf{R}_\Omega^{(3)} \cdot \frac{\partial}{\partial j_k} \left[\mathbf{R}_I^{(1)} \right] \cdot \mathbf{R}_{-\gamma/2}^{(3)} \cdot \mathbf{R}_{-I}^{(1)} \cdot \mathbf{R}_{-\Omega}^{(3)} + \\ &+ \mathbf{R}_\Omega^{(3)} \cdot \mathbf{R}_I^{(1)} \cdot \mathbf{R}_{-\gamma/2}^{(3)} \cdot \frac{\partial}{\partial j_k} \left[\mathbf{R}_{-I}^{(1)} \right] \cdot \mathbf{R}_{-\Omega}^{(3)} + \\ &+ \mathbf{R}_\Omega^{(3)} \cdot \mathbf{R}_I^{(1)} \cdot \mathbf{R}_{-\gamma/2}^{(3)} \cdot \mathbf{R}_{-I}^{(1)} \cdot \frac{\partial}{\partial j_k} \left[\mathbf{R}_{-\Omega}^{(3)} \right] \end{aligned}$$

where

$$\begin{aligned} \frac{\partial}{\partial j_k} \mathbf{R}_\Omega^{(3)} &= \begin{pmatrix} -\frac{\delta_{2,k}}{H_{Roy}} + \frac{j_2}{H_{Roy}^2} \frac{\partial H_{Roy}}{\partial j_k} & -\frac{\delta_{1,k}}{H_{Roy}} + \frac{j_1}{H_{Roy}^2} \frac{\partial H_{Roy}}{\partial j_k} & 0 \\ \frac{\delta_{1,k}}{H_{Roy}} - \frac{j_1}{H_{Roy}^2} \frac{\partial H_{Roy}}{\partial j_k} & -\frac{\delta_{2,k}}{H_{Roy}} + \frac{j_2}{H_{Roy}^2} \frac{\partial H_{Roy}}{\partial j_k} & 0 \\ 0 & 0 & 0 \end{pmatrix} \\ \frac{\partial}{\partial j_k} \mathbf{R}_I^{(1)} &= \begin{pmatrix} 0 & 0 & 0 \\ 0 & \delta_{3,k} & -\frac{\partial H_{Roy}}{\partial j_k} \\ 0 & \frac{\partial H_{Roy}}{\partial j_k} & \delta_{3,k} \end{pmatrix} \\ \frac{\partial}{\partial j_k} \mathbf{R}_{-I}^{(1)} &= \begin{pmatrix} 0 & 0 & 0 \\ 0 & \delta_{3,k} & \frac{\partial H_{Roy}}{\partial j_k} \\ 0 & -\frac{\partial H_{Roy}}{\partial j_k} & \delta_{3,k} \end{pmatrix} \\ \frac{\partial}{\partial j_k} \mathbf{R}_{-\Omega}^{(3)} &= \begin{pmatrix} -\frac{\delta_{2,k}}{H_{Roy}} + \frac{j_2}{H_{Roy}^2} \frac{\partial H_{Roy}}{\partial j_k} & \frac{\delta_{1,k}}{H_{Roy}} - \frac{j_1}{H_{Roy}^2} \frac{\partial H_{Roy}}{\partial j_k} & 0 \\ -\frac{\delta_{1,k}}{H_{Roy}} + \frac{j_1}{H_{Roy}^2} \frac{\partial H_{Roy}}{\partial j_k} & -\frac{\delta_{2,k}}{H_{Roy}} + \frac{j_2}{H_{Roy}^2} \frac{\partial H_{Roy}}{\partial j_k} & 0 \\ 0 & 0 & 0 \end{pmatrix} \end{aligned}$$

In the previous formulas we have used the Kronecker delta

$$\delta_{hk} = \begin{cases} 1 & \text{if } h = k \\ 0 & \text{if } h \neq k \end{cases}$$

and the derivatives of H_{Roy} with respect to the normalized angular momentum components

$$\frac{\partial H_{Roy}}{\partial j_1} = \frac{j_1}{H_{Roy}}, \quad \frac{\partial H_{Roy}}{\partial j_2} = \frac{j_2}{H_{Roy}}, \quad \frac{\partial H_{Roy}}{\partial j_3} = 0.$$

Indicating with ε an estimate of the rounding off, if $H_{Roy} < \varepsilon$ we assume $\Omega = 0$ and $R_{\Omega}^{(3)} = I$. Then $\frac{\partial}{\partial j_k} \mathbf{R}_{\Omega}^{(3)} \neq 0$ but has to be computed in a non singular way.

We also have

$$\frac{\partial j_h}{\partial x_j} = \frac{\partial}{\partial x_j} \left(\frac{J_h}{Vd} \right) = \frac{1}{Vd} \sum_{i=1}^3 \varepsilon_{jih} y_i - \frac{J_h x_j}{Vd^3} = \frac{1}{Vd} \sum_{i=1}^3 \varepsilon_{jih} y_i - \frac{j_h x_j}{d^2},$$

$$\frac{\partial j_h}{\partial y_j} = \frac{\partial}{\partial y_j} \left(\frac{J_h}{Vd} \right) = \frac{1}{Vd} \sum_{i=1}^3 \varepsilon_{ijh} x_i - \frac{J_h y_j}{dV^3} = \frac{1}{Vd} \sum_{i=1}^3 \varepsilon_{ijh} x_i - \frac{j_h y_j}{V^2}.$$

A.3 The second transformation

The second map is

$$(\mathbf{x}', \mathbf{y}') \rightarrow (\mathbf{x}^{TP}, \mathbf{y}^{TP}) = \left(\beta \mathbf{x}', \frac{1}{\beta} \mathbf{y}' \right)$$

where

$$\beta := \frac{b}{d} = \left(\frac{V^2 d}{V^2 d - 2Gm} \right)^{1/2}.$$

This map is the scaling of the distance from the MTP to the TP: a point having a unit distance from the Earth centre on the MTP corresponds to a point with distance b from the Earth centre on the TP.

The Jacobian matrix of this second transformation is given by the following derivatives:

$$\begin{aligned} \frac{\partial x_i^{TP}}{\partial x'_j} &= \beta \delta_{ij} + \frac{\partial \beta}{\partial d} \frac{x'_j}{d} x'_i, & \frac{\partial x_i^{TP}}{\partial y'_j} &= \frac{\partial \beta}{\partial V} \frac{y'_j}{V} x'_i \\ \frac{\partial y_i^{TP}}{\partial x'_j} &= -\frac{1}{\beta^2} \frac{\partial \beta}{\partial d} \frac{x'_j}{d} y'_i, & \frac{\partial y_i^{TP}}{\partial y'_j} &= \frac{\delta_{ij}}{\beta} - \frac{1}{\beta^2} \frac{\partial \beta}{\partial V} \frac{y'_j}{V} y'_i \end{aligned}$$

and

$$\frac{\partial \beta}{\partial d} = -\frac{Gm\beta^3}{V^2 d^2}, \quad \frac{\partial \beta}{\partial V} = -\frac{2Gm\beta^3}{V^3 d}.$$

A.4 The third transformation

The third map is a rotation to line up the velocity vector with the second axis of the reference system. The rotation matrix \mathcal{S} has rows $\{\mathcal{S}^i\}_{i=1,2,3}$ such that

$$\mathcal{S}^1 := \frac{\mathbf{y}^{TP}}{U}$$

is the velocity direction. The second direction is selected as $\mathbf{e}_3 = (0, 0, 1)$, and then the Graham-Schmidt algorithm is used:

$$\begin{aligned}\mathbf{w} &= \mathbf{e}_3 - (\mathbf{e}_3 \cdot \mathcal{S}^1)\mathcal{S}^1 \\ \mathcal{S}^3 &:= \frac{\mathbf{w}}{\|\mathbf{w}\|} \\ \mathcal{S}^2 &:= \mathcal{S}^1 \times \mathcal{S}^3.\end{aligned}$$

Thus, setting $\mathbf{y}^{TP} = (u_1, u_2, u_3)$, the matrix \mathcal{S} is

$$\mathcal{S} = \begin{pmatrix} \frac{u_1}{U} & \frac{u_2}{U} & \frac{u_3}{U} \\ \frac{u_2}{\sqrt{u_1^2 + u_2^2}} & -\frac{u_1}{\sqrt{u_1^2 + u_2^2}} & 0 \\ -\frac{u_1 u_3}{U\sqrt{u_1^2 + u_2^2}} & -\frac{u_2 u_3}{U\sqrt{u_1^2 + u_2^2}} & \frac{u_1^2 + u_2^2}{U\sqrt{u_1^2 + u_2^2}} \end{pmatrix},$$

where $U = \sqrt{u_1^2 + u_2^2 + u_3^2}$. To compute the partial derivatives, we need to take into account that

$$\frac{\partial \mathcal{S}}{\partial \mathbf{x}^{TP}} = \mathbf{0},$$

and therefore

$$\begin{aligned}\frac{\partial \bar{x}_i}{\partial x_j^{TP}} &= \mathcal{S}_{ij}, & \frac{\partial \bar{x}_i}{\partial y_j^{TP}} &= \sum_{k=1}^3 \frac{\partial \mathcal{S}_{ik}}{\partial y_j^{TP}} x_k^{TP} \\ \frac{\partial \bar{y}_i}{\partial x_j^{TP}} &= 0, & \frac{\partial \bar{y}_i}{\partial y_j^{TP}} &= \mathcal{S}_{ij} + \sum_{k=1}^3 \frac{\partial \mathcal{S}_{ik}}{\partial y_j^{TP}} y_k^{TP}\end{aligned}$$

The derivatives of \mathcal{S} with respect to (u_1, u_2, u_3) are needed in the previous partials. They are

$$\begin{aligned}\frac{\partial \mathcal{S}^1}{\partial (u_1, u_2, u_3)} &= \frac{1}{U^3} \begin{pmatrix} u_2^2 + u_3^2 & -u_1 u_2 & -u_1 u_3 \\ -u_1 u_2 & u_1^2 + u_3^2 & -u_2 u_3 \\ -u_1 u_3 & -u_2 u_3 & u_1^2 + u_2^2 \end{pmatrix} \\ \frac{\partial \mathcal{S}^2}{\partial (u_1, u_2, u_3)} &= \frac{1}{(u_1^2 + u_2^2)^{3/2}} \begin{pmatrix} -u_1 u_2 & u_1^2 & 0 \\ -u_2^2 & u_1 u_2 & 0 \\ 0 & 0 & 0 \end{pmatrix} \\ \frac{\partial \mathcal{S}^3}{\partial (u_1, u_2, u_3)} &= \frac{1}{U^3 (u_1^2 + u_2^2)^{3/2}} M_3\end{aligned}$$

where

$$M_3 = \begin{pmatrix} u_3[(u_1^2 - U^2)(u_1^2 + u_2^2) + U^2 u_1^2] & u_1 u_2 u_3 (u_1^2 + u_2^2 + U^2) & u_1 (u_3^2 - U^2)(u_1^2 + u_2^2) \\ u_1 u_2 u_3 (u_1^2 + u_2^2 + U^2) & u_3 [(u_2^2 - U^2)(u_1^2 + u_2^2) + U^2 u_2^2] & u_2 (u_3^2 - U^2)(u_1^2 + u_2^2) \\ u_1 u_3^2 (u_1^2 + u_2^2) & u_2 u_3^2 (u_1^2 + u_2^2) & -u_3 (u_1^2 + u_2^2)^2 \end{pmatrix}.$$

A.5 Modified Öpik elements

The *modified Öpik elements* are defined as follows. The first three elements, namely $(U, \alpha, \delta) \in \mathbb{R}^+ \times \mathbb{S}^1 \times [0, \pi]$, are polar coordinates of \mathbf{y}^{TP} . In particular

$$U = \|\mathbf{y}^{TP}\|$$

is the unperturbed planetocentric velocity, and the two angles are such that

$$\begin{cases} u_1 = U \cos \delta \cos \alpha \\ u_2 = U \cos \delta \sin \alpha \\ u_3 = U \sin \delta \end{cases}$$

The three coordinates (ξ, ζ, η) are $\bar{\mathbf{x}}$, just in a different order for historical reasons:

$$\begin{cases} \xi := \bar{x}_2 \\ \zeta := \bar{x}_3 \\ \eta := \bar{x}_1 \end{cases}$$

Concerning the partial of this last map, we can simply obtain

$$\frac{\partial U}{\partial \mathbf{x}^{TP}} = \mathbf{0}, \quad \frac{\partial U}{\partial \mathbf{y}^{TP}} = \frac{\mathbf{y}^{TP}}{\|\mathbf{y}^{TP}\|}.$$

By writing $\alpha = \arctan \frac{u_2}{u_1}$ and $\delta = \arcsin \frac{u_3}{U}$ we compute

$$\frac{\partial \alpha}{\partial \mathbf{x}^{TP}} = \mathbf{0}, \quad \frac{\partial \delta}{\partial \mathbf{x}^{TP}} = \mathbf{0}$$

and

$$\begin{aligned} \frac{\partial \alpha}{\partial u_1} &= -\frac{u_2}{u_1^2 + u_2^2}, & \frac{\partial \alpha}{\partial u_2} &= \frac{u_1}{u_1^2 + u_2^2}, & \frac{\partial \alpha}{\partial u_3} &= 0, \\ \frac{\partial \delta}{\partial u_1} &= -\frac{u_1 u_3}{U^2 \sqrt{u_1^2 + u_2^2}}, & \frac{\partial \delta}{\partial u_2} &= -\frac{u_2 u_3}{U^2 \sqrt{u_1^2 + u_2^2}}, & \frac{\partial \delta}{\partial u_3} &= \frac{\sqrt{u_1^2 + u_2^2}}{U^2}. \end{aligned}$$

Moreover, since the modified Öpik elements are the components of $\mathcal{S}\mathbf{x}^{TP}$, we obtain

$$\frac{\partial \xi}{\partial \mathbf{x}^{TP}} = \mathcal{S}^2, \quad \frac{\partial \xi}{\partial y_j^{TP}} = \sum_{k=1}^3 \frac{\partial \mathcal{S}_{2k}}{\partial y_j^{TP}} x_k^{TP}, \quad j = 1, 2, 3$$

and

$$\frac{\partial \zeta}{\partial \mathbf{x}^{TP}} = \mathcal{S}^3, \quad \frac{\partial \zeta}{\partial y_j^{TP}} = \sum_{k=1}^3 \frac{\partial \mathcal{S}_{3k}}{\partial y_j^{TP}} x_k^{TP}, \quad j = 1, 2, 3.$$

Appendix B

The Farey sequence

B.1 Arithmetical functions

Definition B.1. An *arithmetical function* is a function $f : \mathbb{N}^* \rightarrow \mathbb{C}$, where \mathbb{N}^* is the set of non-zero natural numbers.

The set of the arithmetical functions can be endowed with two natural operations, the sum and the scalar multiplication (over \mathbb{C}).

Definition B.2. Let f and g be two arithmetical functions. Their *Dirichlet convolution* is the arithmetical function $f * g$ defined by

$$(f * g)(n) := \sum_{d|n} f(d)g\left(\frac{n}{d}\right).$$

With these three operations, the set of the arithmetical functions turns out to be a commutative algebra. The identity function for the convolution is the arithmetical function

$$e(n) := \begin{cases} 1 & \text{if } n = 1 \\ 0 & \text{if } n > 1 \end{cases}.$$

To fix the notation, we also define

$$1(n) := 1 \quad \text{for all } n \in \mathbb{N}^*$$

and

$$i(n) := n \quad \text{for all } n \in \mathbb{N}^*.$$

B.1.1 Euler totient function

Definition B.3. For each integer $n \geq 1$ we define $\varphi(n)$ as the number of positive integers $\leq n$ and relatively prime with n . The function φ is called the *Euler totient function*.

Three basic properties hold for the function φ . Their proof can be found in Hardy et al. (2008).

- (1) φ is a multiplicative function, i.e. $\varphi(nm) = \varphi(n)\varphi(m)$ for all integers n and m such that $(n, m) = 1$.
- (2) If p is prime, then $\varphi(p) = p - 1$.
- (3) If p is prime, then $\varphi(p^n) = p^n - p^{n-1} = p^n \left(1 - \frac{1}{p}\right)$.

Theorem B.4. For all $n > 1$

$$\varphi(n) = n \prod_{p|n} \left(1 - \frac{1}{p}\right).$$

Proof. From the fundamental theorem of arithmetic we can write $n = \prod_{p|n} p^{a_p}$ in a unique way. From the previous properties

$$\begin{aligned} \varphi(n) &= \varphi\left(\prod_{p|n} p^{a_p}\right) = \prod_{p|n} \varphi(p^{a_p}) = \prod_{p|n} (p^{a_p} - p^{a_p-1}) = \\ &= \prod_{p|n} p^{a_p} \left(1 - \frac{1}{p}\right) = \prod_{p|n} p^{a_p} \prod_{p|n} \left(1 - \frac{1}{p}\right) = n \prod_{p|n} \left(1 - \frac{1}{p}\right). \end{aligned}$$

□

B.1.2 The Möbius function

Definition B.5. The *Möbius function* is the arithmetical function defined by

$$\mu(n) := \begin{cases} 1 & \text{if } n = 1 \\ 0 & \text{if } p^e \mid n \text{ for some prime } p \text{ and } e > 1 \\ (-1)^r & \text{if } n \text{ is the product of } r \text{ distinct primes} \end{cases}$$

Note that $\mu(n) = 0$ if and only if n has a square factor > 1 . As well as the totient function, μ is a multiplicative function, as directly follows from the definition.

Proposition B.6. For every $n \geq 1$

$$\sum_{d|n} \mu(d) = \begin{cases} 1 & \text{se } n = 1 \\ 0 & \text{se } n > 1 \end{cases},$$

that is $1 * \mu = e$.

Proof. The statement is clearly true for $n = 1$. Assume, then, that $n > 1$ and write $n = \prod_{i=1}^m p_i^{a_i}$. In the sum $\sum_{d|n} \mu(d)$, the only non-zero terms come from $d = 1$ and from those divisors of n which are products of distinct primes. Thus

$$\begin{aligned} \mu(n) &= \mu(1) + \sum_i \mu(p_i) + \sum_{i<j} \mu(p_i p_j) + \dots + \mu(p_1 p_2 \dots p_m) = \\ &= \sum_{i=0}^m (-1)^i \binom{m}{i} = (1-1)^m = 0. \end{aligned}$$

□

Proposition B.7. For each $n \geq 1$

$$\varphi(n) = \sum_{d|n} \mu(d) \frac{n}{d},$$

that is $\varphi = i * \mu$.

Proof. From Proposition B.6 we can write

$$\varphi(n) = \sum_{\substack{k=1 \\ (k,n)=1}}^n 1 = \sum_{k=1}^n \sum_{d|(k,n)} \mu(d) = \sum_{k=1}^n \sum_{\substack{d|k \\ d|n}} \mu(d).$$

Let d be a divisor of n . The two conditions on k can be written as $k = qd$ and $1 \leq q \leq \frac{n}{d}$, thus

$$\varphi(n) = \sum_{d|n} \sum_{1 \leq q \leq \frac{n}{d}} \mu(d) = \sum_{d|n} \mu(d) \sum_{1 \leq q \leq \frac{n}{d}} 1 = \sum_{d|n} \mu(d) \frac{n}{d}.$$

□

B.2 Dirichlet series

Definition B.8. A *Dirichlet series* is a series

$$\sum_{n=1}^{\infty} \frac{f(n)}{n^s}, \quad (\text{B.1})$$

where f is an arithmetical function and $s \in \mathbb{C}$. This series is also called the *generating function* of f .

The following are two classical results. More details on Dirichlet series and generating functions can be found in Apostol (1976, Chapter 11).

Theorem B.9. *Suppose the series*

$$\sum_{n=1}^{\infty} \left| \frac{f(n)}{n^s} \right|$$

does not converge for all s or diverge for all s . Then there exists a real number $\bar{\sigma}$ such that the series (B.1) converges absolutely for $\operatorname{Re}(s) > \bar{\sigma}$ and does not converge absolutely for $\operatorname{Re}(s) < \bar{\sigma}$.

Proof. First note that if $\operatorname{Re}(s) > \sigma_0$, then

$$\left| \frac{f(n)}{n^s} \right| \leq \frac{|f(n)|}{n^{\sigma_0}}.$$

Therefore, if a Dirichlet series converges absolutely for a certain s_0 with $\operatorname{Re}(s_0) = \sigma_0$, then it is absolutely convergent for all s with $\operatorname{Re}(s) \geq \sigma_0$, by the comparison test.

Let D be the set of all real σ such that $\sum_{n=1}^{\infty} \left| \frac{f(n)}{n^s} \right|$ diverges. Thus D is not empty because the series does not converge for all s , and D is bounded above because the series does not diverge for all s . Therefore there exists $\bar{\sigma} = \sup D$. If $\sigma < \bar{\sigma}$ then $\sigma \in D$ because otherwise σ would be an upper bound for D smaller than the least upper bound $\bar{\sigma}$. If $\sigma > \bar{\sigma}$ then $\sigma \notin D$ since $\bar{\sigma}$ is an upper bound for D . \square

In case the series (B.1) converges absolutely for all s we define $\bar{\sigma} = -\infty$, whereas if the series does not converge absolutely for all s we define $\bar{\sigma} = +\infty$. In this way, $\bar{\sigma}$ is called the *abscissa of absolute convergence* of the series.

Theorem B.10. *Let $F(s)$ and $G(s)$ be the two Dirichlet series*

$$F(s) = \sum_{n=1}^{\infty} \frac{f(n)}{n^s} \quad \text{and} \quad G(s) = \sum_{n=1}^{\infty} \frac{g(n)}{n^s},$$

and let $\bar{\sigma}_1$ and $\bar{\sigma}_2$ the two abscissas of absolute convergence. Then, in the half-plane where both series converge absolutely we have

$$F(s)G(s) = \sum_{n=1}^{\infty} \frac{(f * g)(n)}{n^s}.$$

Proof. The half-plane where the two series are absolutely convergent is $\operatorname{Re}(s) > \max(\bar{\sigma}_1, \bar{\sigma}_2)$. For any such s , we have

$$F(s)G(s) = \sum_{n=1}^{\infty} \frac{f(n)}{n^s} \sum_{m=1}^{\infty} \frac{g(m)}{m^s} = \sum_{n=1}^{\infty} \sum_{m=1}^{\infty} \frac{f(n)g(m)}{(nm)^s}.$$

Because of absolute convergence, we can multiply these series together and rearrange the terms in any way we please without altering the sum. Collect together those terms for which mn is constant, say $mn = k$. Thus

$$F(s)G(s) = \sum_{k=1}^{\infty} \frac{1}{k^s} \sum_{mn=k} f(n)g(m) = \sum_{k=1}^{\infty} \frac{(f * g)(k)}{k^s}.$$

□

Definition B.11. The *Riemann zeta function* is

$$\zeta(s) := \sum_{n=1}^{\infty} \frac{1}{n^s}.$$

The Riemann zeta function is absolutely convergent on the half-plane $\operatorname{Re}(s) > 1$, and when $s = 1$ the series diverges. Therefore $\bar{\sigma} = 1$. Furthermore, the zeta function has an analytic continuation in the entire complex plane, except for a simple pole at $s = 1$ with residue 1 (Apostol (1976, Chapter 12)).

Theorem B.12. The generating function of the Möbius function μ is

$$\sum_{n=1}^{\infty} \frac{\mu(n)}{n^s} = \frac{1}{\zeta(s)}.$$

Proof. From Proposition B.6 we know that $1 * \mu = e$. Note that the generating function of the arithmetical function 1 is the Riemann zeta function $\zeta(s)$, and that the generating function of e is 1. The proof now follows from Theorem B.10. □

Theorem B.13. For $x > 1$ we have

$$\sum_{n \leq x} \varphi(n) = \frac{1}{2\zeta(2)} x^2 + \mathcal{O}(x \log x).$$

Proof. We start from the relation

$$\varphi(n) = \sum_{d|n} \mu(d) \frac{n}{d}$$

from Proposition B.7, and obtain

$$\begin{aligned} \sum_{n \leq x} \varphi(n) &= \sum_{n \leq x} \sum_{qd=n} q \cdot \mu(d) = \sum_{\substack{q,d \\ qd \leq x}} q \cdot \mu(d) = \sum_{d \leq x} \mu(d) \sum_{q \leq \frac{x}{d}} q = \\ &= \sum_{d \leq x} \mu(d) \cdot \frac{1}{2} \left[\frac{x}{d} \right] \left(\left[\frac{x}{d} \right] + 1 \right) = \\ &= \frac{1}{2} \sum_{d \leq x} \mu(d) \left(\frac{x^2}{d^2} + \mathcal{O}\left(\frac{x}{d}\right) \right) = \\ &= \frac{x^2}{2} \sum_{d \leq x} \frac{\mu(d)}{d^2} + \mathcal{O}\left(x \sum_{d \leq x} \frac{1}{d}\right) = \\ &= \frac{x^2}{2} \left(\sum_{d=1}^{\infty} \frac{\mu(d)}{d^2} - \sum_{d > x} \frac{\mu(d)}{d^2} \right) + \mathcal{O}(x \log x), \end{aligned}$$

where we have also used the well known result $\sum_{d \leq x} \frac{1}{d} = \log x + \mathcal{O}(1)$. Concerning the series remainder, we have

$$\sum_{d > x} \frac{\mu(d)}{d^2} \leq \int_{[x]}^{\infty} \frac{du}{u^2} = \mathcal{O}\left(\frac{1}{x}\right).$$

The proof ends using this estimate and Theorem B.12. \square

B.3 The Farey sequence

Definition B.14. The *Farey sequence* \mathcal{F}_n of order n is the ascending sequence of irreducible fractions between 0 and 1 whose denominators do not exceed n .

Thus $\frac{h}{k} \in \mathcal{F}_n$ if and only if $0 \leq h \leq k \leq n$ and $(h, k) = 1$. The numbers 0 and 1 are included in the form $\frac{0}{1}$ and $\frac{1}{1}$.

Example B.15. For $n = 5$, the elements of \mathcal{F}_5 are the following:

$$\frac{0}{1}, \frac{1}{5}, \frac{1}{4}, \frac{1}{3}, \frac{2}{5}, \frac{1}{2}, \frac{3}{5}, \frac{2}{3}, \frac{3}{4}, \frac{4}{5}, \frac{1}{1}.$$

By definition $\mathcal{F}_{n-1} \subseteq \mathcal{F}_n$ for all $n > 1$, and the smallest Farey sequence is that of order $n = 1$

$$\mathcal{F}_1 = \left\{ \frac{0}{1}, \frac{1}{0} \right\}.$$

Proposition B.16. *The length of the Farey sequence of order n is*

$$|\mathcal{F}_n| = 1 + \sum_{k=1}^n \varphi(k).$$

Proof. To create \mathcal{F}_n from \mathcal{F}_{n-1} , we have just to add to \mathcal{F}_{n-1} the irreducible fractions with denominator n . The number of such fraction is exactly $\varphi(n)$, since this function counts the integers between 1 and n which are relatively prime to n . Thus for all $n > 1$

$$|\mathcal{F}_n| = |\mathcal{F}_{n-1}| + \varphi(n).$$

Of course the length of the Farey sequence of order 1 is $|\mathcal{F}_1| = 2$. As a consequence, the length of the Farey sequence of order n is given by

$$|\mathcal{F}_n| = 2 + \sum_{k=2}^n \varphi(k) = 1 + \sum_{k=1}^n \varphi(k).$$

□

Theorem B.17. *As $n \rightarrow +\infty$*

$$|\mathcal{F}_n| \sim \frac{3}{\pi^2} n^2.$$

Proof. Start from Proposition B.16 and use Theorem B.13. □

Corollary B.18. *As $n \rightarrow +\infty$*

$$\sum_{k=1}^n |\mathcal{F}_k| \sim \frac{1}{\pi^2} n^3.$$

Proof. The sequence $b_n = n^3$ is increasing and $\lim_{n \rightarrow +\infty} b_n = +\infty$. The thesis follows from Theorem B.17 and from the Stoltz-Cesaro theorem since

$$\frac{\sum_{k=1}^{n+1} |\mathcal{F}_k| - \sum_{k=1}^n |\mathcal{F}_k|}{(n+1)^3 - n^3} = \frac{|\mathcal{F}_{n+1}|}{3n^2 + 3n + 1} = \frac{|\mathcal{F}_{n+1}|}{(n+1)^2} \frac{(n+1)^2}{3n^2 + 3n + 1} \rightarrow \frac{1}{\pi^2}.$$

□

Analogous results hold in case we consider the irreducible fractions between any two integers r and $s > r$ and with denominator not exceeding n . Let us denote that set of fraction with $\mathcal{F}_n^{r,s}$.

Lemma B.19. *Each unit interval $[\ell, \ell + 1]$ contains exactly as many irreducible fractions with denominator not exceeding n as $[0, 1]$. That is, $|\mathcal{F}_n| = |\mathcal{F}_n^{\ell, \ell+1}|$.*

Proof. It suffices to prove that there exists a bijection between \mathcal{F}_n and $\mathcal{F}_n^{\ell, \ell+1}$. If $\frac{h}{k} \in \mathcal{F}_n$, then consider $\frac{h}{k} + \ell$: it belongs to $[\ell, \ell + 1]$ and it is irreducible since $(h, h + k\ell) = 1$ (otherwise $(h, k) > 1$). Thus $\frac{h}{k} + \ell \in \mathcal{F}_n^{\ell, \ell+1}$. Analogously, if $\frac{h}{k} \in \mathcal{F}_n^{\ell, \ell+1}$ then $\frac{h}{k} - \ell$ belongs to $[0, 1]$ and it is irreducible. \square

Theorem B.20. *For $s > r$ integers, as $n \rightarrow +\infty$*

$$|\mathcal{F}_n^{r,s}| \sim \frac{3(s-r)}{\pi^2} n^2 \quad \text{and} \quad \sum_{k=1}^n |\mathcal{F}_k^{r,s}| \sim \frac{s-r}{\pi^2} n^3.$$

Proof. it is possible to write $[r, s]$ as the union of adjacent unit intervals as $[r, s] = \bigcup_{i=0}^{s-r} [r+i-1, r+i]$. As a consequence and also by applying the above lemma we get

$$|\mathcal{F}_n^{r,s}| = (s-r)|\mathcal{F}_n| - (s-r-1).$$

The thesis follows from Theorem B.17. \square

Appendix C

Recap of manifolds and integration

In this appendix we recall some basic definitions about manifolds and integration on manifolds. We basically follow Acquistapace (2018).

Definition C.1. A subset V of \mathbb{R}^N is a *regular r -dimensional manifold* if for all $\mathbf{x}_0 \in V$ there exist a neighbourhood U of \mathbf{x}_0 in \mathbb{R}^N and a map $\mathbf{F} : U \rightarrow \mathbb{R}^{N-r}$ of class C^k , $k \geq 1$ such that

- (i) $D\mathbf{F}(\mathbf{x})$ has rank $N - r$ (is full rank) for every $\mathbf{x} \in U$:
- (ii) $V \cap U = \{\mathbf{x} \in U : \mathbf{F}(\mathbf{x}) = \mathbf{0}\}$.

Thus r -dimensional manifolds are those subsets that, locally, are the zero loci of functions of class at least C^1 with Jacobian matrix that is full rank.

Theorem C.2. Let V be a subset of \mathbb{R}^N . The set V is a regular r -dimensional manifold in \mathbb{R}^N if and only if for all $\mathbf{x}_0 \in V$ there exist an open neighbourhood U of \mathbf{x}_0 in \mathbb{R}^N , an open set $A \subseteq \mathbb{R}^r$ and a function $\mathbf{h} : A \rightarrow \mathbb{R}^{N-r}$ of class C^k , $k \geq 1$, such that $V \cap U$ is the graph of the function \mathbf{h} , that is

$$V \cap U = \{(\mathbf{y}, \mathbf{z}) \in \mathbb{R}^N : \mathbf{y} \in A, \mathbf{z} = \mathbf{h}(\mathbf{y})\}.$$

Theorem C.3. Let V be a subset of \mathbb{R}^N . The set V is a regular r -dimensional manifold in \mathbb{R}^N if and only if for all $\mathbf{x}_0 \in V$ there exist an open neighbourhood U of \mathbf{x}_0 in \mathbb{R}^N , an open set $A \subseteq \mathbb{R}^r$ and a homeomorphism $G : A \rightarrow \mathbb{R}^N$ of class C^k , $k \geq 1$, such that

- (i) $D\mathbf{G}(\mathbf{u})$ has rank r (is full rank) for every $\mathbf{u} \in A$:
- (ii) $V \cap U = \mathbf{G}(A)$.

In the hypotheses of Theorem C.3, the map \mathbf{G} is a *local parametrization* of V . Furthermore, note that (ii) implies that $\mathbf{G}(A)$ is open in V . The equivalent definition of manifold stated in Theorem C.3 is usually the more convenient. In what follows we always consider global parametrizations that are not necessarily homeomorphisms. In particular, we give a set $V = \mathbf{G}(T)$, where T is a subset of \mathbb{R}^r such that there exists an open set $A \subseteq \mathbb{R}^r$ for which $A \subseteq T \subseteq \bar{A}$, and $\mathbf{G} : T \rightarrow \mathbb{R}^N$ is a map of class C^k , $k \geq 1$, with Jacobian matrix $D\mathbf{G}(\mathbf{t})$ that is full rank for each $\mathbf{t} \in A$. The set V is called r -dimensional manifold.

Let $\{\mathbf{e}_1, \dots, \mathbf{e}_N\}$ be the canonical base of \mathbb{R}^N and consider the r vectors of \mathbb{R}^n

$$D\mathbf{G}(\mathbf{t})\mathbf{e}_i = \frac{\partial \mathbf{G}}{\partial t^i}(\mathbf{t}), \quad i = 1, \dots, r,$$

where $\mathbf{t} \in A$. The quantity

$$\mathcal{I}(\mathbf{t}) := \left| \frac{\partial \mathbf{G}}{\partial t^1}(\mathbf{t}) \wedge \dots \wedge \frac{\partial \mathbf{G}}{\partial t^r}(\mathbf{t}) \right|_{N,r}$$

represents the r -dimensional volume of the parallelepiped generated by the vectors $\frac{\partial \mathbf{G}}{\partial t^1}(\mathbf{t}), \dots, \frac{\partial \mathbf{G}}{\partial t^r}(\mathbf{t})$ ¹. It is strictly positive in each $\mathbf{t} \in A$ since $D\mathbf{G}(\mathbf{t})$ is full rank in A .

Definition C.4. Let $V = \mathbf{G}(T) \subseteq \mathbb{R}^N$ be an r -dimensional manifold. The r -dimensional measure of V is the non-negative quantity (possibly infinite)

$$v_r(V) := \int_T \left| \frac{\partial \mathbf{G}}{\partial t^1}(\mathbf{t}) \wedge \dots \wedge \frac{\partial \mathbf{G}}{\partial t^r}(\mathbf{t}) \right|_{N,r} dt$$

Definition C.5. Let $V = \mathbf{G}(T) \subseteq \mathbb{R}^N$ be an r -dimensional manifold and let f be a continuous function defined over an open set of \mathbb{R}^n that contains V . If the function $(f \circ \mathbf{G}) \cdot \mathcal{I}$ is Lebesgue-integrable on T , then we define the integral of f on V with respect to the measure v_r to be

$$\begin{aligned} \int_V f d\mathbf{v}_r &:= \int_T f(\mathbf{G}(\mathbf{t}))\mathcal{I}(\mathbf{t}) dt = \\ &= \int_T f(\mathbf{G}(\mathbf{t})) \left| \frac{\partial \mathbf{G}}{\partial t^1}(\mathbf{t}) \wedge \dots \wedge \frac{\partial \mathbf{G}}{\partial t^r}(\mathbf{t}) \right|_{N,r} dt. \end{aligned}$$

¹In the definition of \mathcal{I} , $|\cdot|_{N,r}$ is the norm induced by the standard product on the space $\mathbb{R}_r^N := ((\mathbb{R}^N)^*)^*$ of the alternating r -linear functions on $((\mathbb{R}^N)^*)^r$.

From the definition of exterior product and from results in calculus, we have that

$$\begin{aligned}\mathcal{I}(\mathbf{t}) &= \left| \frac{\partial \mathbf{G}}{\partial t^1}(\mathbf{t}) \wedge \cdots \wedge \frac{\partial \mathbf{G}}{\partial t^r}(\mathbf{t}) \right|_{N,r} = \sqrt{\det \left\{ \left\langle \frac{\partial \mathbf{G}}{\partial t^i}(\mathbf{t}), \frac{\partial \mathbf{G}}{\partial t^j}(\mathbf{t}) \right\rangle_N \right\}} = \\ &= \sqrt{\det [D\mathbf{G}(\mathbf{t})^\top \cdot D\mathbf{G}(\mathbf{t})]},\end{aligned}\tag{C.1}$$

that is the square root of the Gramian of the columns of $D\mathbf{G}(\mathbf{t})$. The differentiable form $d\mathbf{v}_r$ is referred to as the *volume form* on V .

Appendix D

Orbit determination: mathematical theory

D.1 The problem

Definition D.1. Let $\mathbf{f} : \mathbb{R}^p \times \mathbb{R} \times \mathbb{R}^{p'} \rightarrow \mathbb{R}^p$ be a function obeying some regularity requirement. The *equation of motion* is an ordinary differential equation

$$\frac{d\mathbf{y}}{dt} = \mathbf{f}(\mathbf{y}, t, \boldsymbol{\mu}),$$

where \mathbf{y} is the *state vector*, t is the *time* and $\boldsymbol{\mu}$ are the *dynamical parameters*. Let t_0 be the initial time, so that $\mathbf{y}_0 = \mathbf{y}(t_0)$ are the *initial conditions*.

We want to solve the Cauchy problem formed by the previous differential equation and the initial conditions. The existence and uniqueness of a solution in a neighbourhood of (\mathbf{y}_0, t_0) is guaranteed if \mathbf{f} is continuous and locally Lipschitz in an open set contained in $\mathbb{R}^p \times \mathbb{R}$.

Definition D.2. An *orbit* is a solution of the equation of motion with assigned initial conditions.

All the orbits together form the general solution $\mathbf{y} = \mathbf{y}(t, \mathbf{y}_0, \boldsymbol{\mu})$, also known as *integral flow* when considered as a mapping from the initial conditions (and dynamical parameters) to the current state at time t :

$$\mathbf{y}(t) = \Phi_{t_0}^t(\mathbf{y}_0, \boldsymbol{\mu}).$$

Let $\boldsymbol{\nu} \in \mathbb{R}^{p''}$ be a vector of *kinematical parameters*. The *observation function* is a function $R(\mathbf{y}, t, \boldsymbol{\nu})$, assumed to be differentiable.

Definition D.3. The composition of the general solution with the observation function is the *prediction function* $r(t) := R(\mathbf{y}(t), t, \boldsymbol{\nu})$.

Remark D.4. The observation function can depend also upon the index i , the most common case being the use of a 2-dimensional observation function like (right ascension, declination) or (range, range-rate), in which case R has two different analytical expressions, one for i even, the other for i odd.

The prediction function is used to predict the outcome of a specific observation at some time t_i , with $i = 1, \dots, m$. However, the observation result r_i is generically not equal to the prediction.

Definition D.5. The difference between the observation and the corresponding prediction is the *residual*

$$\xi_i := r_i - R(\mathbf{y}(t_i), t_i, \boldsymbol{\nu}) \quad i = 1, \dots, m.$$

The vector of the residuals is $\boldsymbol{\xi} = (\xi_i)_{i=1, \dots, m} \in \mathbb{R}^m$, which is in principle a function of all the $p + p' + p''$ variables $(\mathbf{y}_0, \boldsymbol{\mu}, \boldsymbol{\nu})$.

D.2 The minimum principle

The basic tool of the classical theory of orbit determination (Gauss 1809) is the definition of a target function $\mathcal{Q}(\boldsymbol{\xi})$ depending on the vector of residuals $\boldsymbol{\xi}$. The target function cannot be chosen arbitrarily, but needs to satisfy suitable conditions of regularity and convexity. We shall focus on the simplest case, in which \mathcal{Q} is proportional to the sum of squares of all the residuals.

Definition D.6. The *target function* is the function $\mathcal{Q} : \mathbb{R}^m \rightarrow \mathbb{R}$ defined to be

$$\mathcal{Q}(\boldsymbol{\xi}) := \frac{1}{m} \boldsymbol{\xi}^\top \boldsymbol{\xi} = \frac{1}{m} \sum_{i=1}^m \xi_i^2.$$

Since each residual is a function of all the parameters, the target function is also a function of $(\mathbf{y}_0, \boldsymbol{\mu}, \boldsymbol{\nu})$. The next step is to select the parameters to be fit to the data: let $\mathbf{x} \in \mathbb{R}^N$ be a sub-vector of $(\mathbf{y}_0, \boldsymbol{\mu}, \boldsymbol{\nu}) \in \mathbb{R}^{p+p'+p''}$, that is $\mathbf{x} = (x_i)$, with $i = 1, \dots, N$ and with each x_i either a component of the initial conditions, or a dynamical parameter, or a kinematical parameter. Then we consider the target function

$$Q(\mathbf{x}) := \mathcal{Q}(\boldsymbol{\xi}(\mathbf{x}))$$

as a function of \mathbf{x} only, leaving the vector of the *consider parameters* $\boldsymbol{\kappa} \in \mathbb{R}^{p+p'+p''-N}$ (all the parameters not included in \mathbf{x}) fixed at the assumed value. The *minimum principle* selects as *nominal solution* the point $\mathbf{x}^* \in \mathbb{R}^N$ where the target function Q has its minimum value Q^* .

D.3 The least squares method

D.3.1 Non-linear least squares

The target function of the non-linear least squares problem

$$Q(\mathbf{x}) := \frac{1}{m} \boldsymbol{\xi}(\mathbf{x})^\top \boldsymbol{\xi}(\mathbf{x})$$

is a differentiable function of the fit parameters \mathbf{x} , although it is not just a quadratic function. The partial derivatives of the residuals with respect to the fit parameters are assembled in the arrays

$$B := \frac{\partial \boldsymbol{\xi}}{\partial \mathbf{x}}(\mathbf{x}), \quad H := \frac{\partial^2 \boldsymbol{\xi}}{\partial \mathbf{x}^2}(\mathbf{x})$$

where the design matrix B is an $m \times N$ matrix, with $m \geq N$, and H is a 3-index array of shape $m \times N \times N$. In the context of orbit determination, the partial derivatives of the residuals are the partials of the prediction function (with sign changed). These can be computed by using the chain rule from the partials of the observation function R and the partials of the general solution $\mathbf{y}(t) = \mathbf{y}(\mathbf{y}_0, \boldsymbol{\mu}, \boldsymbol{\nu})$ of the equation of motion

$$\frac{\partial \xi_i}{\partial x_k} = -\frac{\partial R}{\partial \mathbf{y}}(\mathbf{y}(t_i)) \frac{\partial \mathbf{y}}{\partial x_k}(t_i) - \frac{\partial R}{\partial x_k}(\mathbf{y}(t_i)),$$

where the first term is relevant if x_k is a component of the vector $(\mathbf{y}_0, \boldsymbol{\mu})$ (either an initial condition or a dynamical parameter), the second one if x_k is a component of $\boldsymbol{\nu}$ (a kinematical parameter). The formula for H is less simple, containing first and second derivatives of the general solution of the equation of motion.

To find the minimum, we look for stationary points of $Q(\mathbf{x})$:

$$\frac{\partial Q}{\partial \mathbf{x}} = \frac{2}{m} \boldsymbol{\xi}^\top B = \mathbf{0}.$$

Two problems contribute in making this case not as simple as the linear one. First, the equation above is a system of non-linear equations, and generally does not have an explicit solution. Second, a stationary point does not need to be the absolute minimum point: it could be a saddle, or a local minimum. The first problem can be handled by using some iterative method, such as the Newton method, or some modification of it. The second one requires to check the Hessian matrix of second derivatives to exclude saddles; the methods to ensure that a local minimum found by some iterative method is the absolute minimum are computationally expensive.

The Newton method

The standard Newton method involves the computation of the second derivatives of the target function:

$$\frac{\partial^2 Q}{\partial \mathbf{x}^2} = \frac{2}{m} (B^\top B + \boldsymbol{\xi}^\top H) = \frac{2}{m} C_{new}$$

where C_{new} is a $N \times N$ matrix, non-negative in the neighbourhood of a local minimum. Given the residuals $\boldsymbol{\xi}(\mathbf{x}_k)$ obtained from the value \mathbf{x}_k of the parameters at iteration k , the (non-zero) gradient is expanded around \mathbf{x}_k

$$\frac{\partial Q}{\partial \mathbf{x}}(\mathbf{x}) = \frac{\partial Q}{\partial \mathbf{x}}(\mathbf{x}_k) + \frac{\partial^2 Q}{\partial \mathbf{x}^2}(\mathbf{x}_k)(\mathbf{x} - \mathbf{x}_k) + \dots$$

where the dots stand for terms of higher order in $(\mathbf{x} - \mathbf{x}_k)$. If this gradient has to be zero in $\mathbf{x} = \mathbf{x}^*$

$$\mathbf{0} = \frac{\partial Q}{\partial \mathbf{x}}(\mathbf{x}_k) + \frac{\partial^2 Q}{\partial \mathbf{x}^2}(\mathbf{x}_k)(\mathbf{x}^* - \mathbf{x}_k) + \dots$$

that is

$$C_{new}(\mathbf{x}^* - \mathbf{x}_k) = -B^\top \boldsymbol{\xi} + \dots$$

Neglecting the higher order terms, if the matrix C_{new} , as computed at the point \mathbf{x}_k , is invertible then the iteration $k+1$ of the Newton method provides a correction $\mathbf{x}_{k+1} - \mathbf{x}_k$ with

$$\mathbf{x}_{k+1} = \mathbf{x}_k + C_{new}^{-1} D, \quad D = -B^\top \boldsymbol{\xi},$$

where also $D = D(\mathbf{x}_k)$. The point \mathbf{x}_{k+1} should be a better approximation to \mathbf{x}^* than \mathbf{x}_k . In practice, the Newton method may converge or not, depending upon the choice of the first guess \mathbf{x}_0 selected to start the iterations.

Differential corrections

The most used method is a variant of the Newton method, known in this context as *differential corrections*, with each iteration making the correction

$$\mathbf{x}_{k+1} = \mathbf{x}_k - (B^\top B)^{-1} B^\top \boldsymbol{\xi}$$

where the normal matrix $C = B^\top B$, computed at \mathbf{x}_k , replaces the matrix C_{new} . This amounts to neglecting, on top of the terms of order ≥ 2 in $(\mathbf{x}^* - \mathbf{x}_k)$, also the term $\boldsymbol{\xi}^\top H(\mathbf{x}^* - \mathbf{x}_k)$. The additional neglected term is of the first order in $(\mathbf{x}^* - \mathbf{x}_k)$ but contains also the residuals, thus it is smaller than $C(\mathbf{x}^* - \mathbf{x}_k)$ if the residuals are small enough.

The main practical motivation for this simplification of the Newton method is that the computation of the three-index arrays of second derivatives $\partial B/\partial \mathbf{x} = \partial^2 \boldsymbol{\xi}/\partial \mathbf{x}^2$ for $P = p' + p''$ dynamical parameters (p' initial conditions and p'' parameters to be solved appearing in the equation of motion) requires to solve $p'P^2$ scalar differential equations on top of the usual $p' + p'P$ for the equation of motion and the variational equation.

One iteration of differential corrections is just the solution of a linear least squares problem, with normal equation

$$C(\mathbf{x}_{k+1} - \mathbf{x}_k) = D$$

where the right hand side $D = -B^\top \boldsymbol{\xi}$ is the same as in the Newton method. This linear problem can be obtained by truncation of the target function

$$Q(\mathbf{x}) \simeq Q(\mathbf{x}_k) + \frac{2}{m} \boldsymbol{\xi}^\top B(\mathbf{x} - \mathbf{x}_k) + \frac{1}{m} (\mathbf{x} - \mathbf{x}_k)^\top C(\mathbf{x} - \mathbf{x}_k) ,$$

which is not the Taylor expansion to order 2, since C_{new} is replaced by C .

Bibliography

- [1] P. Acquistapace, *Appunti di Analisi Matematica II*, 2018
- [2] T. Apostol, *Introduction to Analytic Number Theory*, Undergraduate Texts in Mathematics, Springer New York, 1976
- [3] J. Baer, S. R. Chesley, and R. D. Matson, *Astrometric Masses of 26 Asteroids and Observations on Asteroid Porosity*, *AJ* **141**, May 2011
- [4] J. Baer, S. R. Chesley, and A. Milani, *Development of an observational error model*, *Icarus* **212**: 438–447, Mar. 2011
- [5] D. A. Bini, *Numerical computation of polynomial zeros by means of Aberth's method*, *Numer. Algorithms* **13**(2): 179–200, Feb. 1996
- [6] R. P. Binzel, *The Torino Impact Hazard Scale*, *Planet. Space Sci.* **48**: 297–303, Apr. 2000
- [7] R. P. Binzel, D. Lupishko, M. di Martino, R. J. Whiteley, and G. J. Hahn, *Physical Properties of Near-Earth Objects*, in: *Asteroids III*, ed. by W. F. Bottke Jr., A. Cellino, P. Paolicchi, and R. P. Binzel, Mar. 2002: pp. 255–271
- [8] E. Bowell, R. M. West, H.-H. Heyer, J. Quebatte, L. E. Cunningham, S. J. Bus, A. W. Harris, R. L. Millis, and B. G. Marsden, *(4015) 1979 VA = Comet Wilson-Harrington (1949 III)*, *IAU Circ.* **5585**, Aug. 1992
- [9] E. Bowell and K. Muinonen, *Earth-crossing Asteroids and Comets: Groundbased Search Strategies*, in: *Hazards Due to Comets and Asteroids*, ed. by T. Gehrels, M. S. Matthews, and A. M. Schumann, 1994

- [10] K. Brauer, M. W. Busch, L. A. M. Benner, M. Brozovic, E. S. Howell, M. C. Nolan, A. Springmann, J. D. Giorgini, P. A. Taylor, and J. S. Jao, *The Shape of Near-Earth Asteroid 275677 (2000 RS11) From Inversion of Arecibo and Goldstone Radar Images*, in: *AAS/Division for Planetary Sciences Meeting Abstracts*, vol. 47, AAS/Division for Planetary Sciences Meeting Abstracts, Nov. 2015
- [11] M. Carpino, A. Milani, and S. R. Chesley, *Error statistics of asteroid optical astrometric observations*, *Icarus* **166**: 248–270, Dec. 2003
- [12] B. Carry, *Density of asteroids*, *Planet. Space Sci.* **73**: 98–118, Dec. 2012
- [13] B. Carry, *Solar System Science with ESA Euclid*, *Astron. Astrophys.* **609**, 2018
- [14] B. Carry, *The reservoir of solar system objects available to discovery by Gaia*, in: *Gaia-FUN-SSO-3*, Nov. 2014
- [15] A. Carusi, L. Kresák, and G. B. Valsecchi, *Orbital patterns of interplanetary objects at close encounters with Jupiter*, *Bulletin of the Astronomical Institutes of Czechoslovakia* **33**: 141–150, May 1982
- [16] A. Carusi, G. B. Valsecchi, and R. Greenberg, *Planetary close encounters - Geometry of approach and post-encounter orbital parameters*, *Celestial Mech. Dynam. Astronom.* **49**: 111–131, 1990
- [17] S. R. Chesley, *Potential impact detection for Near-Earth asteroids: the case of 99942 Apophis (2004 MN4)*, in: *Asteroids, Comets, Meteors*, ed. by L. Daniela, M. Sylvio Ferraz, and F. J. Angel, vol. 229, IAU Symposium, 2006: pp. 215–228
- [18] S. R. Chesley, *Very short arc orbit determination: the case of asteroid 2004FU₁₆₂*, in: *IAU Colloq. 197: Dynamics of Populations of Planetary Systems*, ed. by Z. Knežević and A. Milani, Feb. 2005: pp. 255–258
- [19] S. R. Chesley, S. J. Ostro, D. Vokrouhlický, D. Čapek, J. D. Giorgini, M. C. Nolan, J.-L. Margot, A. A. Hine, L. A. M. Benner, and A. B. Chamberlin, *Direct Detection of the Yarkovsky Effect by Radar Ranging to Asteroid 6489 Golevka*, *Science* **302**: 1739–1742, Dec. 2003
- [20] S. R. Chesley, D. Farnocchia, P. Pravec, and D. Vokrouhlický, *Direct Detections of the Yarkovsky Effect: Status and Outlook*, in: *Asteroids: New Observations, New Models*, ed. by S. R. Chesley, A. Morbidelli, R. Jedicke, and D. Farnocchia, vol. 318, IAU Symposium, Jan. 2016: pp. 250–258

- [21] S. R. Chesley, D. Farnocchia, M. C. Nolan, D. Vokrouhlický, P. W. Chodas, A. Milani, F. Spoto, B. Rozitis, L. A. M. Benner, W. F. Bottke, M. W. Busch, J. P. Emery, E. S. Howell, D. S. Lauretta, J.-L. Margot, and P. A. Taylor, *Orbit and bulk density of the OSIRIS-REx target Asteroid (101955) Bennu*, *Icarus* **235**: 5–22, June 2014
- [22] S. R. Chesley, P. W. Chodas, A. Milani, G. B. Valsecchi, and D. K. Yeomans, *Quantifying the Risk Posed by Potential Earth Impacts*, *Icarus* **159**: 423–432, Oct. 2002
- [23] S. R. Chesley, J. Baer, and D. G. Monet, *Treatment of star catalog biases in asteroid astrometric observations*, *Icarus* **210**: 158–181, Nov. 2010
- [24] P. W. Chodas and D. K. Yeomans, *Could Asteroid 1997 XF11 Collide with Earth After 2028?*, in: *AAS/Division of Dynamical Astronomy Meeting*, vol. 31, Bulletin of the American Astronomical Society, Sept. 1999
- [25] P. W. Chodas and D. K. Yeomans, *The orbital motion and impact circumstances of Comet Shoemaker-Levy 9*, in: *IAU Colloq. 156: The Collision of Comet Shoemaker-Levy 9 and Jupiter*, ed. by K. S. Noll, H. A. Weaver, and P. D. Feldman, 1996: pp. 1–30
- [26] B. E. Clark, R. P. Binzel, E. S. Howell, E. A. Cloutis, M. Ockert-Bell, P. Christensen, M. A. Barucci, F. DeMeo, D. S. Lauretta, H. Connolly, A. Soderberg, C. Hergenrother, L. Lim, J. Emery, and M. Mueller, *Asteroid (101955) 1999 RQ36: Spectroscopy from 0.4 to 2.4 μm and meteorite analogs*, *Icarus* **216**: 462–475, Dec. 2011
- [27] J. M. A. Danby, *Fundamentals of celestial mechanics*, 1992
- [28] A. Del Vigna, A. Milani, F. Spoto, A. Chessa, and G. B. Valsecchi, *Completeness of Impact Monitoring*, *Icarus* **321**, 2019
- [29] A. Del Vigna, L. Faggioli, F. Spoto, A. Milani, D. Farnocchia, and B. Carry, *Detecting the Yarkovsky effect among near-Earth asteroids from astrometric data*, *Astron. Astrophys.* **617**, Sept. 2018
- [30] A. Einstein, L. Infeld, and B. Hoffmann, *The Gravitational Equations and the Problem of Motion*, *Ann. of Math. (2)* **39**(1): 65–100, 1938
- [31] J. P. Emery, Y. R. Fernández, M. S. P. Kelley, K. T. Warden (née Crane), C. Hergenrother, D. S. Lauretta, M. J. Drake, H. Campins, and J. Ziffer, *Thermal infrared observations and thermophysical characterization of OSIRIS-REx target asteroid (101955) Bennu*, *Icarus* **234**: 17–35, May 2014

- [32] E. Everhart, *An efficient integrator that uses Gauss-Radau spacings*, in: *Dynamics of Comets: Their Origin and Evolution*, ed. by A. Carusi and G. B. Valsecchi, Reidel, Dordrecht, 1985
- [33] D. Farnocchia and S. R. Chesley, *Apophis: Complex rotation and hazard assessment*, in: *2015 IEEE Aerospace Conference*, Mar. 2015: pp. 1–7
- [34] D. Farnocchia and S. R. Chesley, *Assessment of the 2880 impact threat from Asteroid (29075) 1950 DA*, *Icarus* **229**: 321–327, Feb. 2014
- [35] D. Farnocchia, S. R. Chesley, D. J. Tholen, and M. Micheli, *High precision predictions for near-Earth asteroids: the strange case of (3908) Nyx*, *Celestial Mech. Dynam. Astronom.* **119**(3): 301–312, Aug. 2014
- [36] D. Farnocchia, D. J. Tholen, M. Micheli, W. Ryan, E. G. Rivera-Valentin, P. A. Taylor, and J. D. Giorgini, *Mass estimate and close approaches of near-Earth asteroid 2015 TC25*, in: *AAS/Division for Planetary Sciences Meeting Abstracts #49*, vol. 49, AAS/Division for Planetary Sciences Meeting Abstracts, Oct. 2017
- [37] D. Farnocchia, S. R. Chesley, A. Milani, G. F. Gronchi, and P. W. Chodas, *Orbits, Long-Term Predictions, Impact Monitoring*, in: *Asteroids IV*, ed. by P. Michel, F. E. DeMeo, and W. F. Bottke, University of Arizona Press, 2015: pp. 815–834
- [38] D. Farnocchia, S. R. Chesley, and A. B. Chamberlin, *Scout: orbit analysis and hazard assessment for NEOCP objects*, in: *AAS/Division for Planetary Sciences Meeting Abstracts #48*, vol. 48, AAS/Division for Planetary Sciences Meeting Abstracts, Oct. 2016
- [39] D. Farnocchia, S. R. Chesley, A. B. Chamberlin, and D. J. Tholen, *Star catalog position and proper motion corrections in asteroid astrometry*, *Icarus* **245**: 94–111, Jan. 2015
- [40] D. Farnocchia, S. R. Chesley, and M. Micheli, *Systematic ranging and late warning asteroid impacts*, *Icarus* **258**: 18–27, Sept. 2015
- [41] D. Farnocchia, P. Jenniskens, D. K. Robertson, S. R. Chesley, L. Dimare, and P. W. Chodas, *The impact trajectory of asteroid 2008 TC₃*, *Icarus* **294**: 218–226, Sept. 2017
- [42] D. Farnocchia, P. Jenniskens, D. K. Robertson, S. R. Chesley, L. Dimare, and P. W. Chodas, *The impact trajectory of asteroid 2008 TC₃*, *Icarus* **294**: 218–226, Sept. 2017

- [43] D. Farnocchia, S. R. Chesley, P. W. Chodas, M. Micheli, D. J. Tholen, A. Milani, G. T. Elliott, and F. Bernardi, *Yarkovsky-driven impact risk analysis for asteroid (99942) Apophis*, *Icarus* **224**: 192–200, May 2013
- [44] D. Farnocchia and S. R. Chesley, *Assessment of the 2880 impact threat from Asteroid (29075) 1950 DA*, *Icarus* **229**: 321–327, 2014
- [45] D. Farnocchia, S. R. Chesley, D. Vokrouhlický, A. Milani, F. Spoto, and W. F. Bottke, *Near Earth Asteroids with measurable Yarkovsky effect*, *Icarus* **224**: 1–13, 2013
- [46] W. M. Folkner, J. G. Williams, D. H. Boggs, R. S. Park, and P. Kuchynka, *The Planetary and Lunar Ephemerides DE430 and DE431*, Interplanetary Network Progress Report **196**: 1–81, Feb. 2014
- [47] A. Fujiwara et al., *The Rubble-Pile Asteroid Itokawa as Observed by Hayabusa*, *Science* **312**: 1330–1334, June 2006
- [48] A. G. A. Gaia Collaboration: Brown and et al., *Gaia Data Release 2 Summary of the contents and survey properties*, Submitted to Astronomy and Astrophysics, 2018
- [49] F. Gaia Collaboration: Spoto, P. Tanga, F. Mignard, and et al, *Gaia Data Release 2: observations of Solar System objects*, Submitted to Astronomy and Astrophysics, 2018
- [50] Gaia Collaboration et al., *Gaia Data Release 1. Summary of the astrometric, photometric, and survey properties*, *Astron. Astrophys.* **595**, Nov. 2016
- [51] K. F. Gauss, *Theoria motus corporum coelestium in sectionibus conicis solem ambientium*, 1809
- [52] J. D. Giorgini, S. J. Ostro, L. A. M. Benner, P. W. Chodas, S. R. Chesley, R. S. Hudson, M. C. Nolan, A. R. Klemola, E. M. Standish, R. F. Jurgens, R. Rose, A. B. Chamberlin, D. K. Yeomans, and J.-L. Margot, *Asteroid 1950 DA's Encounteqr with Earth in 2880: Physical Limits of Collision Probability Prediction*, in: *AAS/Division of Dynamical Astronomy Meeting #33*, vol. 34, Bulletin of the American Astronomical Society, Sept. 2002
- [53] J. D. Giorgini, L. A. M. Benner, S. J. Ostro, M. C. Nolan, and M. W. Busch, *Predicting the Earth encounters of (99942) Apophis*, *Icarus* **193**: 1–19, Jan. 2008
- [54] M. Granvik, J. Virtanen, D. Oszkiewicz, and K. Muinonen, *OpenOrb: Open-source asteroid orbit computation software including statistical ranging*, *Meteoritics and Planetary Science* **44**: 1853–1861, Jan. 2009

- [55] M. Granvik, J. Vaubaillon, and R. Jedicke, *The population of natural Earth satellites*, *Icarus* **218**: 262–277, Mar. 2012
- [56] A. H. Greenberg, J.-L. Margot, A. K. Verma, P. A. Taylor, S. P. Naidu, M. Brozovic, and L. A. M. Benner, *Asteroid 1566 Icarus's Size, Shape, Orbit, and Yarkovsky Drift from Radar Observations*, *AJ* **153**, Mar. 2017
- [57] A. H. Greenberg, J.-L. Margot, A. K. Verma, P. A. Taylor, and S. E. Hodge, *Yarkovsky Drift Detections for 159 Near-Earth Asteroids*, 2017
- [58] R. Greenberg, A. Carusi, and G. B. Valsecchi, *Outcomes of planetary close encounters - A systematic comparison of methodologies*, *Icarus* **75**: 1–29, July 1988
- [59] G. F. Gronchi and A. Milani, *Proper Elements for Earth-Crossing Asteroids*, *Icarus* **152**: 58–69, July 2001
- [60] G. Hardy, E. Wright, R. Heath-Brown, and J. Silverman, *An Introduction to the Theory of Numbers*, Oxford mathematics, OUP Oxford, 2008
- [61] R. S. Hudson, S. J. Ostro, and D. J. Scheeres, *High-resolution model of Asteroid 4179 Toutatis*, *Icarus* **161**: 346–355, Feb. 2003
- [62] A. S. Konopliv, S. W. Asmar, W. M. Folkner, Ö. Karatekin, D. C. Nunes, S. E. Smrekar, C. F. Yoder, and M. T. Zuber, *Mars high resolution gravity fields from MRO, Mars seasonal gravity, and other dynamical parameters*, *Icarus* **211**: 401–428, Jan. 2011
- [63] LSST Science Collaborations and LSST Project, *LSST Science Book*, Version 2.0, arXiv:0912.0201, 2009
- [64] L. Lindegren et al., *Gaia Data Release 1 - Astrometry: one billion positions, two million proper motions and parallaxes*, *Astron. Astrophys.* **595**, 2016
- [65] A. Mainzer et al., *NEOWISE Observations of Near-Earth Objects: Preliminary Results*, *ApJ* **743**, Dec. 2011
- [66] B. G. Marsden, *A discourse on 1997 XF₁₁*, *Journal of the British Interplanetary Society* **52**: 195–202, 1999
- [67] B. G. Marsden, Z. Sekanina, and D. K. Yeomans, *Comets and non-gravitational forces. V*, *AJ* **78**, Mar. 1973
- [68] M. Micheli, D. J. Tholen, and G. T. Elliott, *2012 LA, an optimal astrometric target for radiation pressure detection*, *Icarus* **226**: 251–255, Sept. 2013

- [69] M. Micheli, D. J. Tholen, and G. T. Elliott, *Detection of radiation pressure acting on 2009 BD*, *New A* **17**: 446–452, May 2012
- [70] M. Micheli, D. J. Tholen, and G. T. Elliott, *Radiation Pressure Detection and Density Estimate for 2011 MD*, *ApJ* **788**, June 2014
- [71] F. Mignard, A. Cellino, K. Muinonen, P. Tanga, M. Delbò, A. Dell’Oro, M. Granvik, D. Hestroffer, S. Mouret, W. Thuillot, and J. Virtanen, *The Gaia Mission: Expected Applications to Asteroid Science*, *Earth Moon and Planets* **101**: 97–125, Dec. 2007
- [72] A. Milani, *The Asteroid Identification Problem. I. Recovery of Lost Asteroids*, *Icarus* **137**: 269–292, Feb. 1999
- [73] A. Milani, S. R. Chesley, and G. B. Valsecchi, *Asteroid close encounters with Earth: risk assessment*, *Planet. Space Sci.* **48**: 945–954, Aug. 2000
- [74] A. Milani, A. Cellino, Z. Knežević, B. Novaković, F. Spoto, and P. Paolicchi, *Asteroid families classification: Exploiting very large datasets*, *Icarus* **239**: 46–73, Sept. 2014
- [75] A. Milani, S. R. Chesley, and G. B. Valsecchi, *Close approaches of asteroid 1999 AN10: resonant and non-resonant returns*, *Astron. Astrophys.* **346**: L65–L68, 1999
- [76] A. Milani and Z. Knežević, *From Astrometry to Celestial Mechanics: Orbit Determination with Very Short Arcs*, *Celestial Mech. Dynam. Astronom.* **92**: 1–18, Apr. 2005
- [77] A. Milani, S. R. Chesley, M. E. Sansaturio, F. Bernardi, G. B. Valsecchi, and O. Arratia, *Long term impact risk for (101955) 1999RQ36*, *Icarus* **203**: 460–471, Oct. 2009
- [78] A. Milani, M. Sansaturio, G. Tommei, O. Arratia, and S. R. Chesley, *Multiple solutions for asteroid orbits: Computational procedure and applications*, *Astron. Astrophys.* **431**: 729–746, Feb. 2005
- [79] A. Milani, G. F. Gronchi, and Z. Knežević, *New Definition of Discovery for Solar System Objects*, *Earth Moon and Planets* **100**: 83–116, Apr. 2007
- [80] A. Milani, S. Chesley, M. E. Sansaturio, G. Tommei, and G. B. Valsecchi, *Nonlinear impact monitoring: line of variation searches for impactors*, *Icarus* **173**: 362–384, 2 2005
- [81] A. Milani, G. F. Gronchi, M. De’ Michieli Vitturi, and Z. Knežević, *Orbit determination with very short arcs. I admissible regions*, *Celestial Mech. Dynam. Astronom.* **90**(1-2): 57–85, Apr. 2004

- [82] A. Milani and G. B. Valsecchi, *The Asteroid Identification Problem. II. Target Plane Confidence Boundaries*, *Icarus* **140**: 408–423, Aug. 1999
- [83] A. Milani, M. E. Sansaturio, and S. R. Chesley, *The Asteroid Identification Problem IV: Attributions*, *Icarus* **151**: 150–159, June 2001
- [84] A. Milani and G. F. Gronchi, *Theory of Orbit Determination*, Cambridge University Press, 2010
- [85] A. Milani, G. F. Gronchi, D. Farnocchia, Z. Knežević, R. Jedicke, L. Denneau, and F. Pierfederici, *Topocentric orbit determination: Algorithms for the next generation surveys*, *Icarus* **195**: 474–492, May 2008
- [86] A. Milani, S. Chesley, A. Boattini, and G. B. Valsecchi, *Virtual Impactors: search and destroy*, *Icarus* **145(1)**: 12–24, 2000
- [87] M. Mommert, J. L. Hora, D. Farnocchia, S. R. Chesley, D. Vokrouhlický, D. E. Trilling, M. Mueller, A. W. Harris, H. A. Smith, and G. G. Fazio, *Constraining the Physical Properties of Near-Earth Object 2009 BD*, *ApJ* **786**, May 2014
- [88] M. Mommert, D. Farnocchia, J. L. Hora, S. R. Chesley, D. E. Trilling, P. W. Chodas, M. Mueller, A. W. Harris, H. A. Smith, and G. G. Fazio, *Physical Properties of Near-Earth Asteroid 2011 MD*, *ApJ* **789**, July 2014
- [89] T. Moyer, *Formulation for observed and computed values of Deep Space Network data types for navigation*, Deep-space communications and navigation series, Wiley-Interscience, 2003
- [90] B. E. A. Mueller, N. H. Samarasinha, and M. J. S. Belton, *The Diagnosis of Complex Rotation in the Lightcurve of 4179 Toutatis and Potential Applications to Other Asteroids and Bare Cometary Nuclei*, *Icarus* **158**: 305–311, Aug. 2002
- [91] K. Muinonen, I. N. Belskaya, A. Cellino, M. Delbò, A.-C. Levasseur-Regourd, A. Penttilä, and E. F. Tedesco, *A three-parameter magnitude phase function for asteroids*, *Icarus* **209**: 542–555, Oct. 2010
- [92] K. Muinonen and E. Bowell, *Asteroid orbit determination using Bayesian probabilities*, *Icarus* **104**: 255–279, Aug. 1993
- [93] K. Muinonen, G. Fedorets, A. Pentikäinen, T. Pieniluoma, D. Oszkiewicz, M. Granvik, J. Virtanen, P. Tanga, F. Mignard, J. Berthier, A. Dell’Oro, B. Carry, and W. Thuillot, *Asteroid orbits with Gaia using random-walk statistical ranging*, *Planet. Space Sci.* **123**: 95–100, 2015

- [94] K. Muinonen, G. Fedorets, A. Pentikäinen, T. Pieniluoma, D. Oszkiewicz, M. Granvik, J. Virtanen, P. Tanga, F. Mignard, J. Berthier, A. Dell’Oro, B. Carry, and W. Thuillot, *Asteroid orbits with Gaia using random-walk statistical ranging*, Planet. Space Sci. **123**: 95–100, 2016
- [95] K. Muinonen, J. Virtanen, and E. Bowell, *Collision Probability for Earth-Crossing Asteroids Using Orbital Ranging*, Celestial Mech. Dynam. Astronom. **81**: 93–101, 2001
- [96] T. G. Müller, C. Kiss, P. Scheirich, P. Pravec, L. O’Rourke, E. Vilenius, and B. Altieri, *Thermal infrared observations of asteroid (99942) Apophis with Herschel*, A&A **566**, June 2014
- [97] S. P. Naidu, J.-L. Margot, M. W. Busch, P. A. Taylor, M. C. Nolan, M. Brozovic, L. A. M. Benner, J. D. Giorgini, and C. Magri, *Radar imaging and physical characterization of near-Earth Asteroid (162421) 2000 ET70*, Icarus **226**: 323–335, Sept. 2013
- [98] M. C. Nolan, C. Magri, E. S. Howell, L. A. M. Benner, J. D. Giorgini, C. W. Hergenrother, R. S. Hudson, D. S. Lauretta, J.-L. Margot, S. J. Ostro, and D. J. Scheeres, *Shape model and surface properties of the OSIRIS-REx target Asteroid (101955) Bennu from radar and lightcurve observations*, Icarus **226**: 629–640, Sept. 2013
- [99] C. R. Nugent, J. L. Margot, S. R. Chesley, and D. Vokrouhlický, *Detection of Semimajor Axis Drifts in 54 Near-Earth Asteroids: New Measurements of the Yarkovsky Effect*, AJ **144**, Aug. 2012
- [100] E. J. Öpik, ed., *Interplanetary encounters: Close-range gravitational interactions*, vol. 2, June 1976
- [101] D. Oszkiewicz, K. Muinonen, J. Virtanen, and M. Granvik, *Asteroid orbital ranging using Markov-Chain Monte Carlo*, Meteoritics and Planetary Science **44**: 1897–1904, Jan. 2009
- [102] P. Pravec and A. W. Harris, *Binary asteroid population. 1. Angular momentum content*, Icarus **190**: 250–259, Sept. 2007
- [103] T. Prusti, *The promises of Gaia*, Astronomische Nachrichten **333**, June 2012
- [104] V. Reddy, J. A. Sanchez, W. F. Bottke, A. Thirouin, E. G. Rivera-Valentin, M. S. Kelley, W. Ryan, E. A. Cloutis, S. C. Tegler, E. V. Ryan, P. A. Taylor, J. E. Richardson, N. Moskovitz, and L. Le Corre, *Physical Characterization of ~2-meter Diameter Near-Earth Asteroid 2015 TC₂₅: A Possible Boulder from E-type Asteroid (44) Nysa*, AJ **152**, Dec. 2016

- [105] B. Rozitis, E. Maclennan, and J. P. Emery, *Cohesive forces prevent the rotational breakup of rubble-pile asteroid (29075) 1950 DA*, *Nature* **512**: 174–176, Aug. 2014
- [106] M. E. Sansaturio and O. Arratia, *Apophis: the Story Behind the Scenes*, *Earth Moon and Planets* **102**: 425–434, June 2008
- [107] D. J. Scheeres, D. Britt, B. Carry, and K. A. Holsapple, *Asteroid Interiors and Morphology*, in: *Asteroids IV*, ed. by P. Michel, F. E. DeMeo, and W. F. Bottke, 2015: pp. 745–766
- [108] P. Scheirich et al., *The binary near-Earth Asteroid (175706) 1996 FG₃ - An observational constraint on its orbital evolution*, *Icarus* **245**: 56–63, Jan. 2015
- [109] M. H. Shaddad, P. Jenniskens, D. Numan, A. M. Kudoda, S. Elsir, I. F. Riyad, A. E. Ali, M. Alameen, N. M. Alameen, O. Eid, A. T. Osman, M. I. Abubaker, M. Yousif, S. R. Chesley, P. W. Chodas, J. Albers, W. N. Edwards, P. G. Brown, J. Kuiper, and J. M. Friedrich, *The recovery of asteroid 2008 TC₃*, *Meteoritics and Planetary Science* **45**: 1557–1589, Oct. 2010
- [110] O. Solin and M. Granvik, *Monitoring near-Earth-object discoveries for imminent impactors*, *A&A* **616**, Sept. 2018
- [111] J. R. Spencer et al., *The lightcurve of 4179 Toutatis: Evidence for complex rotation.*, *Icarus* **117**: 71–89, Sept. 1995
- [112] F. Spoto, A. Milani, and Z. Knežević, *Asteroid family ages*, *Icarus* **257**: 275–289, Sept. 2015
- [113] F. Spoto, A. Milani, D. Farnocchia, S. R. Chesley, M. Micheli, G. B. Valsecchi, D. Perna, and O. Hainaut, *Nongravitational perturbations and virtual impactors: the case of asteroid (410777) 2009 FD*, *Astron. Astrophys.* **572**, Dec. 2014
- [114] F. Spoto, A. Del Vigna, A. Milani, G. Tommei, P. Tanga, F. Mignard, B. Carry, W. Thuillot, and P. David, *Short arc orbit determination and imminent impactors in the Gaia era*, *Astron. Astrophys.* **614**, June 2018
- [115] F. Spoto and A. Milani, *Shadowing Lemma and chaotic orbit determination*, *Celestial Mech. Dynam. Astronom.* **124**: 295–309, 2016
- [116] E. M. Standish and R. W. Hellings, *A determination of the masses of Ceres, Pallas, and Vesta from their perturbations upon the orbit of Mars*, *Icarus* **80**: 326–333, Aug. 1989

- [117] P. Tanga, M. Delbò, D. Hestroffer, A. Cellino, and F. Mignard, *Gaia observations of Solar System objects: Impact on dynamics and ground-based observations*, *Advances in Space Research* **40**: 209–214, 2007
- [118] P. Tanga, F. Mignard, A. Dell’Oro, K. Muinonen, T. Pauwels, W. Thuillot, J. Berthier, A. Cellino, D. Hestroffer, J.-M. Petit, B. Carry, P. David, M. Delbo’, G. Fedorets, L. Galluccio, M. Granvik, C. Ordenovic, and H. Pentikäinen, *The daily processing of asteroid observations by Gaia*, *Planet. Space Sci.* **123**: 87–94, Apr. 2016
- [119] C. Tardioli, D. Farnocchia, B. Rozitis, D. Cotto-Figueroa, S. R. Chesley, T. S. Statler, and M. Vasile, *Constraints on the near-Earth asteroid obliquity distribution from the Yarkovsky effect*, *A&A* **608**, Dec. 2017
- [120] W. Thuillot, B. Carry, J. Berthier, P. David, D. Hestroffer, and P. Rocher, *Gaia-FUN-SSO: a network for ground-based follow-up observations of Solar System Objects*, in: *SF2A-2014: Proceedings of the Annual meeting of the French Society of Astronomy and Astrophysics*, ed. by J. Ballet, F. Martins, F. Bornaud, R. Monier, and C. Reylé, Dec. 2014: pp. 445–448
- [121] G. Tommei, *Nonlinear impact monitoring: 2-dimensional sampling*, in: *IAU Colloquium 197: Dynamics of Populations of Planetary Systems*, ed. by A. Milani and Z. Knežević, Cambridge University Press, 2005: pp. 259–264
- [122] G. Tommei, *Impact Monitoring of NEOs: theoretical and computational results*, PhD thesis, University of Pisa, 2006
- [123] G. B. Valsecchi, *Geometric Conditions for Quasi-Collisions in Öpik’s Theory*, in: *Dynamics of Extended Celestial Bodies and Rings*, ed. by J. Souchay, vol. 682, Lecture Notes in Physics, Berlin Springer Verlag, 2006
- [124] G. B. Valsecchi, E. M. Alessi, and A. Rossi, *An analytical treatment of the swing-by problem.*, *Mem. Soc. Astron. Italiana* **87**, 2016
- [125] G. B. Valsecchi, E. M. Alessi, and A. Rossi, *Cartography of the b-plane of a close encounter I: semimajor axes of post-encounter orbits*, *Celestial Mech. Dynam. Astronom.* **130**, Feb. 2018
- [126] G. B. Valsecchi, E. M. Alessi, and A. Rossi, *Erratum: Erratum to: An analytical solution for the swing-by problem*, *Celestial Mech. Dynam. Astronom.* **123**: 167–167, 2015

- [127] G. B. Valsecchi, A. Milani, G. F. Gronchi, and S. R. Chesley, *Resonant returns to close approaches: Analytical theory*, *Astron. Astrophys.* **408**: 1179–1196, 2003
- [128] G. B. Valsecchi, A. Milani, G. F. Gronchi, and S. R. Chesley, *The Distribution of Energy Perturbations at Planetary Close Encounters*, *Celestial Mech. Dynam. Astronom.* **78**: 83–91, 2000
- [129] G. B. Valsecchi, A. Del Vigna, and M. Ceccaroni, *The evolution of the Line of Variations at close encounters: an analytic approach*, *Celestial Mech. Dynam. Astronom.* **131**(10), 2019
- [130] P. Vereš, D. Farnocchia, S. R. Chesley, and A. B. Chamberlin, *Statistical analysis of astrometric errors for the most productive asteroid surveys*, *Icarus* **296**: 139–149, Nov. 2017
- [131] J. Virtanen, K. Muinonen, and E. Bowell, *Statistical Ranging of Asteroid Orbits*, *Icarus* **154**: 412–431, Dec. 2001
- [132] D. Vokrouhlický, S. R. Chesley, and R. D. Matson, *Orbital Identification for Asteroid 152563 (1992 BF) Through the Yarkovsky Effect*, *AJ* **135**: 2336–2340, June 2008
- [133] D. Vokrouhlický, W. F. Bottke, S. R. Chesley, D. J. Scheeres, and T. S. Statler, *The Yarkovsky and YORP Effects*, in: *Asteroids IV*, ed. by P. Michel, F. E. DeMeo, and W. F. Bottke, University of Arizona Press, 2015: pp. 509–531
- [134] D. Vokrouhlický, D. Farnocchia, D. Čapek, S. R. Chesley, P. Pravec, P. Scheirich, and T. G. Müller, *The Yarkovsky effect for 99942 Apophis*, *Icarus* **252**: 277–283, May 2015
- [135] D. Vokrouhlický, A. Milani, and S. R. Chesley, *Yarkovsky Effect on Small Near-Earth Asteroids: Mathematical Formulation and Examples*, *Icarus* **148**: 118–138, Nov. 2000
- [136] D. Vokrouhlický, D. Čapek, S. R. Chesley, and S. J. Ostro, *Yarkovsky detection opportunities. II. Binary systems*, *Icarus* **179**: 128–138, Dec. 2005
- [137] D. Vokrouhlický, A. Milani, and S. R. Chesley, *Yarkovsky effect on small Near-Earth Asteroids: mathematical formulation and examples*, *Icarus* **148**: 118–138, 2000
- [138] D. Vokrouhlický, M. Brož, W. F. Bottke, D. Nesvorný, and A. Morbidelli, *Yarkovsky/YORP chronology of asteroid families*, *Icarus* **182**: 118–142, May 2006
- [139] C. M. Will, *Theory and Experiment in Gravitational Physics*, Cambridge University Press, Mar. 1993

-
- [140] D. K. Yeomans, P. G. Antreasian, J.-P. Barriot, S. R. Chesley, D. W. Dunham, R. W. Farquhar, J. D. Giorgini, C. E. Helfrich, A. S. Konopliv, J. V. McAdams, J. K. Miller, W. M. Owen, D. J. Scheeres, P. C. Thomas, J. Veverka, and B. G. Williams, *Radio Science Results During the NEAR-Shoemaker Spacecraft Rendezvous with Eros*, *Science* **289**: 2085–2088, Sept. 2000